THE UNIVERSITY OF CHICAGO

CHEMICAL BIOLOGY OF THIOESTERS: (1) CHEMICAL APPROACHES TO PROBE THE REGULATION OF S-PALMITOYLATION; (2) THIOESTER-BASED ACYLATION REAGENT WITH AN ESTER CAGE

A DISSERTATION SUBMITTED TO

THE FACULTY OF THE DIVISION OF THE PHYSICAL SCIENCES

IN CANDIDACY FOR THE DEGREE OF

DOCTOR OF PHILOSOPHY

DEPARTMENT OF CHEMISTRY

BY

TIAN QIU

CHICAGO, ILLINOIS

JUNE 2022

Try to learn something about everything and everything about something.

--Thomas Huxley

I dedicate this thesis to my chemistry enlightenment teacher Ms. Hongfang Zhang, who guided me into the chemistry world; and to my family, whose unconditional love and unwavering support have continuously encouraged me to dream big and never give up.

TABLE OF CONTENTS

LIST OF FIGURES

LIST OF SCHEMES

LIST OF TABLES

ACKNOWLEDGEMENTS

First and foremost, I would like to sincerely thank my mentor Dr. Bryan Dickinson for being extensively engaged throughout the entirety of my Ph.D. Steve keeps open-minded and enthusiastic about almost all kinds of science. He encouraged and motivated me with his passion for chemical. He always had an open door to discuss any successes or failures in the experiments, and offered me lots of opportunities to communicate and collaborate within or outside the lab. This dissertation would not have been possible without Bryan's thoughtful input and constant support

I was extremely fortunate to work with such an amazing group of people throughout my PhD. I would like to thank all current and former members of the Dickinson Lab for creating a professional, collaborative, and friendly working environment. In particular, I would like to take this opportunity to thank the individuals who played a crucial role during my PhD. When I first joined the lab, it was Dr. Michael Beck who patiently introduced me to and familiarized me with many techniques that were vital for my work. Throughout the first 4 years in the Dickinson lab, Dr. Rahul Kathayat acted as my second mentor. Rahul always went above and beyond to give helpful advice and suggestions in response to any scientific or life question I could possibly have. It was often Rahul's thoughtful guidance and input that motivated me to keep trying and pushing projects to their completion. Dr. Saara-Anne Azizi was the first graduate student I have ever mentored in the lab. She is

both the best friend and colleague to me. More than half of my thesis work can't be accomplished without Saara's effort. I also wish to acknowledge other group members who directly worked on the same projects as me: Dr. Somayeh Ahmadiantehrani, Dr. Kaitlin Kentala, Shubhashree Pani, Yang Cao, Tong Lan, Noah Brookes, Anneke Thorne. Their thoughtful suggestions and expert assistance have benefited my projects tremendously.

I would also like to acknowledge my thesis committee members, Professors Chuan He and Yamuna Krishnan, for their time, insights, and support over the last five years.

Finally, I would also like to thank my friends and family for their continued support and encouragement during my Ph.D. They were my bedrock throughout the PhD journey, urging me to push through the difficulties and celebrate the successes, all while reminding me not to lose sight of what is truly most important. I also want to express my special gratitude to Dr. Yue Liu, who have accompanied me through the last 4 years. It would be so hard without her support and help.

ABSTRACT

Thioesters are ubiquitous functional groups in both chemistry and biology owing to their unique chemical properties. Thioester bonds are less stable than ester or amide bonds, but they are relatively stable in physiological environment. My main focus is the chemical biology of thioesters in this thesis. In the first part, I demonstrated the development of several chemical tools to study the protein *S*-palmitoylation, a biological original thioester. These chemical tools including a second-generation fluorescence-based turn-on depalmitoylation probe DPP-5 (Chapter 2) and mitochondrial-targeted APT inhibitor mitoFP (Chapter 3) to probe *S*-palmitoylation “eraser” activity in the live cells, as well as a fluorescence-based turn-on palmitoylation probes for high-throughput screening of *S*-palmitoylation “writer” inhibitors (Chapter 4). Furthermore, I demonstrated how these chemical tools could be applied to biological research by showing the discovery of a mitochondrial *S*-depalmitoylase, ABHD10, and how *S*-depalmitoylation regulates mitochondrial redox homeostasis by one of the ABHD10's substrates, PRDX5. In the second part, I first explored the utility of highly reactive thioester in the biomolecule labeling. Then I employed a bio-orthogonal ester-esterase technology developed by our lab towards the creation of an RNA labeling method via the unique ester-masked enol ester acylating reagents (Chapter 5). It is my hope that chemical tools described in this thesis will facilitate more discoveries in the protein *S*-palmitoyaltion research, which in

turn fuels advancements in pharmacological tools to understand and treat human diseases. I also expect the ester masked thioester system could be further optimized for biomolecule proximity labeling purposes, and also provide insights to the development of novel approaches to mask highly reactive species.

LIST OF PUBLICATIONS

1. **Qiu, T.***; Kathayat, R.S.*; Cao, Y.*; Beck, M.; Dickinson, B.C. A fluorescent probe with improved water solubility permits the analysis of protein S-depalmitoylation activity in live cells. *Biochemistry, **2018**, 57: 221-225. (* co-first authors)*
   (Adapted, Chapter 2)
2. Cao, Y.*, **Qiu, T.***, Kathayat, R.*, Azizi, S.-A., Thorne, A.K., Ahn, D., Fukata, Y., Fukata, M., Rice, P., Dickinson, B.C. ABHD10 is an S-depalmitoylase affecting redox homeostasis through peroxiredoxin-5. *Nature Chemical Biology, **2019**, 15: 1232-1240. (* co-first authors)*
   (Adapted, Chapter 3)
3. **Qiu, T**. and Dickinson, B.C. A stop sign for RAS trafficking. *Nature Chemical Biology, **2021**, 17: 840-841. (News & Views)*
4. Azizi, S.-A., **Qiu, T**., Brookes, N., Dickinson, B.C. Regulation of ERK2 activity by dynamic S-acylation. *eLife, in revision*
5. **Qiu, T**.*, Azizi, S.-A.*, Brookes, N., Lan, T., Dickinson, B.C. A high-throughput fluorescent turn-on assay for inhibitors of DHHC family proteins. *ACS Chemical Biology, in revision. (* co-first authors)*
   (Adapted, Chapter 4)
6. Luebben, A.V., Bender, D., Becker, S., Crowther, L.M.; Erven, I., Hofmann, K., Söding, J., Klemp, H., Bellotti, C., Stäuble, A., **Qiu, T.**, Kathayat, R.S., Dickinson, B.C., Gärtner, J., Sheldrick, G.M., Krätzner, R., Steinfeld, R. Cln5 represents a new type of cysteine-based S-depalmitoylase linked to neurodegeneration. *Science Advance, **2022**, 8, eabj8633*

CHAPTER 1

INTRODUCTION

1.1 General introduction to thioesters

Thioesters are a class of compounds resulting from the bonding of sulfur with an acyl group with the general formula R-S-CO-R'. They are the product of esterification between a carboxylic acid and a thiol. The thioester bond is a common functional group in both chemistry and biology as it displays a wealth of attractive properties[1]. Based on the thiolate species, thioesters can be categorized into S-alkyl thioester and S-aryl thioester. Most biologically relevant thioesters are S-alkyl thioesters due to their higher thermostability compared to S-aryl thioesters.

Thioesters belong to a broader class of acyl compounds. Among biologically relevant acyl compounds, thioesters are more reactive than amides and esters[2]. For example, the transfer of an acyl group from acetyl-CoA to water produces acetic acid (or more properly, its conjugate base acetate, which predominates at neutral pH). This is simply the hydrolysis of acetyl-CoA, and such a hydrolysis has a relatively large negative biochemical standard free energy change (ΔG°') associated with it: ΔG°' = −7.5 kcal/mol (−31.4 kJ/mol), which is slightly more exergonic than hydrolysis of the terminal phosphate of ATP. Acyl-CoA has a relatively high acyl group transfer potential. By comparison, the ΔG°' for hydrolysis of a typical ester is about −5 kcal/mol (−21 kJ/mol). The ester stability is mediated by resonance structures, in which the lone pair of oxygen atom donates electron density to the antibonding orbital of the carbonyl bond. This causes the C-O bond to be partially double-bonded and prevents it from rotating. However, the C-S bond in the thioester does not have as many multiple-bond properties as the C-O bond in the ester,

because the 3p orbital of sulfur does not overlap well with the 2p orbital of carbon[3]. Thus, the carbonyl thioesters have a higher partial positive charge than their corresponding ester carbons, which makes them more likely to be attacked by nucleophiles[4]. Furthermore, thiolates or thiols are both more stable leaving groups, as the larger sulfur atom allows the negative charge to be distributed more evenly[5].

Therefore, the thermodynamic stability of thioesters[6], especially S-alkyl thioester, places them at the center of a reactivity scale toward nucleophile addition, somewhere above unreactive amides and poorly reactive oxoesters, but below overactivated carboxylic acid anhydrides and acyl chlorides. Such an intermediate level of reactivity confers them with the capacity to transfer their acyl group under relatively mild conditions and on a biologically relevant time scale.

S-aryl thioesters, on the other hand, are an important reaction intermediate in organic synthesis. Aryl thiol compounds generally have lower pKa than alkyl thiol compounds, making them a better leaving group in acyl transfer reactions. For example, aryl thiols are widely used as catalysts in the native chemical ligation reaction to boost both thiol-thol exchange reaction and acyl transfer reaction[7].

1.2 Chemical transformation of thioesters

There is a broad range of strategies for thioester synthesis. Esterification of an acyl compound with a thiol compound represents the most widely used approach to synthesize thioesters. Acyl chlorides or anhydrides can react with thiol compounds in the presence of base at ambient temperature. Carboxylic acids can be preactivated by coupling reagents such as ethyl-3(3-dimethylaminopropyl)carbodiimide (EDC)[8,9], dicyclohexylcarbodiimide

(DCC)[10], carbonyldiimidazole (CDI)[11], ynamide[12] or other activation reagents[13,14], then react with thiol compounds to form a thioester. Metal-catalyzed routes for thioester synthesis[15] have also been developed, including carbonylation of olefins and aryl halides, coupling of aryl electrophiles and thiol-carboxylates, and oxidative coupling of aldehydes and thiols.

In organic synthesis, numerous one-step transformations have been developed to make aldehydes[16], ketones[17–19], acids[20], amides[21], esters[22], thioethers[23] or heterocycles[24]. One of the most significant conversions is the transformation of thioesters into amides. A thioester can readily react with a primary or secondary amine to yield an amide at an over 100-fold faster reaction rate compared to oxoester[4].

1.3 Thioesters in biology: Ubiquitin ligase

Ubiquitination is a protein post-translational modification that regulates multiple cellular processes including cell cycle control, DNA repair, signal transduction, and immunity[25]. It requires the sequential interaction and activity of three enzymes (E1, E2, and E3)[26]. Ubiquitin (Ub) can be attached to target proteins in various ways: as a monomeric molecule or as a variety of polymeric chains linked by seven lysine residues or the N-terminal methionine of Ub[27]. The modifications can be removed by isopeptidases[28], and are thus highly dynamic and tightly controlled.

Canonical Ub conjugation cascades entail ATP-dependent Ub adenylation by an E1 activating enzyme, forming a high-energy thioester bond between a Ub and a catalytic cysteine residue on E1. This is followed by the recruitment of E2 conjugating enzymes and the transfer of Ub from the E1 catalytic cysteine to the E2 catalytic cysteine in a process

called E1–E2 thioester transfer (or transthioesterification)[29,30]. Then, an amino group from the substrate attacks the E2-Ub thioester to form an amide bond. This process can be catalyzed either noncovalently or by forming an E3-Ub thioester bond prior to conjugation using E3 protein ligases[31].

Studies have shown that the thioester bond between ubiquitin and Ub ligase is resistant to 'natural' hydrolysis (in absence of any other nucleophile or subsequent ligases)[32]. The long half-life of S-alkyl thioester intermediates relative to the lifespan of short-lived cellular proteins suggests that ubiquitin-like modifications may initiate from thioester intermediates that are already present in cells, instead of always starting from adenylation. Ub ligase-Ub thioester intermediates may act as reservoirs of Ub that react rapidly to external stimuli[33].

1.4 Thioesters in biology: Coenzyme A (CoA)

The most common biologically derived small molecule thioester, Coenzyme A, was identified by Fritz Lipmann in 1946[34] and its structure was determined in 1953[35]. The structure, is composed of the pantothenic acid (vitamin B), cysteamine, and an adenine nucleotide with both a 5'-pyrophosphate and a 3'-monophosphate. Coenzyme A (CoA) functions as a cofactor for numerous enzyme-catalyzed reactions in animal, plant, and microbial metabolism[36,37].

CoA occurs in cells as several forms including free CoA, its acyl-CoA thioester and 4'-phosphopantetheine[38]. Most carboxylic acids must be activated to enter metabolic pathways by conversion to their corresponding acyl-CoA thioesters[39]. The conversion of a carboxyl group to a thioester occurs in biochemical reactions by four main routes: (1)

Esterification of a carboxyl group, driven by ATP hydrolysis: generally, thioesters originate from or interconverted with an acyl phosphate or an acyl adenylate[40], both of which are synthesized from ATP and carboxylic acid via phosphorylation or adenylation. This process is catalyzed by acyl-CoA synthetases[41]; (2) Oxidative decarboxylation of an α-keto acid: under aerobic conditions, pyruvate, originating from glycolysis and β-oxidation of fatty acids, is oxidized in the mitochondria[42]. This irreversible reaction is catalyzed by pyruvate dehydrogenase to generate acetyl-CoA[43]; (3) Thiol exchange reaction; (4) Acyl group exchange reaction. These latter two reactions are not a net synthesis of thioester, rather the use of a thioester intermediate.

As mentioned in 1.1, the S-alkyl thioester has favorable thermodynamic and kinetic properties for acyl-CoA involved biochemical reactions. Thermodynamically, the thioester linkage releases more free energy upon hydrolysis than an oxygen ester. The high transfer potential facilitates the acyl transfer reaction to form a more stable amide and ester bond, or leads to thiol exchange and conversion to acyl phosphate[44]. Kinetically, the pK_a of the thioester α-proton has been reported to be two units less than that of the corresponding oxoester or ketone[45]. The enhanced acidity of thioesters over other carbonyl derivatives serves as an advantage for thioesters for soft enolization. Subsequently, the thioester enolate reacts with an electrophile to form a new carbon-carbon bond, as in the formation of acetoacetate[46] or citrate[47].

1.5 Thioesters in biology: Protein S-palmitoylation

Protein S-acylation refers to the protein post translational modification of the cysteine thiol group by conjugation with long chain fatty acid derived acyl groups via

thioester linkage. These acyl additions can range in length from 16–20 carbons, with palmitate (C16:0) (S-palmitoylation) being the most common form, though myristate (C14:0), palmitoleate (C16:1), stearate (C18:0), oleate (C18:1), and arachidonate (C20:4) have also been observed[48–52]. S-acylation, in particular S-palmitoylation, has attracted much interest in the protein post translational modification field due to the enzymatic regulation of both its addition and removal, as well as its wide-ranging effects on the activity and localization of substrate proteins, with more than 10% of the human proteome susceptible to S-palmitoylation[53,54].

S-palmitoylation is catalyzed by two classes of evolutionarily conserved enzymes: “writers” (protein acyltransferases) catalyze acyl group addition, while “erasers” (acyl protein thioesterases) cleave the resultant thioester bond. In humans, there are 23 known Asp–His–His–Cys (DHHC) domain-containing protein acyltransferases, which are thought to be membrane proteins associated with the Golgi, endoplasmic reticulum and plasma membranes[55,56]. In addition, seven identified metabolic serine hydrolase (mSH) superfamily acyl protein thioesterases are localized primarily in lysosomes (PPT1 and 2) and the cytosol (APT1 and 2; ABHD17A, B and C)[57].

1.5.1 Biological Implications of Protein S-Palmitoylation

Since its discovery in viral envelope glycoproteins over 40 years ago[58,59], protein S-palmitoylation has been documented in a wide range of proteins including cytoskeletal elements[60–62], soluble enzymes[63,64], signal transducers[65–69], scaffolds[70–72], receptors[73,74], ion channels[75–78], and adhesion molecules[79,80]. The incorporation of the hydrophobic palmitate group changes the biochemical and biophysical properties of modified proteins,

affecting their stability, trafficking, localization, activity, and signaling[81–84], all of which have implications for the pathogenogenesis of cancer[85,86], neurodegenerative diseases[87], and microbial infections[88].

1.5.2 Tools and Techniques for Studying Protein S-Palmitoylation

This subchapter describes the basic principles and specific details of the main biochemical approaches that researchers used to study protein S-palmitoylation.

Metabolic labeling by radiolabeled palmitate isotopes: Historically, protein palmitoylation study has been hindered by the lack of efficient, specific, rapid, and highly sensitive detection methods. Traditional methods to detect and quantify palmitoylated proteins have depended on metabolic incorporation of isotope-labeled fatty acids followed by immunoprecipitation[89,90]. In this experiment, cultured cells expressing the target protein are treated with [^{3}H]-palmitate, which is nearly identical to the naturally occurring palmitate, for a duration that depends on the protein and its S-palmitoylation turnover rate. During the treatment time, the [^{3}H]-palmitate will be incorporated into endogenous S-palmitoylation site(s), resulting in radiolabeled protein that can be visualized by autoradiography. Alternatively, a pulse-chase mode could be applied to study dynamic protein S-palmitoylation turnover. After cultured cells have been incubated for a certain time with [^{3}H]-palmitate, the media is swapped with normal [^{1}H]-palmitate, which results in the decrease of radioactivity over time. While this approach is the least perturbative compared to other approaches, described below, it has several drawbacks compared to other metabolic labeling methods. It requires a long exposure time (usually weeks to months), primarily due to the weak radioactive signal. Peseckis et. al. described an improved approach by using

the radioactive iodinated fatty acid analog ω-[^{125}I]-palmitate to yield brighter signals with shorter exposure times[91]. However, the use of radioactive reagents presents serious safety challenges.

Metabolic labeling by clickable palmitate analogs: To avoid the use of radioactive palmitate analogs, clickable fatty acid analogs are synthesized by introducing a small chemical tag (alkyne or azide) at the ω or methyl end of the fatty acid[92]. The small size of the chemical tags minimize interference with fatty acyltransferase substrate recognition and catalytic efficiency. After metabolic incorporation into endogenous S-palmitoylation site by hijacking existing cellular biosynthesis machinery, a bio-orthogonal copper catalyzed Huisgen 1,3-dipolar cycloaddition reaction[93] conjugates the fatty acid-modified proteins to fluorophores or affinity tags (e.g., biotin). Thus, the fatty acid modified proteins, now conjugated with fluorophores, can be visualized by fluorescence microscopy or in-gel fluorescence; those conjugated with biotin can be used for both detection (immunoblot) and enrichment (pulldown). In addition, hydroxylamine treatment at neutral pH selectively cleaves the thioester bond[94], making it suitable for distinguishing the fatty acid modification between amide and thioester linkage.

Both alkyne and azide versions of fatty acid analogues have been developed. The azido fatty acid probes were first developed[95,96] and used to identify 21 putative palmitoylated proteins in the mitochondrial matrix of rat liver cells. Later, the alkyne fatty acid probes were synthesized and showed efficient metabolic incorporation into fatty acylated proteins[97–99]. Alkyne and azide fatty acid probes both effectively labeled cellular fatty acylated proteins. However, metabolic labeling with alkyne fatty acids in combination with azide conjugates exhibited lower background signal than the reverse click partner,

resulting in improved detection sensitivity[100,101]. All these studies demonstrated that Alk-C18 (17-octadecynoic acid or 17-ODYA) can be used to robustly label protein S-palmitoylation.

The metabolic labeling by clickable palmitate analogs has been widely and routinely used in assays studying target protein S-palmitoylation, such as: (1) Validation of target protein S-palmitoylation; (2) Identification and validation of target protein S-palmitoylation site; (3) Visualization of cellular distribution of palmitoylated protein[102–104]; (4) Identification of writers and erasers[84]; (5) Study of target protein S-palmitoylation turnover rate[98]. Most importantly, in combination with quantitative proteomic methods such as stable isotope labeling by amino acid in culture (SILAC)[105], 17-ODYA metabolic labeling can be used to quantify dynamic protein palmitoylation, leading to the discovery of numerous novel palmitoylated proteins[106,107]. For example, Martin et. al. used 17-ODYA metabolic labeling to profile the dynamic protein S-palmitoylation in the presence of a pan-serine hydrolase inhibitor and identified palmitoylation events that were stabilized by lipase inhibition, and those events for which rapid turnover is independent of inhibitor treatment[108].

Despite 17-ODYA metabolic labeling being the least invasive approach compared to others, it suffers two main drawbacks. First, treatment with high concentrations of fatty acid analogues can exert pleiotropic effects on metabolism[40,109]. Palmitate can not only evoke mitochondrial fragmentation but can also cause marked dilation of the endoplasmic reticulum (ER)[110]. Second, the efficiency of metabolic incorporation highly depends on the stability of target protein and its palmitoylation turnover rate[111,112]. Thus, multiple approaches should be applied to validate protein S-palmitoylation.

Acyl-biotin exchange (ABE): The labile nature of S-acylation provides the opportunity for selective cleavage of the thioester bond, exposing a free sulfhydryl group on the cysteine residue to which can be stably attached functionalities such as the biotin affinity group in ABE[113]. In a typical ABE experiment, free cysteine thiols are first alkylated with the thiol-reactive compounds N-ethylmaleimide (NEM), methyl methanethiosulphonate (MMTS)[114], or 2,2'-dithiodipyridine (DTDP)[115]. Half of the sample is then treated with hydroxylamine (HA) under neutral pH to selectively hydrolyze thioester linkages. The negative control is treated identically with the same reaction buffer without HA. The newly generated free thiol group then reacts with another thiol-reactive reagent coupled to an affinity tag like biotin, such as Biotin-HPDP. Stably biotinylated proteins are then enriched with streptavidin agarose beads and can be detected by immunoblot or mass spectroscopy techniques.

The ABE method quantifies protein S-palmitoylation at a given moment, and thus it doesn't depend on the S-palmitoylation turnover rate, making it a more sensitive approach to identify protein S-palmitoylation. However, both false positive and false negative results can occur during the assay. False negative results are mainly caused by the loss of thioester linkage prior to HA treatment. False positive results may come from incomplete thiol alkylation before HA treatment[116] and the enrichment of thioester modifications other than palmitoylation[117]. Thus, both ABE and 17-ODYA metabolic labeling are necessary to validate protein S-palmitoylation: ABE to validate S-acylation and 17-ODYA to validate palmitoylation.

Acyl-resin-assisted capture (Acyl-RAC): Acyl-RAC is a recently described alternative technique[118] derived from a modification of the biotin switch assay for protein S-nitrosothiols

(SNOs)[119]. It works similarly to ABE assays, except the Acyl-RAC assay uses thiol-reactive Sepharose beads to capture free sulfhydryl groups after HA treatment. Compared with the ABE assay, Acyl-RAC uses fewer steps, decreasing the possibility of errors occurring during the assay. However, the Acyl-RAC assay is less robust for the protein targets that I have been working on compared with the ABE assay.

Acyl-PEG exchange (APE): Both ABE and Acyl-RAC assays fail to provide the quantitative information on isoform of target protein S-palmitoylation. To analyze the endogenous levels of protein S-palmitoylation in cells, a mass-tag labeling method based on hydroxylamine-sensitivity of thioesters and selective maleimide modification of cysteines was developed[120,121]. It works similarly to ABE assay except the APE assay uses 5KD or 10KD PEG linked maleimide to capture free sulfhydryl groups after HA treatment, resulting in mobility shifts of S-acylated proteins that can be readily monitored by Western blot of target proteins. Ideally, Acyl-PEG exchange can not only quantify the number of acylation sites, but also show the relative amount of protein in each acylation state. However, some proteins are resistant to PEGylation at cysteine residues, possibly due to steric constraints.

In cellulo imaging techniques. Fluorescence microscopy is routinely used to test the subcellular localization and trafficking of palmitoylated proteins. Typically, the localization of endogenous palmitoylated proteins can be monitored by immunofluorescence, in which cells are fixed and incubated with antibodies raised against the desired proteins to detect the palmitoylated proteins. However, this approach cannot distinguish between unmodified protein and its S-palmitoylation isoformss. To tackle this limitation, Gao et. al. combined 17-ODYA metabolic labeling and proximity ligation assay (PLA) to visualize cellular protein S-palmitoylation at the single protein level[102–104]. An acyl group reporter must be present

on the target protein for a signal to be detected. The major drawback of this method is that it can't monitor dynamic protein S-palmitoylation due to the fixation step.

Exogenously expressed palmitoylated proteins are frequently used to examine the localization of mutant variants[122]. This approach usually requires fusing the target protein to a genetically encoded tag, such HA, FLAG, myc or a fluorescent protein. Fluorescent protein tagging has been used to monitor both steady-state and transient localization for many S-palmitoylated proteins. However, the large size of fluorescent proteins may cause target protein mis-localization[123]. On the other hand, small tags like HA or FLAG have smaller effects on protein localization. But only steady-state localization information can be acquired due to the fixation step.

In conclusion, there is no single assay that can confirm target S-palmitoylation owing to non-overlapping drawbacks and caveats associated with each different assay. Therefore, multiple assays are necessary to validate target protein S-palmitoylation and site identification. When one studies how S-palmitoylation influence target protein localization, *in cellulo* imaging methods can provide direct visualization information, but other types of experiments are needed to confirm the observation.

1.5.3 "Writer": DHHC Protein S-Acyltransferases (DHHC-PATs)

The enzyme that catalyzes S-acylation was found in yeast nearly 20 years after palmitoylation was first discovered[124,125]. Palmitoylation writer enzymes, DHHC Protein S-Acyltransferases (DHHC-PATs), were named after the highly conserved Asp-His-His-Cys tetrapeptide motif in the enzyme active site. Prokaryotes don't encode DHHC-PATs, although bacterial proteins can hijack the DHHC-PATs in eukaryotic hosts[126–128]. In

eukaryotic cells, there are 5-7 DHHC enzymes in yeast and 23 DHHC enzymes in mammals[129]. These enzymes are multidomain integral membrane proteins that localize to organelle membranes such as plasma membrane, Golgi apparatus and endoplasmic reticulum. In recent years, the development of chemical biological tools allowed researchers to study the physiological and pathophysiological function of DHHCs and annotate the substrates for each DHHC isoform.

DHHC proteins use a two-step ping-pong mechanism for catalysis[130]. First, the active site cysteine reacts with acyl-CoA and is autoacylated. Then, the acyl chain is transferred from the DHHC protein to a cysteine residue on the substrate protein. The Asp-His-Cys residues form a catalytic triad in which Asp and His increase the nucleophilicity of the thiol group on cysteine. Point mutations of any of these three amino acids yields a catalytically incompetent enzyme[131]. However, further understanding of the DHHC enzyme mechanism is largely hindered by the lack of high-resolution structures of this family[132].

The first crystal structures of DHHC proteins were reported in 2018[133]. The atomic structures of two different DHHC-PATs, namely human DHHC20 (zDHHC20) and a catalytically inactive mutant of zebrafish zDHHC15 (zfDHHS15) were determined, as well as the structure of zDHHC20 in complex with the suicide inhibitor 2-bromopalmitate (2BP)[134]. The structures reveal that the four transmembrane (TM) helices of DHHC-PATs form a teepee-like structure, with the DHHC cysteine-rich domain (DHHC-CRD) and the C terminus projecting into the cytosol. Two zinc ions bind to the DHHC-CRD in CCHC zinc-finger domain[135] that impart structure stability and help position the active site cysteine. Above the active site, four TM helices form a cavity where the acyl chain of acyl-CoA is inserted. The structure also points to key hydrophobic residues on the TM helices and

cavity lining that likely determine acyl chain recognition and chain-length selectivity. In addition, the zDHHC20 structure also suggests the existence of a basic patch for CoA binding, which was confirmed by recent study from the same group[136]. In this new work, Banerjee group combines X-ray crystallography with all-atom molecular dynamics simulations to elucidate the structure of the precatalytic complex of human zDHHC20 in complex with palmitoyl-CoA. The structure confirms that the CoA headgroup binds to the basic patch though polar and ionic interactions and palmitoyl-CoA acts as a bivalent ligand where the interaction of the DHHC enzyme with both the fatty acyl chain and the CoA headgroup is important for catalytic chemistry to proceed.

It is worth noting that the structures determined so far are essentially identical, despite the different catalytic states, origin species, DHHC members and crystallization conditions. Alphafold prediction gives similar structures across all 23 human DHHC isoforms[137,138], suggesting the DHHC family enzymes may share similar structural features.

Another intriguing aspect about DHHC-PATs has been the mechanisms of substrate recognition since certain DHHC-PATs feature protein-protein interaction domains. Among the human DHHC isoforms, DHHC3, 7, 5, 8, 14, 16, 17, 20, and 21 are predicted to have PDZ-binding motifs, and DHHC6 is predicted to have an SH3 domain[139]. Some DHHC-PATs have also been shown to interact quite specifically with their substrates[140,141], but no crystal structure of the full-length DHHC-PAT-substrate complex has yet been reported, except the crystal structure of the complex of the ankyrin-repeat (AR) domain of DHHC17 with SNAP25 peptide fragment[142]. Several studies have shown that DHHC-PATs can work on multiple substrates and individual substrates can be S-acylated by multiple DHHC-PATs[143–146]. However, a comprehensive analysis of the key motifs and/or domains that

govern enzyme-substrate interactions is required to understand the biological function of DHHC-PATs and provide insights to develop selective inhibitors against individual DHHC-PATs isoform.

1.5.4 DHHC inhibitors

Although genetic tools have already been widely used to perturb activity of DHHC-PATs to gain insights into their cellular function, compensatory effects among DHHC-PATs remain the major drawback. In addition, genetic perturbation often requires long experimental time periods, makes it unsuitable to study the temporal regulation of DHHC-PATs. Thus, chemical perturbation is an attractive approach to study the highly dynamic S-palmitoylation process. However, DHHC inhibitor development remains scant due to the lack of robust high-throughput assays for DHHCs. Recently, the acylation-coupled lipophilic induction of polarization (Acyl-cLIP) assay was successfully adapted for DHHC-PATs[147–149]. In this assay, a 5-carboxyfluorescein–tagged peptide from human NRas (aa177-189) is palmitoylated by DHHC-PATs and inserted into detergent micelles, resulting in a change in fluorescence polarization (FP). In our group, this assay achieves a z-value of ~0.7, suggesting the potential application for high-throughput screening. But the assay suffers from limited dynamic range, and also requires a relatively large amount of protein, which is difficult to purify.

As mentioned above, only a limited number of poorly defined DHHC inhibitors have been reported. Lipid-based covalent inhibitors represent the largest group of DHHC inhibitors that feature an aliphatic chain that can presumably insert into DHHC lipid binding pocket and an electrophilic warhead for covalent cysteine binding. Of previously reported

lipid based covalent inhibitors, including 2-bromopalmitate (2BP)[134], tunicamycin[150] and cerulenin[151], 2BP remains the most routinely used agent for the study of S-acylation in cells. However, the low potency, poor selectivity[152,153] and high cytotoxicity[154] curtail their application. In addition, 2-BP has also shown to inhibit APT enzyme activity within its range of working concentrations in cells[155]. Therefore, extra caution should be considered when applying 2BP as a putative DHHC inhibitor.

The major drawbacks of 2BP come from poor amino acid selectivity of highly active α-bromo carbonyl group[156] and potential metabolic conversion of carboxylate into CoA moieties in cells[157]. To develop a pan inhibitor with improved specificity and selectivity against DHHC-PATs, our group recently disclosed an acrylamide-based zDHHC inhibitor, CMA, which has decreased cytotoxicity and an altered reactivity profile as compared to 2BP[149]. CMA features a C14 linear alkyl chain and an N-cyanomethyl group, it shows slightly improved inhibition in Acyl-cLIP assay, less toxicity and an altered reactivity profile as compared to 2BP. However, CMA is also a lipid-based covalent inhibitor and preliminary proteomics reveals it could potentially react with over 270 protein targets in HEK293T cells.

Non-lipid based small molecules are particularly appealing as they might be able to avoid off-targets caused by lipid binding. Screens that focus on S-acylation of particular proteins have revealed several inhibitors with diverse scaffolds. Several peptides derived from putative binding interface were also shown to inhibit S-acylation of specific targets in cells[158,159].

Taken together, current DHHC inhibitors highlight the need for novel small molecules with high affinity and good selectivity against DHHC-PATs to assign biological roles to enzymes and substrates associated with their widespread modification. The

development of robust methods for both the study of DHHC proteins as well as for high-throughput screening and optimizing inhibitors requires a profound biological and biochemical understanding of the DHHC proteins. Furthermore, due to the growing recognition of the important roles of palmitoylation in human pathophysiology, targeted DHHC isoform-specific inhibitors not only provide useful pharmacological tools, may prove beneficial in treating various human diseases.

1.5.5 "Eraser": Acyl protein thioesterase (APT)

The first enzymes that catalyze the S-deacylation were discovered earlier than DHHC-PATs[160,161]. Most palmitoylation eraser enzymes, acyl protein thioesterase (APT), belong to the metabolic serine hydrolase (mSH) superfamily including APT1/2, PPT1, and ABHD17A/B/C. Several APT structures have been solved and they reveal some common features of APTs[162–168]. All known APTs share a characteristic α/β-hydrolase fold, a hydrophobic cleft that accommodates the acyl chain and an active site S-H-D catalytic triad[57]. Mechanistically, the carboxylate side chain of aspartic acid serves as a general base to activate serine nucleophile, then hydroxylate side chain of serine attacks the thioester carbonyl group to scissile the bond, resulting in a fatty acid ester. A water molecule then hydrolyses the ester to release the fatty acid product and regenerate the free serine residue for entry into the next reaction cycle of the active enzyme[169].

The development of the activity-based protein profiling (ABPP) technique provides a robust and powerful tool to assay serine hydrolase family protein, including APTs[170]. In a typical assay for serine hydrolase profiling, a reporter-tagged fluorophosphate probe is added to a complex proteome to covalently react with serine hydrolase protein. Typically,

FP-tetramethylrhodamine (FP-TAMRA) is used for rapid gel-based analysis and FP-Biotin is used for mass-spectrometry based quantitative analysis. Slight modification of the ABPP workflow makes the assay suitable for inhibitor identification. The so-called competitive-ABPP assay contains a small molecule pretreatment step prior to the reaction with FP-TAMRA; any reduction in probe labeling thus corresponds to inhibition[171]. Competitive-ABPP lead to the discovery of several highly potent and specific APT inhibitors that have been widely used to study the biological function of APTs.

In addition, to understand dynamic APT regulation, our group has developed both turn-on and ratiometric fluorescent probes to monitor APT activity in physiological contexts. Turn-on depalmitoylation probes (DPPs) feature an S-acylated cysteine conjugated to a pro-fluorescent molecule via a carbamate linker. Enzymatic de-acylation generates a free thiol on the cysteine, which triggers a rapid cyclization reaction and releases a fluorescent product[172]. An S-octanoyl cysteine surrogate was used instead of S-palmitoyl cysteine to improve solubility for application in live cells, yielding DPP-2 probes that can robustly detect APT activity *in cellulo*. Modification of DPP-2 with an additional lysine group to mimic APT1 substrate HRas[173] yields DPP-3 that has a preferred detection of APT1 over APT2. Deployment of DPP-3 in A431 cells successfully revealed that rapid growth factor stimulation results in the inhibition of APT activity. To study mitochondrial APT activity, mitoDPP-2 and mitoDPP-3 were synthesized[123]. Based on DPP-2 and DPP-3, they were equipped with an extra triphenylphosphonium (TPP) group for mitochondria targeting[174]. We observed active APT activity in mitochondria, and further established that APT1, which is previously assumed to reside in the cytosol and on the Golgi apparatus, is also localized to mitochondria.

Ratiometric probes (RDPs) feature an α, β-unsaturated cyanoacetamide linker between a coumarin fluorophore and a S-octanoyl cysteine. The free thiol generated from APT S-deacylation proceed intramolecular Michael addition reaction, resulting in the decreased π-system and blue-shifting the fluorophore emission[175]. The fluorescence ratio of deprotected (λem = 470 nm) to protected (λem = 575 nm) RDPs permits normalization of fluorescent signal to probe concentration. RDPs were successfully applied to monitor APT activity in colon organoids, an *ex vivo* model of human metabolism.

1.5.6 APT inhibitors

Both reversible and irreversible APT inhibitors with various structure scaffolds have been developed, including Benzodiazepinediones[176], β-Lactones[177–179], Boronic acids[180], Triazole urea[181,182], Chloroisocoumarins[183], Piperazine amides[184], Fluorophosphate[108].

Palmostatin B/M (PalmB/M) are the most commonly used pan-APT inhibitors, due to their high potency (APT1 IC_{50} = 5.4 nM for PalmB and 2.5 nM for PalmM)[177–179]. Treatment of PalmB or PalmM induces NRas mis-localization from the plasma membrane and partially restores E-Cadherin localization at cell–cell junctions. However, siRNA knockdown of APT1 did not statistically alter the N-Ras localization, which suggests that PalmB inhibits other APTs. Indeed, the latter study used ABPP to identify ABHD17A/B/C as additional targets of PalmB, and these enzymes can regulate N-Ras palmitate turnover and subcellular localization[185]. This observation is further validated by showing ABD957, a potent and selective covalent inhibitor of the ABHD17 family proteins, can impair N-Ras depalmitoylation and localization[186]. In addition, ABD957 impaired N-Ras signaling and worked in synergy with the MEK inhibitor PD901 to hamper cell growth in N-Ras mutant

cancer cells, which suggests that ABHD17 inhibitors may have value as targeted therapies for NRAS-mutant cancers.

APT1 and APT2 have 68% sequence identity[187], therefore immense effort has been made to develop isoform specific inhibitor. Ultimately, a high-throughput screening effort used a fluorescence polarization-based competitive ABPP assay against both APT1 and APT2 reveals common piperazine amide chemotype[181], but diverges through additional modifications to impart isoform selectivity. Further optimization leads to the highly potent and isoform selective inhibitor ML348 for APT1, and ML349 for APT2[184].

1.6 Current Challenges, Opportunities

Christian de Duve[188] once proposed a Hadean “Thioester World” which should have preceded the succeeding the RNA world. The “Thioester World” represents a very early hypothetical stage in the origin of life in which thioesters provided the energetic and catalytic framework via its high-energy bond and high acyl transfer reactivity. The thioester world is an important hypothesis in the understanding of early life processes, and may explain essential reactions expected in the prebiotic world. Even in modern life, thioesters are still considered as an important biological species.

In particular, protein S-palmitoylation has drawn lots of attention in recent decades as the modification itself and the enzymes that catalyze the reversible reaction are implicated in a number of diseases. Our knowledge of the therapeutic relevance of this modification increased with the development of chemical tools to assay or perturb this enzymatic process.

The first DHHC-PAT structures provide an atomic view of how the palmitoyl group is recognized and transferred, and novel *in vitro* screening assays allow the development of more potent and safer DHHC inhibitors[189]. Better high-throughput screening assays are urgently needed to accelerate the pace to discover diverse scaffold for more potent and selective DHHC inhibitors.

The novel imaging probes and selective APT inhibitors have greatly boosted the S-depalmitoylation study, and provide a more discriminating view to dissect the biological function of each APT[190]. However, it is possible that more APTs remain uncovered, based on the fact that genetic knockdown of known APTs has little effect on target protein S-palmitoylation. Development of second generation DPPs with improved S-depalmitoylase selectivity will provide a robust tool to help annotate new APTs. In addition, localized targeted chemical tools will provide opportunities to explore new biology in specific organelles.

Apart from its biological relevance, thioesters are also widely used in chemistry. For example, thioester-based polymers have been synthesized[191,192]. Introducing thioesters in place of ester or amide analogues allows the modification of polymer thermal properties without compromising structural similarity. Further thioester functionalization via exchange reactions and amidation are well established in incorporating further functionalities. Another example is the use of an aryl thiol compound as a catalyst to generate more reactive S-aryl thioesters in native chemical ligation. The unique chemical properties of thioesters provides opportunities to develop novel chemical biology tools[193]. The second part of this thesis will present the development of a thioester-based acylation reagent with an ester cage.

1.7 Scope of this Thesis

Chapter 2 presents the development of a new generation of DPPs to improve the specificity of S-depalmitoylase detection.

Chapter 3 presents the development of a novel mitochondrial-targeted APT inhibitor to elucidate how mitochondrial APT regulates antioxidant buffering in that organelle, and the identification of ABHD10 as a novel mitochondrial APT that regulates mitochondrial redox homeostasis through PRDX5 activation.

Chapter 4 introduces a turn-on fluorescence based high-throughput screening assay for DHHC-PATs.

Chapter 5 presents the design and synthesis of an ester caged thioester acylation reagent for RNA labeling.

Chapter 6 summarizes this dissertation, and provides a broader perspective and outlook.

1.8 References

(1) Bracher, P. J.; Snyder, P. W.; Bohall, B. R.; Whitesides, G. M. The relative rates of thiol-thioester exchange and hydrolysis for alkyl and aryl thioalkanoates in water. *Origins of life and evolution of the biosphere : the journal of the International Society for the Study of the Origin of Life* 2011, *41* (5), 399–412. DOI: 10.1007/s11084-011-9243-4. Published Online: Jul. 5, 2011.

(2) JENCKS, W. P.; CORDES, S.; CARRIUOLO, J. The free energy of thiol ester hydrolysis. *The Journal of biological chemistry* 1960, *235*, 3608–3614.

(3) Marlier, J. F.; Fogle, E. J.; Redman, R. L.; Stillman, A. D.; Denison, M. A.; Robins, L. I. A mechanistic study of thioester hydrolysis with heavy atom kinetic isotope effects. *The Journal of organic chemistry* 2015, *80* (3), 1905–1908. DOI: 10.1021/jo502472m. Published Online: Jan. 12, 2015.

(4) Yang, W.; Drueckhammer, D. G. Understanding the relative acyl-transfer reactivity of oxoesters and thioesters: computational analysis of transition state delocalization effects.

Journal of the American Chemical Society 2001, *123* (44), 11004–11009. DOI: 10.1021/ja010726a.

(5) Koval', I. V. Synthesis, Structure, and Physicochemical Characteristics of Thiols. *Russ J Org Chem* 2005, *41* (5), 631–648. DOI: 10.1007/s11178-005-0220-0.

(6) Worrell, B. T.; Mavila, S.; Wang, C.; Kontour, T. M.; Lim, C.-H.; McBride, M. K.; Musgrave, C. B.; Shoemaker, R.; Bowman, C. N. A user's guide to the thiol-thioester exchange in organic media: scope, limitations, and applications in material science. *Polym. Chem.* 2018, *9* (36), 4523–4534. DOI: 10.1039/C8PY01031E.

(7) Dawson, P. E.; Muir, T. W.; Clark-Lewis, I.; Kent, S. B. Synthesis of proteins by native chemical ligation. *Science (New York, N.Y.)* 1994, *266* (5186), 776–779. DOI: 10.1126/science.7973629.

(8) Jordan, A.; Sneddon, H. F. Development of a solvent-reagent selection guide for the formation of thioesters. *Green Chem.* 2019, *21* (8), 1900–1906. DOI: 10.1039/C9GC00355J.

(9) Bonnett, S. A.; Whicher, J. R.; Papireddy, K.; Florova, G.; Smith, J. L.; Reynolds, K. A. Structural and stereochemical analysis of a modular polyketide synthase ketoreductase domain required for the generation of a cis-alkene. *Chemistry & biology* 2013, *20* (6), 772–783. DOI: 10.1016/j.chembiol.2013.04.014.

(10) Neises, B.; Steglich, W. Simple Method for the Esterification of Carboxylic Acids. *Angew. Chem. Int. Ed. Engl.* 1978, *17* (7), 522–524. DOI: 10.1002/anie.197805221.

(11) Klopries, S.; Sundermann, U.; Schulz, F. Quantification of N-acetylcysteamine activated methylmalonate incorporation into polyketide biosynthesis. *Beilstein journal of organic chemistry* 2013, *9*, 664–674. DOI: 10.3762/bjoc.9.75. Published Online: Apr. 5, 2013.

(12) Wang, X.; Zhao, Y.; Yang, J.; Li, Y.; Luo, Y.; Xu, M.; Zhao, J. Ynamide-Mediated Thioester Synthesis. *The Journal of organic chemistry* 2021, *86* (24), 18265–18277. DOI: 10.1021/acs.joc.1c01949. Published Online: Dec. 7, 2021.

(13) Iranpoor, N.; Firouzabadi, H.; Khalili, D.; Motevalli, S. Easily prepared azopyridines as potent and recyclable reagents for facile esterification reactions. An efficient modified mitsunobu reaction. *The Journal of organic chemistry* 2008, *73* (13), 4882–4887. DOI: 10.1021/jo8000782. Published Online: May. 31, 2008.

(14) Chou, Y.-L.; Jhong, Y.; Swain, S. P.; Hou, D.-R. Microwave-Assisted Direct Thioesterification of Carboxylic Acids. *The Journal of organic chemistry* 2017, *82* (19), 10201–10208. DOI: 10.1021/acs.joc.7b01705. Published Online: Sep. 18, 2017.

(15) Hirschbeck, V.; Gehrtz, P. H.; Fleischer, I. Metal-Catalyzed Synthesis and Use of Thioesters: Recent Developments. *Chemistry (Weinheim an der Bergstrasse, Germany)* 2018, *24* (28), 7092–7107. DOI: 10.1002/chem.201705025. Published Online: Feb. 5, 2018.

(16) Fukuyama, T.; Lin, S. C.; Li, L. Facile reduction of ethyl thiol esters to aldehydes: application to a total synthesis of (+)-neothramycin A methyl ether. *Journal of the American Chemical Society* 1990, *112* (19), 7050–7051. DOI: 10.1021/ja00175a043.

(17) Mukaiyama, T.; Araki, M.; Takei, H. Reaction of S-(2-pyridyl) thioates with Grignard reagents. Convenient method for the preparation of ketones. *Journal of the American Chemical Society* 1973, *95* (14), 4763–4765. DOI: 10.1021/ja00795a055.

(18) Gehrtz, P. H.; Kathe, P.; Fleischer, I. Nickel-Catalyzed Coupling of Arylzinc Halides with Thioesters. *Chemistry (Weinheim an der Bergstrasse, Germany)* 2018, *24* (35), 8774–8778. DOI: 10.1002/chem.201801887. Published Online: May. 25, 2018.

(19) Wang, J.; Cary, B. P.; Beyer, P. D.; Gellman, S. H.; Weix, D. J. Ketones from Nickel-Catalyzed Decarboxylative, Non-Symmetric Cross-Electrophile Coupling of Carboxylic Acid Esters. *Angew. Chem. Int. Ed. Engl.* 2019, *58* (35), 12081–12085. DOI: 10.1002/anie.201906000. Published Online: Jul. 30, 2019.

(20) Iimura, S.; Manabe, K.; Kobayashi, S. Hydrophobic polymer-supported catalyst for organic reactions in water: acid-catalyzed hydrolysis of thioesters and transprotection of thiols. *Organic letters* 2003, *5* (2), 101–103. DOI: 10.1021/ol026906m.

(21) Davis, A. P.; Walsh, J. J. Amide bond formation via pentafluorothiophenyl active esters. *Tetrahedron Letters* 1994, *35* (27), 4865–4868. DOI: 10.1016/S0040-4039(00)76989-9.

(22) Masamune, S.; Kamata, S.; Schilling, W. Letter: Syntheses of macrolide antibiotics. III. Direct ester and lactone synthesis from S-tert-butyl thioate (thiol ester). *Journal of the American Chemical Society* 1975, *97* (12), 3515–3516. DOI: 10.1021/ja00845a039.

(23) Ichiishi, N.; Malapit, C. A.; Woźniak, Ł.; Sanford, M. S. Palladium- and Nickel-Catalyzed Decarbonylative C-S Coupling to Convert Thioesters to Thioethers. *Organic letters* 2018, *20* (1), 44–47. DOI: 10.1021/acs.orglett.7b03305. Published Online: Dec. 7, 2017.

(24) Alvarez-Ibarra, C.; Mendoza, M.; Orellana, G.; Quiroga, M. L. A Novel Method of Synthesis of 2-Methylthio-1,3-oxazoles. *Synthesis* 1989, *1989* (07), 560–562. DOI: 10.1055/s-1989-27320.

(25) Swatek, K. N.; Komander, D. Ubiquitin modifications. *Cell research* 2016, *26* (4), 399–422. DOI: 10.1038/cr.2016.39. Published Online: Mar. 25, 2016.

(26) Cappadocia, L.; Lima, C. D. Ubiquitin-like Protein Conjugation: Structures, Chemistry, and Mechanism. *Chemical reviews* 2018, *118* (3), 889–918. DOI: 10.1021/acs.chemrev.6b00737. Published Online: Feb. 24, 2017.

(27) Yau, R.; Rape, M. The increasing complexity of the ubiquitin code. *Nature cell biology* 2016, *18* (6), 579–586. DOI: 10.1038/ncb3358.

(28) Lam, Y. A.; Xu, W.; DeMartino, G. N.; Cohen, R. E. Editing of ubiquitin conjugates by an isopeptidase in the 26S proteasome. *Nature* 1997, *385* (6618), 737–740. DOI: 10.1038/385737a0.

(29) Olsen, S. K.; Lima, C. D. Structure of a ubiquitin E1-E2 complex: insights to E1-E2 thioester transfer. *Molecular cell* 2013, *49* (5), 884–896. DOI: 10.1016/j.molcel.2013.01.013. Published Online: Feb. 14, 2013.

(30) Yuan, L.; Lv, Z.; Adams, M. J.; Olsen, S. K. Crystal structures of an E1-E2-ubiquitin thioester mimetic reveal molecular mechanisms of transthioesterification. *Nature*

communications 2021, *12* (1), 2370. DOI: 10.1038/s41467-021-22598-y. Published Online: Apr. 22, 2021.

(31) Dove, K. K.; Stieglitz, B.; Duncan, E. D.; Rittinger, K.; Klevit, R. E. Molecular insights into RBR E3 ligase ubiquitin transfer mechanisms. *EMBO reports* 2016, *17* (8), 1221–1235. DOI: 10.15252/embr.201642641. Published Online: Jun. 16, 2016.

(32) Song, J.; Wang, J.; Jozwiak, A. A.; Hu, W.; Swiderski, P. M.; Chen, Y. Stability of thioester intermediates in ubiquitin-like modifications. *Protein science : a publication of the Protein Society* 2009, *18* (12), 2492–2499. DOI: 10.1002/pro.254.

(33) Takada, K.; Hirakawa, T.; Yokosawa, H.; Okawa, Y.; Taguchi, H.; Ohkawa, K. Isolation of ubiquitin-E2 (ubiquitin-conjugating enzyme) complexes from erythroleukaemia cells using immunoaffinity techniques. *The Biochemical journal* 2001, *356* (Pt 1), 199–206. DOI: 10.1042/0264-6021:3560199.

(34) Lipmann, F. ACETYLATION OF SULFANILAMIDE BY LIVER HOMOGENATES AND EXTRACTS. *The Journal of biological chemistry* 1945, *160* (1), 173–190. DOI: 10.1016/S0021-9258(18)43110-9.

(35) BEINERT, H. Enzymatic synthesis and structure of CoA: Discussion. *Federation proceedings* 1953, *12* (3), 681–682.

(36) Leonardi, R.; Zhang, Y.-M.; Rock, C. O.; Jackowski, S. Coenzyme A: back in action. *Progress in lipid research* 2005, *44* (2-3), 125–153. DOI: 10.1016/j.plipres.2005.04.001. Published Online: Apr. 20, 2005.

(37) Mignani, L.; Gnutti, B.; Zizioli, D.; Finazzi, D. Coenzyme a Biochemistry: From Neurodevelopment to Neurodegeneration. *Brain sciences* 2021, *11* (8). DOI: 10.3390/brainsci11081031. Published Online: Aug. 2, 2021.

(38) Grevengoed, T. J.; Klett, E. L.; Coleman, R. A. Acyl-CoA metabolism and partitioning. *Annual review of nutrition* 2014, *34*, 1–30. DOI: 10.1146/annurev-nutr-071813-105541. Published Online: Apr. 10, 2014.

(39) Trefely, S.; Lovell, C. D.; Snyder, N. W.; Wellen, K. E. Compartmentalised acyl-CoA metabolism and roles in chromatin regulation. *Molecular metabolism* 2020, *38*, 100941. DOI: 10.1016/j.molmet.2020.01.005. Published Online: Feb. 14, 2020.

(40) Li, L. O.; Klett, E. L.; Coleman, R. A. Acyl-CoA synthesis, lipid metabolism and lipotoxicity. *Biochimica et biophysica acta* 2010, *1801* (3), 246–251. DOI: 10.1016/j.bbalip.2009.09.024. Published Online: Oct. 8, 2009.

(41) Soupene, E.; Kuypers, F. A. Mammalian long-chain acyl-CoA synthetases. *Experimental biology and medicine (Maywood, N.J.)* 2008, *233* (5), 507–521. DOI: 10.3181/0710-MR-287. Published Online: Mar. 28, 2008.

(42) Martínez-Reyes, I.; Chandel, N. S. Mitochondrial TCA cycle metabolites control physiology and disease. *Nature communications* 2020, *11* (1), 102. DOI: 10.1038/s41467-019-13668-3. Published Online: Jan. 3, 2020.

(43) Patel, M. S.; Nemeria, N. S.; Furey, W.; Jordan, F. The pyruvate dehydrogenase complexes: structure-based function and regulation. *The Journal of biological chemistry*

2014, *289* (24), 16615–16623. DOI: 10.1074/jbc.R114.563148. Published Online: May. 5, 2014.

(44) Lu, Y.-J.; Zhang, F.; Grimes, K. D.; Lee, R. E.; Rock, C. O. Topology and active site of PlsY: the bacterial acylphosphate:glycerol-3-phosphate acyltransferase. *The Journal of biological chemistry* 2007, *282* (15), 11339–11346. DOI: 10.1074/jbc.M700374200. Published Online: Feb. 16, 2007.

(45) Bordwell, F. G.; Fried, H. E. Heterocyclic aromatic anions with 4n + 2 .pi.-electrons. *J. Org. Chem.* 1991, *56* (13), 4218–4223. DOI: 10.1021/jo00013a027.

(46) Staunton, J.; Weissman, K. J. Polyketide biosynthesis: a millennium review. *Natural product reports* 2001, *18* (4), 380–416. DOI: 10.1039/A909079G.

(47) Wiegand, G.; Remington, S. J. Citrate synthase: structure, control, and mechanism. *Annual review of biophysics and biophysical chemistry* 1986, *15*, 97–117. DOI: 10.1146/annurev.bb.15.060186.000525.

(48) O'Brien, P. J.; St Jules, R. S.; Reddy, T. S.; Bazan, N. G.; Zatz, M. Acylation of disc membrane rhodopsin may be nonenzymatic. *The Journal of biological chemistry* 1987, *262* (11), 5210–5215. DOI: 10.1016/S0021-9258(18)61175-5.

(49) Hallak, H.; Muszbek, L.; Laposata, M.; Belmonte, E.; Brass, L. F.; Manning, D. R. Covalent binding of arachidonate to G protein alpha subunits of human platelets. *The Journal of biological chemistry* 1994, *269* (7), 4713–4716.

(50) Liang, X.; Nazarian, A.; Erdjument-Bromage, H.; Bornmann, W.; Tempst, P.; Resh, M. D. Heterogeneous fatty acylation of Src family kinases with polyunsaturated fatty acids regulates raft localization and signal transduction. *The Journal of biological chemistry* 2001, *276* (33), 30987–30994. DOI: 10.1074/jbc.M104018200. Published Online: Jun. 21, 2001.

(51) Liang, X.; Lu, Y.; Neubert, T. A.; Resh, M. D. Mass spectrometric analysis of GAP-43/neuromodulin reveals the presence of a variety of fatty acylated species. *The Journal of biological chemistry* 2002, *277* (36), 33032–33040. DOI: 10.1074/jbc.M204607200. Published Online: Jun. 24, 2002.

(52) Wilson, J. P.; Raghavan, A. S.; Yang, Y.-Y.; Charron, G.; Hang, H. C. Proteomic analysis of fatty-acylated proteins in mammalian cells with chemical reporters reveals S-acylation of histone H3 variants. *Molecular & cellular proteomics : MCP* 2011, *10* (3), M110.001198. DOI: 10.1074/mcp.M110.001198. Published Online: Nov. 14, 2010.

(53) Blanc, M.; David, F.; Abrami, L.; Migliozzi, D.; Armand, F.; Bürgi, J.; van der Goot, F. G. SwissPalm: Protein Palmitoylation database. *F1000Research* 2015, *4*, 261. DOI: 10.12688/f1000research.6464.1. Published Online: Jul. 16, 2015.

(54) Blanc, M.; David, F. P. A.; van der Goot, F. G. SwissPalm 2: Protein S-Palmitoylation Database. *Methods in molecular biology (Clifton, N.J.)* 2019, *2009*, 203–214. DOI: 10.1007/978-1-4939-9532-5_16.

(55) Greaves, J.; Chamberlain, L. H. DHHC palmitoyl transferases: substrate interactions and (patho)physiology. *Trends in biochemical sciences* 2011, *36* (5), 245–253. DOI: 10.1016/j.tibs.2011.01.003. Published Online: Mar. 8, 2011.

(56) Korycka, J.; Łach, A.; Heger, E.; Bogusławska, D. M.; Wolny, M.; Toporkiewicz, M.; Augoff, K.; Korzeniewski, J.; Sikorski, A. F. Human DHHC proteins: a spotlight on the hidden player of palmitoylation. *European journal of cell biology* 2012, *91* (2), 107–117. DOI: 10.1016/j.ejcb.2011.09.013. Published Online: Dec. 16, 2011.

(57) Won, S. J.; Cheung See Kit, M.; Martin, B. R. Protein depalmitoylases. *Critical reviews in biochemistry and molecular biology* 2018, *53* (1), 83–98. DOI: 10.1080/10409238.2017.1409191. Published Online: Dec. 14, 2017.

(58) Schmidt, M. F.; Bracha, M.; Schlesinger, M. J. Evidence for covalent attachment of fatty acids to Sindbis virus glycoproteins. *Proceedings of the National Academy of Sciences of the United States of America* 1979, *76* (4), 1687–1691. DOI: 10.1073/pnas.76.4.1687.

(59) Schlesinger, M. J.; Magee, A. I.; Schmidt, M. F. Fatty acid acylation of proteins in cultured cells. *The Journal of biological chemistry* 1980, *255* (21), 10021–10024.

(60) Planey, S. L.; Keay, S. K.; Zhang, C.-O.; Zacharias, D. A. Palmitoylation of cytoskeleton associated protein 4 by DHHC2 regulates antiproliferative factor-mediated signaling. *Molecular biology of the cell* 2009, *20* (5), 1454–1463. DOI: 10.1091/mbc.E08-08-0849. Published Online: Jan. 14, 2009.

(61) Navarro-Lérida, I.; Sánchez-Perales, S.; Calvo, M.; Rentero, C.; Zheng, Y.; Enrich, C.; Del Pozo, M. A. A palmitoylation switch mechanism regulates Rac1 function and membrane organization. *The EMBO journal* 2012, *31* (3), 534–551. DOI: 10.1038/emboj.2011.446. Published Online: Dec. 9, 2011.

(62) Wang, X.; Qian, P.; Cui, H.; Yao, L.; Yuan, J. A protein palmitoylation cascade regulates microtubule cytoskeleton integrity in Plasmodium. *The EMBO journal* 2020, *39* (13), e104168. DOI: 10.15252/embj.2019104168. Published Online: May. 12, 2020.

(63) Gonzalo, S.; Linder, M. E. SNAP-25 palmitoylation and plasma membrane targeting require a functional secretory pathway. *Molecular biology of the cell* 1998, *9* (3), 585–597. DOI: 10.1091/mbc.9.3.585.

(64) Greaves, J.; Gorleku, O. A.; Salaun, C.; Chamberlain, L. H. Palmitoylation of the SNAP25 protein family: specificity and regulation by DHHC palmitoyl transferases. *The Journal of biological chemistry* 2010, *285* (32), 24629–24638. DOI: 10.1074/jbc.M110.119289. Published Online: Jun. 2, 2010.

(65) Song, S.-P.; Hennig, A.; Schubert, K.; Markwart, R.; Schmidt, P.; Prior, I. A.; Böhmer, F.-D.; Rubio, I. Ras palmitoylation is necessary for N-Ras activation and signal propagation in growth factor signalling. *The Biochemical journal* 2013, *454* (2), 323–332. DOI: 10.1042/BJ20121799.

(66) Akimzhanov, A. M.; Boehning, D. Rapid and transient palmitoylation of the tyrosine kinase Lck mediates Fas signaling. *Proceedings of the National Academy of Sciences of the United States of America* 2015, *112* (38), 11876–11880. DOI: 10.1073/pnas.1509929112. Published Online: Sep. 8, 2015.

(67) Runkle, K. B.; Kharbanda, A.; Stypulkowski, E.; Cao, X.-J.; Wang, W.; Garcia, B. A.; Witze, E. S. Inhibition of DHHC20-Mediated EGFR Palmitoylation Creates a Dependence on EGFR Signaling. *Molecular cell* 2016, *62* (3), 385–396. DOI: 10.1016/j.molcel.2016.04.003.

(68) Busquets-Hernández, C.; Triola, G. Palmitoylation as a Key Regulator of Ras Localization and Function. *Frontiers in molecular biosciences* 2021, *8*, 659861. DOI: 10.3389/fmolb.2021.659861. Published Online: Mar. 17, 2021.

(69) Blaustein, M.; Piegari, E.; Martínez Calejman, C.; Vila, A.; Amante, A.; Manese, M. V.; Zeida, A.; Abrami, L.; Veggetti, M.; Guertin, D. A.; van der Goot, F. G.; Corvi, M. M.; Colman-Lerner, A. Akt Is S-Palmitoylated: A New Layer of Regulation for Akt. *Frontiers in cell and developmental biology* 2021, *9*, 626404. DOI: 10.3389/fcell.2021.626404. Published Online: Feb. 15, 2021.

(70) Topinka, J.; Bredt, D. S. N-Terminal Palmitoylation of PSD-95 Regulates Association with Cell Membranes and Interaction with K+ Channel Kv1.4. *Neuron* 1998, *20* (1), 125–134. DOI: 10.1016/S0896-6273(00)80440-7.

(71) Fukata, M.; Fukata, Y.; Adesnik, H.; Nicoll, R. A.; Bredt, D. S. Identification of PSD-95 palmitoylating enzymes. *Neuron* 2004, *44* (6), 987–996. DOI: 10.1016/j.neuron.2004.12.005.

(72) Matt, L.; Kim, K.; Chowdhury, D.; Hell, J. W. Role of Palmitoylation of Postsynaptic Proteins in Promoting Synaptic Plasticity. *Frontiers in molecular neuroscience* 2019, *12*, 8. DOI: 10.3389/fnmol.2019.00008. Published Online: Jan. 31, 2019.

(73) Adams, M. N.; Christensen, M. E.; He, Y.; Waterhouse, N. J.; Hooper, J. D. The role of palmitoylation in signalling, cellular trafficking and plasma membrane localization of protease-activated receptor-2. *PloS one* 2011, *6* (11), e28018. DOI: 10.1371/journal.pone.0028018. Published Online: Nov. 29, 2011.

(74) Sanders, S. S.; Simone, F. I. de; Thomas, G. M. mTORC1 Signaling Is Palmitoylation-Dependent in Hippocampal Neurons and Non-neuronal Cells and Involves Dynamic Palmitoylation of LAMTOR1 and mTOR. *Frontiers in cellular neuroscience* 2019, *13*, 115. DOI: 10.3389/fncel.2019.00115. Published Online: Apr. 2, 2019.

(75) Gubitosi-Klug, R. A.; Mancuso, D. J.; Gross, R. W. The human Kv1.1 channel is palmitoylated, modulating voltage sensing: Identification of a palmitoylation consensus sequence. *Proceedings of the National Academy of Sciences of the United States of America* 2005, *102* (17), 5964–5968. DOI: 10.1073/pnas.0501999102. Published Online: Apr. 18, 2005.

(76) Shipston, M. J. Ion channel regulation by protein palmitoylation. *The Journal of biological chemistry* 2011, *286* (11), 8709–8716. DOI: 10.1074/jbc.R110.210005. Published Online: Jan. 7, 2011.

(77) Pei, Z.; Xiao, Y.; Meng, J.; Hudmon, A.; Cummins, T. R. Cardiac sodium channel palmitoylation regulates channel availability and myocyte excitability with implications for arrhythmia generation. *Nature communications* 2016, *7*, 12035. DOI: 10.1038/ncomms12035. Published Online: Jun. 23, 2016.

(78) Sanders, S. S.; Hernandez, L. M.; Soh, H.; Karnam, S.; Walikonis, R. S.; Tzingounis, A. V.; Thomas, G. M. The palmitoyl acyltransferase ZDHHC14 controls Kv1-family potassium channel clustering at the axon initial segment. *eLife* 2020, *9.* DOI: 10.7554/eLife.56058. Published Online: Nov. 13, 2020.

(79) Lievens, P. M.-J.; Kuznetsova, T.; Kochlamazashvili, G.; Cesca, F.; Gorinski, N.; Galil, D. A.; Cherkas, V.; Ronkina, N.; Lafera, J.; Gaestel, M.; Ponimaskin, E.; Dityatev, A. ZDHHC3 Tyrosine Phosphorylation Regulates Neural Cell Adhesion Molecule Palmitoylation. *Molecular and cellular biology* 2016, *36* (17), 2208–2225. DOI: 10.1128/MCB.00144-16. Published Online: Aug. 12, 2016.

(80) Aramsangtienchai, P.; Spiegelman, N. A.; Cao, J.; Lin, H. S-Palmitoylation of Junctional Adhesion Molecule C Regulates Its Tight Junction Localization and Cell Migration. *The Journal of biological chemistry* 2017, *292* (13), 5325–5334. DOI: 10.1074/jbc.M116.730523. Published Online: Feb. 14, 2017.

(81) Chan, P.; Han, X.; Zheng, B.; DeRan, M.; Yu, J.; Jarugumilli, G. K.; Deng, H.; Pan, D.; Luo, X.; Wu, X. Autopalmitoylation of TEAD proteins regulates transcriptional output of the Hippo pathway. *Nature chemical biology* 2016, *12* (4), 282–289. DOI: 10.1038/nchembio.2036. Published Online: Feb. 22, 2016.

(82) Chen, S.; Zhu, B.; Yin, C.; Liu, W.; Han, C.; Chen, B.; Liu, T.; Li, X.; Chen, X.; Li, C.; Hu, L.; Zhou, J.; Xu, Z.-X.; Gao, X.; Wu, X.; Goding, C. R.; Cui, R. Palmitoylation-dependent activation of MC1R prevents melanomagenesis. *Nature* 2017, *549* (7672), 399–403. DOI: 10.1038/nature23887. Published Online: Sep. 6, 2017.

(83) Brownlee, C.; Heald, R. Importin α Partitioning to the Plasma Membrane Regulates Intracellular Scaling. *Cell* 2019, *176* (4), 805-815.e8. DOI: 10.1016/j.cell.2018.12.001. Published Online: Jan. 10, 2019.

(84) Zhang, M.; Zhou, L.; Xu, Y.; Yang, M.; Xu, Y.; Komaniecki, G. P.; Kosciuk, T.; Chen, X.; Lu, X.; Zou, X.; Linder, M. E.; Lin, H. A STAT3 palmitoylation cycle promotes TH17 differentiation and colitis. *Nature* 2020, *586* (7829), 434–439. DOI: 10.1038/s41586-020-2799-2. Published Online: Oct. 7, 2020.

(85) Ko, P.-J.; Dixon, S. J. Protein palmitoylation and cancer. *EMBO reports* 2018, *19* (10). DOI: 10.15252/embr.201846666. Published Online: Sep. 19, 2018.

(86) Fhu, C. W.; Ali, A. Protein Lipidation by Palmitoylation and Myristoylation in Cancer. *Frontiers in cell and developmental biology* 2021, *9*, 673647. DOI: 10.3389/fcell.2021.673647. Published Online: May. 20, 2021.

(87) Cho, E.; Park, M. Palmitoylation in Alzheimer's disease and other neurodegenerative diseases. *Pharmacological research* 2016, *111*, 133–151. DOI: 10.1016/j.phrs.2016.06.008. Published Online: Jun. 9, 2016.

(88) Sobocińska, J.; Roszczenko-Jasińska, P.; Ciesielska, A.; Kwiatkowska, K. Protein Palmitoylation and Its Role in Bacterial and Viral Infections. *Frontiers in immunology* 2017, *8*, 2003. DOI: 10.3389/fimmu.2017.02003. Published Online: Jan. 19, 2018.

(89) Paige, L. A.; Nadler, M. J.; Harrison, M. L.; Cassady, J. M.; Geahlen, R. L. Reversible palmitoylation of the protein-tyrosine kinase p56lck. *The Journal of biological chemistry* 1993, *268* (12), 8669–8674. DOI: 10.1016/S0021-9258(18)52927-6.

(90) Degtyarev, M. Y.; Spiegel, A. M.; Jones, T. L. Increased palmitoylation of the Gs protein alpha subunit after activation by the beta-adrenergic receptor or cholera toxin. *The Journal of biological chemistry* 1993, *268* (32), 23769–23772.

(91) Peseckis, S. M.; Deichaite, I.; Resh, M. D. Iodinated fatty acids as probes for myristate processing and function. Incorporation into pp60v-src. *The Journal of biological chemistry* 1993, *268* (7), 5107–5114.

(92) Gao, X.; Hannoush, R. N. A Decade of Click Chemistry in Protein Palmitoylation: Impact on Discovery and New Biology. *Cell chemical biology* 2018, *25* (3), 236–246. DOI: 10.1016/j.chembiol.2017.12.002. Published Online: Dec. 28, 2017.

(93) Wang, Q.; Chan, T. R.; Hilgraf, R.; Fokin, V. V.; Sharpless, K. B.; Finn, M. G. Bioconjugation by copper(I)-catalyzed azide-alkyne 3 + 2 cycloaddition. *Journal of the American Chemical Society* 2003, *125* (11), 3192–3193. DOI: 10.1021/ja021381e.

(94) Muszbek, L.; Laposata, M. Covalent modification of platelet proteins by palmitate. *Blood* 1989, *74* (4), 1339–1347.

(95) Hang, H. C.; Geutjes, E.-J.; Grotenbreg, G.; Pollington, A. M.; Bijlmakers, M. J.; Ploegh, H. L. Chemical probes for the rapid detection of Fatty-acylated proteins in Mammalian cells. *Journal of the American Chemical Society* 2007, *129* (10), 2744–2745. DOI: 10.1021/ja0685001. Published Online: Feb. 17, 2007.

(96) Kostiuk, M. A.; Corvi, M. M.; Keller, B. O.; Plummer, G.; Prescher, J. A.; Hangauer, M. J.; Bertozzi, C. R.; Rajaiah, G.; Falck, J. R.; Berthiaume, L. G. Identification of palmitoylated mitochondrial proteins using a bio-orthogonal azido-palmitate analogue. *FASEB journal : official publication of the Federation of American Societies for Experimental Biology* 2008, *22* (3), 721–732. DOI: 10.1096/fj.07-9199com. Published Online: Oct. 30, 2007.

(97) Martin, B. R.; Cravatt, B. F. Large-scale profiling of protein palmitoylation in mammalian cells. *Nature methods* 2009, *6* (2), 135–138. DOI: 10.1038/nmeth.1293. Published Online: Jan. 11, 2009.

(98) Hannoush, R. N.; Arenas-Ramirez, N. Imaging the lipidome: omega-alkynyl fatty acids for detection and cellular visualization of lipid-modified proteins. *ACS chemical biology* 2009, *4* (7), 581–587. DOI: 10.1021/cb900085z.

(99) Charron, G.; Zhang, M. M.; Yount, J. S.; Wilson, J.; Raghavan, A. S.; Shamir, E.; Hang, H. C. Robust fluorescent detection of protein fatty-acylation with chemical reporters. *Journal of the American Chemical Society* 2009, *131* (13), 4967–4975. DOI: 10.1021/ja810122f.

(100) Speers, A. E.; Cravatt, B. F. Profiling enzyme activities in vivo using click chemistry methods. *Chemistry & biology* 2004, *11* (4), 535–546. DOI: 10.1016/j.chembiol.2004.03.012.

(101) Agard, N. J.; Baskin, J. M.; Prescher, J. A.; Lo, A.; Bertozzi, C. R. A comparative study of bioorthogonal reactions with azides. *ACS chemical biology* 2006, *1* (10), 644–648. DOI: 10.1021/cb6003228.

(102) Gao, X.; Hannoush, R. N. Method for cellular imaging of palmitoylated proteins with clickable probes and proximity ligation applied to Hedgehog, tubulin, and Ras. *Journal of the American Chemical Society* 2014, *136* (12), 4544–4550. DOI: 10.1021/ja410068g. Published Online: Mar. 17, 2014.

(103) Gao, X.; Hannoush, R. N. Single-cell imaging of Wnt palmitoylation by the acyltransferase porcupine. *Nature chemical biology* 2014, *10* (1), 61–68. DOI: 10.1038/nchembio.1392. Published Online: Nov. 24, 2013.

(104) Gao, X.; Hannoush, R. N. Single-cell in situ imaging of palmitoylation in fatty-acylated proteins. *Nature protocols* 2014, *9* (11), 2607–2623. DOI: 10.1038/nprot.2014.179. Published Online: Oct. 9, 2014.

(105) Ong, S.-E.; Mann, M. A practical recipe for stable isotope labeling by amino acids in cell culture (SILAC). *Nature protocols* 2006, *1* (6), 2650–2660. DOI: 10.1038/nprot.2006.427.

(106) Storck, E. M.; Serwa, R. A.; Tate, E. W. Chemical proteomics: a powerful tool for exploring protein lipidation. *Biochemical Society transactions* 2013, *41* (1), 56–61. DOI: 10.1042/BST20120283.

(107) Peng, T.; Thinon, E.; Hang, H. C. Proteomic analysis of fatty-acylated proteins. *Current opinion in chemical biology* 2016, *30*, 77–86. DOI: 10.1016/j.cbpa.2015.11.008. Published Online: Dec. 2, 2015.

(108) Martin, B. R.; Wang, C.; Adibekian, A.; Tully, S. E.; Cravatt, B. F. Global profiling of dynamic protein palmitoylation. *Nature methods* 2011, *9* (1), 84–89. DOI: 10.1038/nmeth.1769. Published Online: Nov. 6, 2011.

(109) Glatz, J. F. C.; Luiken, J. J. F. P.; Bonen, A. Membrane fatty acid transporters as regulators of lipid metabolism: implications for metabolic disease. *Physiological reviews* 2010, *90* (1), 367–417. DOI: 10.1152/physrev.00003.2009.

(110) Xu, S.; Nam, S. M.; Kim, J.-H.; Das, R.; Choi, S.-K.; Nguyen, T. T.; Quan, X.; Choi, S. J.; Chung, C. H.; Lee, E. Y.; Lee, I.-K.; Wiederkehr, A.; Wollheim, C. B.; Cha, S.-K.; Park, K.-S. Palmitate induces ER calcium depletion and apoptosis in mouse podocytes subsequent to mitochondrial oxidative stress. *Cell death & disease* 2015, *6*, e1976. DOI: 10.1038/cddis.2015.331. Published Online: Nov. 19, 2015.

(111) Baker, T. L.; Zheng, H.; Walker, J.; Coloff, J. L.; Buss, J. E. Distinct rates of palmitate turnover on membrane-bound cellular and oncogenic H-ras. *The Journal of biological chemistry* 2003, *278* (21), 19292–19300. DOI: 10.1074/jbc.M206956200. Published Online: Mar. 17, 2003.

(112) Zhang, M. M.; Tsou, L. K.; Charron, G.; Raghavan, A. S.; Hang, H. C. Tandem fluorescence imaging of dynamic S-acylation and protein turnover. *Proceedings of the National Academy of Sciences of the United States of America* 2010, *107* (19), 8627–8632. DOI: 10.1073/pnas.0912306107. Published Online: Apr. 26, 2010.

(113) Drisdel, R. C.; Green, W. N. Labeling and quantifying sites of protein palmitoylation. *BioTechniques* 2004, *36* (2), 276–285. DOI: 10.2144/04362RR02.

(114) Edmonds, M. J.; Geary, B.; Doherty, M. K.; Morgan, A. Analysis of the brain palmitoyl-proteome using both acyl-biotin exchange and acyl-resin-assisted capture methods. *Scientific reports* 2017, *7* (1), 3299. DOI: 10.1038/s41598-017-03562-7. Published Online: Jun. 12, 2017.

(115) Zhou, B.; Wang, Y.; Yan, Y.; Mariscal, J.; Di Vizio, D.; Freeman, M. R.; Yang, W. Low-Background Acyl-Biotinyl Exchange Largely Eliminates the Coisolation of Non-S-Acylated Proteins and Enables Deep S-Acylproteomic Analysis. *Analytical chemistry* 2019, *91* (15), 9858–9866. DOI: 10.1021/acs.analchem.9b01520. Published Online: Jul. 11, 2019.

(116) Brewer, C. F.; Riehm, J. P. Evidence for possible nonspecific reactions between N-ethylmaleimide and proteins. *Analytical Biochemistry* 1967, *18* (2), 248–255. DOI: 10.1016/0003-2697(67)90007-3.

(117) Schulte-Zweckel, J.; Dwivedi, M.; Brockmeyer, A.; Janning, P.; Winter, R.; Triola, G. A hydroxylamine probe for profiling S-acylated fatty acids on proteins. *Chemical communications (Cambridge, England)* 2019, *55* (75), 11183–11186. DOI: 10.1039/C9CC05989J.

(118) Forrester, M. T.; Hess, D. T.; Thompson, J. W.; Hultman, R.; Moseley, M. A.; Stamler, J. S.; Casey, P. J. Site-specific analysis of protein S-acylation by resin-assisted capture. *Journal of lipid research* 2011, *52* (2), 393–398. DOI: 10.1194/jlr.D011106. Published Online: Nov. 2, 2010.

(119) Forrester, M. T.; Thompson, J. W.; Foster, M. W.; Nogueira, L.; Moseley, M. A.; Stamler, J. S. Proteomic analysis of S-nitrosylation and denitrosylation by resin-assisted capture. *Nature biotechnology* 2009, *27* (6), 557–559. DOI: 10.1038/nbt.1545. Published Online: May. 31, 2009.

(120) Howie, J.; Reilly, L.; Fraser, N. J.; Vlachaki Walker, J. M.; Wypijewski, K. J.; Ashford, M. L. J.; Calaghan, S. C.; McClafferty, H.; Tian, L.; Shipston, M. J.; Boguslavskyi, A.; Shattock, M. J.; Fuller, W. Substrate recognition by the cell surface palmitoyl transferase DHHC5. *Proceedings of the National Academy of Sciences of the United States of America* 2014, *111* (49), 17534–17539. DOI: 10.1073/pnas.1413627111. Published Online: Nov. 24, 2014.

(121) Percher, A.; Ramakrishnan, S.; Thinon, E.; Yuan, X.; Yount, J. S.; Hang, H. C. Mass-tag labeling reveals site-specific and endogenous levels of protein S-fatty acylation. *Proceedings of the National Academy of Sciences of the United States of America* 2016, *113* (16), 4302–4307. DOI: 10.1073/pnas.1602244113. Published Online: Apr. 4, 2016.

(122) Aicart-Ramos, C.; Valero, R. A.; Rodriguez-Crespo, I. Protein palmitoylation and subcellular trafficking. *Biochimica et biophysica acta* 2011, *1808* (12), 2981–2994. DOI: 10.1016/j.bbamem.2011.07.009. Published Online: Jul. 23, 2011.

(123) Kathayat, R. S.; Cao, Y.; Elvira, P. D.; Sandoz, P. A.; Zaballa, M.-E.; Springer, M. Z.; Drake, L. E.; Macleod, K. F.; van der Goot, F. G.; Dickinson, B. C. Active and dynamic mitochondrial S-depalmitoylation revealed by targeted fluorescent probes. *Nature communications* 2018, *9* (1), 334. DOI: 10.1038/s41467-017-02655-1. Published Online: Jan. 23, 2018.

(124) Lobo, S.; Greentree, W. K.; Linder, M. E.; Deschenes, R. J. Identification of a Ras palmitoyltransferase in Saccharomyces cerevisiae. *The Journal of biological chemistry* 2002, *277* (43), 41268–41273. DOI: 10.1074/jbc.M206573200. Published Online: Aug. 21, 2002.

(125) Roth, A. F.; Feng, Y.; Chen, L.; Davis, N. G. The yeast DHHC cysteine-rich domain protein Akr1p is a palmitoyl transferase. *The Journal of cell biology* 2002, *159* (1), 23–28. DOI: 10.1083/jcb.200206120. Published Online: Oct. 7, 2002.

(126) Hicks, S. W.; Charron, G.; Hang, H. C.; Galán, J. E. Subcellular targeting of Salmonella virulence proteins by host-mediated S-palmitoylation. *Cell host & microbe* 2011, *10* (1), 9–20. DOI: 10.1016/j.chom.2011.06.003.

(127) Lin, Y.-H.; Doms, A. G.; Cheng, E.; Kim, B.; Evans, T. R.; Machner, M. P. Host Cell-catalyzed S-Palmitoylation Mediates Golgi Targeting of the Legionella Ubiquitin Ligase GobX. *The Journal of biological chemistry* 2015, *290* (42), 25766–25781. DOI: 10.1074/jbc.M115.637397. Published Online: Aug. 27, 2015.

(128) Schroeder, G. N.; Aurass, P.; Oates, C. V.; Tate, E. W.; Hartland, E. L.; Flieger, A.; Frankel, G. Legionella pneumophila Effector LpdA Is a Palmitoylated Phospholipase D Virulence Factor. *Infection and immunity* 2015, *83* (10), 3989–4002. DOI: 10.1128/IAI.00785-15. Published Online: Jul. 27, 2015.

(129) Mitchell, D. A.; Vasudevan, A.; Linder, M. E.; Deschenes, R. J. Protein palmitoylation by a family of DHHC protein S-acyltransferases. *Journal of lipid research* 2006, *47* (6), 1118–1127. DOI: 10.1194/jlr.R600007-JLR200. Published Online: Apr. 1, 2006.

(130) Jennings, B. C.; Linder, M. E. DHHC protein S-acyltransferases use similar ping-pong kinetic mechanisms but display different acyl-CoA specificities. *The Journal of biological chemistry* 2012, *287* (10), 7236–7245. DOI: 10.1074/jbc.M111.337246. Published Online: Jan. 13, 2012.

(131) Mitchell, D. A.; Mitchell, G.; Ling, Y.; Budde, C.; Deschenes, R. J. Mutational analysis of Saccharomyces cerevisiae Erf2 reveals a two-step reaction mechanism for protein palmitoylation by DHHC enzymes. *The Journal of biological chemistry* 2010, *285* (49), 38104–38114. DOI: 10.1074/jbc.M110.169102. Published Online: Sep. 17, 2010.

(132) Stix, R.; Lee, C.-J.; Faraldo-Gómez, J. D.; Banerjee, A. Structure and Mechanism of DHHC Protein Acyltransferases. *Journal of molecular biology* 2020, *432* (18), 4983–4998. DOI: 10.1016/j.jmb.2020.05.023. Published Online: Jun. 6, 2020.

(133) Rana, M. S.; Kumar, P.; Lee, C.-J.; Verardi, R.; Rajashankar, K. R.; Banerjee, A. Fatty acyl recognition and transfer by an integral membrane S-acyltransferase. *Science (New York, N.Y.)* 2018, *359* (6372). DOI: 10.1126/science.aao6326.

(134) Webb, Y.; Hermida-Matsumoto, L.; Resh, M. D. Inhibition of protein palmitoylation, raft localization, and T cell signaling by 2-bromopalmitate and polyunsaturated fatty acids. *The Journal of biological chemistry* 2000, *275* (1), 261–270. DOI: 10.1074/jbc.275.1.261.

(135) González Montoro, A.; Quiroga, R.; Valdez Taubas, J. Zinc co-ordination by the DHHC cysteine-rich domain of the palmitoyltransferase Swf1. *The Biochemical journal* 2013, *454* (3), 427–435. DOI: 10.1042/BJ20121693.

(136) Lee, C.-J.; Stix, R.; Rana, M. S.; Shikwana, F.; Murphy, R. E.; Ghirlando, R.; Faraldo-Gómez, J. D.; Banerjee, A. Bivalent recognition of fatty acyl-CoA by a human integral membrane palmitoyltransferase. *Proceedings of the National Academy of Sciences of the United States of America* 2022, *119* (7). DOI: 10.1073/pnas.2022050119.

(137) Tunyasuvunakool, K.; Adler, J.; Wu, Z.; Green, T.; Zielinski, M.; Žídek, A.; Bridgland, A.; Cowie, A.; Meyer, C.; Laydon, A.; Velankar, S.; Kleywegt, G. J.; Bateman, A.; Evans, R.; Pritzel, A.; Figurnov, M.; Ronneberger, O.; Bates, R.; Kohl, S. A. A.; Potapenko, A.; Ballard, A. J.; Romera-Paredes, B.; Nikolov, S.; Jain, R.; Clancy, E.; Reiman, D.; Petersen, S.; Senior, A. W.; Kavukcuoglu, K.; Birney, E.; Kohli, P.; Jumper, J.; Hassabis, D. Highly accurate protein structure prediction for the human proteome. *Nature* 2021, *596* (7873), 590–596. DOI: 10.1038/s41586-021-03828-1. Published Online: Jul. 22, 2021.

(138) Jumper, J.; Evans, R.; Pritzel, A.; Green, T.; Figurnov, M.; Ronneberger, O.; Tunyasuvunakool, K.; Bates, R.; Žídek, A.; Potapenko, A.; Bridgland, A.; Meyer, C.; Kohl, S. A. A.; Ballard, A. J.; Cowie, A.; Romera-Paredes, B.; Nikolov, S.; Jain, R.; Adler, J.; Back, T.; Petersen, S.; Reiman, D.; Clancy, E.; Zielinski, M.; Steinegger, M.; Pacholska, M.; Berghammer, T.; Bodenstein, S.; Silver, D.; Vinyals, O.; Senior, A. W.; Kavukcuoglu, K.; Kohli, P.; Hassabis, D. Highly accurate protein structure prediction with AlphaFold. *Nature* 2021, *596* (7873), 583–589. DOI: 10.1038/s41586-021-03819-2. Published Online: Jul. 15, 2021.

(139) Malgapo, M. I. P.; Linder, M. E. Substrate recruitment by zDHHC protein acyltransferases. *Open biology* 2021, *11* (4), 210026. DOI: 10.1098/rsob.210026. Published Online: Apr. 21, 2021.

(140) Nadolski, M. J.; Linder, M. E. Molecular recognition of the palmitoylation substrate Vac8 by its palmitoyltransferase Pfa3. *The Journal of biological chemistry* 2009, *284* (26), 17720–17730. DOI: 10.1074/jbc.M109.005447. Published Online: May. 5, 2009.

(141) González Montoro, A.; Chumpen Ramirez, S.; Quiroga, R.; Valdez Taubas, J. Specificity of transmembrane protein palmitoylation in yeast. *PloS one* 2011, *6* (2), e16969. DOI: 10.1371/journal.pone.0016969. Published Online: Feb. 24, 2011.

(142) Verardi, R.; Kim, J.-S.; Ghirlando, R.; Banerjee, A. Structural Basis for Substrate Recognition by the Ankyrin Repeat Domain of Human DHHC17 Palmitoyltransferase. *Structure (London, England : 1993)* 2017, *25* (9), 1337-1347.e6. DOI: 10.1016/j.str.2017.06.018. Published Online: Jul. 27, 2017.

(143) Huang, K.; Sanders, S.; Singaraja, R.; Orban, P.; Cijsouw, T.; Arstikaitis, P.; Yanai, A.; Hayden, M. R.; El-Husseini, A. Neuronal palmitoyl acyl transferases exhibit distinct substrate specificity. *FASEB journal : official publication of the Federation of American Societies for Experimental Biology* 2009, *23* (8), 2605–2615. DOI: 10.1096/fj.08-127399. Published Online: Mar. 19, 2009.

(144) Ohno, Y.; Kashio, A.; Ogata, R.; Ishitomi, A.; Yamazaki, Y.; Kihara, A. Analysis of substrate specificity of human DHHC protein acyltransferases using a yeast expression system. *Molecular biology of the cell* 2012, *23* (23), 4543–4551. DOI: 10.1091/mbc.E12-05-0336. Published Online: Oct. 3, 2012.

(145) Lemonidis, K.; Sanchez-Perez, M. C.; Chamberlain, L. H. Identification of a Novel Sequence Motif Recognized by the Ankyrin Repeat Domain of zDHHC17/13 S-Acyltransferases. *The Journal of biological chemistry* 2015, *290* (36), 21939–21950. DOI: 10.1074/jbc.M115.657668. Published Online: Jul. 21, 2015.

(146) Plain, F.; Howie, J.; Kennedy, J.; Brown, E.; Shattock, M. J.; Fraser, N. J.; Fuller, W. Control of protein palmitoylation by regulating substrate recruitment to a zDHHC-protein

acyltransferase. *Communications biology* 2020, *3* (1), 411. DOI: 10.1038/s42003-020-01145-3. Published Online: Jul. 31, 2020.

(147) Lanyon-Hogg, T.; Ritzefeld, M.; Sefer, L.; Bickel, J. K.; Rudolf, A. F.; Panyain, N.; Bineva-Todd, G.; Ocasio, C. A.; O'Reilly, N.; Siebold, C.; Magee, A. I.; Tate, E. W. Acylation-coupled lipophilic induction of polarisation (Acyl-cLIP): a universal assay for lipid transferase and hydrolase enzymes. *Chemical science* 2019, *10* (39), 8995–9000. DOI: 10.1039/c9sc01785b. Published Online: Jul. 1, 2019.

(148) Hong, J. Y.; Malgapo, M. I. P.; Liu, Y.; Yang, M.; Zhu, C.; Zhang, X.; Tolbert, P.; Linder, M. E.; Lin, H. High-Throughput Enzyme Assay for Screening Inhibitors of the ZDHHC3/7/20 Acyltransferases. *ACS chemical biology* 2021, *16* (8), 1318–1324. DOI: 10.1021/acschembio.1c00258. Published Online: Aug. 10, 2021.

(149) Azizi, S.-A.; Lan, T.; Delalande, C.; Kathayat, R. S.; Banales Mejia, F.; Qin, A.; Brookes, N.; Sandoval, P. J.; Dickinson, B. C. Development of an Acrylamide-Based Inhibitor of Protein S-Acylation. *ACS chemical biology* 2021, *16* (8), 1546–1556. DOI: 10.1021/acschembio.1c00405. Published Online: Jul. 26, 2021.

(150) Patterson, S. I.; Skene, J. H. Novel inhibitory action of tunicamycin homologues suggests a role for dynamic protein fatty acylation in growth cone-mediated neurite extension. *The Journal of cell biology* 1994, *124* (4), 521–536. DOI: 10.1083/jcb.124.4.521.

(151) Lawrence, D. S.; Zilfou, J. T.; Smith, C. D. Structure-activity studies of cerulenin analogues as protein palmitoylation inhibitors. *Journal of medicinal chemistry* 1999, *42* (24), 4932–4941. DOI: 10.1021/jm980591s.

(152) Zheng, B.; DeRan, M.; Li, X.; Liao, X.; Fukata, M.; Wu, X. 2-Bromopalmitate analogues as activity-based probes to explore palmitoyl acyltransferases. *Journal of the American Chemical Society* 2013, *135* (19), 7082–7085. DOI: 10.1021/ja311416v. Published Online: May. 3, 2013.

(153) Zheng, B.; Zhu, S.; Wu, X. Clickable analogue of cerulenin as chemical probe to explore protein palmitoylation. *ACS chemical biology* 2015, *10* (1), 115–121. DOI: 10.1021/cb500758s. Published Online: Oct. 23, 2014.

(154) Resh, M. D. Use of analogs and inhibitors to study the functional significance of protein palmitoylation. *Methods (San Diego, Calif.)* 2006, *40* (2), 191–197. DOI: 10.1016/j.ymeth.2006.04.013.

(155) Pedro, M. P.; Vilcaes, A. A.; Tomatis, V. M.; Oliveira, R. G.; Gomez, G. A.; Daniotti, J. L. 2-Bromopalmitate reduces protein deacylation by inhibition of acyl-protein thioesterase enzymatic activities. *PloS one* 2013, *8* (10), e75232. DOI: 10.1371/journal.pone.0075232. Published Online: Oct. 2, 2013.

(156) Jackson, P. A.; Widen, J. C.; Harki, D. A.; Brummond, K. M. Covalent Modifiers: A Chemical Perspective on the Reactivity of α,β-Unsaturated Carbonyls with Thiols via Hetero-Michael Addition Reactions. *Journal of medicinal chemistry* 2017, *60* (3), 839–885. DOI: 10.1021/acs.jmedchem.6b00788. Published Online: Dec. 20, 2016.

(157) Davda, D.; El Azzouny, M. A.; Tom, C. T. M. B.; Hernandez, J. L.; Majmudar, J. D.; Kennedy, R. T.; Martin, B. R. Profiling targets of the irreversible palmitoylation inhibitor 2-

bromopalmitate. *ACS chemical biology* 2013, *8* (9), 1912–1917. DOI: 10.1021/cb400380s. Published Online: Jul. 25, 2013.

(158) Yao, H.; Lan, J.; Li, C.; Shi, H.; Brosseau, J.-P.; Wang, H.; Lu, H.; Fang, C.; Zhang, Y.; Liang, L.; Zhou, X.; Wang, C.; Xue, Y.; Cui, Y.; Xu, J. Inhibiting PD-L1 palmitoylation enhances T-cell immune responses against tumours. *Nature biomedical engineering* 2019, *3* (4), 306–317. DOI: 10.1038/s41551-019-0375-6. Published Online: Mar. 25, 2019.

(159) Yao, H.; Li, C.; He, F.; Song, T.; Brosseau, J.-P.; Wang, H.; Lu, H.; Fang, C.; Shi, H.; Lan, J.; Fang, J.-Y.; Xu, J. A peptidic inhibitor for PD-1 palmitoylation targets its expression and functions. *RSC chemical biology* 2021, *2* (1), 192–205. DOI: 10.1039/d0cb00157k. Published Online: Nov. 3, 2020.

(160) Camp, L. A.; Hofmann, S. L. Purification and properties of a palmitoyl-protein thioesterase that cleaves palmitate from H-Ras. *The Journal of biological chemistry* 1993, *268* (30), 22566–22574.

(161) Duncan, J. A.; Gilman, A. G. A cytoplasmic acyl-protein thioesterase that removes palmitate from G protein alpha subunits and p21(RAS). *The Journal of biological chemistry* 1998, *273* (25), 15830–15837. DOI: 10.1074/jbc.273.25.15830.

(162) Bellizzi, J. J.; Widom, J.; Kemp, C.; Lu, J. Y.; Das, A. K.; Hofmann, S. L.; Clardy, J. The crystal structure of palmitoyl protein thioesterase 1 and the molecular basis of infantile neuronal ceroid lipofuscinosis. *Proceedings of the National Academy of Sciences of the United States of America* 2000, *97* (9), 4573–4578. DOI: 10.1073/pnas.080508097.

(163) Das, A. K.; Bellizzi, J. J.; Tandel, S.; Biehl, E.; Clardy, J.; Hofmann, S. L. Structural basis for the insensitivity of a serine enzyme (palmitoyl-protein thioesterase) to phenylmethylsulfonyl fluoride. *The Journal of biological chemistry* 2000, *275* (31), 23847–23851. DOI: 10.1074/jbc.M002758200.

(164) Calero, G.; Gupta, P.; Nonato, M. C.; Tandel, S.; Biehl, E. R.; Hofmann, S. L.; Clardy, J. The crystal structure of palmitoyl protein thioesterase-2 (PPT2) reveals the basis for divergent substrate specificities of the two lysosomal thioesterases, PPT1 and PPT2. *The Journal of biological chemistry* 2003, *278* (39), 37957–37964. DOI: 10.1074/jbc.M301225200. Published Online: Jul. 10, 2003.

(165) Devedjiev, Y.; Dauter, Z.; Kuznetsov, S. R.; Jones, T. L.; Derewenda, Z. S. Crystal structure of the human acyl protein thioesterase I from a single X-ray data set to 1.5 A. *Structure (London, England : 1993)* 2000, *8* (11), 1137–1146. DOI: 10.1016/s0969-2126(00)00529-3.

(166) Won, S. J.; Davda, D.; Labby, K. J.; Hwang, S. Y.; Pricer, R.; Majmudar, J. D.; Armacost, K. A.; Rodriguez, L. A.; Rodriguez, C. L.; Chong, F. S.; Torossian, K. A.; Palakurthi, J.; Hur, E. S.; Meagher, J. L.; Brooks, C. L.; Stuckey, J. A.; Martin, B. R. Molecular Mechanism for Isoform-Selective Inhibition of Acyl Protein Thioesterases 1 and 2 (APT1 and APT2). *ACS chemical biology* 2016, *11* (12), 3374–3382. DOI: 10.1021/acschembio.6b00720. Published Online: Oct. 31, 2016.

(167) Wepy, J. A.; Galligan, J. J.; Kingsley, P. J.; Xu, S.; Goodman, M. C.; Tallman, K. A.; Rouzer, C. A.; Marnett, L. J. Lysophospholipases cooperate to mediate lipid homeostasis

and lysophospholipid signaling. *Journal of lipid research* 2019, *60* (2), 360–374. DOI: 10.1194/jlr.M087890. Published Online: Nov. 27, 2018.

(168) Abrami, L.; Audagnotto, M.; Ho, S.; Marcaida, M. J.; Mesquita, F. S.; Anwar, M. U.; Sandoz, P. A.; Fonti, G.; Pojer, F.; Dal Peraro, M.; van der Goot, F. G. Palmitoylated acyl protein thioesterase APT2 deforms membranes to extract substrate acyl chains. *Nature chemical biology* 2021, *17* (4), 438–447. DOI: 10.1038/s41589-021-00753-2. Published Online: Mar. 11, 2021.

(169) Long, J. Z.; Cravatt, B. F. The metabolic serine hydrolases and their functions in mammalian physiology and disease. *Chemical reviews* 2011, *111* (10), 6022–6063. DOI: 10.1021/cr200075y. Published Online: Jun. 23, 2011.

(170) Liu, Y.; Patricelli, M. P.; Cravatt, B. F. Activity-based protein profiling: the serine hydrolases. *Proceedings of the National Academy of Sciences of the United States of America* 1999, *96* (26), 14694–14699. DOI: 10.1073/pnas.96.26.14694.

(171) Leung, D.; Hardouin, C.; Boger, D. L.; Cravatt, B. F. Discovering potent and selective reversible inhibitors of enzymes in complex proteomes. *Nature biotechnology* 2003, *21* (6), 687–691. DOI: 10.1038/nbt826. Published Online: May. 12, 2003.

(172) Kathayat, R. S.; Elvira, P. D.; Dickinson, B. C. A fluorescent probe for cysteine depalmitoylation reveals dynamic APT signaling. *Nature chemical biology* 2017, *13* (2), 150–152. DOI: 10.1038/nchembio.2262. Published Online: Dec. 19, 2016.

(173) Kong, E.; Peng, S.; Chandra, G.; Sarkar, C.; Zhang, Z.; Bagh, M. B.; Mukherjee, A. B. Dynamic palmitoylation links cytosol-membrane shuttling of acyl-protein thioesterase-1 and acyl-protein thioesterase-2 with that of proto-oncogene H-ras product and growth-associated protein-43. *The Journal of biological chemistry* 2013, *288* (13), 9112–9125. DOI: 10.1074/jbc.M112.421073. Published Online: Feb. 8, 2013.

(174) Zielonka, J.; Joseph, J.; Sikora, A.; Hardy, M.; Ouari, O.; Vasquez-Vivar, J.; Cheng, G.; Lopez, M.; Kalyanaraman, B. Mitochondria-Targeted Triphenylphosphonium-Based Compounds: Syntheses, Mechanisms of Action, and Therapeutic and Diagnostic Applications. *Chemical reviews* 2017, *117* (15), 10043–10120. DOI: 10.1021/acs.chemrev.7b00042. Published Online: Jun. 27, 2017.

(175) Beck, M. W.; Kathayat, R. S.; Cham, C. M.; Chang, E. B.; Dickinson, B. C. Michael addition-based probes for ratiometric fluorescence imaging of protein S-depalmitoylases in live cells and tissues. *Chemical science* 2017, *8* (11), 7588–7592. DOI: 10.1039/c7sc02805a. Published Online: Sep. 11, 2017.

(176) Deck, P.; Pendzialek, D.; Biel, M.; Wagner, M.; Popkirova, B.; Ludolph, B.; Kragol, G.; Kuhlmann, J.; Giannis, A.; Waldmann, H. Development and biological evaluation of acyl protein thioesterase 1 (APT1) inhibitors. *Angewandte Chemie (International ed. in English)* 2005, *44* (31), 4975–4980. DOI: 10.1002/anie.200462625.

(177) Dekker, F. J.; Rocks, O.; Vartak, N.; Menninger, S.; Hedberg, C.; Balamurugan, R.; Wetzel, S.; Renner, S.; Gerauer, M.; Schölermann, B.; Rusch, M.; Kramer, J. W.; Rauh, D.; Coates, G. W.; Brunsveld, L.; Bastiaens, P. I. H.; Waldmann, H. Small-molecule inhibition of APT1 affects Ras localization and signaling. *Nature chemical biology* 2010, *6* (6), 449–456. DOI: 10.1038/nchembio.362. Published Online: Apr. 25, 2010.

(178) Hedberg, C.; Dekker, F. J.; Rusch, M.; Renner, S.; Wetzel, S.; Vartak, N.; Gerding-Reimers, C.; Bon, R. S.; Bastiaens, P. I. H.; Waldmann, H. Development of highly potent inhibitors of the Ras-targeting human acyl protein thioesterases based on substrate similarity design. *Angew. Chem. Int. Ed. Engl.* 2011, *50* (42), 9832–9837. DOI: 10.1002/anie.201102965. Published Online: Sep. 9, 2011.

(179) Rusch, M.; Zimmermann, T. J.; Bürger, M.; Dekker, F. J.; Görmer, K.; Triola, G.; Brockmeyer, A.; Janning, P.; Böttcher, T.; Sieber, S. A.; Vetter, I. R.; Hedberg, C.; Waldmann, H. Identification of acyl protein thioesterases 1 and 2 as the cellular targets of the Ras-signaling modulators palmostatin B and M. *Angew. Chem. Int. Ed. Engl.* 2011, *50* (42), 9838–9842. DOI: 10.1002/anie.201102967. Published Online: Sep. 9, 2011.

(180) Zimmermann, T. J.; Bürger, M.; Tashiro, E.; Kondoh, Y.; Martinez, N. E.; Görmer, K.; Rosin-Steiner, S.; Shimizu, T.; Ozaki, S.; Mikoshiba, K.; Watanabe, N.; Hall, D.; Vetter, I. R.; Osada, H.; Hedberg, C.; Waldmann, H. Boron-based inhibitors of acyl protein thioesterases 1 and 2. *Chembiochem : a European journal of chemical biology* 2013, *14* (1), 115–122. DOI: 10.1002/cbic.201200571. Published Online: Dec. 13, 2012.

(181) Adibekian, A.; Hsu, K.-L.; Speers, A. E.; Brown, S. J.; Spicer, T.; Fernandez-Vega, V.; Ferguson, J.; Cravatt, B. F.; Hodder, P.; Rosen, H. *Probe Reports from the NIH Molecular Libraries Program*:*Optimization and characterization of a triazole urea inhibitor for alpha/beta hydrolase domain-containing protein 11 (ABHD11): anti-probe for LYPLA1/LYPLA2 dual inhibitor ML211*, 2010.

(182) Kemp, L. E.; Rusch, M.; Adibekian, A.; Bullen, H. E.; Graindorge, A.; Freymond, C.; Rottmann, M.; Braun-Breton, C.; Baumeister, S.; Porfetye, A. T.; Vetter, I. R.; Hedberg, C.; Soldati-Favre, D. Characterization of a serine hydrolase targeted by acyl-protein thioesterase inhibitors in Toxoplasma gondii. *The Journal of biological chemistry* 2013, *288* (38), 27002–27018. DOI: 10.1074/jbc.M113.460709. Published Online: Aug. 2, 2013.

(183) Child, M. A.; Hall, C. I.; Beck, J. R.; Ofori, L. O.; Albrow, V. E.; Garland, M.; Bowyer, P. W.; Bradley, P. J.; Powers, J. C.; Boothroyd, J. C.; Weerapana, E.; Bogyo, M. Small-molecule inhibition of a depalmitoylase enhances Toxoplasma host-cell invasion. *Nature chemical biology* 2013, *9* (10), 651–656. DOI: 10.1038/nchembio.1315. Published Online: Aug. 11, 2013.

(184) Adibekian, A.; Martin, B. R.; Chang, J. W.; Hsu, K.-L.; Tsuboi, K.; Bachovchin, D. A.; Speers, A. E.; Brown, S. J.; Spicer, T.; Fernandez-Vega, V.; Ferguson, J.; Hodder, P. S.; Rosen, H.; Cravatt, B. F. Confirming target engagement for reversible inhibitors in vivo by kinetically tuned activity-based probes. *Journal of the American Chemical Society* 2012, *134* (25), 10345–10348. DOI: 10.1021/ja303400u. Published Online: Jun. 12, 2012.

(185) Lin, D. T. S.; Conibear, E. ABHD17 proteins are novel protein depalmitoylases that regulate N-Ras palmitate turnover and subcellular localization. *eLife* 2015, *4*, e11306. DOI: 10.7554/eLife.11306. Published Online: Dec. 23, 2015.

(186) Remsberg, J. R.; Suciu, R. M.; Zambetti, N. A.; Hanigan, T. W.; Firestone, A. J.; Inguva, A.; Long, A.; Ngo, N.; Lum, K. M.; Henry, C. L.; Richardson, S. K.; Predovic, M.; Huang, B.; Dix, M. M.; Howell, A. R.; Niphakis, M. J.; Shannon, K.; Cravatt, B. F. ABHD17 regulation of plasma membrane palmitoylation and N-Ras-dependent cancer growth.

Nature chemical biology 2021, *17* (8), 856–864. DOI: 10.1038/s41589-021-00785-8. Published Online: Apr. 29, 2021.

(187) Toyoda, T.; Sugimoto, H.; Yamashita, S. Sequence, expression in Escherichia coli, and characterization of lysophospholipase II. *Biochimica et biophysica acta* 1999, *1437* (2), 182–193. DOI: 10.1016/s1388-1981(99)00007-4.

(188) Duve, C. de. The Beginnings of Life on Earth. *American Scientist* 1995, *83* (5), 428–437.

(189) Lan, T.; Delalande, C.; Dickinson, B. C. Inhibitors of DHHC family proteins. *Current opinion in chemical biology* 2021, *65*, 118–125. DOI: 10.1016/j.cbpa.2021.07.002. Published Online: Aug. 28, 2021.

(190) Azizi, S.-A.; Kathayat, R. S.; Dickinson, B. C. Activity-Based Sensing of S-Depalmitoylases: Chemical Technologies and Biological Discovery. *Accounts of chemical research* 2019, *52* (11), 3029–3038. DOI: 10.1021/acs.accounts.9b00354. Published Online: Oct. 2, 2019.

(191) Folikumah, M. Y.; Behl, M.; Lendlein, A. Thiol-Thioester Exchange Reactions in Precursors Enable pH-Triggered Hydrogel Formation. *Biomacromolecules* 2021, *22* (5), 1875–1884. DOI: 10.1021/acs.biomac.0c01690. Published Online: Mar. 16, 2021.

(192) Wang, C.; Mavila, S.; Worrell, B. T.; Xi, W.; Goldman, T. M.; Bowman, C. N. Productive Exchange of Thiols and Thioesters to Form Dynamic Polythioester-Based Polymers. *ACS Macro Lett.* 2018, *7* (11), 1312–1316. DOI: 10.1021/acsmacrolett.8b00611.

(193) Agouridas, V.; El Mahdi, O.; Diemer, V.; Cargoët, M.; Monbaliu, J.-C. M.; Melnyk, O. Native Chemical Ligation and Extended Methods: Mechanisms, Catalysis, Scope, and Limitations. *Chemical reviews* 2019, *119* (12), 7328–7443. DOI: 10.1021/acs.chemrev.8b00712. Published Online: May. 3, 2019.

CHAPTER 2

A FLUORESCENT PROBE WITH IMPROVED WATER SOLUBILITY PERMITS THE ANALYSIS OF PROTEIN S-DEPALMITOYLATION ACTIVITY IN LIVE CELLS

2.1 Introduction

As stated in 1.5.5, our group recently unveiled depalmitoylation probes (DPPs), a new family of fluorescent probes that permit the analysis of APT activity in real time and in live cells[1]. We found that DPPs are capable of measuring endogenous levels of APTs in a range of cell types. Moreover, we used the DPPs to uncover rapid growth factor-mediated alterations in the APT activity, revealing connections between receptor tyrosine kinases and dynamic lipidation signaling.

Depalmitoylation probe 1 (DPP-1), the simplest DPP with a palmitoylated substrate, was quite insoluble and failed in live cell experiments. To create DPPs capable of deployment in live cells, we found that we needed instead to use a non-natural surrogate acylation substrate mimetic, S-octanoylation (a C8 lipid), in our first-generation S-depalmitoylase probes, DPP-2 and DPP-3. This shorter lipid modification increased water solubility and cell permeability, as indicated by the ability to perform *in vitro* biochemical assays without detergents and the robust signal in live cells due to endogenous S-depalmitoylases, respectively. However, the usage of a shorter lipid modification is potentially problematic, as thioesterases that cannot act on a natural S-palmitoyl protein thioester and are not components of the S-depalmitoylation pathway could process these first-generation DPPs, resulting in false-positive signals. Therefore,

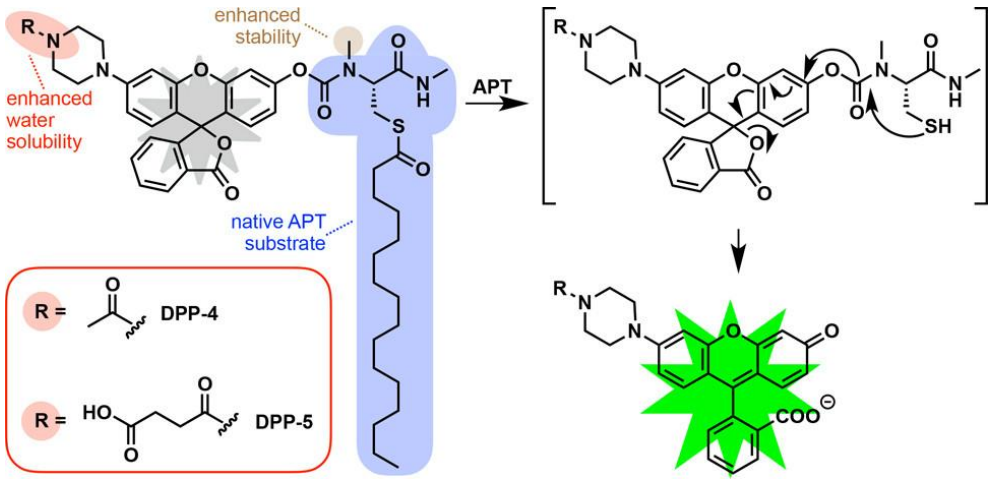

Figure 2.1 Structure and mechanism of enzymatic activation of DPP-4 and DPP-5. An S-palmitoylated peptide substrate is tethered to a rhodol fluorophore through a carbamate linkage. Thioesterase activity on the substrate results in carbamate cleavage and release of a fluorescent product. A piperazine linker allows derivatization of the probes with additional functional groups to increase water solubility and utility in live cells.

the utility and specificity of the DPPs could be dramatically enhanced if they utilized a natural palmitoyl lipid modification as a substrate.

2.2 Results

We reasoned that we could improve the design of the first-generation DPPs and allow for a palmitoyl modification by increasing the solubility of the probe scaffold. The rhodol-based scaffold on which the DPPs are based affords several synthetically tractable positions at which to install solubilizing groups. We chose to use a piperazine moiety on the xanthene portion of the rhodol scaffold, which has previously been used to make modified fluorescent probes[2]. We targeted two new molecules: (1) depalmitoylation probe 4 (DPP-4), which has an acetyl-amide modification on the piperazine, and (2) depalmitoylation probe 5 (DPP-5), which has a succinylated amide and therefore features a carboxylic acid. Both DPP-4 and DPP-5 utilize a simple palmitoylated cysteine residue

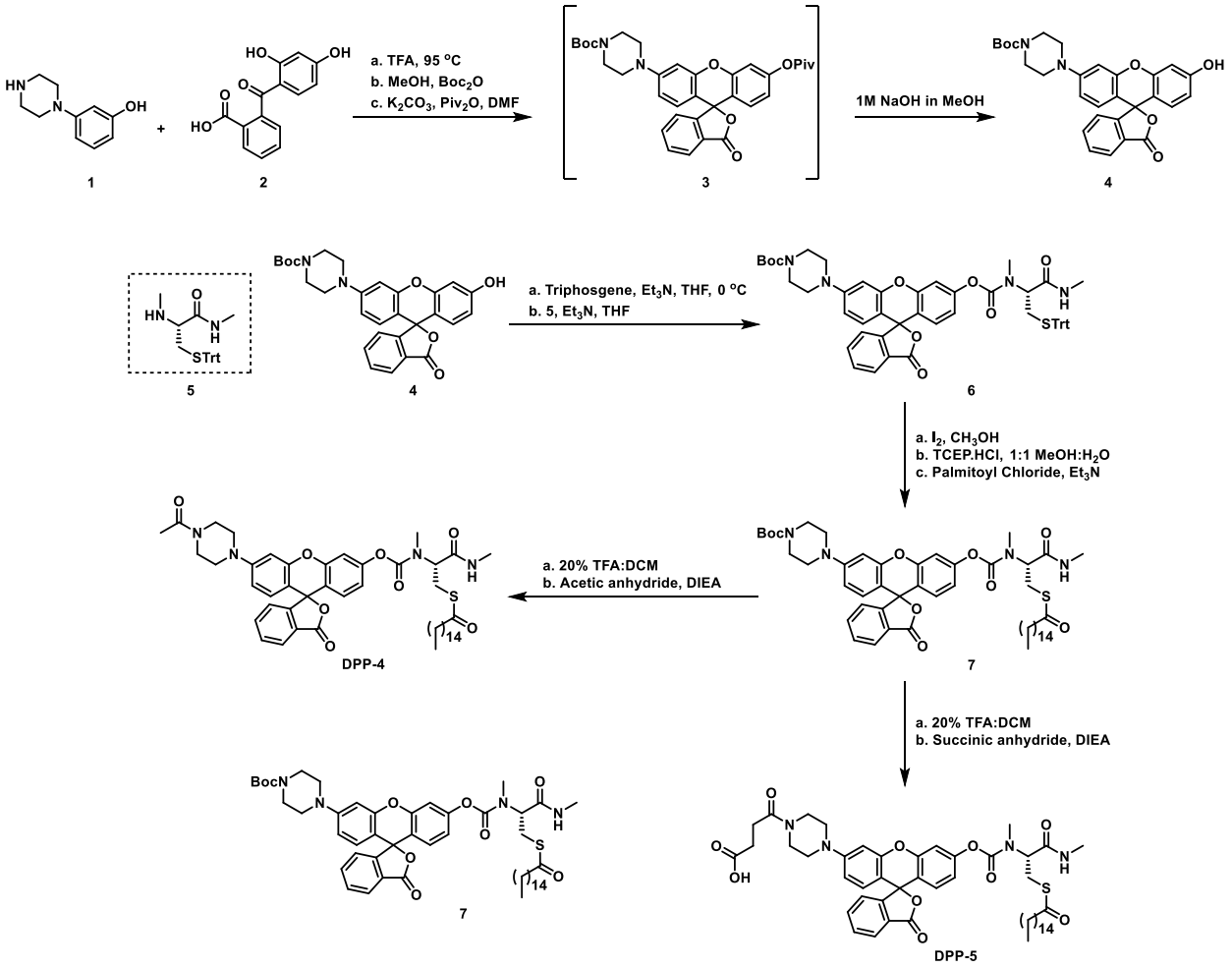

Scheme 2.1 Synthetic scheme for DPP-4 and DPP-5.

with a methyl-amide modification and the substrate for the S-depalmitoylases (**Figure 2.1**). Importantly, the new modifications are not located at the key substrate recognition portion of the probe, which we reasoned would minimize interference with APT enzymatic activity.

Synthesis of DPP-4 and DPP-5 each proceeded smoothly over four steps (**Scheme 2.1**). Once we had them in hand, we compared the new probes to DPP-1 in *in vitro* assays with recombinantly expressed human APT1 and APT2 (**Figure 2.2A**). Both DPP-1 (**Figure 2.2B**) and DPP-4 (**Figure 2.2C**) display very slow kinetics with APT1 and

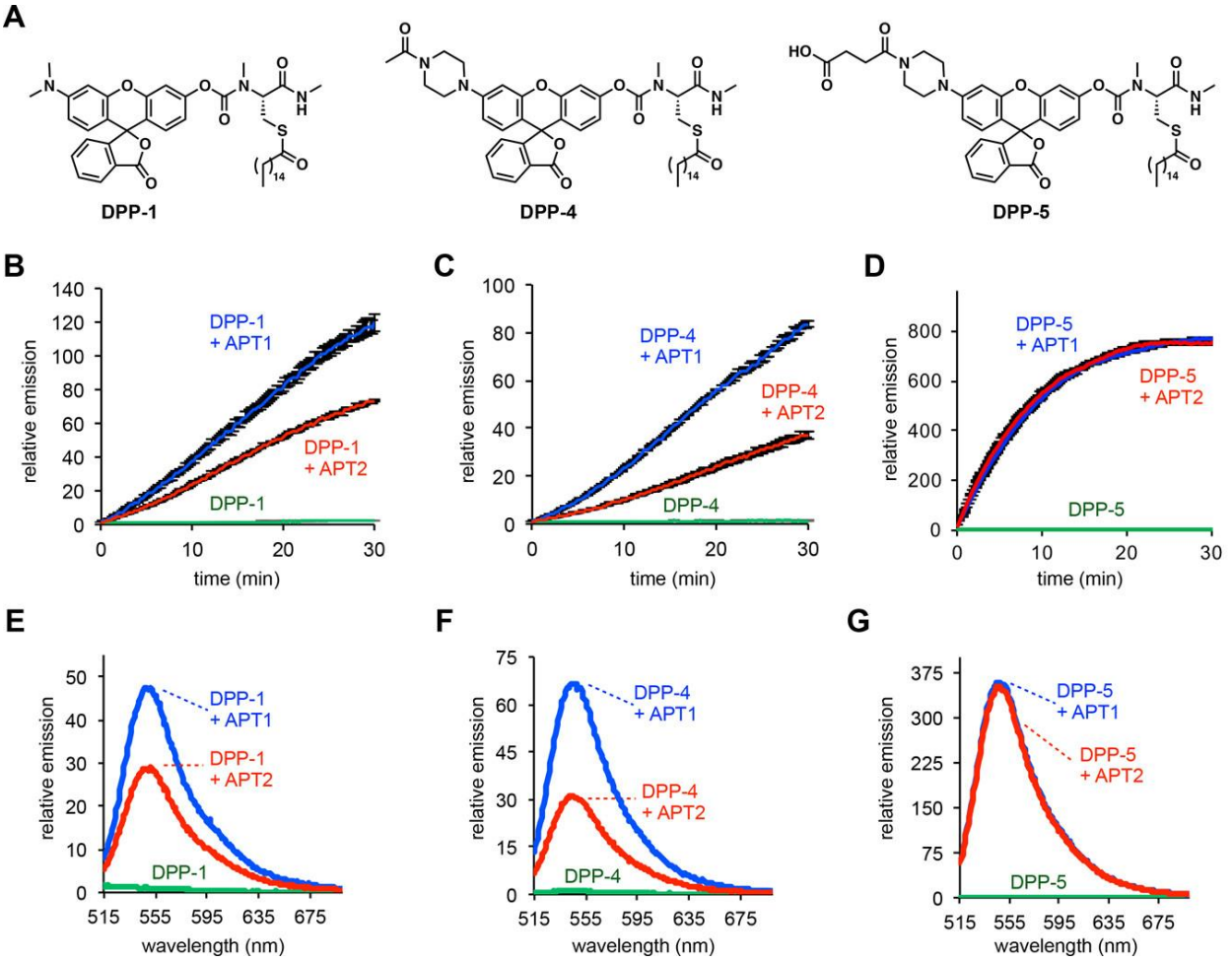

Figure 2.2 *In vitro* activation of DPPs. (A) Structures of DPP-1 (first-generation probe) and the two new probes, DPP-4 and DPP-5. *In vitro* assays of 1 μM (B) DPP-1, (C) DPP-4, and (D) DPP-5 in HEPES (20 mM, pH 7.4, 150 mM NaCl) with or without 50 nM purified APT1 or 50 nM APT2 (λ_{ex} 490/20 nm; λ_{em} 545/20 nm). Error bars are standard errors of the mean (n = 4). Fluorescence emission spectra of (E) DPP-1, (F) DPP-4, and (G) DPP-5 in HEPES (20 mM, pH 7.4, 150 mM NaCl) after treatment for 30 min with or without 50 nM APT1 or 50 nM APT2 (λ_{ex} 485 nm). All data normalized to the background of the probe alone.

APT2 in the absence of detergents. After incubation for 30 min with 1 μM probe and 50 nM APT1 or APT2, DPP-1 and DPP-4 showed only 50- or 30-fold and 70- or 30-fold enhancement in the intensities of their fluorescence signals, respectively (**Figure 2.2E,F**). DPP-5, however, showed a rapid turn-on response to both APT1 and APT2 (**Figure 2.2D**), with a 350-fold increase in the intensity of the fluorescent signal with both enzymes

(**Figure 2.2G**), likely due to enhanced water solubility afforded by the additional carboxylate.

Indeed, LogP analysis of DPP-1, DPP-4, and DPP-5 corroborates the higher water solubility of DPP-5 compared to those of DPP-1 and DPP-4 (**Table 2.1**). Kinetic analysis revealed DPP-5 has kinetic parameters comparable to those of previously reported N-

Table 2.1 LogP analysis of DPP-1, DPP-4 and DPP-5

	LogP
DPP-1	1.57
DPP-4	1.74
DPP-5	0.79

Table 2.2 Kinetic Parameters of APT1 and APT2 with DPP-5

	K_M (μM)	k_{cat} (s^{-1})	k_{cat}/K_M (s^{-1} M^{-1})
APT1	1.6	0.044	2.8×10^4
APT2	2.1	0.066	3.1×10^4

Ras-based semisynthetic substrates for APT1 and APT2 (**Table 2.2**). We were unable to perform quantitative analysis of DPP-1 and DPP-4 because of their slow kinetics in the absence of detergents. Given that DPP-5 showed robust activity with APT1 and APT2 in the absence of detergents, we next assessed whether the *in vitro* performance enhancement translated to live cells.

We loaded HEK293T cells with 1 μM DPP-5 for 20 min and then analyzed the fluorescent signal by fluorescence microscopy. Cells loaded with DPP-5 displayed a bright, intracellular fluorescent signal (**Figures 2.3A**). To determine whether the observed signal was due to endogenous S-depalmitoylases, we deployed PalmB[3,4], a β-lactone-based pan-inhibitor of the S-depalmitoylases. Pretreatment of the HEK293T cells prior to

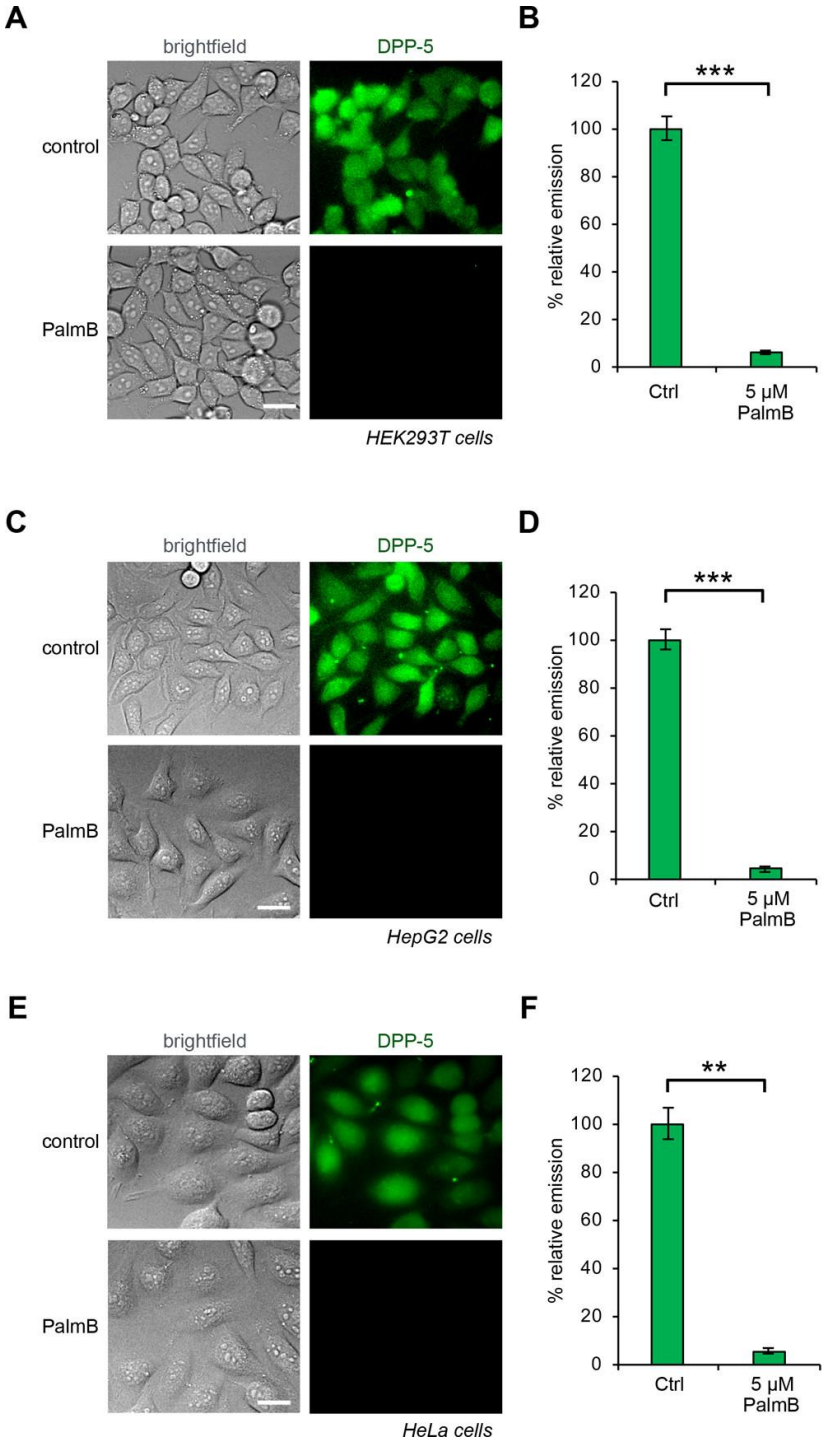

Figure 2.3 Activation of DPP-5 by endogenous S-depalmitoylases in live mammalian cells. (A) HEK293T (C) HepG2 (E) Hela cells treated with either DMSO or 5 μM PalmB for 30 min, washed, loaded with 1 μM DPP-5 with DMSO and 5 μM PalmB for 20 min, and imaged by epifluorescence microscopy. (B) HEK293T (D) HepG2 (F) Hela quantification of the experiment depicted in panel A, C, E. Error bars are standard errors of the mean (n = 3). Statistical analysis performed with a two-tailed student's t test with unequal variance: **P < 0.01, and ***P < 0.005. Scale bars are 20 μm.

addition of DPP-5 abolished ~95% of the fluorescent signal (**Figure 2.3B**). We next sought to assay whether DPP-5 also functions in other cell lines. We repeated the PalmB imaging experiments in HepG2 (**Figure 2.3C,D**) and HeLa cells (**Figure 2.3E,F**). Treatment of both cell lines with 1 μM probe for 20 min resulted in a robust intracellular fluorescent signal. Critically, pretreatment of the cells with 5 μM PalmB blocked more than ~95% of the turn-on response, confirming DPP-5 is measuring endogenous enzyme-mediated S-depalmitoylation. Additionally, 10 μM ML348, an APT1-specific inhibitor, decreased the intensity of the signal from DPP-5 by ~30% in HepG2, whereas 10 μM ML349, an APT2-specific inhibitor, resulted in no change in signal[5] (**Figure 2.4**). Furthermore, treating cells with a combination of both inhibitors affects DPP-5 to the levels similar to that seen with the APT1 inhibitor alone. The unaccounted differential reduction in the intensity of the DPP-5 signal with PalmB and ML348 reinforces the general reactivity of DPP-5 with all possible S-depalmitoylases and suggests enzyme-targeted analogues of DPP-5 would be useful additions to the S-palmitoylation toolbox.

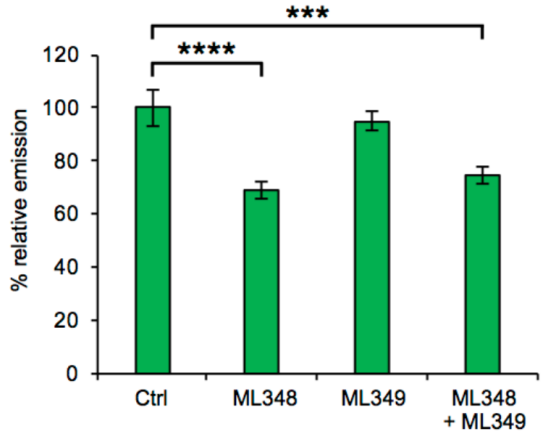

Figure 2.4 Quantification of live cell imaging of DPP-5 with APT1 and APT2 selective inhibitors. HepG2 cells treated for 30 min with 1 μM Hoechst 33342, and either DMSO, 10 μM ML348 (APT1 specific inhibitor), ML349 (APT2 specific inhibitor) or 10 μM of each ML348 and ML349, washed, loaded with 1 μM DPP-5 20 min, and then analyzed by epifluorescence microscopy. Error bars are s.e.m., n = 12. Statistical analysis performed with a two-tailed Student's t-test with unequal variance, *** P value < 0.005, **** P value < 0.0008.

To compare the signal obtained with DPP-5 to DPP-1 and DPP-4, we performed imaging experiments in HEK293T cells with identical concentrations of each probe and

identical microscope settings. While DPP-5 treatment resulted in a robust fluorescent signal, DPP-1 and DPP-4 displayed very low, almost undetectable levels of fluorescence (**Figure 2.5**). Collectively, these results indicate that the additional carboxylate functional group dramatically improves the performance of DPP-5 both *in vitro* and in live cells.

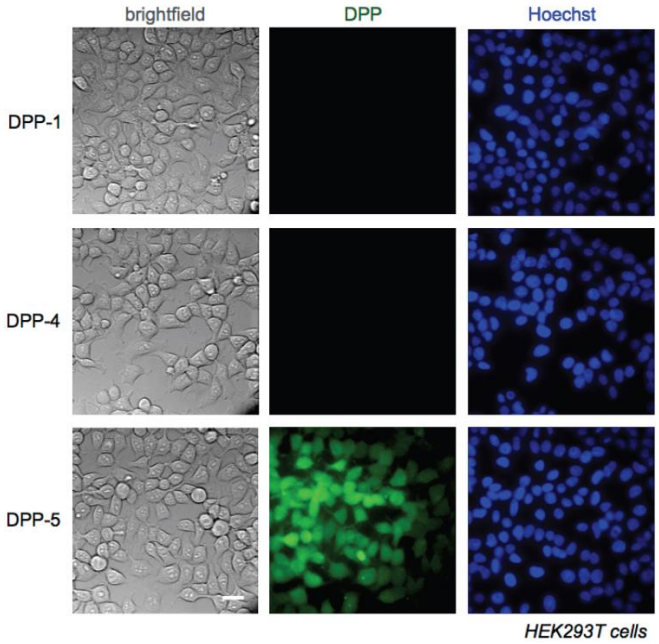

Figure 2.5 Comparison of DPP-1, DPP-4 and DPP-5. HEK293T cells treated for 30 min with 1 μM Hoechst 33342, washed, loaded with 1 μM of either DPP-1, DPP-4 or DPP-5 for 20 min, and then analyzed by epifluorscence microscopy. Images for brightfield, DPP-1/DPP-4/DPP-5, Hoechst 33342 nuclear stain, and an overlay of DPP-1/DPP-4/DPP-5 and Hoechst 33342 are shown for each set of conditions. 20 μm scale bar shown.

Finally, we sought to test whether DPP-5 could detect dynamic alterations in the S-depalmitoylases. Exogenous palmitate has been shown to cause ER stress and affects β-cell viability[6,7]. Aberrant S-palmitoylation has been demonstrated to be one of the mechanisms by which excess palmitate induces ER stress, but the role of S-palmitoylation dynamics in this process is largely unexplored. To this end, we chose to test whether lipid stress through palmitate treatment causes a response from the S-depalmitoylases. We found that pretreatment of HepG2 cells with 1 mM palmitate for 6 h poststarvation resulted in an ~50% increase in the intensity of the S-depalmitoylase signal as measured by DPP-5 (**Figure 2.6A,B**). Furthermore, pretreatment of HepG2 cells with PalmB reduces the intensity of the DPP-5 signal, indicating that palmitate induces activation of S-depalmitoylase activity at the

location at which DPP-5 is measuring the signal (**Figure 2.6B**). To rule out the possibility that the changes in fluorescence signal are due to differential accumulation of DPP-5 in cells upon palmitate treatment, we performed imaging with a control probe, diacetyl rhodol, which maintains the pro-fluorophore core. Once it enters cells, the diacetyl rhodol probe will be rapidly activated by intracellular esterases, allowing us to measure cell permeability and uptake of a related, non-APT active compound (**Figure 2.7A**). We found no measurable effect on the fluorescence signal from HepG2 cells loaded with 1 μM diacetyl rhodol probe with 1 mM palmitate addition in cells (**Figure 2.7B,C**). Collectively, these data show that the S-depalmitoylases respond to local lipid homeostatic levels. This observation also suggests that caution should be taken when adding exogenous lipids to

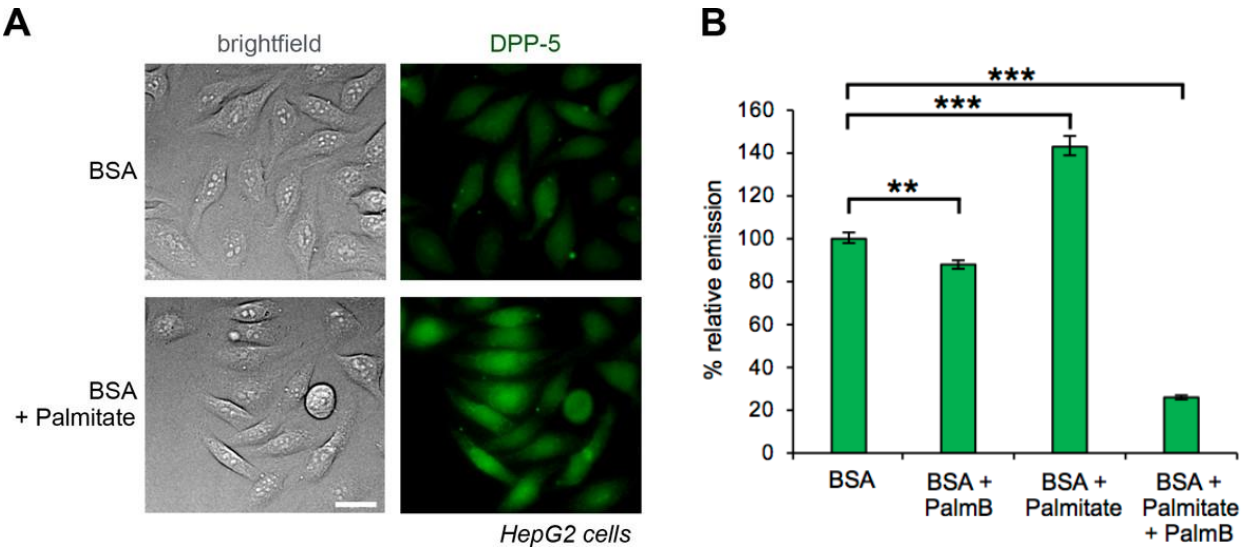

Figure 2.6 Exogenous palmitate activates S-depalmitoylase activity. (A) HepG2 cells treated with 1% BSA with or without 1 mM palmitate for 6 h poststarvation, washed, loaded with 1 μM DPP-5 for 20 min, and imaged by epifluorescence microscopy. (B) Quantification of experiment in HepG2 cells, pretreated with 1% BSA ± 1 mM Palmitate, treated with 1 μM Hoechst 33342 and DMSO/5 μM PalmB for 30 min, washed, loaded with 1 μM DPP5 for 20 min, and then analyzed by epifluorescence microscopy is shown. Error bars are s.e.m., n = 10. Statistical analysis performed with a two-tailed Student's t-test with unequal variance, ** P value = 0.003, *** P value < 0.0001. We have noticed that PalmB is not effective in presence of BSA. Scale bars are 20 μm.

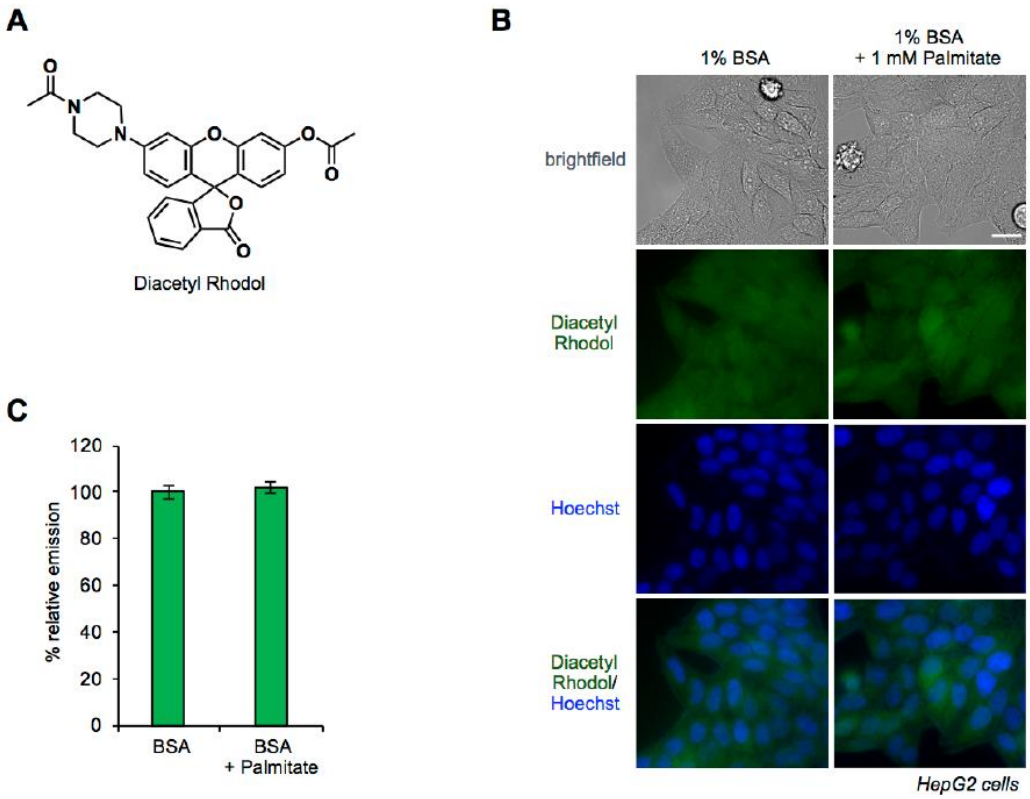

Figure 2.7 Palmitate treatment doesn't influence cell uptake of diacetylrhodol. (A) Structure of diacetyl-rhodol. (B) HepG2 cells, pretreated with 1% BSA ± 1 mM Palmitate, treated with 1 µM Hoechst 33342 for 30 min, washed, loaded with 1 µM Diacetyl-rhodol for 20 min, and then analyzed by epifluorescence microscopy. Two representative images for each treatment with brightfield, DPP-5, Hoechst 33342 nuclear stain, and an overlay of DPP-5, and Hoechst 33342 are shown for each set of conditions. (C) Quantification of experiments shown in (B). 20 µm scale bar shown.

metabolically label the proteome with lipids, as the lipid changes could cause alterations in the activities of the S-depalmitoylases, perturbing the system. Moreover, we have observed different responses to palmitate stress with other probes[8], which are based on an intramolecular cyclization of an electrophilic coumarin derivative[9] to yield a ratiometric response on APT activity, possibly because of differences in subcellular localization of the probes or APT preference, further illustrating the complexity of S-depalmitoylase regulation. Further investigation of these differential responses, and the downstream effects on proteome lipidation levels, is therefore warranted.

2.3 Discussion

To conclude, we presented the design, synthesis, and biological evaluation of DPP-4 and DPP-5, two new fluorescent probes for monitoring S-depalmitoylase activities. We found that DPP-5 is capable of measuring S-depalmitoylase activity robustly *in vitro* and in live cells because of the enhanced solubility endowed by an additional carboxylic acid modification. DPP-5 improves upon the previously developed DPPs by utilizing a natural lipid substrate, rather than a surrogate synthetic substrate. DPP-5, along with future derivatives with additional substrate modifications to enhance S-depalmitoylase selectivity[1], will provide important tools for studying the regulation of proteome lipidation through dynamic S-depalmitoylases.

2.4 Experimental Details

General materials and methods. DMEM Glutamax (10569-010, Gibco), FBS (Gibco/Life Technologies, Qualified US origin), Live Cell Imaging Solution (A14291DJ, Molecular Probes), Opti-MEM (31985-070, Gibco), Hoechst 33342 (Fisher), were purchased as mentioned in parenthesis. Silica gel P60 (SiliCycle, 40-63 μm, 230-400 mesh) was used for column chromatography. Analytical thin layer chromatography was performed using SiliCycle 60 F254 silica gel (precoated sheets, 0.25 mm thick). All chemicals for synthesis were purchased from Sigma-Aldrich (St. Louis, MO) or Fisher Scientific (Pittsburgh, PA) and used as received. ^{1}H NMR and ^{13}C NMR spectra were collected in NMR solvents CDCl3 (Sigma-Aldrich, St. Louis, MO) at 25 ºC using a 500 MHz Bruker Avance II+ spectrometer with 5 mm QNP probe or 400 MHz bruker DRX400 at the Department of Chemistry NMR Facility at the University of Chicago. ^{1}H-NMR chemical shifts are reported

in parts per million (ppm) relative to the peak of residual proton signals from (CDCl3 7.26 ppm). Multiplicities are given as: s (singlet), d (doublet), t (triplet), q (quartet), dd (doublet of doublets), m (multiplet). ^{13}C-NMR chemical shifts are reported in parts per million (ppm) relative to the peak of residual proton signals from (CDCl3 77.16 ppm). Analysis of NMR was done in iNMR version 5.5.1. and NMR plots were obtained from Topspin 2.1. High resolution mass was obtained from Agilent 6224 TOF High Resolution Accurate Mass Spectrometer (HRA-MS) using combination of APCI and ESI at the Department of Chemistry Mass Spectrometry Facility at the University of Chicago. Low resolution mass spectral analyses and liquid chromatography analysis were carried out on an Advion Expression-L mass spectrometer (Ithaca, NY) coupled with an Agilent 1220 Infinity LC System (Santa Clara, CA). *In vitro* biochemical assays with purified APT1/APT2 enzymes were performed on Biotek synergy Neo2 plate reader.

***In vitro* kinetic assays and emission spectra of DPP-1, DPP-4, and DPP-5**. 150 µL of 2 µM DPP-1, DPP4 or DPP-5 in HEPES (20 mM, pH = 7.4, 150 mM NaCl) were added to a 96-well optical bottom plate (Nunc 265301, Thermo Scientific) at room temperature. 150 µL of either HEPES buffer alone or HEPES buffer containing 100 nM APT1 or APT2 (purification using previous methods[1]), was added using a multi-channel pipette, resulting in a final concentration of 1 µM DPP-1/DPP4/DPP-5 and 50 nM APT1 or APT2. Fluorescence intensities (λex 490/20 nm, λem 545/20 nm, Gain 80, read from bottom with height 4.5 mm, and sweep method) were measured at 15 s time intervals for 30 min at 37 °C. Following the 30 min kinetic run, emission spectra were obtained (λex 480/20 nm, λem 515-700 nm, Gain 80, read from bottom with height 4.5 mm, and sweep method).

Enzyme kinetics analysis of DPP5. 150 µL of 1 M DTT in HEPES buffer was added to different concentrations of 150 µL DPP-5 and then the stable fluorescence intensities of totally deacylated product were measured by the methods described above. Fluorescence intensity of per molar deacylated-product was then calculated by linear least-squares fitting of plots of fluorescence vs. concentration. For Michaelis-Menten constant, *in vitr*o kinetics curves were obtained for different final concentrations of DPP-5 in HEPES with 50 nM APT1 or APT2. The fluorescence intensities measured were then normalized to the concentrations of product by fluorescence-intensity-per molar-product. A Lineweaver–Burk plot was used to calculate the Michaelis constant, KM, and the maximum velocity, Vmax, which is proportional to kcat by concentration of APT1 or APT2. All fits have R2 values of > 0.99.

LogP ananyis of DPP-1, DPP-4 and DPP-5. 2 µL of 1 mM of DPP-1/4/5 was dissolved in 500 µL of HEPES buffer in two 1.5 ml tubes. To one of those added 500 µL of 1-octanol and shaken for 10 min followed by keeping undisturbed for 10 min and then withdrawing 10 µl of aqueous phase from both tubes and taken in 96 well plate reader. To this 190 µL of 1M NaOH added and fluorescence intensities (λex 490/20 nm, λem 545/20 nm, Gain 80, read from bottom with height 4.5 mm, and sweep method) were measured at 15 s time intervals for 1 hr at room temperature. The fluorescence read out at saturation was used to calculate LogP values by following equation:

$\log P = \log (F_{°Ct} / F_{aq})$

$F_{°Ct} = F_{total} - F_{aq}$

Where,

$F_{°Ct}$ = Fluorescence of 1-°Ctanol fraction.

F_{aq} = Fluorescence of the aqueous fraction after treatment with 1-°Ctanol.

F_{total} = Fluorescence of the aqueous fraction with no treatment with 1-°Ctanol.

Cell culture and maintenance. HEK293T (ATCC), HeLa cells (ATCC) and HepG2 cells (gift from Prof. Yamuna Krishnan) were maintained in DMEM Glutamax (10% FBS, 1% P/S) at 37 °C and 5% CO2. HEK293T and HeLa cells are listed in the database of commonly misidentified cell lines maintained by ICLAC (http://iclac.org/databases/cross-contaminations/). We obtained fresh cells from ATCC or early passage aliquots from the Cellular Screening Center, University of Chicago, which were frozen down at an early passage (passage 6) in individual aliquots. The cells were then used for less than 30 passages for all experiments. Multiple biological replicates were performed with cells from different passages and freshly thawed aliquots. There was no testing for mycoplasma infection or further authentication because early passage cells were used for all experiments.

Epifluorescent imaging of DPP-5 with PalmB. 250,000 HEK293T cells/well, 120,000 HeLa cells/well, or 100,000 HepG2 cells/well were plated in 700 µL DMEM glutamax (10% FBS + 1% P/S) into 4-well chambered imaging dish (D35C4-20-1.5-N, Cellvis), which were precoated with 5 µg Poly-D-lysine (30-70 KDa, Alfa Aesar) for 2 h. After 20-24 h, the media was replaced by 1 µM Hoechst 33342 and DMSO/5 µM PalmB in 400 µL DMEM glutamax. After 30 min of incubation at 37 °C, the cells were washed with 400 µL of Live

Cell Imaging Solution and replaced by 1 μM DPP-5 with DMSO or 5 μM of PalmB in Live Cell Imaging Solution. After 20 min of incubation at 37 °C, images were obtained on an inverted epifluorescence microscope (Olympus IX83) attached with EMCCD camera (Photometrics Evolve Delta) with 40x oil objective (N/A 1.3) for DPP-5 (excitation filter 500/20, dichroic chroma 89007, emission filter 535/30), Hoechst 33342 (excitation filter 402/15, emission filter 455/50, dichroic chroma 89013), and brightfield. Analyses were performed in ImageJ (Wayne Rasband, NIH). For data analysis, the average fluorescence intensity per image in each experimental condition was obtained by selecting ROI in Brightfield and applying that to the corresponding DPP-5 image, average background fluorescence intensity was subtracted and data was normalized to the average fluorescence intensity of the DMSO control. Each experiment was repeated in at least two biological replicates with identical results.

Epifluorescent imaging of DPP-5 with ML348 and ML349. 16,000 HepG2 cells/well were plated in 100 μL DMEM glutamax (10% FBS) into 4 wells of a 96-well chambered imaging dish (P96-1-N, Cellvis), which were precoated with 0.7 μg Poly-D-lysine (30-70 KDa, Alfa Aesar) for 2 hrs. After 24 h, cells were washed with Live Cell Imaging Solution and replaced by 1 μM Hoechst 33342 and DMSO/10 μM ML348/10 μM ML349/10 μM of both ML348 and ML349 in 100 μL DMEM glutamax. After 30 min of incubation at 37 °C, the cells were washed with 100 μL of Live Cell Imaging Solution and replaced by 1 μM DPP-5 in Live Cell Imaging Solution. After 20 min of incubation at 37 °C, images were obtained on an inverted epifluorescence microscope (Lieca DMi8) equipped with a camera (Hamamatsu Orca-Flash 4.0) with 63x oil objective (N/A 1.4) and light source

(Sutter Lamda XL, 300 W Xenon) for DPP-5 (YFP filter cube 1525306), Hoechst 33342 (DAPI filter cube), and brightfield using leica LASX software. Analyses were performed in ImageJ (Wayne Rasband, NIH). Each experiment was repeated in three biological replicates and 8-12 images were considered for plotting bar graphs for quantification. For detailed data analysis, the average fluorescence intensity per image in each experimental condition was obtained by selecting ROI in Brightfield and applying that to the corresponding DPP-5 image, average background fluorescence intensity was subtracted and data was normalized to the average fluorescence intensity of the control experiment.

Epifluorescent imaging for comparing DPP-1, DPP-4 and DPP-5. 250,000 HEK293T cells/well were plated in 700 µL DMEM glutamax (10% FBS + 1% P/S) into three wells of a 4-well chambered imaging dish (D35C4-20-1.5-N, Cellvis), which were precoated with 5 µg Poly-Dlysine (30-70 KDa, Alfa Aesar) for 2 h. After 18 h, the media was replaced by 1 µM Hoechst 33342 in 400 µL DMEM glutamax. After 30 min of incubation at 37 °C, the cells were washed with 400 µL of Live Cell Imaging Solution and replaced by 1 µM DPP-1/DPP-4/DPP-5 in Live Cell Imaging Solution. After 20 min of incubation at 37 °C, images were obtained and analyzed as described above.

Epifluorescent imaging of DPP-5 with palmitate. 100,000 HepG2 cells/well were plated in 700 µL DMEM glutamax (10% FBS) into two wells of a 4-well chambered imaging dish (D35C4-201.5-N, Cellvis), which were precoated with 5 µg Poly-D-lysine (30-70 KDa, Alfa Aesar) for 2 hrs. After 18 h, media was replaced by 500 µL DMEM glutamax for starvation. After 6 h of starvation, cells were treated for another 6 h with 500

µL of 1% BSA ± 1 mM Palmitate made with DMEM glutamax. Then, 20 µL of 21 µM Hoechst 33342 in DMEM glutamax was added to each well such that final concentration of Hoechst 33342 is 1 µM. After 30 min of incubation at 37 °C, the cells were washed with 400 µL of Live Cell Imaging Solution and replaced by 1 µM DPP-5 in Live Cell Imaging Solution. After 20 min of incubation at 37 °C, images were obtained and analysis was performed as described above. Each experiment was repeated in two biological replicates with identical results.

Epifluorescent imaging of DPP-5 with PalmB on palmitate treatment. 13,000 HepG2 cells/well were plated in 100 µL DMEM glutamax (10% FBS) into 4 wells of a 96-well chambered imaging dish (P96-1-N, Cellvis). After 18 h, media was replaced by 100 µL DMEM glutamax for starvation. After 6 h of starvation, cells were treated for another 6 h with 100 µL of 1% BSA ± 1 mM Palmitate made with DMEM glutamax. Then, 100 µL of 1 µM Hoechst 33342 prepared in 1% BSA ± 1 mM Palmitate with DMSO/5 µM PalmB was added to respective wells. After 30 min of incubation at 37 °C, the cells were washed with 100 µL of Live Cell Imaging Solution and replaced by 1 µM DPP-5 in Live Cell Imaging Solution. After 20 min of incubation at 37 °C, images were obtained on Leica epi-fluorescent microscope and analyzed as described above.

Epifluorescent imaging of diacetyl rhodol on palmitate treatment. 13,000 HepG2 cells/well were plated in 100 µL DMEM glutamax (10% FBS) into 2 wells of a 96-well chambered imaging dish (P96-1-N, Cellvis). After 18 h, media was replaced by 100 µL DMEM glutamax for starvation. After 6 h of starvation, cells were treated for another 6 h

with 100 µL of 1% BSA ± 1 mM Palmitate made with DMEM glutamax. Then, 100 µL of 1 µM Hoechst 33342 prepared in 1% BSA ± 1 mM Palmitate was added to respective wells. After 30 min of incubation at 37 °C, the cells were washed with 100 µL of Live Cell Imaging Solution and replaced by 1 µM diacetyl rhodol in Live Cell Imaging Solution. After 20 min of incubation at 37 °C, images were obtained on Leica epifluorescent microscope and analyzed as described above.

2.5 Synthetic procedures

Synthesis of 4 (Boc-Rhodol). Adapted from literature[2]. To a mixture of **1** (2.143 g, 1.0 eq, 12.02 mmol) and **2**[10] (3.053 g, 1.0 eq, 11.82 mmol) in a pressure flask, TFA (5 mL) was added, and the resulting reaction mixture was stirred at 95 °C for 9 h. The reaction mixture was diluted 3x with 30 mL of DCM, followed by rotatory evaporation to remove the residual TFA. To the resultant crude material, Et_3N (7.2 mL, 5 eq, 51.7 mmol) and MeOH (25 mL) were added. After stirring for 5 min, Boc_2O (2.106 g, 0.93 eq, 9.6 mmol) was added. After stirring the resultant reaction mixture overnight at room temperature, the MeOH was removed by rotatory evaporation. To the crude mixture, K_2CO_3 (4.287 g, 3.0 eq, 31.0 mmol), pivalic anhydride (2.1 mL, 1.0 eq, 10.3 mmol) and DMF (15 mL) were added and the reaction stirred for 1 h. The reaction mixture was diluted with 30 mL DCM, filtered, and evaporated. The crude product was purified by column chromatography (Silica; 0-20% EtOAc:DCM) to yield 3. The combined fractions of 3 were evaporated and dissolved in MeOH (60 mL), to which 3 M NaOH (30 mL) was added, and reaction mixture stirred for 30 min at room temperature. The reaction mixture was then evaporated by rotatory evaporation, the crude product was diluted by DCM (50 mL), and then washed

by aq. HCl (pH ~ 3-4). The aqueous layer was further extracted by DCM 2 x 30 mL, the combined organic layer was dried over Na_2SO_4, and then evaporated to give a crude product. Purification by column chromatography (Silica; 0-5% MeOH:DCM) yielded 4 (3.892 g, 65%). R_f: 0.41 (Silica; 5% MeOH:DCM). ^{1}H-NMR (500 MHz; $CDCl_3$): δ 9.04-8.92 (b, 1H), 8.02 (dd, J = 6.4, 1.9 Hz, 1H), 7.61-7.55 (m, 2H), 7.10-7.09 (m, 1H), 6.73 (d, J = 8.8 Hz, 1H), 6.67-6.64 (m, 2H), 6.60-6.52 (m, 3H), 3.51 (d, J = 4.7 Hz, 4H), 3.21 (s, 4H), 1.46 (s, 9H). ^{13}C-NMR (126 MHz; $CDCl_3$):170.3, 162.1, 154.9, 153.8, 153.5, 148.6, 134.0, 129.8, 129.6, 129.5, 129.2, 126.2, 125.2, 114.3, 112.5, 111.3, 110.7, 103.1. 80.6, 53.5, 52.4, 49.2, 47.7, 28.5, 27.2, 27.1. HRA-MS(+): Calculated for $C_{29}H_{28}N_2O_6$ [M+] 500.1947; found 500.1953.

Synthesis of 6. To a solution of **4** (306.4 mg, 0.612 mmol, 1.0 eq) in dry THF (7 mL). Et_3N (0.8 M, 0.77 mL, 0.613 mmol, 1.0 eq) was added. The resultant solution was added dropwise over 15 min to a solution of triphosgene (181.6 mg, 0.612 mmol, 1.0 eq) in dry THF (5 mL) in an ice bath. After 5 min, the ice bath was replaced by a 40 °C water bath and N_2 flushed through the reaction mixture to evaporate the solvent completely. Then, the 40 °C water bath was removed and the crude product was suspended in dry THF (4 mL). To this reaction mixture, **5**[1] (0.32 M, 1.88 mL, 0.609 mmol, 1.0 eq), followed by Et_3N (0.8 M, 0.77 mL, 0.613 mmol, 1.0 eq), were added dropwise. After 15 min of stirring, the reaction mixture was quenched by five drops of 1M HCl and the solvent evaporated by rotary evaporation. The crude reaction crude was purified by column chromatography (Silica; 5-25% EtOAc:DCM) to yield **6** (259.8 mg; 46%). R_f: 0.39 (Silica; 15% EtOAc:DCM). ^{1}H-NMR (500 MHz; $CDCl_3$): δ 8.05 (t, J = 6.5 Hz, 1H), 7.70-7.62 (m, 2H),

7.50-7.45 (m, 6H), 7.33-7.09 (m, 11H), 6.84-6.63 (m, 5H), 6.15-6.07 (m, 1H), 4.35 (m, 4.9 Hz, 1H), 3.61 (t, J = 4.8 Hz, 4H), 3.25 (d, J = 4.5 Hz, 4H), 2.90 (d, J = 0.8 Hz, 2H), 2.83-2.68 (m, 5H), 1.53 (s, 10H). ^{13}C-NMR (126 MHz; $CDCl_3$): δ 169.4, 169.1, 169.1, 155.0, 154.6, 153.0, 153.0, 152.9, 152.8, 152.4, 152.2, 151.9, 151.9, 144.4, 135.1, 129.8, 129.6, 129.5, 128.9, 128.8, 128.0, 126.8, 126.6, 125.0, 124.0, 123.9, 117.3, 117.3, 116.5, 116.4, 112.3, 110.3, 110.2, 109.1, 102.2, 82.8, 82.7, 80.1, 67.2, 67.1, 67.1, 67.0, 58.5, 48.1, 31.3, 30.8, 30.7, 30.3, 28.4, 26.3, 26.1. HRA-MS(+): Calculated for $C_{54}H_{52}N_4O_8S$ [M+] 916.3506; found 916.3508.

Synthesis of 7. To a solution of **6** (408 mg, 0.445 mmol, 1.0 eq) in MeOH (10 mL), I2 (226 mg in 4 mL MeOH; 0.890 mmol, 2.0 eq) was added dropwise over 5 min. The reaction mixture was quenched with a solution of 0.2 M sodium citrate and 0.2 M sodium ascorbate at pH ~3-4 until the yellow color disappeared. The quenched reaction mix was diluted with DCM (25 mL) and washed with brine (25 mL). The aqueous layer was washed again with DCM (25 mL). The combined organic layers were dried over Na_2SO_4 and evaporated by rotary evaporation. The resultant crude containing the disulfide product was suspended with 1 mL H_2O and dissolved with minimal amount of MeOH. Then TCEP-HCl (638 mg, 2.23 mmol, 5.0 eq) was added. The reaction mixture was stirred at room temperature until no starting material was observed by LC-MS. The reaction was treated with 20 mL 0.1 M HCl and extracted with 25 mL DCM. The aqueous layer was washed again with DCM (25 mL). The combined organic layers were dried over Na_2SO_4 and evaporated by rotary evaporation. The resultant crude containing the free thiol product was dissolved with 4 mL DCM and added into palmitoyl chloride (405 µL, 1.335 mmol,

3.0 eq). The red solution was treated with Et_3N dropwisely until no starting material was observed by LC-MS. The resulting reaction mixture was diluted with DCM (25 mL) and washed with concentrated $NaHCO_3$ followed by brine (20 mL). The aqueous layer was washed again with DCM (20 mL) and the combined organic layers were dried over Na2SO4 and evaporated by rotary evaporation. Purification by column chromatography (Silica; 0-100% Ethyl acetate in Hexane plus 2% MeOH) afforded 7 as light red oil (240.4 mg, 59.2%). Purity was assayed by LC/MS. R_f: 0.53 (Silica; 1:2 EtOAc:DCM). ^{1}H-NMR (500 MHz; $CDCl_3$): δ. 8.03 (d, J = 7.5 Hz, 1H), 7.69-7.61 (m, 2H), 7.16-7.10 (m, 2H), 6.83-6.77 (m, 2H), 6.70-6.61 (m, 3H), 6.26 (m, 1H), 4.83-4.71 (m, 1H), 3.59 (s, 4H), 3.48 (dd, J = 14.2, 5.9 Hz, 1H), 3.37-3.31 (m, 1H), 3.23 (s, 4H), 3.06 (s, 2H), 2.95 (s, 1H), 2.87 (t, J = 4.7 Hz, 1H), 2.81 (t, J = 4.2 Hz, 2H), 2.56 (m, 2H), 1.65 (dt, J = 14.9, 7.5 Hz, 3H), 1.27 (s, 32H), 0.89 (t, J = 6.9 Hz, 3H). ^{13}C-NMR (126 MHz; $CDCl_3$): δ 198.6, 169.3, 169.2, 155.1, 154.6, 152.8, 152.3, 152.2, 151.9, 135.1, 129.8, 128.9, 126.6, 125.2, 80.1, 44.1, 31.9, 29.6, 29.5, 29.4, 29.3, 29.2, 29.1, 28.9, 28.4, 27.3, 25.5, 22.6, 14.1. HRA-MS(+): Calculated for $C_{51}H_{68}N_4O_9S$ [M+] 912.4707; found 912.4720.

Synthesis of DPP-4. A solution of **7** (61.0 mg, 66.8 µmol, 1.0 eq) in 20% TFA:DCM (5 mL) was stirred for 30 min at room temperature, followed by dilution with DCM (3x 20 mL) and evaporation by rotatory evaporation. The resulting crude was suspended in DCM (5 mL) and acetic anhydride (51 µL, 0.540 mmol, 8.0 eq) was added followed by slowly addition of DIEA until reaction was completed. The reaction mix was diluted with DCM (20 mL) then washed with concentrated $NaHCO_3$ followed by brine (20 mL). The aqueous layer was washed again with DCM (20 mL) and the combined organic layers were dried

over Na_2SO_4 and evaporated by rotary evaporation. Purification by column chromatography (Silica; 50% DCM in ethyl acetate with 0-5% MeOH) afforded DPP-4 as colorless oil (35.0 mg, 61.4%). R_f: 0.2 (Silica; 1:1 EtOAc:DCM). ^{1}H-NMR (500 MHz; $CDCl_3$): δ 8.03 (s, 1H), 7.69-7.62 (m, 2H), 7.17-7.10 (m, 2H), 6.85-6.77 (m, 2H), 6.70-6.67 (m, 2H), 6.62 (dd, J = 8.9, 2.2 Hz, 1H), 6.25 (br, 1H), 4.82-4.70 (m, 1H), 3.79-3.74 (m, 2H), 3.63 (t, J = 4.9 Hz, 2H), 3.48 (dd, J = 14.1, 5.9 Hz, 1H), 3.37-3.24 (m, 5H), 3.06 (s, 2H), 2.96 (s, 1H), 2.88 (t, J = 3.7 Hz, 1H), 2.83 (t, J = 3.8 Hz, 2H), 2.56 (m, 2H), 1.66 (m, 2H), 1.27 (m, 27H), 0.89 (t, J = 7.0 Hz, 3H). ^{13}C-NMR (126 MHz; $CDCl_3$): δ 198.8, 171.3, 169.5, 169.3, 169.2, 155.3, 153.1, 152.6, 152.5, 152.3, 152.0, 135.2, 129.9, 129.0, 128.9, 126.7, 125.2, 124.1, 117.4, 116.7, 112.5, 110.3, 109.6, 102.5, 82.7, 60.5, 58.8, 48.5, 48.2, 46.0, 44.2, 41.1, 32.0, 31.2, 29.8, 29.7, 29.5, 29.3, 29.0, 27.4, 26.4, 25.7, 22.8, 21.4, 21.2, 14.3, 14.2. HRA-MS(+): Calculated for $C_{48}H_{62}N_4O_8S$ [M+] 854.4288; found 854.4261.

Synthesis of DPP-5. A solution of **7** (63.4 mg, 69.4 μmol, 1.0 eq) in 20% TFA-DCM (5 mL) was stirred for 30 min at room temperature, followed by dilution with DCM (3x 20 mL) and evaporation by rotatory evaporation. The resulting crude was suspended in DCM (5 mL) and succinic anhydride (55.6 mg, 0.555 mmol, 8.0 eq) was added followed by slowly addition of DIEA until reaction was completed. The reaction mix was acidified with 10 mL 1M HCl and diluted with DCM (20 mL) then washed with brine (20 mL). The aqueous layer was washed again with DCM (20 mL) and the combined organic layers were dried over Na_2SO_4 and evaporated by rotary evaporation. Purification by column chromatography (Silica; 0-10% MeOH in DCM) afforded DPP-5 as a pink solid (43.8 mg,

69.1%). R_f: 0.33 (Silica; 5% MeOH:DCM). ^{1}H-NMR (500 MHz; $CDCl_3$): δ 8.03 (d, J = 7.5 Hz, 1H), 7.69-7.62 (m, 2H), 7.16-7.09 (m, 2H), 6.85-6.76 (m, 2H), 6.67 (dd, J = 7.8, 4.9 Hz, 2H), 6.60 (dd, J = 8.9, 2.0 Hz, 1H), 6.44 (d, J = 4.8 Hz, 1H), 4.81-4.71 (m, 1H), 3.76 (s, 2H), 3.70 (s, 2H), 3.64 (s, 1H), 3.47 (dd, J = 14.1, 6.1 Hz, 1H), 3.35-3.23 (m, 4H), 3.06 (s, 2H), 2.95 (s, 1H), 2.87 (t, J = 4.1 Hz, 1H), 2.81 (dd, J = 4.7, 2.8 Hz, 2H), 2.72-2.65 (m, 4H), 2.57 (q, J = 7.2 Hz, 2H), 1.67-1.60 (m, 2H), 1.25 (d, J = 7.0 Hz, 24H), 0.89 (t, J = 6.9 Hz, 3H). ^{13}C-NMR (126 MHz; $CDCl_3$): δ 198.9, 176.6, 170.4, 169.5, 169.4, 155.3, 153.1, 152.5, 152.3, 152.0, 135.2, 130.0, 129.0, 128.9, 126.6, 125.2, 124.1, 117.4, 116.6, 112.4, 110.3, 109.5, 102.4, 82.8, 48.2, 48.0, 45.0, 44.2, 41.5, 32.0, 31.2, 31.1, 29.8, 29.7, 29.5, 29.4, 29.3, 29.0, 28.8, 28.0, 27.4, 26.6, 26.5, 25.6, 22.8, 14.2. HRA-MS(+): Calculated for $C_{50}H_{64}N_4O_{10}S$ [M+] 912.4343; found 912.4344.

2.6 References

(1) Kathayat, R. S.; Elvira, P. D.; Dickinson, B. C. A fluorescent probe for cysteine depalmitoylation reveals dynamic APT signaling. *Nature chemical biology* **2017**, *13* (2), 150–152.

(2) Dickinson, B. C.; Chang, C. J. A targetable fluorescent probe for imaging hydrogen peroxide in the mitochondria of living cells. *Journal of the American Chemical Society* **2008**, *130* (30), 9638–9639.

(3) Rusch, M.; Zimmermann, T. J.; Bürger, M.; Dekker, F. J.; Görmer, K.; Triola, G.; Brockmeyer, A.; Janning, P.; Böttcher, T.; Sieber, S. A.; Vetter, I. R.; Hedberg, C.; Waldmann, H. Identification of acyl protein thioesterases 1 and 2 as the cellular targets of the Ras-signaling modulators palmostatin B and M. *Angewandte Chemie (International ed. in English)* **2011**, *50* (42), 9838–9842.

(4) Dekker, F. J.; Rocks, O.; Vartak, N.; Menninger, S.; Hedberg, C.; Balamurugan, R.; Wetzel, S.; Renner, S.; Gerauer, M.; Schölermann, B.; Rusch, M.; Kramer, J. W.; Rauh, D.; Coates, G. W.; Brunsveld, L.; Bastiaens, P. I. H.; Waldmann, H. Small-molecule inhibition of APT1 affects Ras localization and signaling. *Nature chemical biology* **2010**, *6* (6), 449–456.

(5) Adibekian, A.; Martin, B. R.; Chang, J. W.; Hsu, K.-L.; Tsuboi, K.; Bachovchin, D. A.; Speers, A. E.; Brown, S. J.; Spicer, T.; Fernandez-Vega, V.; Ferguson, J.; Hodder, P. S.; Rosen, H.; Cravatt, B. F. Confirming target engagement for reversible inhibitors in vivo

by kinetically tuned activity-based probes. *Journal of the American Chemical Society* **2012**, *134* (25), 10345–10348.

(6) Baldwin, A. C.; Green, C. D.; Olson, L. K.; Moxley, M. A.; Corbett, J. A. A role for aberrant protein palmitoylation in FFA-induced ER stress and β-cell death. *American journal of physiology. Endocrinology and metabolism* **2012**, *302* (11), E1390-8.

(7) Cunha, D. A.; Hekerman, P.; Ladrière, L.; Bazarra-Castro, A.; Ortis, F.; Wakeham, M. C.; Moore, F.; Rasschaert, J.; Cardozo, A. K.; Bellomo, E.; Overbergh, L.; Mathieu, C.; Lupi, R.; Hai, T.; Herchuelz, A.; Marchetti, P.; Rutter, G. A.; Eizirik, D. L.; Cnop, M. Initiation and execution of lipotoxic ER stress in pancreatic beta-cells. *Journal of cell science* **2008**, *121* (Pt 14), 2308–2318.

(8) Beck, M. W.; Kathayat, R. S.; Cham, C. M.; Chang, E. B.; Dickinson, B. C. Michael addition-based probes for ratiometric fluorescence imaging of protein S-depalmitoylases in live cells and tissues. *Chemical science* **2017**, *8* (11), 7588–7592.

(9) Cho, A. Y.; Choi, K. A Coumarin-based Fluorescence Sensor for the Reversible Detection of Thiols. *Chem. Lett.* **2012**, *41* (12), 1611–1612.

(10) Smith, G. A.; Metcalfe, J. C.; Clarke, S. D. The design and properties of a series of calcium indicators which shift from rhodamine-like to fluorescein-like fluorescence on binding calcium. *J. Chem. Soc., Perkin Trans. 2* **1993** (6), 1195.

Appendix to Chapter 2: NMR Spectra

Compound 4

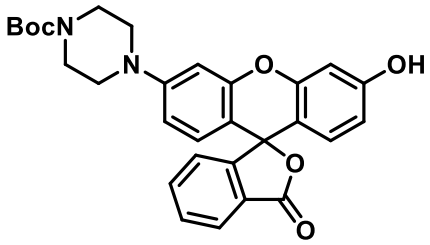

^{1}H-NMR (500 MHz; $CDCl_3$)

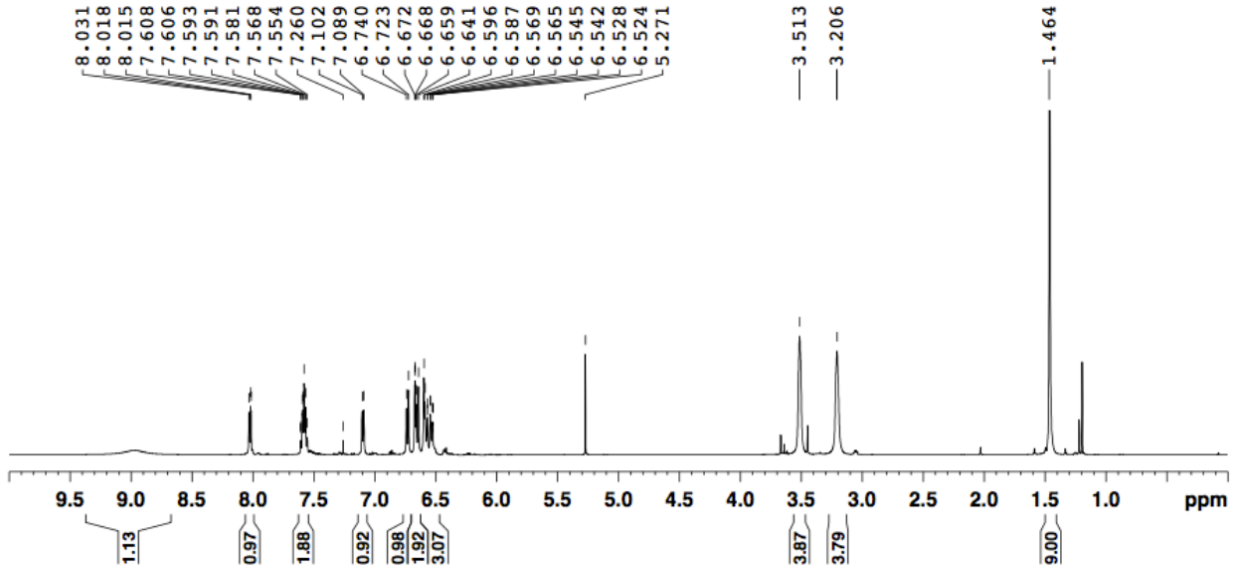

^{13}C-NMR (126 MHz; $CDCl_3$)

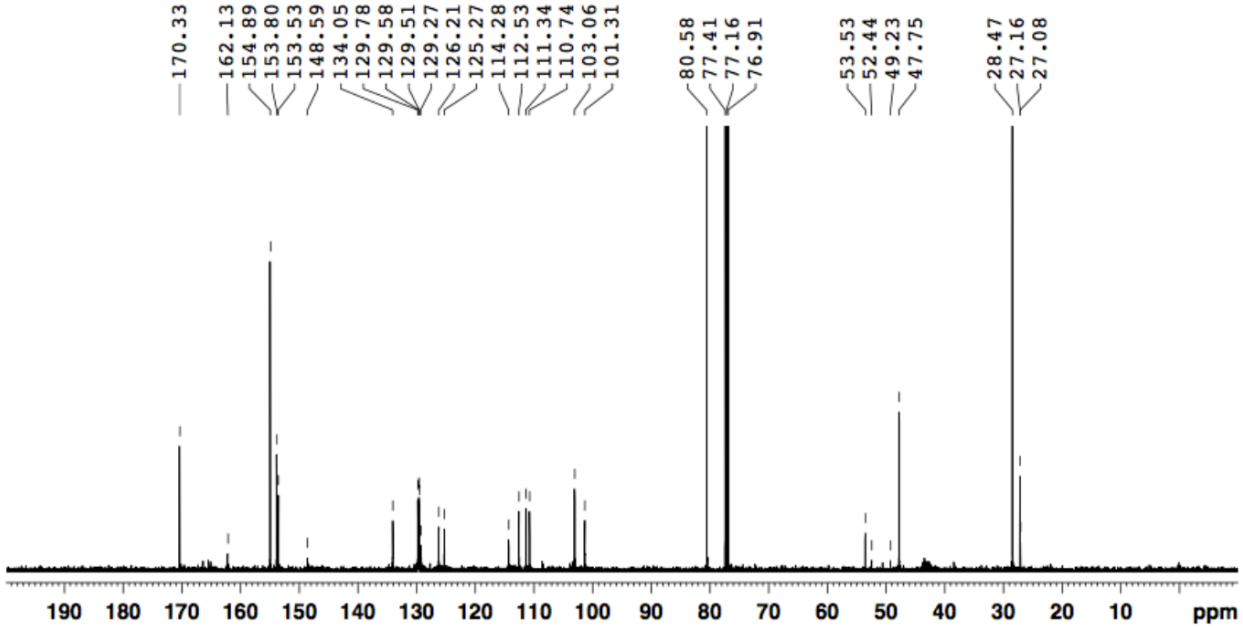

Compound 6

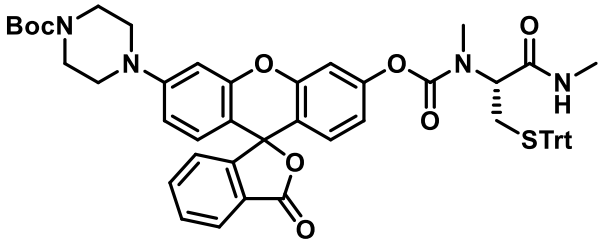

^{1}H-NMR (500 MHz; $CDCl_3$)

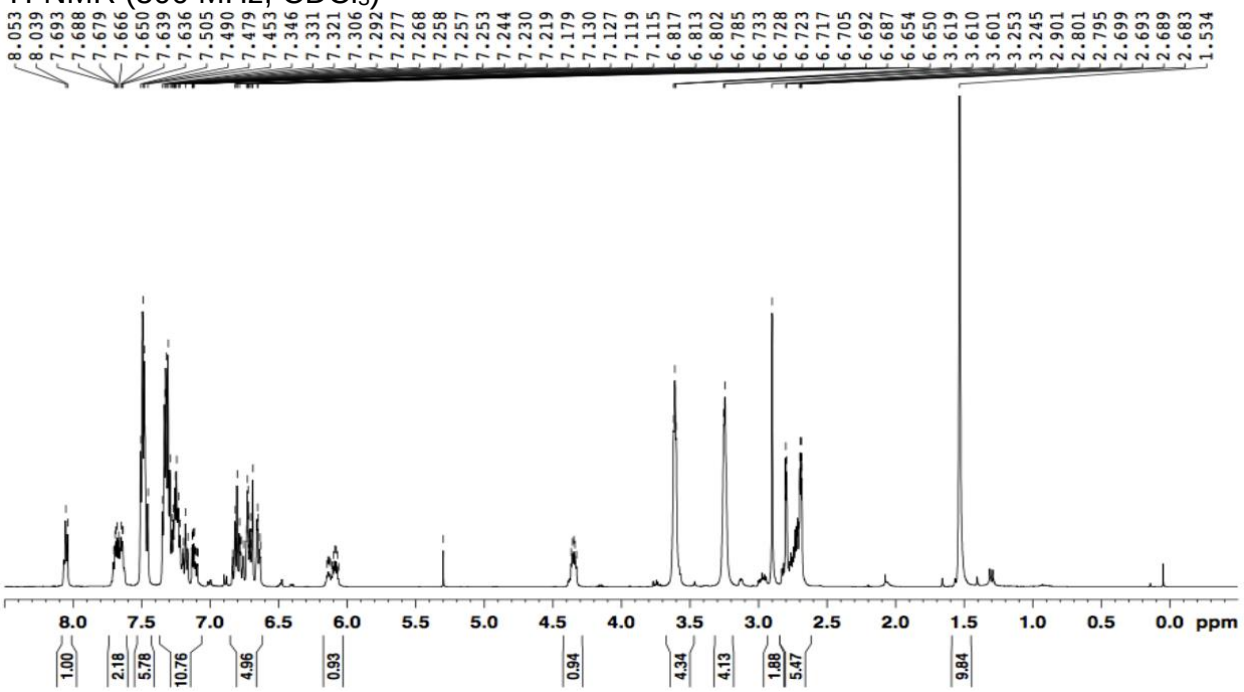

^{13}C-NMR (126 MHz; $CDCl_3$)

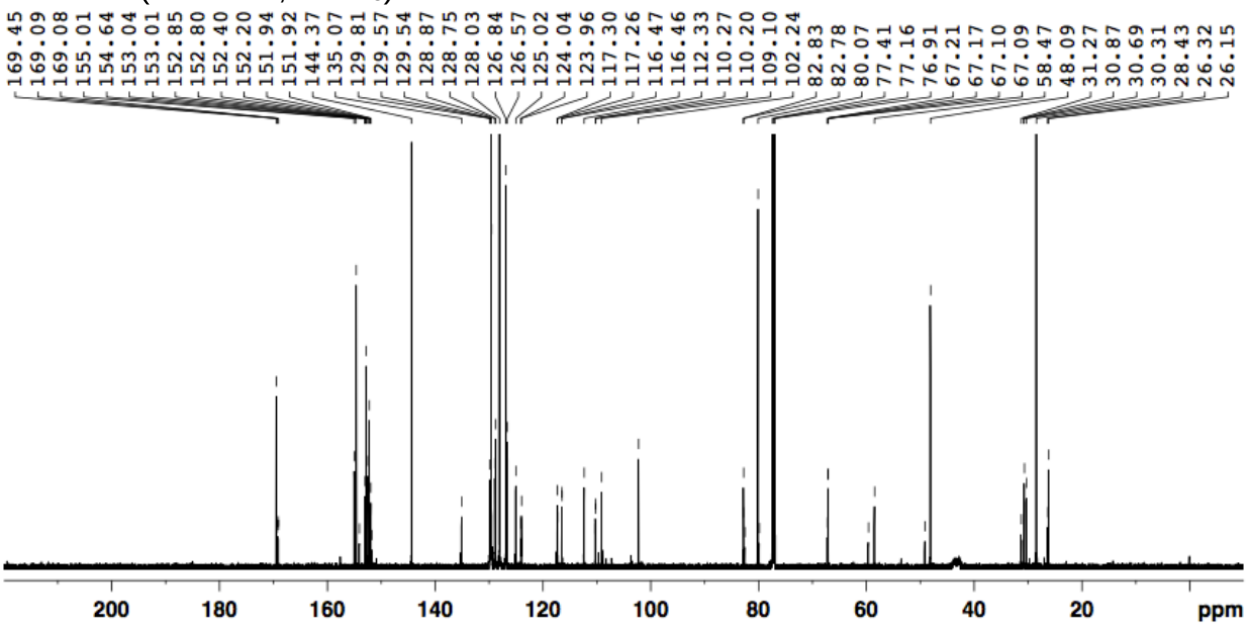

Compound 7

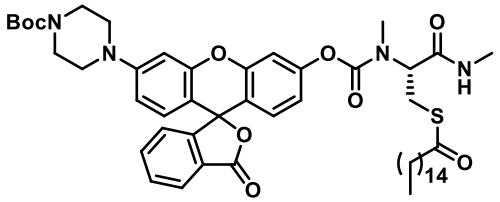

^{1}H-NMR (500 MHz; $CDCl_3$)

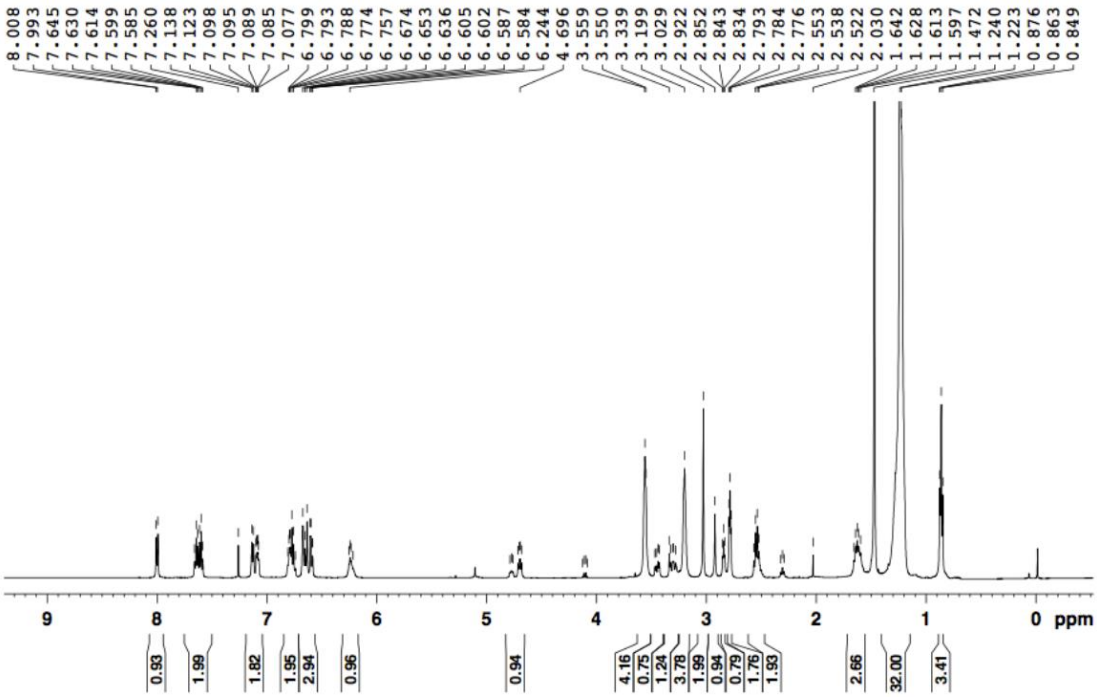

^{13}C-NMR (126 MHz; $CDCl_3$)

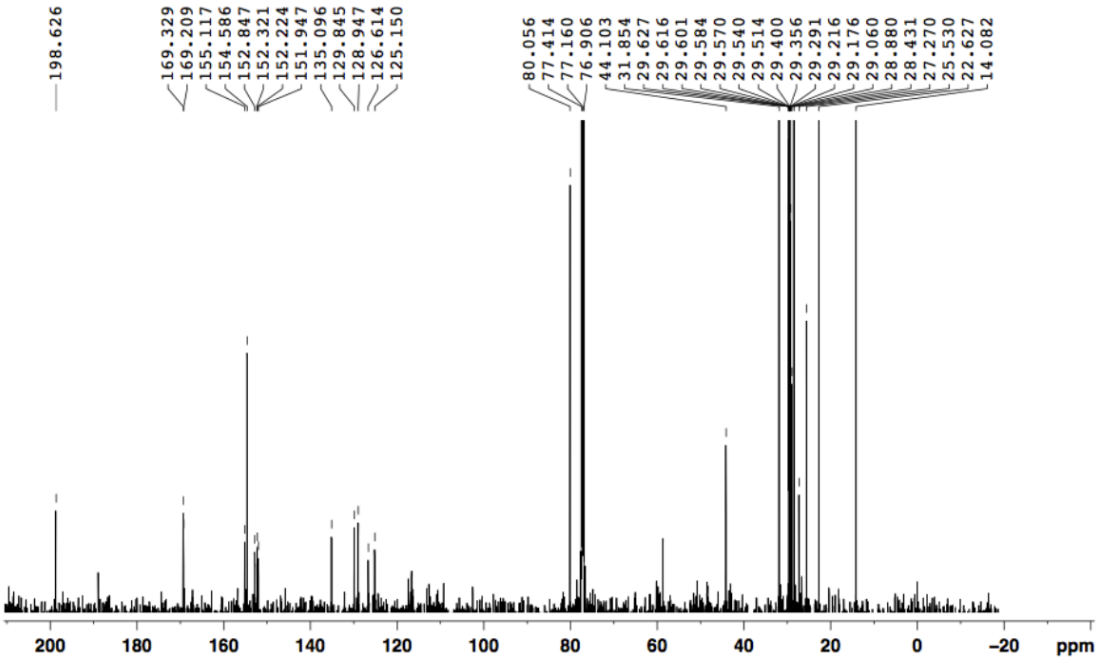

DPP-4

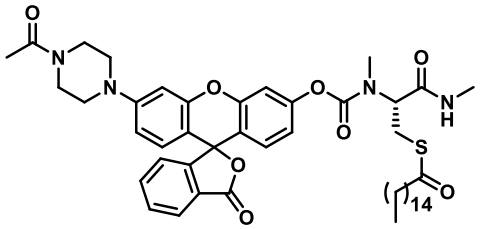

^{1}H-NMR (500 MHz; $CDCl_3$)

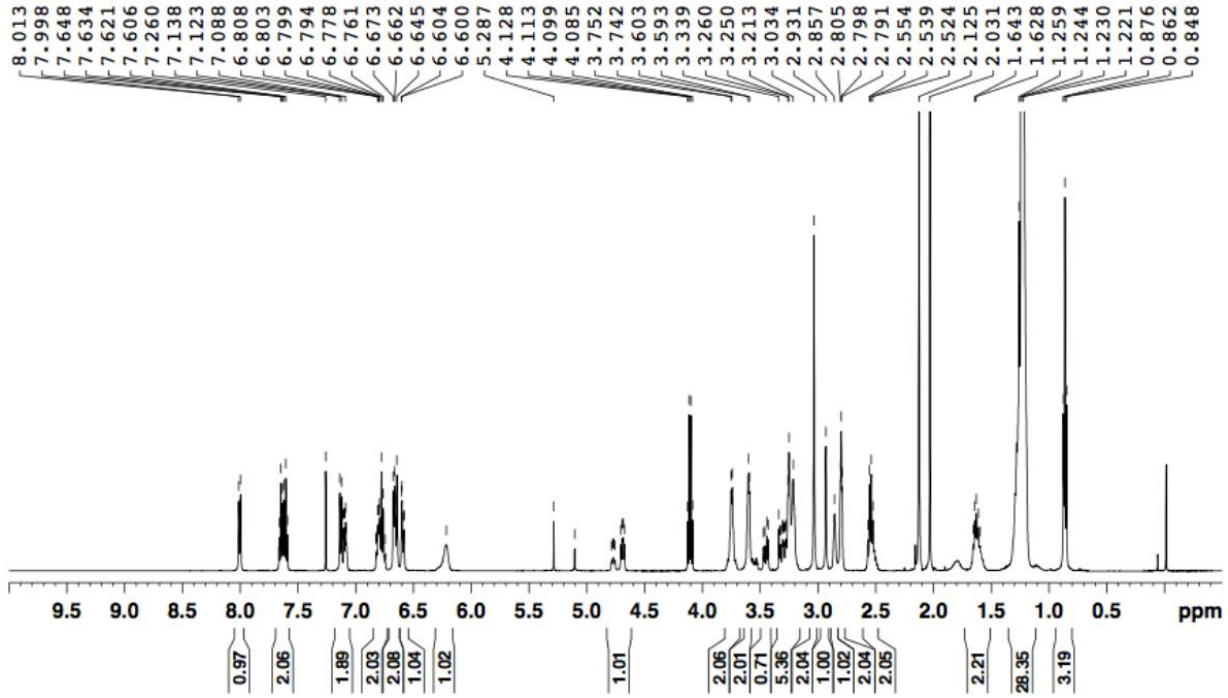

^{13}C-NMR (126 MHz; $CDCl_3$)

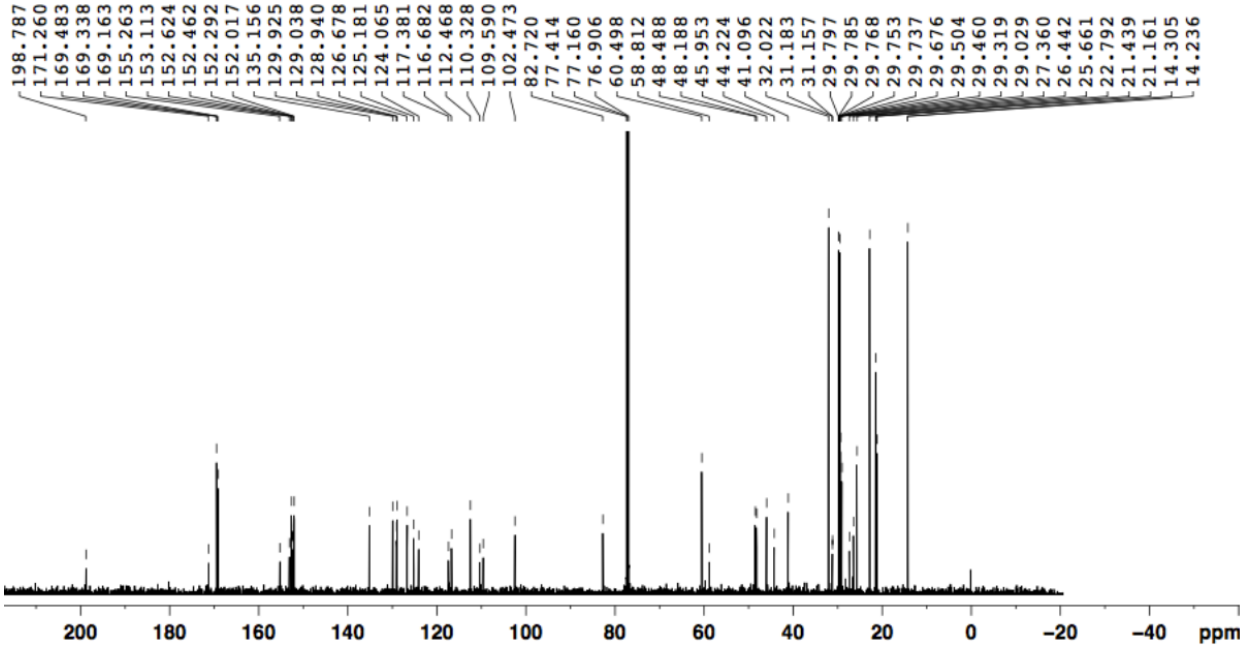

DPP-5

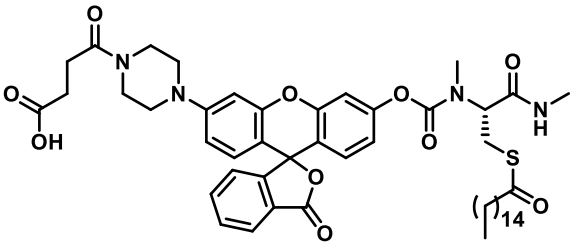

^{1}H-NMR (500 MHz; $CDCl_3$)

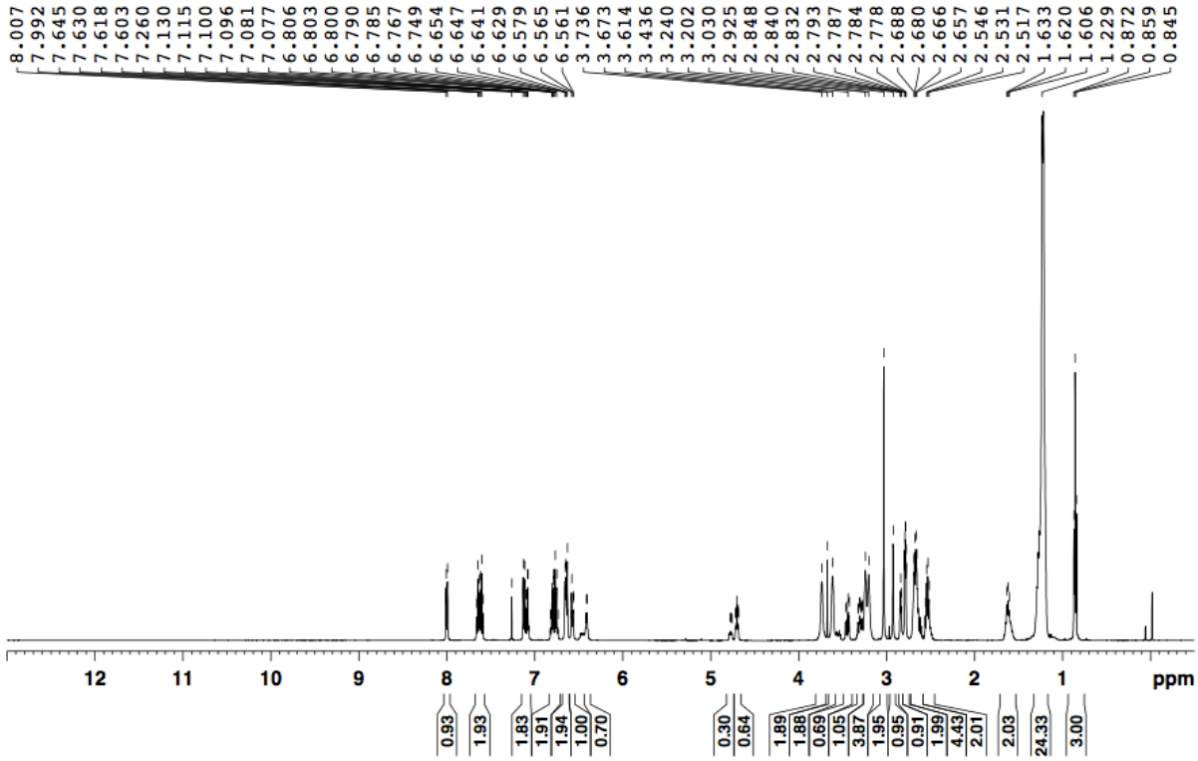

^{13}C-NMR (126 MHz; $CDCl_3$)

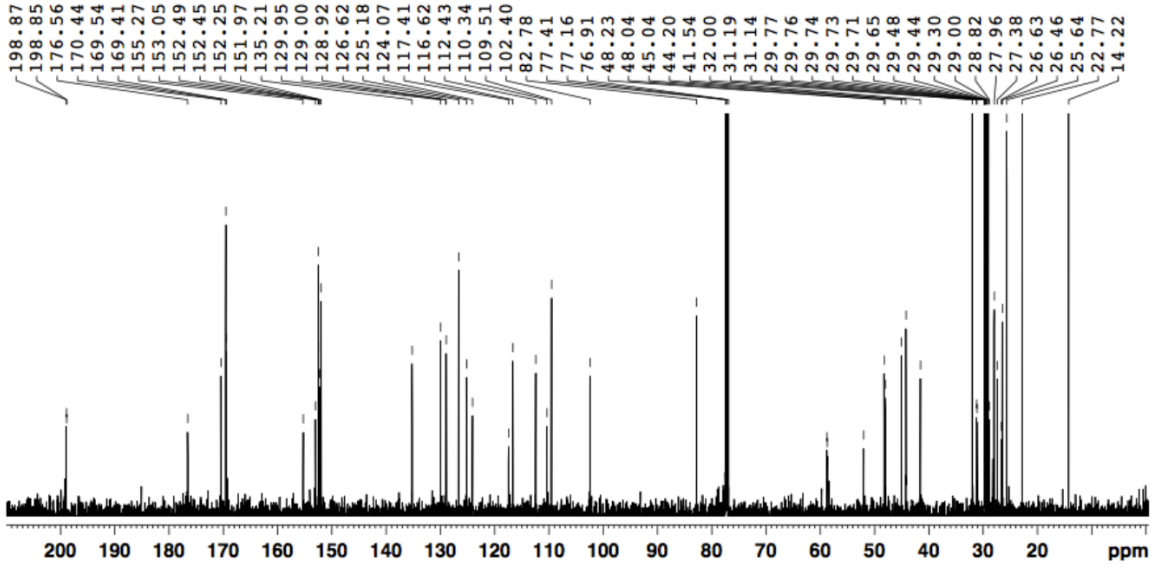

CHAPTER 3

ABHD10 IS AN S-DEPALMITOYLASE AFFECTING REDOX HOMEOSTASIS THROUGH PEROXIREDOXIN-5

3.1 Introduction

As stated in 1.5.5, unbiased mass spectrometry-based protein profiling approaches have revealed that many resident mitochondrial proteins are S-palmitoylated, including those involved in fatty acid transport and metabolism, the electron transport chain, ATP synthesis and antioxidant defense and redox signaling, such as the peroxiredoxins (PRDXs)[1–3]. The presence of S-palmitoylated mitochondrial proteins is particularly interesting because the enzymatic machinery for the installation and removal of protein lipidation in the mitochondria is, to date, mostly undescribed. Aside from reports implicating DHHC8 and 13 in mitochondrial function, data regarding DHHC activity and localization in mitochondria remain limited[4,5]. Until very recently, there were no reports of enzyme-mediated S-depalmitoylation in this organelle. To look for potential mitochondrial APTs, we generated mitochondrial-targeted S-depalmitoylation probes (mitoDPPs), a toolkit of small molecule-based fluorescent probes that are selectively targeted to the mitochondria and measure S-deacylase activity within this compartment[6,7]. Using mitoDPPs, we uncovered S-depalmitoylation activity in mitochondria and found that APT1, which was previously annotated primarily as a cytosolic protein[8], is also localized to this organelle—revealing a potential for enzymatic regulation of mitochondrial protein lipidation[6]. However, although we observed mitochondrial APT (peptide S-deacylation) activity in mitochondria, and despite the multitude of mitochondrial proteins that appear

in the mass spectrometry-based S-palmitoylation catalogs, no function of mitochondrial S-depalmitoylation had been identified.

Here, we sought to determine whether there is a functional consequence of protein S-depalmitoylation in mitochondria. Using a pan-APT inhibitor, we first observed that blocking global S-depalmitoylation diminishes the antioxidant capacity of mitochondria. To confirm that the diminished antioxidant capacity was not mediated by a cytosolic target, we then synthesized and validated a spatially constrained mitochondrial pan-APT inhibitor, mitoFP, which strongly suggested that the phenotype was due to a mitochondrial-localized protein. Surprisingly, we determined that this regulatory function was not modulated by APT1, the only annotated mitochondrial APT, but by ABHD10, a putative mitochondrial-resident protein related to APT1 that belongs to the metabolic serine hydrolase (mSH) superfamily[9]. We characterized ABHD10 through *in vitro* biochemical and cell-based assays, as well as high-resolution structural studies, which revealed that ABHD10 has peptide S-depalmitoylase activity. Finally, we found that the antioxidant activity of PRDX5[10], a key player in the mitochondrial antioxidant machinery, is regulated by ABHD10 via S-depalmitoylation of its active site, providing a connection between lipidation-regulated ABHD10 activity and mitochondrial redox homeostasis. Collectively, these results provide an example of a cellular function mediated by mitochondrial S-depalmitoylation, expand the family of S-depalmitoylases with a new APT family member and reveal a novel mode of redox regulation by PRDX lipidation.

3.2 Results

Although we recently found that APT1 is enriched in mitochondria and multiple mitochondrial proteins appear in unbiased S-palmitoylation datasets, no functional role for S-depalmitoylation has been described in mitochondria. However, perturbing DHHC writer S-palmitoylases has been shown to influence mitochondrial function[4,5], including redox buffering, oxidative phosphorylation and apoptosis[11], which indicates that protein lipidation is important for mitochondrial physiology. We reasoned that the alterations in mitochondrial function resulting from treatment with APT inhibitors would offer clues as to which S-palmitoylated mitochondrial targets are functionally relevant.

Mitochondria are a major source of reactive oxygen species (ROS)[12], and a multitude of mitochondrial ROS regulatory proteins have been identified in S-palmitoylation datasets[1,13]. To test whether S-depalmitoylation plays a role in the regulation of mitochondrial redox status, we first used a pan-APT inhibitor PalmB[14], to inhibit all APTs. To measure mitochondrial antioxidant buffering capacity, we used mitoPY1, a turn-on fluorescent probe, whose signal reflects H_2O_2 levels in mitochondria[15]. If APTs regulate the redox buffering capacity of mitochondria, then inhibiting APTs with PalmB would alter the ability of cells to combat oxidative stress, resulting in an enhanced mitoPY1 signal. We treated HEK293T cells with either 10 μM PalmB or DMSO vehicle in the presence of 2 μM mitoPY1, followed by induction of oxidative stress (100 μM H_2O_2 for 10 min). We observed enhanced mitoPY1 signal following H_2O_2 stimulation in cells treated with PalmB as compared to the DMSO-pretreated controls (**Figure 3.1A,B**), suggesting that inhibition of S-depalmitoylation is connected to deactivation of the cellular machinery that regulates mitochondrial H_2O_2 levels.

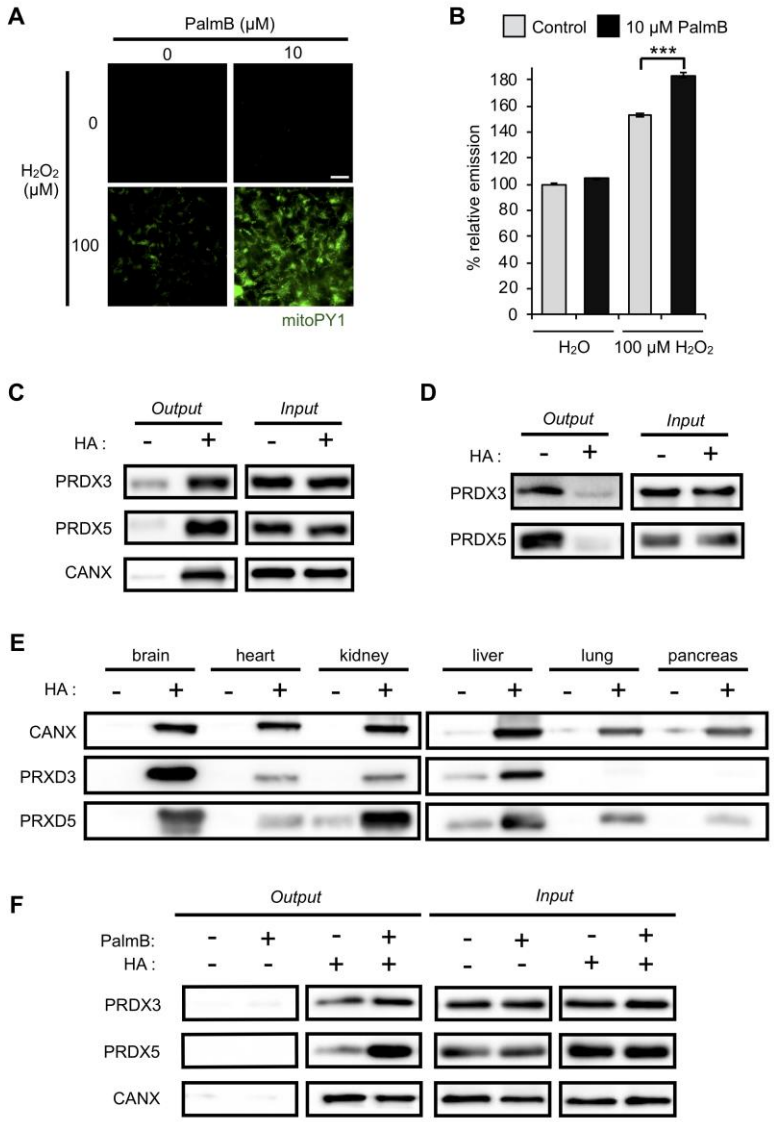

Figure 3.1 Connections between S-depalmitoylation and mitochondrial redox buffering capacity. (A) Representative images showing that PalmB treatment diminishes the mitochondrial redox buffering capacity, as measured by mitoPY1 in HEK293T cells when exposed to H_2O_2. Scale bar, 25 μm. (B) Quantification of the relative fluorescence intensity from mitoPY1 shown in (A). Statistical analyses performed with a two-tailed Student's t-test with unequal variance (n = 6 images). Data expressed as mean ± s.e.m. and normalized to control cells treated with DMSO. (C) ABE assay confirms S-acylation of PRDX3 and PRDX5 in HEK293T cells, with calnexin as a known S-palmitoylated protein control. Input: total protein before enrichment; Output: S-acylated protein enriched via biotin-labeled thiols on hydroxylamine (HA) treatment. (D) Metabolic labeling with 17-ODYA (50 μM) further validates that PRDX3 and PRDX5 are S-palmitoylated in HEK293T cells. The signal difference between −HA and +HA lanes indicates that the palmitoylation modification occurs on cysteine residues. (E) PRDX3 and PRDX5 are prone to S-acylation *in vivo* as determined by an ABE assay performed on mouse tissues. (F) Pan-APT inhibitor PalmB treatment increases the S-palmitoylation level of PRDX3 and PRDX5, as determined by an ABE assay in HEK293T cells.

To further underscore the connection between APT activity and mitochondrial redox regulation, we looked to see if treatment with PalmB influences the lipidation levels of key mitochondrial H_2O_2 first-responder antioxidant proteins, PRDX3 and PRDX5[16]. First, we used an acyl–biotin exchange (ABE) assay[17] to confirm cysteine acylation, and then 17-octadecynoic acid (17-ODYA) metabolic labeling[18,19] to confirm that PRDX3 and PRDX5 are susceptible to S-palmitoylation (**Figure 3.1C,D**). Additionally, we performed ABE on various mouse tissues to validate PRDX3 and PRDX5 lipidation *in vivo* (**Figure 3.1E**). After establishing PRDX3 and PRDX5 S-palmitoylation, we then observed that inhibiting APTs with PalmB resulted in an increase in the lipidation status of PRDX5 (**Figure 3.1F**), providing a potential connection between APT inhibition, mitochondrial PRDX lipidation and redox buffering capacity in the mitochondria. However, although the PalmB-mediated mitochondrial ROS effect phenotype is intriguing, PalmB inhibits S-depalmitoylation activity in all cellular compartments, including the cytosol[20] and mitochondria[6]. As a result, we cannot attribute the diminished mitochondrial antioxidant capacity specifically to either cytosolic or mitochondrial APTs.

To elucidate the direct role of mitochondrial APTs in the observed phenotype, we set out to develop a spatially constrained pan-APT inhibitor. We based our inhibitor on hexadecyl fluorophosphonate (HDFP)[19], which relies on a serine-reactive electrophilic fluorophosphonate moiety coupled with a lipid to target lipid-active mSHs, including all known APTs (**Figure 3.2A**). We reasoned that a derivative of HDFP could be targeted to mitochondria with the addition of a triphenylphosphonium (TPP) group[21], which has been successfully used to deliver a range of cargo to the mitochondria on the basis of the electrochemical gradient. We also shortened the lipid chain to enhance membrane

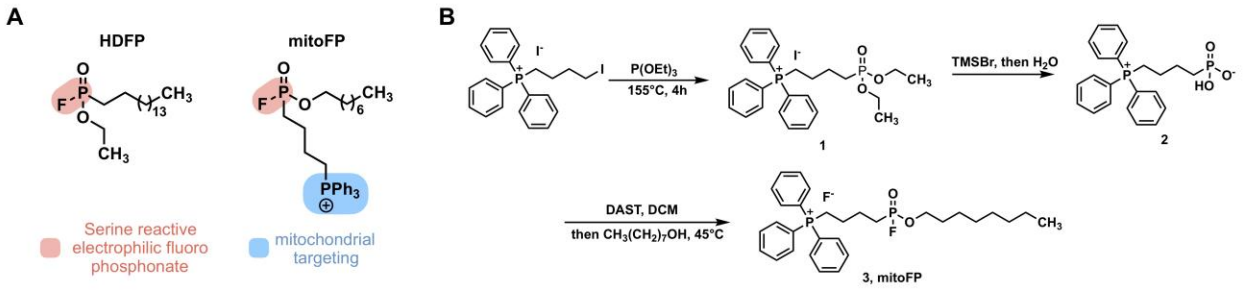

Figure 3.2 Design and synthesis of mitoFP. (A) Design of mitoFP (right), based on the known pan-lipase inhibitor, HDFP (left). The electrophilic fluorophosphonate (red) reacts with active site serine in serine hydrolases, while the triphenylphosphonium group (blue) selectively delivers mitoFP to mitochondria. (B) Schematic for chemical synthesis of mitoFP.

permeability. With this design in hand, we synthesized mitoFP in three steps (**Figure 3.2B**). Briefly, condensation of (4-iodobutyl)triphenylphosphonium with triethyl phosphite yielded intermediate 1. The Lewis acid bromotrimethylsilane facilitated hydrolysis of 1, resulting in the dihydroxy intermediate 2. Difluorination by diethylaminosulfur trifluoride (DAST) and subsequent nucleophilic monosubstitution in the presence of octanol produces mitoFP (3) with a 36% overall yield.

Once synthesized, we confirmed *in vitro* that mitoFP inhibits APT1 using our established fluorescent S-depalmitoylation substrate DPP-5[7,22]; as expected, we observed a dose-dependent inhibition of APT1. Next, we tested whether mitoFP was a mitochondrial-specific APT inhibitor in live cells by measuring APT activity using our previously developed APT probes, DPP-2[20] and mitoDPP-2[6], to assess the effects of mitoFP on cytosolic and mitochondrial APT activity, respectively. We performed a mitoFP dose–response experiment in HEK293T cells and measured DPP-2 and mitoDPP-2 signal via epifluorescence microscopy (**Figure 3.3A**). Even at the highest concentration tested (12 μM), mitoFP had a minimal effect on the DPP-2 signal, indicating that the cytosolic APTs are relatively unperturbed by the inhibitor. In contrast, treatment with

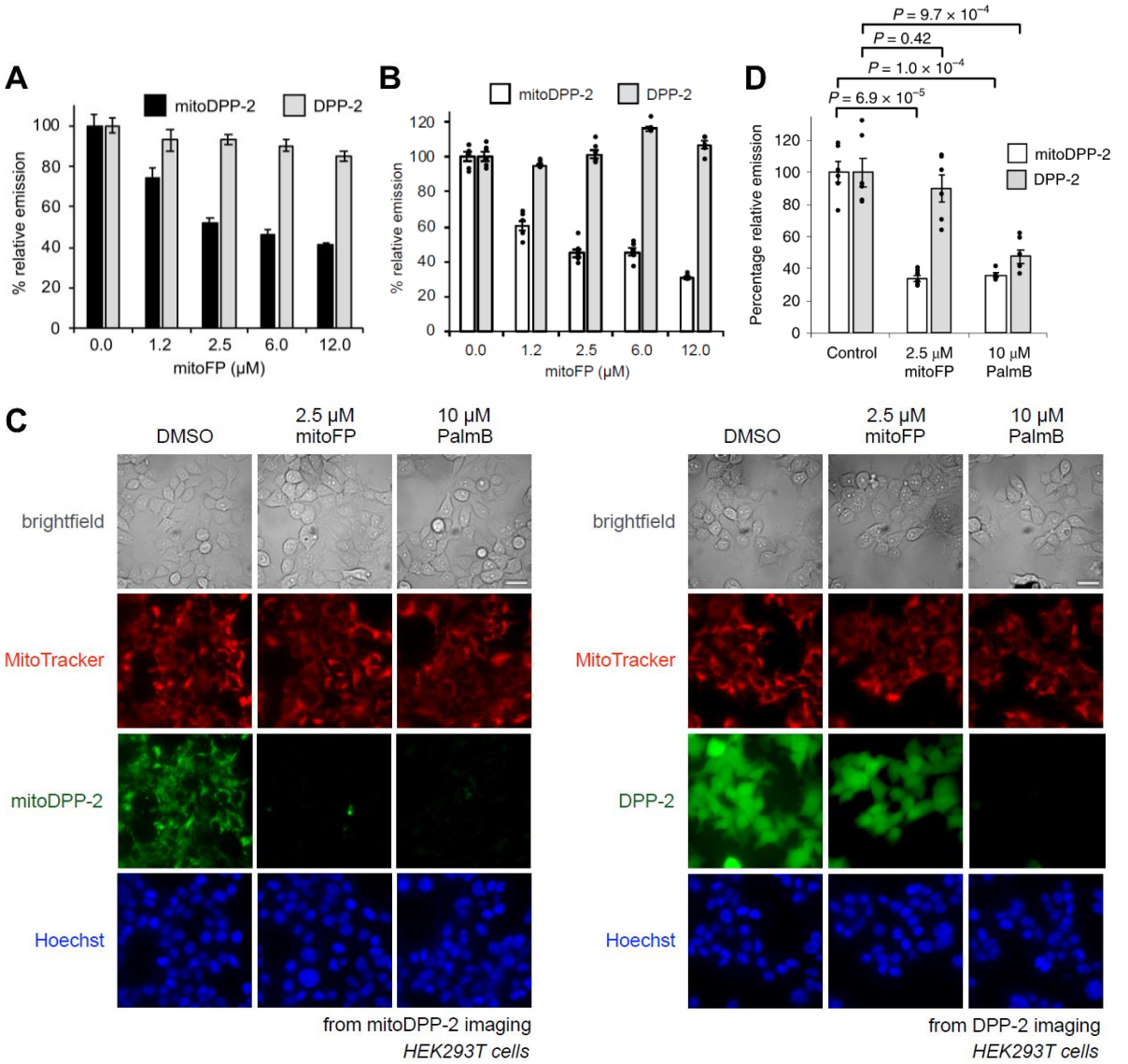

Figure 3.3 MitoFP selectively inhibit mitochondrial APTs. MitoFP dose-dependent response in (A) HEK293T (B) HepG2 cells of mitochondrial and cytosolic APT activity as measured by epifluorescence microscopy using the mitochondrial-localized APT probe, mitoDPP-2, and the cytosolic APT probe, DPP-2. Data expressed as mean ± s.e.m. (n = 6 images) and normalized to control cells treated with DMSO alone. (C) images for comparison of mitoFP potency to deactivate mitochondrial APTs in comarison to PalmB in HEK293T cells. Cells were treated with 1 μM Hoechst 33342, 100 nM MitoTracker Deep Red, and either DMSO as control or 2.5 μM mitoFP or 10 μM PalmB for 30 min. Cells were then washed, loaded with 500 nM mitoDPP-2 (left) or 1μM DPP-2 (right) for 10 min, and then analyzed by epifluorescence microscopy. Images for brightfield, MitoTracker, mitoDPP-2/DPP-2 and Hoechst 33342 nuclear stain are shown for each set of conditions. 25 μm scale bar shown. Two biological replicates with similar results were performed. (D) Quantification of the relative fluorescence intensity from mitoDPP-2 (white) and DPP-2 (gray) in HEK293T cells comparing deactivation of mitochondrial and cytosolic APT activity, respectively, by mitoFP and PalmB.

mitoFP caused a dose-dependent decrease in the mitoDPP-2 signal, validating its efficient, spatially specific inhibition of mitochondrial APTs. Treatment with 2.5 μM mitoFP blocked the mitoDPP-2 signal as efficiently as 10 μM PalmB, indicating robust inhibition of mitochondrial APTs with minimal effect on the cytosolic DPP-2 signal (**Figure 3.3C,D**). We obtained similar results using hepatocellular carcinoma HepG2 cells, confirming the general applicability of mitoFP as a mitochondrial-specific APT inhibitor (**Figure 3.3B**). Together, these experiments establish mitoFP as a tool for perturbing mitochondrial APT activities for functional studies.

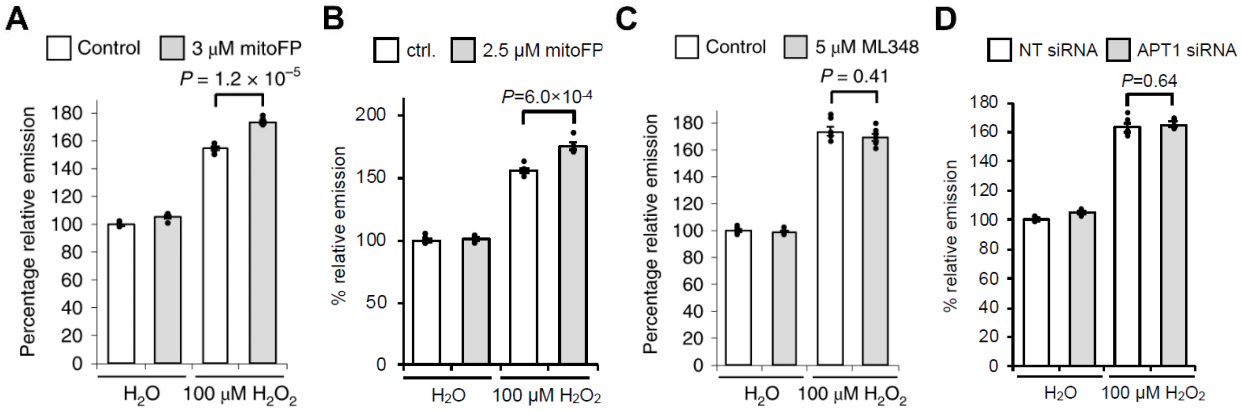

Figure 3.4 Selective inhibition of mitochondrial APTs reduces mitochondrial redox buffering capacity. Quantification of the relative fluorescence intensity from mitoPY1 showing that mitoFP diminishes the mitochondrial redox buffering capacity in (A) HEK293T (B) HepG2 cells exposed to H_2O_2. Quantification of the relative fluorescence intensity from mitoPY1 showing that (C) ML348 (5 μM) or (D) APT1 siRNA knockdown does not alter mitochondrial redox buffering capacity in HEK293T cells exposed to H_2O_2. Statistical analyses performed with a two-tailed Student's t-test with unequal variance (n = 5 images). Data expressed as mean ± s.e.m. and normalized to control cells treated with (C) DMSO or (D) NT siRNA. Dots represent individual data points.

We next investigated whether pretreating cells with mitoFP results in a reduction in mitochondrial antioxidant capacity, as seen with PalmB treatment. We pretreated HEK293T cells with either 3 μM mitoFP or DMSO vehicle in the presence of 2 μM mitoPY1, followed by H_2O_2 stimulation. Cells pretreated with mitoFP showed significantly higher fluorescence signal—and thus higher H_2O_2 levels—than control cells (**Figure**

3.4A). We repeated the experiment in HepG2 cells, which yielded similar results and suggests a role for mitochondrial APTs on mitochondrial redox capacity across cell types (**Figure 3.4B**). The recapitulation of PalmB-triggered diminishment of mitochondrial H_2O_2 buffering capacity with mitoFP points to a direct connection between mitochondrial redox regulation and local APTs, which we presumed was via mitochondrial pools of APT1.

We have demonstrated that the APT1-specific inhibitor ML348[23,24], previously shown to inhibit cytosolic APT1, can efficiently inhibit mitochondrial APT1 as well[6]. Therefore, we tested whether inhibition of APT1 with ML348 decreases mitochondrial antioxidant capacity, which would suggest that mitochondrial pools of APT1 affect the response observed with PalmB and mitoFP. We pretreated HEK293T cells with either 5 μM ML348 or DMSO vehicle in the presence of 2 μM mitoPY1 and stimulated with H2O2 and, intriguingly, found that pharmacological inhibition of APT1 had no effect on the H2O2-induced mitoPY1 signal (**Figure 3.4C**). Genetic perturbation of APT1 via RNAi also showed no significant difference in mitochondrial redox buffering capacity during oxidative stress (**Figure 3.4D**). Taken together, these results suggest that there is a mitochondrial enzyme other than APT1 that is targeted by both PalmB and mitoFP, and which regulates mitochondrial redox buffering capacity.

To identify the potential S-depalmitoylase, we used our S-depalmitoylation probe DPP-2[20] to perform a fluorescence imaging-based screen in cells overexpressing a library of α/β-hydrolase domain-containing protein (ABHD) family members[25] related to APT1 and APT2[9] (**Figure 3.5A**). As expected, we observed an increase in the DPP-2 fluorescence signal in cells overexpressing known S-depalmitoylases, such as APT1, APT2 and PPT1 . Strikingly, overexpression of ABHD10 resulted in an enhancement of

DPP-2 fluorescence similar to that of APT1—suggesting that ABHD10 has peptide S-deacylase activity (**Figure 3.5B**). ABHD10 is a putative mitochondrial protein[26] annotated as a lipase for acyl glucuronide (AcMPAG) deglucuronidation[27,28], but as yet has no identified endogenous substrates. Thus, given that ABHD10 possessed peptide S-deacylase activity in live cells and is purportedly mitochondrial, it became the candidate for further investigation.

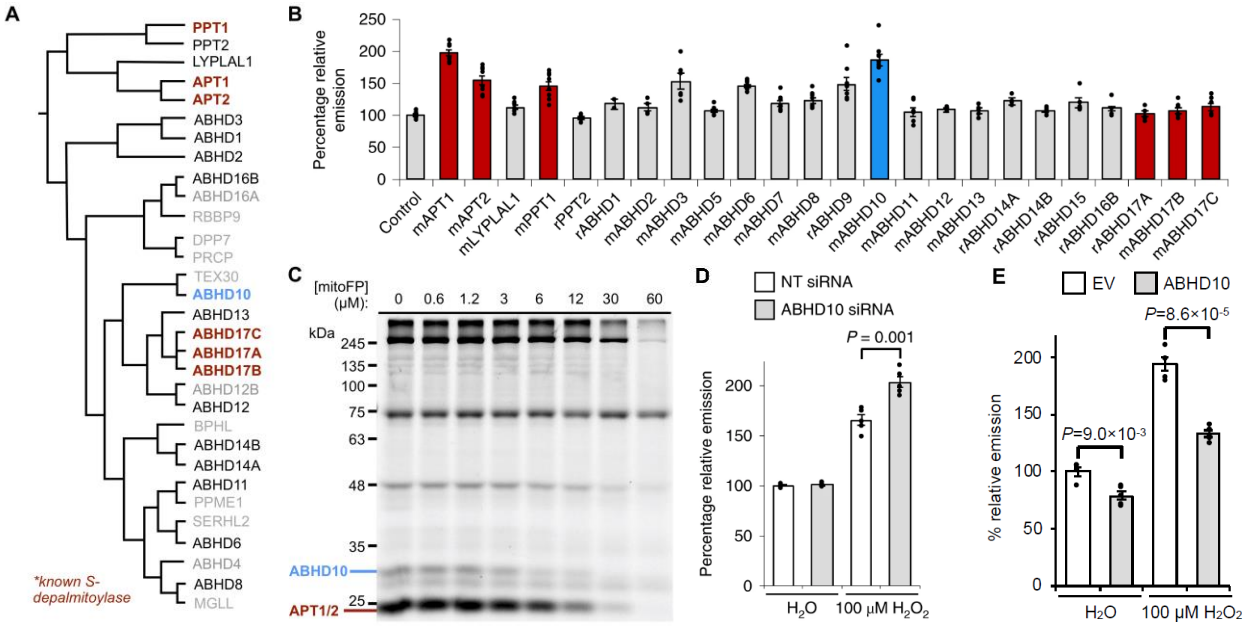

Figure 3.5 ABHD10 regulates mitochondrial redox buffering capacity. (A) Dendrogram depicting known APTs (red) and members of the mSH family screened for potential peptide S-deacylase activity in HEK293T cells. (B) Epifluorescence-based screening with S-deacylase probe DPP-2 in cells overexpressing a library of proteins related to the known APTs. Letters 'm' and 'r' indicate mouse and rat, respectively. Data expressed as mean ± s.e.m. (n ≥ 2 images from two biological replicates) and normalized to control cells treated with empty vector. ABHD10 (blue), a putative mitochondrial protein, enhances DPP-2 signal to a similar extent as APT1 (red). (C) Competitive activity-based protein profiling (ABPP) of serine hydrolases in HEK293T cells treated with the indicated concentrations of mitoFP shows a dose-dependent inhibition of ABHD10 activity. (D) Quantification of the relative fluorescence intensity from mitoPY1 showing that ABHD10 knockdown diminishes the mitochondrial redox buffering capacity in HEK293T cells. (E) Quantification of the relative fluorescence intensity from mitoPY1 showing that ABHD10 overexpression increases mitochondrial redox buffering capacity in HEK293T cells. Statistical analyses performed with a two-tailed Student's t-test with unequal variance (n = 5 images). Data expressed as mean ± s.e.m. and normalized to control cells treated with NT siRNA (D) or empty vector (E). Three biological replicates were performed.

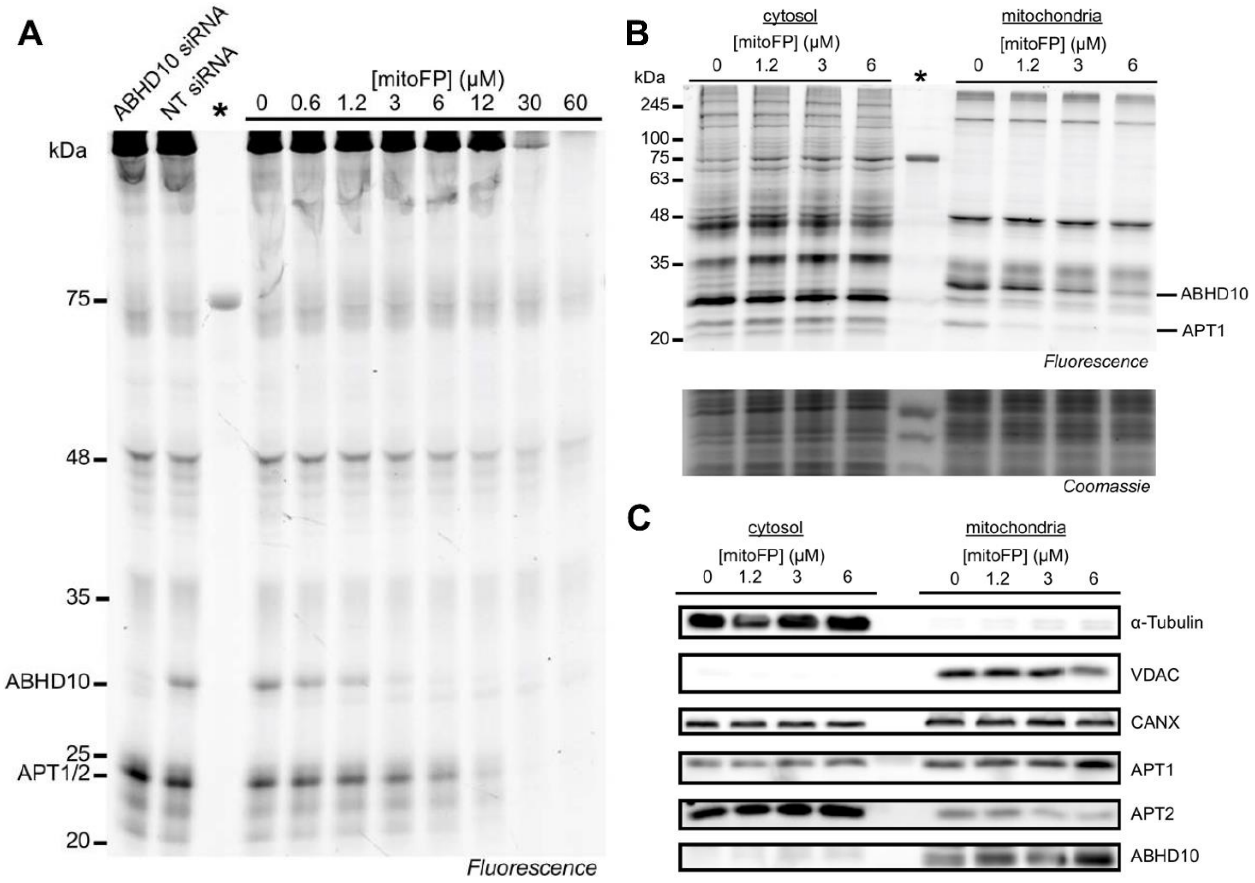

Figure 3.6 Competitive ABPP confirms that ABHD10 is a target of mitoFP. (A) Competitive ABPP in siRNA treated HepG2 cells (first two lanes from left) confirms the bands representing ABHD10. Lanes 4-11 (from left) show that mitoFP inhibits ABHD10 in a dose-dependent manner. The asterisk shows the marker lane. (B) Competitive ABPP (upper panel) to examine cytosolic and mitochondrial serine hydrolase targets of mitoFP in HepG2 cells. Coomassie staining (lower panel) is used as loading control. Asterisk indicates the marker lane. (C) Western blot analysis to examine purity of cytosolic and mitochondrial fractions. High VDAC indicates that fractions are highly enriched for mitochondria. Two biological replicates with similar results were performed.

We assayed whether ABHD10 is inhibited by mitoFP using competitive activity-based protein profiling (ABPP)[23] with the established serine hydrolase ABPP probe, FP-TAMRA, in both HEK293T and HepG2 cells. We observed a dose-dependent decrease of fluorescence signal from a band at ~25 kDa, signifying inhibition of APT1 activity by mitoFP (**Figure 3.5C**). APT1 is not entirely inhibited by mitoFP at low concentrations, as expected, because APT1 is also present in the cytosol. Notably, an additional target at

~28 kDa was inhibited by mitoFP (**Figure 3.5C**), which we identified via RNAi-mediated knockdown as the mitochondrial-targeting peptide-cleaved, mature ABHD10 (**Figure 3.6A**). We also performed ABPP in both enriched mitochondrial and cytosolic fractions prepared from mitoFP-treated HepG2 cells, which further confirmed that ABHD10 is a target of mitoFP and that ABHD10 is highly enriched in mitochondria (**Figure 3.6B,C**).

We investigated whether ABHD10 is the enzyme responsible for the effect on mitochondrial redox homeostasis observed with mitoFP treatment. While the basal mitoPY1 signal was unaffected in cells with RNAi knockdown of ABHD10, oxidative stress resulted in a striking increase in mitochondrial H_2O_2 levels compared to control cells (**Figure 3.5D**). In contrast, overexpression of ABHD10 decreases mitoPY1 signal in both basal and H_2O_2 stimulation conditions (**Figure 3.5E**). Consistent tetramethylrhodamine methyl ester (TMRM) signal between control and various ABHD10 perturbation conditions confirmed that this effect is not due to the disruption of the mitochondrial membrane potential. Additionally, no significant changes in signal from PY1, an indicator of cytosolic H_2O_2 levels[29], on H_2O_2 stimulation confirmed that the diminished mitochondrial antioxidant capacity was not due to alterations in cytoplasmic redox buffering machinery modulated by ABHD10 perturbation. Given that ABHD10 has a role in regulating mitochondrial redox buffering capacity, we next sought to characterize it biochemically and structurally.

To confirm ABHD10 is a mitochondrial S-deacylase in live cells, we expressed ABHD10 in HEK293T cells and measured mitochondrial APT activity using mitoDPP-2, the mitochondria-targeted APT activity probe. Overexpression of wild-type (WT) human ABHD10 results in increased mitoDPP-2 signal, signifying higher S-deacylase activity, as

compared with both overexpression of the catalytically inactive ABHD10 (S152A) mutant (**Figure 3.7A,B**) or the empty vector.

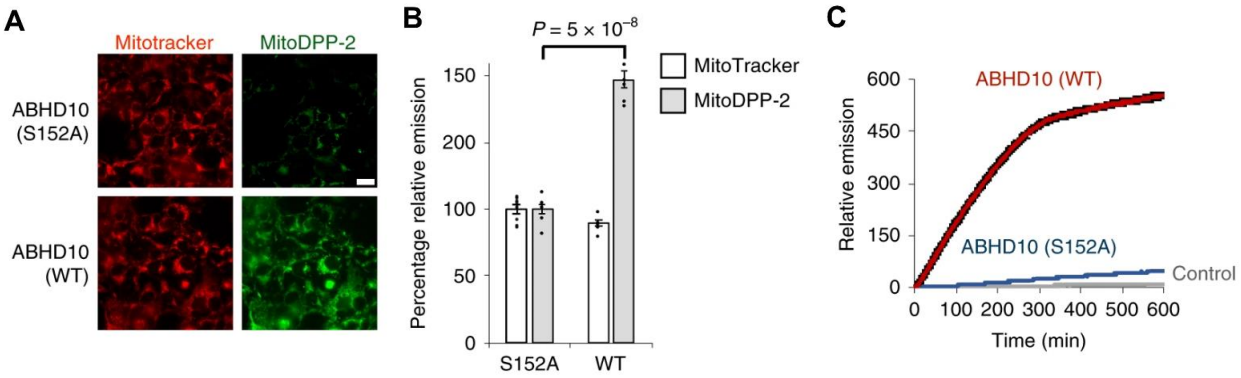

Figure 3.7 Biochemical characterization of ABHD10. (A) Representative images confirming mitochondrial S-deacylation activity of ABHD10 (WT versus S152A) in HEK293T cells as measured using mitoDPP-2, a mitochondrial APT probe. Scale bar, 25 μm. (B) Quantification of relative fluorescence intensities from mitochondrial marker MitoTracker (white) and mitoDPP-2 (gray) in each set of conditions shown in a. Statistical analyses performed with a two-tailed Student's t-test with unequal variance (n = 8 images from two biological replicates). Data expressed as mean ± s.e.m. and normalized to cells expressing ABHD10 (S152A). Dots represent individual data points. (C) *In vitro* kinetic assay showing S-depalmitoylation activity of recombinant mature ABHD10 (500 nM, red) and S152A variant (500 nM, blue) compared to control without added enzyme (gray) as measured using the peptide S-depalmitoylase probe DPP-5 (5 μM). Data expressed as mean ± s.e.m (n = 4 biological replicates) and normalized to relative emission of control (gray) at t = 0.

Given that ABHD10 expression resulted in enhanced APT activity in live cells, as measured by DPP fluorescence, we tested whether it had S-depalmitoylase activity *in vitro*. We purified the mature form of human ABHD10[27] and its active site-mutated variant (S152A) for *in vitro* S-depalmitoylation assays with DPP-5[22]. Unlike DPP-2, which has a surrogate octanoyl lipid rather than a natural palmitoyl lipid, DPP-5 uses a physiologically relevant cysteine S-palmitoyl substrate, and therefore directly reports on peptide S-depalmitoylase activity. Enzymatic assays with DPP-5 revealed that ABHD10 does indeed possess S-depalmitoylase activity (**Figure 3.7C**). Kinetic analysis showed that ABHD10 has a slower turnover rate compared with APT1, but a lower K_M (**Table 3.1**). Consistent

with the ABPP results, the S-depalmitoylation activity of ABHD10 was subject to inhibition by both mitoFP and PalmB. Interestingly, ABHD10 is even more sensitive to mitoFP inhibition *in vitro* (**Table 3.2**). Taken together, these *in vitro* and in live cell assays indicate that ABHD10 possesses mitochondrial S-depalmitoylase activity.

Table 3.1 Kinetic parameters comparison of APT1, APT2 and ABHD10 at 37 °C with substrate DPP-5.

	K_M (μM)	k_{cat} (s^{-1})	k_{cat}/K_M (s^{-1} M^{-1})
APT1	1.6	0.044	2.8×10^4
APT2	2.1	0.066	3.1×10^4
ABHD10	0.21	0.00024	1.1×10^3

Table 3.2 Inhibition Parameters of ABHD10 and APT1 with mitoFP

	K (μM^{-1})	IC50 (μM)
ABHD10	0.89	0.78
APT1	0.38	1.82

In acquiring kinetic parameters for ABHD10, we observed slower kinetic parameters (k_{cat}/K_M) for ABHD10, compared with APT1 *in vitro* (**Table 3.1**). This contrasts with the robust activity observed in live cells (**Figure 3.7A,B**), suggesting additional regulatory controls for ABHD10 activity in live cells may exist. To gain insights into the molecular basis of ABHD10 S-depalmitoylase activity, we managed to acquire the crystal structure of mouse ABHD10.

The crystals produced X-ray diffraction patterns at a resolution of 1.66 Å. As expected, mature ABHD10 possesses a canonical α/β hydrolase domain with a catalytic triad formed by S100–H227–D197 (**Figure 3.8A,B**). Notably, the catalytic serine points directly toward the junction of two pockets, one of which is covered by a ‘cap’ domain and is presumably for lipid chain insertion (binding pocket) on the basis of the hydrophobicity

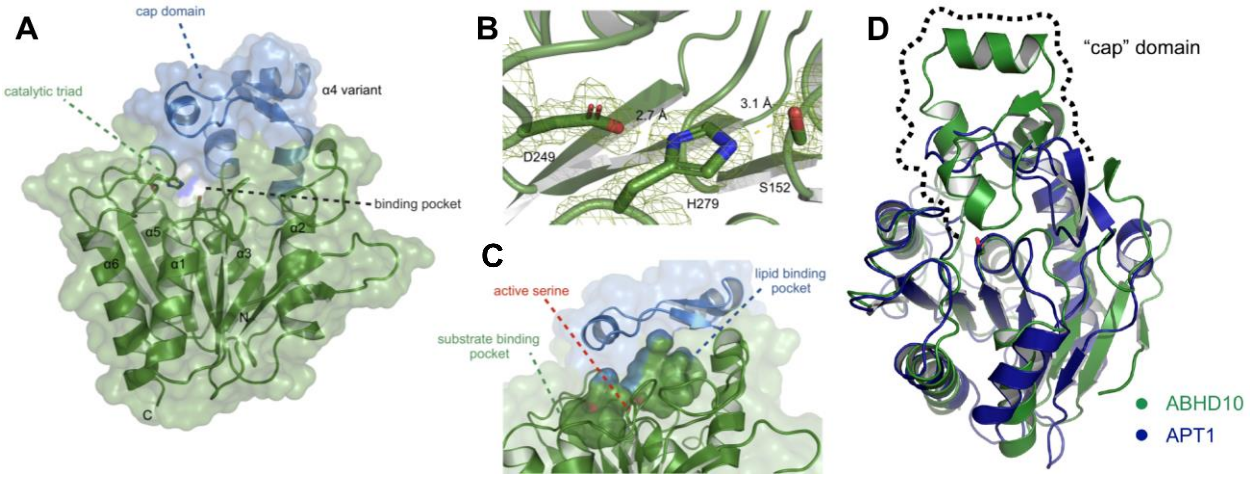

Figure 3.8 Structural characterization of ABHD10. (A) X-ray diffraction structure of mature ABHD10 from Mus musculus (PDB: 6NY9). The 'cap' domain (blue) sits above the catalytic triad (shown as sticks) and forms pockets. (B) Enlarged view of the Asp–His–Ser catalytic triad shown with weighted $2F_o - F_c$ electron density map (carve = 1.5). Length of hydrogen bonds between Asp and His (2.7 Å) and His and Ser (3.1 Å) is shown. (C) The surface of two major cavities within the mouse ABHD10 crystal structure is shown, along with the hydroxyl group of the active serine (shown in sticks), which points towards the junction of the two cavities. (D) Structure alignment of mouse ABHD10 (green) and human APT1 (blue, PDB: 1FJ2). The dotted black line indicates the cap domain of ABHD10, which is replaced with a loop in APT1. Both active site serines of ABHD10 and APT1 are shown in sticks.

of its interior surface, the presence of a methyl pentanediol molecule from the crystallization liquor and comparison with inhibitor-bound APT1[24], while the other pocket is open to the solvent for substrate binding (**Figure 3.8C**). Additionally, alignment of the structures for ABHD10 and APT1 shows that the typical lipase 'cap' domain of ABHD10 is replaced by a loop in APT1 (**Figure 3.8D**)[24,30]. The 'cap' versus loop size difference may affect the accessibility of the catalytic serine and explain the slower turnover rate that we observed. Overall, these structural elements confirm that ABHD10 is suited for S-depalmitoylase activity.

Having characterized the S-depalmitoylase activity of ABHD10 and confirmed that key mitochondrial H_2O_2-reactive antioxidant proteins, such as PRDX3 and PRDX5, are

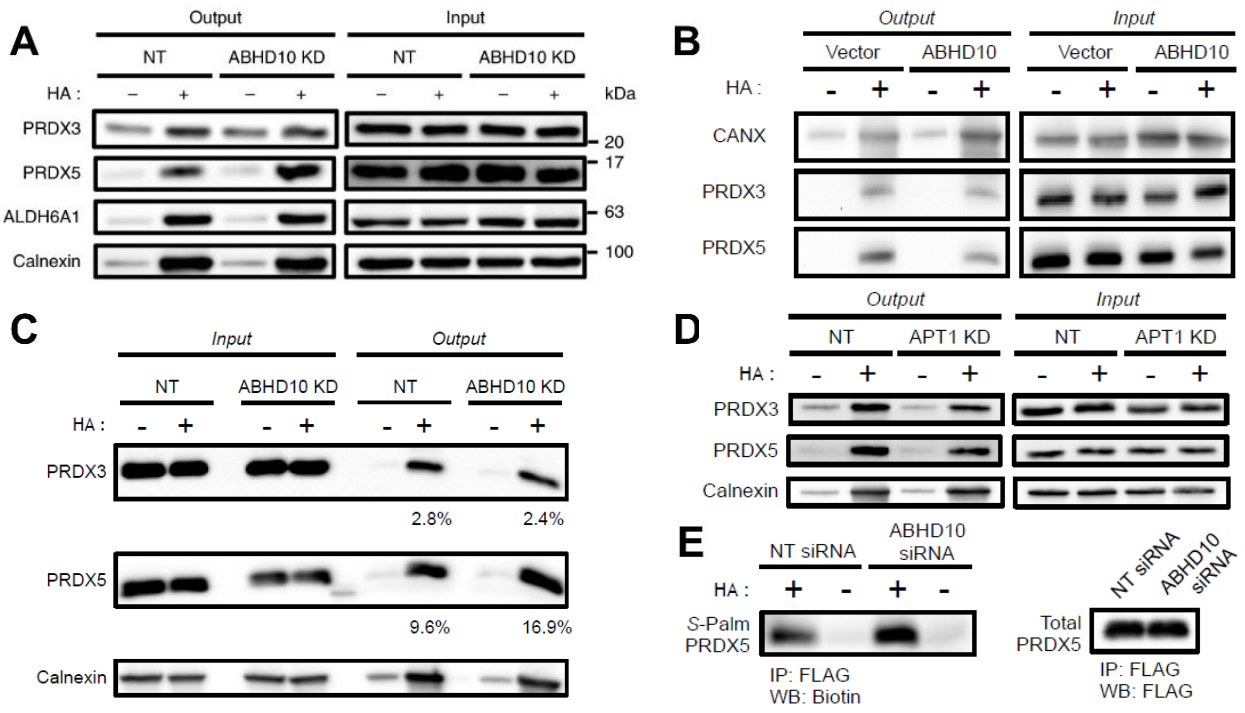

Figure 3.9 ABHD10 modulates PRDX5 S-palmitoylation. (A) ABE assay in HEK293T cells demonstrates that PRDX5 S-palmitoylation level increases on ABHD10 knockdown, whereas no changes are observed for PRDX3 and ALDH6A1. Five biological replicates were performed. (B) ABE assay in HEK293T cells with ABHD10 overexpression compared to empty pcDNA3 vector transfected cells. PRDX5 signal decreased in ABHD10 overexpressing cells. Three biological replicates were performed. (C) ABE assay in HeLa cells demonstrates that PRDX5 S-palmitoylation level increases upon ABHD10 knockdown, whereas no changes are observed for PRDX3. Percentages of S-palmitoylation of PRDX3 and PRDX5 in NT and ABHD10 siRNA treated conditions are shown below respective blot. Experiment was performed once. (D) ABE assay in HEK293T cells demonstrates that APT1 knockdown does not elevate S-palmitoylation level of either PRDX3 or PRDX5. Three biological replicates were performed. (E) ABE assay on immunoprecipitated PRDX5-Flag expressed in HEK293T cells confirms that ABHD10 knockdown enhances S-palmitoylation of overexpressed PRDX5 (left). HEK293T cells were transfected for 16 hr with a PRDX5-flag expression vector and then treated with either NT siRNA or ABHD10 siRNA for 24 hr, and then PRDX5-Flag was pulled down and analyzed by ABE. Two biological replicates with similar results were performed.

palmitoylated (**Figure 3.1C,D**), we tested whether ABHD10 regulates their lipidation levels. In HEK293T cells, we found that ABHD10 knockdown had no significant effect on the lipidation levels of PRDX3 or ALDH6A1, another lipidated mitochondrial protein (**Figure 3.9A**). However, for PRDX5 the ABE assay output signal increased when

ABHD10 was knocked down (**Figure 3.9A**) and decreased when ABHD10 was overexpressed, demonstrating that ABHD10 regulates PRDX5 lipidation levels (**Figure 3.9B**). Similarly, ABHD10 knockdown in HeLa cells also increased the lipidation of PRDX5 (**Figure 3.9C**). APT1 knockdown did not yield any changes in the S-palmitoylation levels of either PRDX3 or PRDX5 (**Figure 3.9D**). Immunoprecipitation ABE further confirmed that the lipidation levels of overexpressed PRDX5-FLAG were increased on ABHD10 knockdown (**Figure 3.9E**). We therefore hypothesized that the ABHD10-mediated changes in PRDX5 lipidation have functional consequences for the antioxidant activity of PRDX5.

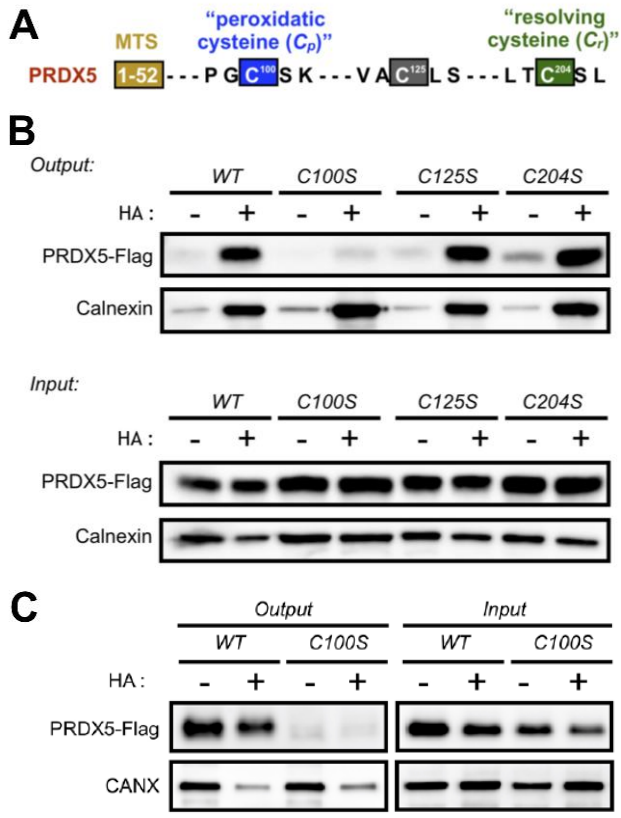

Figure 3.10 PRDX5 S-palmitoylation site is its active site. (A) Protein map showing the three cysteine residues in mature PRDX5. (B) ABE assay in HEK293T cells expressing various PRDX5-Flag constructs (WT and three Cys to Ser mutants) shows that S-palmitoylation occurs at the catalytic site Cys 100. Two biological replicates performed. (C) Metabolic labeling with 17-ODYA in HEK293T cells expressing PRDX5-Flag (WT and C100S mutant) confirms that S-palmitoylation occurs at catalytic site Cys100. Two biological replicates with similar results were performed.

The mature form of PRDX5 contains three cysteine residues at amino acid positions 100, 125 and 204 (**Figure 3.10A**). Of these, Cys 100 and Cys 204 participate in the catalytic cycle of PRDX5 in mitochondria22. To ascertain which cysteine residue(s) on PRDX5 are S-palmitoylated, we expressed wild-type PRDX5-Flag and all three cysteine to serine single point mutants in HEK293T

cells and analyzed their S-acylation levels by ABE (**Figure 3.10B**). While PRDX5WT, PRDX5 C125S and PRDX5 C204S all showed comparable S-palmitoylation levels, we observed a complete abrogation of signal for PRDX5 C100S, indicating that Cys 100 is the primary S-acylation site of PRDX5. We confirmed the S-palmitoylation using metabolic labeling with clickable lipids, again demonstrating complete abrogation of signal enrichment for PRDX5 C100S (**Figure 3.10C**). Intriguingly, Cys 100 is the catalytic residue of PRDX5 and hence is required for nucleophilic attack on H_2O_2, which only occurs when Cys 100 is in the free thiol form. S-Palmitoylation therefore masks the reactivity of this critical residue, and thus, ABHD10 can directly modulate mitochondrial antioxidant ability through depalmitoylation of PRDX5.

Finally, to test for the functional relevance of ABHD10 in mitochondrial redox homeostasis, we examined whether perturbation of ABHD10-dependent redox regulation affected cell viability under various oxidative stress conditions. ABHD10 knockdown resulted in a reduction of cell viability in both HEK293T and HeLa cells under H_2O_2-mediated oxidative stress conditions (**Figure 3.11A,B**). Additionally, treatment of HEK293T cells with paraquat, a potent mitochondrial ROS inducer[31], yields diminished cell viability at concentrations as low as 50 μM in ABHD10 knockdown cells, with minimal effect on control cells (**Figure 3.11C**). We also tested whether the influence of ABHD10 knockdown on cell viability on H_2O_2 stimulation is affected by PRDX5 perturbation by PRDX5 knockdown, which does not affect cell viability under normoxia[32]. We found that PRDX5 knockdown abrogates H_2O_2-induced cell toxicity on ABHD10 knockdown in both HEK293T (**Figure 3.11D**) and HeLa cells (**Figure 3.11E**). Together, these data show that reduced ABHD10 levels with concomitant enhanced PRDX5 lipidation increases cell

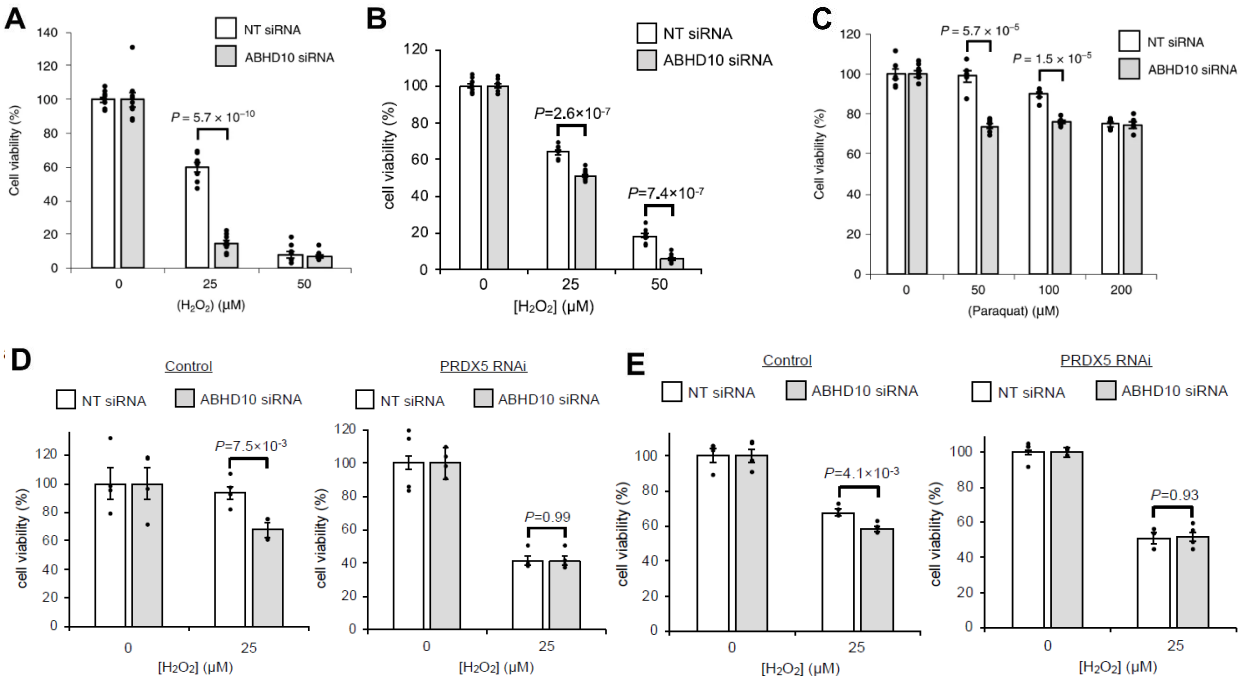

Figure 3.11 ABHD10 knockdown amplifies ROS-induced cell death. (A) HEK293T or (B) Hela cells transfected with either NT siRNA or ABHD10 siRNA were challenged with varying concentrations of H_2O_2 and then analyzed for viability by the MTS assay. Statistical analyses performed with a two-tailed Student's t-test with unequal variance (n = 6 biological replicates in (A) and n = 9 biological replicates in (B)). Data expressed as mean ± s.e.m. and cells with various concentrations of H_2O_2 are normalized to respective cells treated with NT or ABHD10 siRNA and H_2O. Dots represent individual data points. (C) HEK293T transfected with either NT siRNA or ABHD10 siRNA were challenged with varying concentrations of paraquat and then analyzed for viability by the MTS assay. Statistical analyses performed with a two-tailed Student's t-test with unequal variance (n = 6 biological replicates). Data expressed as mean ± s.e.m. and cells with various concentrations of H_2O_2 are normalized to respective cells treated with NT or ABHD10 siRNA and H_2O. Dots represent individual data points. Cell viability assays in (D) HEK293T cells and (E) HeLa cells demonstrate the effect of ABHD10 knockdown induced cell death (left panel) when treated with 25 μM H_2O_2 is abrogated when PRDX5 is knockdown (right panel). Statistical analyses performed with a two-tailed Student's t-test with unequal variance (n = 4 biological replicates). Data expressed as mean ± s.e.m. and cells treated with 25 μM H_2O_2 are normalized to respective cells treated with NT or ABHD10 siRNA and H_2O.

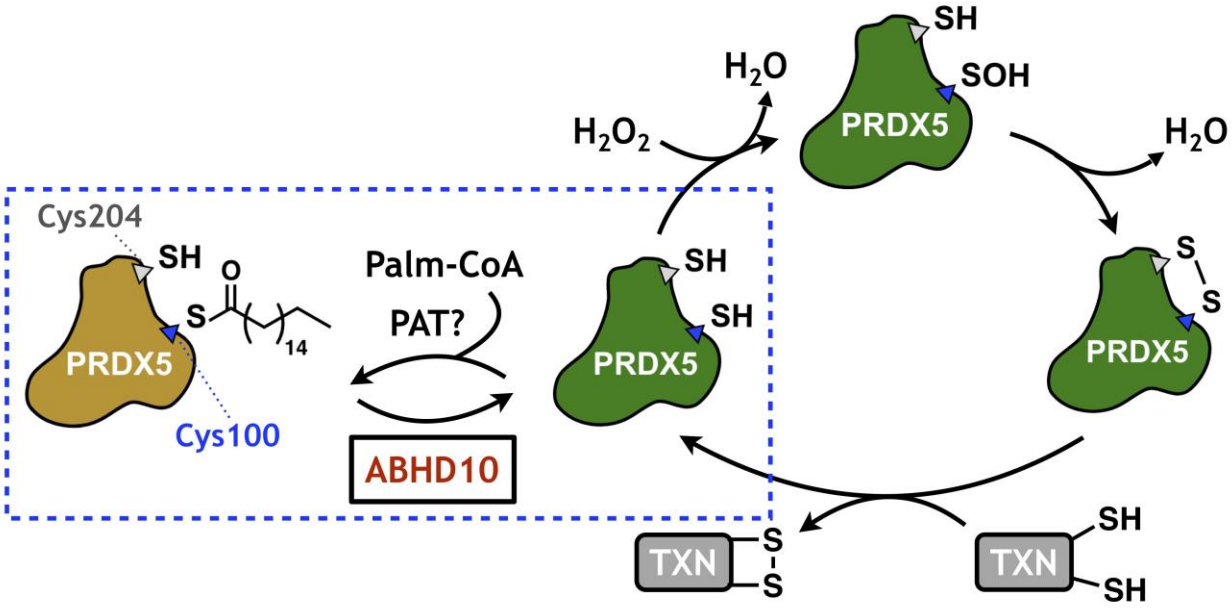

Figure 3.12 PRDX5 regulation by ABHD10-mediated S-depalmitoylation. The active site cysteine of PRDX5 is regulated by S-palmitoylation, which then blocks the H2O2-quenching antioxidant activity of the protein. ABHD10-mediated S-depalmitoylation releases the active form of PRDX5, which then reacts with H2O2 in a disulfide-mediated redox cycling mechanism. TXN, thioredoxin; Palm–CoA, palmitoyl–coenzyme A; PAT, protein acyltransferases.

death under oxidative stress conditions and establishes that ABHD10 regulates mitochondrial redox homeostasis (**Figure 3.12**).

2.3 Conclusion

ABHD10 is different from the other APTs thus far identified. While PPT1 is located in lysosomes, APT2 in the cytosol and the Golgi[25], ABHD17A, B and C in membranes[25] and APT1 in the cytosol, membrane, Golgi and the mitochondria[8,33], ABHD10 appears to be exclusively located in the mitochondria. Additionally, unlike APT1, our structural and biochemical data indicate that ABHD10 has an extensive 'cap' domain and also possesses slower kinetic parameters than APT1 *in vitro*, suggesting additional regulatory

mechanisms. If so, this would not be entirely novel, as we have previously observed growth factor-mediated dynamic regulation of cytosolic APTs[20] and helped to identify the phosphorylation-mediated regulatory site on APT1[34]. While we identified one substrate for ABHD10, potentially it has additional mitochondrial substrates. Recently developed libraries of synthetic palmitoylated peptide substrates could provide powerful methods to study the substrate specificity of ABHD10[35], but assigning natural substrates to APTs is often a challenge due to compensation between APTs and an incomplete understanding of regulatory elements. However, the addition of ABHD10 to the APT family makes assigning more substrates and functions now possible. Indeed, an ABHD10 inhibitor is already available, which will aid in studying its APT function in live cells with temporal control[36].

Mitochondria generate ROS byproducts, which can be both advantageous and deleterious[37]. Therefore, maintaining mitochondrial redox homeostasis is crucial for cellular health. Peroxiredoxins are the major regulators of H_2O_2 levels, due to their high reactivity towards peroxides. Since H_2O_2 is both necessary at low levels and toxic at high levels, the PRDXs are tightly regulated by a variety of processes[16], such as phosphorylation, oxidation and nitrosylation. Our finding that PRDX5 is regulated by S-palmitoylation modification at the active site cysteine not only represents a direct mechanism for regulating the activity of a peroxiredoxin, but is also a rare instance of S-palmitoylation directly modifying an enzyme active site[38]. Future work will involve identifying additional consequences of PRDX5 lipidation, including its impact on PRDX5 stability, trafficking and membrane localization. Additionally, assessing whether other peroxiredoxins are similarly regulated, both in the mitochondria and in other cellular

compartments, will help further to elucidate the role of PRDX lipidation. The redox buffering capacities of compartments within the cell are interconnected, so there is potentially feedback with other PRDXs. The data presented here suggest that other targets of PRDX5 also contribute to cell survival in oxidative stress conditions. Moreover, we showed that PRDX3, another mitochondrial peroxiredoxin, is also lipidated, but is not regulated by ABHD10. This suggests that additional regulatory APTs exist along these pathways, warranting extensive further interrogation.

Determining localization-based enzymatic activities via genetic approaches, that is, knocking down or out a target gene product, is challenging, especially when protein targets reside in several cellular compartments. In this work, we supplemented genetic approaches with the development of a spatially constrained APT inhibitor, mitoFP. While synthesizing TPP-tagged inhibitors is not challenging, confirming the proper localization of a novel inhibitor is often not possible. Here, due to our previous development of spatially constrained activity probes for APTs[6], coupled with organelle-specific ABPP[9,19,39–41], we were able to validate the targeting and potency of mitoFP in live cells. Using mitoFP, we conclude that ABHD10 activity in the mitochondria mediates the antioxidant stress phenotype observed with pan-active, nontargeted APT inhibitors. Further use of mitoFP will help us and others to continue to illuminate mitochondrial S-depalmitoylation function and regulation.

This work focuses entirely on the erasers of S-palmitoylation, the APTs. However, equally important to the regulation of PRDX5 is the lipid installation. Although perturbation of both DHHC8 and 13 disrupts mitochondrial metabolic functions[4,5], no known writers have definitively been localized to the mitochondria. It is possible that PRDX5 is lipidated

before mitochondrial import and then released in an active form once in the mitochondria. In this scenario, the lipid modification could be regulating PRDX5 trafficking to the mitochondria, as was previously observed for BAX[11]. However, there may also be DHHCs, or as yet undiscovered acyltransferases, present in or at the mitochondria that mediate PRDX5 lipidation. Future work exploring acyltransferase activity on these mitochondrial targets, likely involving the development of better chemical probes and inhibitors, will help to complete the regulatory picture of mitochondrial proteome S-palmitoylation.

2.4 Experimental Details

General materials and methods. DMEM GlutaMAX (Gibco), FBS (Gibco/Life Technologies, Qualified US origin or Gemini Benchmark 100–106), Live Cell Imaging Solution (Molecular Probes), Opti-MEM (Gibco), Lipofectamine 3000 reagent (Invitrogen), Lipofectamine RNAiMAX transfection reagent (Invitrogen), polyethylenimine (PEI) (Sigma; average Mw ≈ 25,000 by LS, average Mn ≈ 10,000 by GPC, branched), Dynabead Protein G magnetic beads (Invitrogen), MitoTracker Deep Red FM (Invitrogen), Hoechst 33342 (Fisher), 2-bromopalmitate (Sigma), MitoPY1 (Sigma), PY1 (Sigma), PalmB (EMD Millipore), Charcoal-filtered FBS (ThermoFisher, catalog no. A3382101), MTS (BioVision), phenazine methosulfate (Sigma) were purchased from the sources given in parentheses. Short interfering RNAs (siRNAs) targeting human ABHD10 (SI04229519), human APT1/LYPLA1 (SI03246586) and human PRDX5 (SI00096971, SI02638888, SI02638902), as well as nontargeting (NT) control siRNA (SI03650325), were purchased from Qiagen. Silica gel P60 (40–63 μm, 230–400 mesh; SiliCycle) was

used for column chromatography. Analytical thin-layer chromatography was performed using precoated 60 F254 silica gel sheets (0.25 mm thick; SiliCycle). DPP-2[20], DPP-5[22] and mitoDPP-2[7] were synthesized as previously reported. All chemicals for synthesis were purchased from Sigma-Aldrich or ThermoFisher Scientific and used as received. ML348 was purchased from Tocris. NMR spectra (^{1}H and ^{13}C) were collected in the NMR solvent CDCl3 (Sigma-Aldrich) at 25 °C using a 500 MHz Bruker Avance II+ spectrometer with 5 mm QNP probe at the Department of Chemistry NMR Facility, University of Chicago. ^{1}H-NMR chemical shifts are reported in parts per million (ppm) relative to the peak of residual proton signals ($CDCl_3$: 7.26 ppm). Multiplicities are given as: t (triplet), q (quartet), br (broad), m (multiplet). ^{13}C-NMR chemical shifts are reported in ppm relative to the peak of residual proton signals ($CDCl_3$: 77.16 ppm). NMR analysis was done in TopSpin 3.5pl7. High-resolution mass data were obtained from an Agilent 6224 TOF High-Resolution Accurate Mass Spectrometer (HRA–MS) using a combination of atmospheric pressure chemical ionization and electrospray ionization at the Department of Chemistry Mass Spectrometry Facility, University of Chicago. Low-resolution mass spectrometry and liquid chromatography analyses were carried out on an Advion Expression-L mass spectrometer coupled with an Agilent 1220 Infinity LC System.

Imaging. For fluorescence microscopy, an inverted epifluorescence microscope (Lieca DMi8) equipped with a Hamamatsu Orca-Flash 4.0 camera, a 63× oil objective (numerical aperture 1.4) and a 300 W Xenon light source (Sutter Lamda XL) was used. Leica LASX software was used to obtain images for mitoPY1/DPPs (YFP filter cube 1525306),

Hoechst 33342 (ET 402/15×, Quad-S, ET 455/50 m), MitoTracker (ET 645/30×, Quad-S, ET 705/72 m) and bright field.

Western blots. After SDS–PAGE, proteins were transferred onto methanol-preactivated Immobilon-P PVDF membranes (pore size 0.45 μm; Millipore) using a semi-dry transfer cell (Bio-Rad). After transfer, the membranes were blocked for 1 h with TBST wash buffer (20 mM Tris, pH 7.5, 150 mM NaCl, 0.1% Tween-20) containing 3% BSA (Fisher or Thermo Scientific). Considering the long procedure for the assay, we cut each membrane into several small membranes containing the target protein band on the basis of molecule weight. Each membrane was then incubated with primary antibody in 3% BSA–TBST. The membrane was washed with TBST five times for 5 min (5 × 5 min) followed by 1 h incubation with either anti-rabbit IgG horseradish peroxidase (HRP) or anti-mouse IgGκ BP-HRP in 3% BSA–TBST, washed 5 × 5 min with TBST and then visualized using SuperSignal West Pico PLUS chemiluminescent substrate (ThermoFisher Scientific) and recorded on a chemiluminescent western blot imaging system (Azure Biosystems C300). Additional western blots in this study were performed identically. For antibody dilutions and vendor information, see **Table 3.3**.

Table 3.3 List of the antibodies used in this study. SCB: Santa Cruz Biotechnology; CST: Cell Signaling Technology

Protein	Species	Dilution	Company	Cat. No.
Calnexin	Rabbit	1:4000	Abcam	ab22595
ABHD10	Rabbit	1:1000	Abcam	ab214085
ABHD10	Rabbit	1:1000	Sigma	HPA036991
APT1	Rabbit	1:1000	Abcam	ab91603
APT2	Rabbit	1:1000	Abcam	ab151578
PRDX5	Rabbit	1:1000	Proteintech	17724-1-AP
PRDX3	Rabbit	1:1000	Abcam	ab73349
FLAG	Mouse	1:1000	Invitrogen	MA1-91878
ALDH6A1	Mouse	1:1000	SCB	SC-365160
ACOT1/2	Mouse	1:1000	SCB	sc373919
Streptavidin-HRP conjugates	Goat	1:2000	CST	3999S
α-Tubulin-HRP	Goat	1:2000	Proteintech	hrp-66031
Anti Rabbit IgG- HRP	Goat	1:4000	CST	7074S
Anti Mouse IgGκ BP-HRP- HRP	Goat	1:4000	SCB	sc-516102

Cell culture. Unless otherwise stated, HEK293T (ATCC), HeLa (from C. He, University of Chicago) and HepG2 cells (from Cellular Screening Center, University of Chicago) were plated and maintained in DMEM GlutaMAX (supplemented with 10% BS and 1% penicillin/streptomycin) at 37 °C and 5% CO2. For all experiments, cells had undergone fewer than 25 passages and hence mycoplasma contamination was not tested. HEK293T, HeLa and HepG2 cells are not listed in the database of commonly misidentified cell lines maintained by ICLAC (http://iclac.org/databases/crosscontaminations/). Cells were plated the day before all experiments. For all treatments, cells were first washed with fresh growth medium, which was then replaced with fresh growth medium containing the drug

and/or probe. Where indicated, treatments also included Hoechst 33342 (1 μM) and MitoTracker Deep Red (100 nM) for nuclear and mitochondrial visualization, respectively. Transfections were conducted with either PEI (for plasmids), Lipofectamine 3000 (for plasmids) or Lipofectamine RNAiMAX (for siRNAs) according to the manufacturer's recommended protocols, which were scaled according to the volume of the culture dish.

Plasmid cloning. All plasmids were constructed by Gibson Assembly from PCR products generated using Q5 Hot Start DNA Polymerase (New England Biolabs) or Phusion Polymerase (generated in-house). The pcDNA3 vector was a gift from C. He and pET-30a was used as described previously[20]. Genes for human PRDX5, human ABHD10, mouse ABHD10 and primers were synthesized by Integrated DNA Technologies. The complementary DNAs for PRDX5 and ABHD10 were cloned into the pcDNA3 vector for mammalian expression. In addition, both human and mouse ABHD10 were truncated to remove the mitochondria localization signal peptide (residues 1–52 for human ABHD10 (Q9NUJ1-1) and 1–43 for mouse (Q6PE15-1)), optimized using the IDT Codon Optimizing Tool and cloned into the pET-30a vector containing a His-tag for Escherichia coli expression. All newly constructed plasmids were sequence-verified at the University of Chicago Comprehensive Cancer Center DNA Sequencing and Genotyping Facility and are available on request.

Assessment of mitochondrial H_2O_2 following depalmitoylation inhibition. HEK293T cells (300,000 cells per well) or HepG2 cells (125,000 cells per well) were plated in four-well chamber slides (D35C4-20-1.5-N, Cellvis) precoated with 5 μg poly-D-lysine (30–

70 kDa, Alfa Aesar). After 20–24 h, cells were pretreated with 10 μM PalmB, 5 μM ML348 or 2.5 μM mitoFP for 30 min at 37 °C. Control cells were pretreated with vehicle (DMSO). Hoechst 33342 and MitoTracker Deep Red were included for nuclear and mitochondrial visualization, respectively, as was 2 μM of the mitoPY1 (Sigma). After pretreatment, cells were briefly washed with DPBS, and treated with 100 μM H_2O_2 in fresh DPBS (400 μl) for 10 min at 37 °C. Control cells were untreated. Cells were then imaged on an inverted epifluorescence microscope. Analyses were performed in ImageJ (by W. Rasband, NIH). For data analysis, the average fluorescence intensity per image in each experimental condition was obtained by gating cells using the bright-field image and applying that mask in the corresponding mitoPY1 image. All data were normalized to the average fluorescence intensity of the DMSO-pretreated control that was not exposed to H_2O_2. Each experiment was repeated in at least two biological replicates with identical results.

ABE of cell culture samples. Volumes here are representative of an experiment using cells from a 10 cm plate. HEK293T cells were washed with DPBS, lysed with 1 ml RIPA lysis buffer containing protease inhibitors (1 mM PMSF and 50 mM N-ethylmaleimide (NEM, Acros)) and subject to end-over-end rotation overnight at 4 °C. The cell debris was pelleted by centrifugation at 13,000g for 15–30 min at 4 °C and the supernatant collected. Protein concentration was measured using the BCA assay and equal amounts of total protein from each sample were subjected to acetone precipitation for 2 h at −20 °C. The resulting pellet was dissolved by sonication in 100 μl per mg of protein of 4% SDS buffer (resuspension buffer: 150 mM NaCl, 50 mM HEPES, 5 mM EDTA, pH 7.4) containing 50 mM NEM. Triton buffer (0.2%: 150 mM NaCl, 50 mM HEPES, 5 mM EDTA, pH 7.4;

250 µl per mg of protein) containing 50 mM NEM was added and protein solution was rotated end-over-end for 3 h at 25 °C. Two subsequent acetone precipitations were performed to remove excess NEM. The resulting protein pellet was dissolved in 105 µl of resuspension buffer by sonication. The protein sample was divided into two equal parts for ±HA (Acros) treatment in fresh 50-µl tubes. Each sample was treated with 150 µl of either –HA buffer (0.2% Triton buffer) or +HA buffer (0.2% Triton buffer containing 1.33 mM HA, pH ~7.3). Samples were first incubated at room temperature with shaking for 1 h, and then proteins were precipitated by chloroform–methanol precipitation to remove excess HA. Protein pellets were dried for 20–30 min at room temperature and resuspended by sonication in 60 µl of resuspension buffer containing 10 µM EZ-Link HPDP-Biotin (ThermoFisher, catalog no. 21341). Protein solutions were diluted with 240 µl of biotin buffer (0.2% Triton buffer, 10 µM EZ-Link HPDP-Biotin) and incubated for 2 h at room temperature with shaking. Excess biotin was removed via acetone precipitation. Protein pellets were dissolved in 30 µl per mg of protein of resuspension buffer by sonicating, and the total volume was brought to 1200 µl with 0.2% Triton buffer. Undissolved residues were removed via centrifugation at 14,000 r.p.m. for 5 min at 4 °C. Protein concentrations were measured using the BCA assay. Protein (35 µg) was transferred to a fresh tube to serve as the loading control for normalizing levels of protein of interest (‘input’). Protein (350–400 µg) was transferred to a new tube and diluted to 0.6–0.8 mg ml−1 with wash buffer (0.1% SDS, 0.2% Triton X-100, 150 mM NaCl, 50 mM HEPES, 5 mM EDTA, pH 7.4). Streptavidin–agarose beads (80 µl per mg of protein; ThermoFisher, catalog no. 20361) were added to the protein solution, which was then incubated at 4 °C overnight with end-over-end rotation. Unbound proteins were removed

by washing six times with 1 ml washing buffer and spinning for 1 min at 6,000 r.p.m. each time. Bound proteins were eluted by boiling the beads for 10 min at 95 °C with 1× Laemelli sample buffer (containing 20–30 mM DTT). The protein was resolved on 10% or 12% SDS–PAGE gels and subjected to western blotting using the protocol described above.

Mouse tissues ABE assay. The use of vertebrate animals (Mus musculus, mouse) in the laboratory of B. Dickinson has been approved by the Institutional Animal Care and Use Committee under the Animal Care and Use Protocol no. 72531, 'Mouse models of lipid signaling regulation'. For ABE performed on mouse tissue samples, organs were isolated from 7-week-old female C57BL/6J mice, quickly washed with Hanks' balanced salt solution, and immediately flash-frozen. Following mechanical homogenization, samples were lysed in 2–5 ml (depending on organ mass) of HEPES lysis buffer (150 mM NaCl, 40 mM HEPES, 0.5% Triton, 3 mM EDTA, pH 7.4 with protease inhibitors and 1 mM PMSF) containing 50 mM NEM, vortexed vigorously and rotated end-over-end for 8 h. After centrifugation at 15,000 g, the supernatant was removed and subjected to sequential acetone and chloroform–methanol precipitations to yield dry protein. The resulting protein pellet was then processed as described above.

PalmB ABE assay. A solution of PalmB (10 μM) or DMSO in DMEM GlutaMAX (10% charcoal-filtered FBS and 1% fatty acid-free BSA) was added to HEK293T cells grown to 90% confluency. Cells were incubated for 1.5 h, washed twice with ice-cold PBS and processed as described in the ABE protocol.

17-ODYA Metabolic labeling. Volumes here are representative of an experiment using cells from a 10 cm plate. HEK293T cells were washed with DPBS and then treated with 50 μM 17-ODYA absorbed on 5% BSA in DMEM GlutaMAX supplemented with 10% charcoal-filtered FBS. Cells were then incubated for 6 h, unless noted differently, at 37 °C with a supply of 5% CO_2. Cells were washed once in DPBS, lysed with 1 ml HEPES lysis buffer (150 mM NaCl, 50 mM HEPES, 0.2% SDS, 1% Triton-100, pH 7.4, with EDTA-free protease inhibitor and 1 mM PMSF) and subject to end-over-end rotation overnight at 4 °C. The cell debris was pelleted by centrifugation at 13,000g for 15–30 min at 4 °C and the supernatant collected. Protein concentration was measured using the BCA assay and 1 mg of protein was placed into a new tube. First, the same volume of HEPES buffer (150 mM NaCl, 50 mM HEPES, pH 7.4) was added to adjust the SDS concentration to 0.1%, and then all samples were diluted with the click reaction buffer (150 mM NaCl, 50 mM HEPES, 0.1% SDS, 0.5% Triton-100, pH 7.4) for a final protein concentration of 1 mg ml−1. Master mix (8 μl) made from 22 μl each of 5 mM Azide-PEG3-biotin (Sigma), 5 mM TBTA (Combi-Blocks), 50 mM $CuSO_4$ and 5 mM TCEP was added for a 1 ml 'click' reaction. The resulting solution was incubated for 1 h at room temperature with shaking. EDTA (121 μl of 100 mM solution) was added to quench the click reaction and proteins were precipitated by chloroform–methanol precipitation. The protein pellet was dissolved in 50 μl of resuspension buffer by sonicating and 150 μl of 0.2% Triton buffer was added. Protein was further precipitated by chloroform–methanol precipitation. The resulting protein pellet was dissolved in 105 μl of resuspension buffer by sonication. Protein samples were divided into two equal parts for ±HA treatment by placing 50 μl into fresh tubes. Each sample was treated with 150 μl of either –HA buffer (0.2% Triton buffer) or

+HA buffer (0.2% Triton buffer containing 1.33 mM HA, pH ≈ 7.3). Samples were first incubated at room temperature with shaking for 1 h, and then proteins were precipitated by chloroform–methanol precipitation to remove excess HA. Protein pellets were dried for 20–30 min at room temperature and resuspended in 30 µl of resuspension buffer per mg of protein by sonicating, and the total volume was brought to 1,200 µl with 0.2% Triton buffer. Undissolved residues were removed by centrifugation at 14,000 r.p.m. for 5 min at 4 °C. Protein concentrations were measured using the BCA assay. Protein (35 µg of each) was transferred to a fresh tube to serve as the 'input' sample, as described above. Protein (450–600 µg) was transferred to a new tube and treated as described for the ABE assay.

Dose curve of mitoFP in live cells. HEK293T cells (22,000 cells per well) or HepG2 cells (10,000 cells per well) were plated in ten wells of a 96-well plate (P96-1-N, Cellvis), which were either precoated with 0.7 µg poly-D-lysine (for HEK293T cells) or used as is (for HepG2 cells). After 20–24 h, cells were pretreated with 1.2, 2.5, 6 or 12 µM mitoFP for 30 min at 37 °C. Control cells were treated with DMSO vehicle. All treatments included Hoechst 33342 and MitoTracker Deep Red. Cells were then washed with imaging buffer, and probed for 10 min at 37 °C with either 1 µM DPP-2 or 500 nM mitoDPP-2 in fresh imaging buffer (100 µl). Cells were imaged on an inverted epifluorescence microscope. Six images from two biological replicates were used for analysis. Data analysis was performed as described above, and the data were normalized to the average fluorescence intensity of the DMSO-treated control.

Comparison of PalmB and mitoFP inhibition of APT activity. HEK293T cells (30,000 cells per well) or HepG2 cells (10,000 cells per well) were plated in ten wells of a 96-well plate in the same manner as for the mitoFP dose curve in live cells. After 20–24 h, cells were treated with 2.5 μM mitoFP or 10 μM PalmB for 30 min at 37 °C. Control cells were treated with DMSO vehicle. Cells were then washed with imaging buffer and probed for 13 min at 37 °C with either 1 μM DPP-2 or 500 nM mitoDPP-2 in fresh imaging buffer (100 μl). Images were obtained on an inverted epifluorescence microscope. Six images from two biological replicates were used for analysis. Data analysis was performed as mentioned above, and the data were normalized to the average fluorescence intensity of the DMSO-treated control.

Assessment of APT1, ABHD10 and PRDX5 knockdown efficiency. HEK293T cells (550,000 cells per well) were plated in 2 ml DMEM GlutaMAX (10% FBS) into a six-well dish. After 20–22 h, cells were transfected with 44 pmol of siRNA targeting either APT1 or ABHD10, or a NT siRNA control. At 44 h posttransfection, cells were washed with 1 ml DPBS and lysed with 500 μl of RIPA buffer (50 mM Tris, 150 mM NaCl, 0.5% deoxycholate, 0.1% SDS, 1.0% Triton X-100, pH 7.4, PMSF and protease inhibitor cocktail). Lysed cells were collected and vortexed for 5 s and end-over-end rotated at 4 °C overnight. Protein concentration of each sample was measured by the BCA assay (ThermoFisher Scientific). Laemmli (6×) SDS sample buffer (Alfa Aesar) containing 180 mM DTT was added, and proteins were denatured by heating at 90 °C for 10 min. An equal amount of protein from each sample was resolved on 12% SDS–PAGE gels and subjected to western blotting using the protocol described above. For checking PRDX5

knockdown efficiency, HeLa cells (500,000 cells per well) were plated and 25 pmol of siRNAs was used.

Assessment of mitochondrial H_2O_2 following APT1 or ABHD10 knockdown, and ABHD10 overexpression. HEK293T cells (140,000 cells per well) were plated in four-well chamber slides, as detailed above. After 18–20 h, 150 µl of media was removed from each well and the cells were transfected with 12.5 pmol of siRNA targeting either APT1 or ABHD10. Control cells were transfected with NT siRNA following the manufacturer's conditions. At 44–48 h posttransfection, cells were pretreated with 2 µM mitoPY1 for 30 min at 37 °C. Cells were then washed with DPBS and treated with fresh DPBS with or without 100 µM H_2O_2 for 10 min at 37 °C. Images were obtained on an inverted epifluorescence microscope. Data analysis was performed as described above. Data were normalized to the average fluorescence intensity of the NT siRNA-transfected control that was not treated with H_2O_2. Each experiment was repeated in at least two biological replicates with identical results. Similar experiments were also done in HEK293T cells transfected with 600 ng of ABHD10 vector or control vector.

Assessment of cytoplasmic H_2O_2 following knockdown of ABHD10. HEK293T cells (150,000 cells per well) were plated in four-well chamber slides, as detailed above. After 18–20 h, 150 µl of media was removed from each well and the cells were transfected with 12.5 pmol of siRNA targeting either ABHD10 or NT siRNA control following manufacturer's conditions. At 48 h posttransfection, cells were pretreated with 5 µM PY1 for 30 min at 37 °C. Cells were then washed with DPBS (400 µl) and treated with fresh DPBS (400 µl)

with or without 100 μM H_2O_2 for 13 min at 37 °C. Images were obtained on an inverted epifluorescence microscope. Data analysis was performed as described above. Data were normalized to the average fluorescence intensity of the NT siRNA-transfected control that was not treated with H_2O_2.

Epifluorescence-based genetic overexpression screen. HEK293T cells (16,000–18,000 cells per well) were plated in 96-well plates as described above. After 18–22 h, cells were transfected with 80 ng of either empty vector plasmid or individual plasmids containing the protein targets. At 40–44 h posttransfection, the media was replaced with 100 μl of fresh media containing 1 μM Hoechst 33342 and 100 nM MitoTracker Deep Red. After 30 min, the cells were washed with 100 μl of imaging buffer and 70 μl of 1 μM DPP-2 in fresh imaging buffer was added to the cells. Cell were incubated for 10 min at 37 °C and then imaged from 25 min onwards on an inverted epifluorescence microscope set on automated focus mode. Multiple images from two biological replicates were used for analysis. Data analysis was performed as described above, and the data were normalize d to the average fluorescence intensity of empty vector plasmid-transfected control cells.

ABPP. HEK293T or HepG2 cells were incubated with various concentrations of mitoFP for 2 h, and lysed in SDS-free RIPA lysis buffer. Knockdown lysates from APT1 or ABHD10 siRNA-transfected cells were obtained by treating cells with SDS-free RIPA lysis buffer. After 30 min of lysis on ice, 50 μg of protein from total cell, cytosolic and mitochondrial fractions were incubated with 2 μM FP-TAMRA[19] (ThermoFisher) for 1 h at room temperature, then quenched with 6× Laemelli sample buffer (containing 60 mM DTT). Proteins were resolved with 12% SDS–PAGE and visualized with Chemidoc XRS (Bio-

Rad) using the Cy3 channel. As a loading control, Coomassie Blue was used to stain total protein.

Mitochondria isolation. Mitochondrial and cytosolic fractions from HepG2 cells were performed according to the manufacturer's recommended protocol with Mitochondria Isolation Kit for Cultured Cells (Pierce, catalog no. 89874).

Imaging with mitoDPP-2. HEK293T cells (140,000 cells per well) were plated in four-well chamber slides as described above. After 18–20 h, the cells were transfected with 600 ng of either pcDNA3-ABHD10 WT or -ABHD10 S152A. Control cells were transfected with the empty pcDNA3 vector backbone. At 32–35 h posttransfection, nuclei and mitochondria were stained with Hoechst 33342 and MitoTracker Deep Red, respectively, for 30 min at 37 °C. Cells were then briefly washed with imaging solution and probed with 500 nM mitoDPP-2 in fresh imaging solution. After 10 min at 37 °C, images were obtained on an inverted epifluorescence microscope, and data analyses were performed as described above. For data analysis, the average fluorescence intensity per image in each experimental condition was obtained by gating cells using the bright-field image, and applying that mask to the corresponding MitoTracker and mitoDPP-2 images. Eight images from two biological replicates were used to quantify the images, and the data were normalized to the average fluorescence intensity of the MitoTracker channel of cells transfected with the empty vector plasmid.

For assessing mitochondrial membrane integrity in HEK293T, cells were plated, treated as described above and replaced with fresh growth media containing 1 μM

Hoechst 33342 and 100 nM TMRM. Cells were then incubated at 37 °C for 30 min, washed and replaced with 400 µl of imaging solution. Images were obtained on an inverted epifluorescence microscope using TRITC/RFP filter settings, and data analyses were performed as described above. Eight images from two biological replicates were used to quantify the images, and the data were normalized to the average fluorescence intensity of control cells.

***In vitro* kinetic assay of APTs following mitoFP-mediated inhibition**. *In vitro* biochemical assays with purified APT1 or ABHD10 enzymes were performed on a Biotek synergy Neo2 plate reader. APT1 or ABHD10 (100 nM) was incubated for 30 min at 37 °C with 1.2, 2.4, 6, 12, 24, 60 or 120 µM mitoFP equal in HEPES buffer (20 mM, pH 7.8, 150 mM NaCl). Controls were incubated with an equal volume of DMSO. At the end of 30 min, the incubated APT1 or ABHD10 solutions (150 µl) were added to a 96-well optical bottom plate (ThermoFisher Scientific, Nunc 265301) at room temperature. Wells containing HEPES buffer alone served as negative controls. Using a multichannel pipette, 150 µl of a solution of 2 µM DPP-5 in HEPES buffer was added, for a final concentration of: 1 µM DPP-5; 50 nM enzyme; and 0, 0.6, 1.2, 3, 6, 12, 30 or 60 µM mitoFP. Fluorescence intensities (excitation wavelength λ_{ex} = 490/20 nm, emission wavelength λ_{em} = 545/20 nm, Gain 80, read from bottom with height 4.5 mm and sweep method) were measured at 15s time intervals for 30 min at 37 °C. Incubations of 12 µM PalmB with 100 nM APT1, and 6 µM PalmB with 100 nM ABHD10 were run in parallel and served as positive controls. The initial velocity was calculated from linear regression of the first 20 data points of APT1 and the first 30 data points for ABHD10 (n = 4) and the one-phase

exponential decay analysis (Y = Span × exp(−KX) + Plateau) was done using GraphPad Prism v.6.0e.

Purification of recombinant ABHD10. BL21-competent E. coli were transformed with both the pGro7 chaperone plasmid and plasmids encoding transit peptide-cleaved human ABHD10 (either WT or S152A) or mouse ABHD10. The cells were cultured in 500 ml 2× YT media with 33 μg ml^{-1} chloramphenicol, 40 μg ml^{-1} kanamycin and 0.5 mg ml^{-1} L-arabinose in a 2L flask shaking at 37 °C until optical density OD600 ≈ 0.6, at which point 1 mM IPTG was added. Cultures were then grown at 25 °C for an additional 20 h. Bacteria were harvested by centrifugation and lysed by sonication in 25 ml lysis buffer (50 mM Tris, 1 M NaCl, 20% glycerol, 10 mM TCEP, pH 7.5). Cell debris was discarded and the lysis supernatant was incubated with 1 mL Takara His60 Ni Superflow Resin with gentle rotation at 4 °C for 1 h. The His-tagged proteins were purified using a standard protocol of washing and eluting the resin with wash buffer-1 (20 mM imidazole, 50 mM Tris, 1 M NaCl, 20% glycerol, 10 mM TCEP, pH 7.5), wash buffer-2 (40 mM imidazole, 50 mM Tris, 1 M NaCl, 20% glycerol, 10 mM TCEP, pH 7.5) and elution buffer (300 mM imidazole, 50 mM Tris, 1 M NaCl, 20% glycerol, 10 mM TCEP, pH 7.5). The purified proteins were then desalted on GE Disposable PD-10 Desalting Columns and stored in the protein storage buffer (50 mM Tris, 100 mM NaCl, 2 mM TCEP, 50% glycerol, pH 7.5). The purity of the elution fractions was validated by 12% SDS–PAGE gel. Purified proteins were stored in individual aliquots in protein storage buffer at −20 °C (for more immediate use) or −80 °C (for long-term storage).

***In vitro* kinetics of recombinant human and mouse ABHD10**. DPP-5 (150 µl of 10 µM) in HEPES (20 mM, pH 7.8, 150 mM NaCl) was added to the 96-well optical bottom plate. HEPES buffer alone (150 µl) or HEPES buffer containing 1 µM proteins (human, mouse or S152A variant ABHD10, purified as described above; 150 µl) were added using a multichannel pipette, resulting in a final concentration of 5 µM DPP-5 and 500 nM proteins. Fluorescence intensities (λ_{ex} = 490/20 nm, λ_{em} = 545/20 nm, gain 50, read from bottom with height 4.5 mm and sweep method) were measured at 1-min time intervals for 12 h at 37 °C. The Michaelis–Menten kinetics regression analysis was performed using GraphPad Prism v.6.0e.

Crystallization of truncated mouse ABHD10. Mouse ABHD10 was purified from Ni-resin as described above. Mouse ABHD10 was solubilized in buffer A (20 mM Tris, pH 8.0) with PD-10 Desalting Columns and loaded onto a Q Sepharose Ion-Exchange column for gradient-elution with buffer B (1 M NaCl, 20 mM Tris, pH 8.0). Fractions were collected and verified by 12% SDS–PAGE. Pure fractions were combined and loaded onto a Superdex 200 Increase 10/300 GL column (GE Healthcare Life Sciences). The fractions eluted by SEC buffer (10 mM Tris, 50 mM NaCl, pH 8.0) were again verified by SDS–PAGE and concentrated to 35 mg ml−1. The pure protein was then aliquoted, flash-frozen in liquid nitrogen and stored at −80 °C. The crystallization was performed using the hanging-drop vapor diffusion technique. The high-throughput screening of crystallization conditions was set up by a Mosquito Crystallization Robot (TTP Labtech) at 4 °C using commercially available screening kits from Hampton Research Corp. The best crystals were obtained from 25 mg ml−1 proteins mixed with the precipitant solution from Natrix 2

(0.08 M strontium chloride hexahydrate, 0.04 M sodium cacodylate trihydrate, pH 6.0, 35% v/v (±)-2-methyl-2,4-pentanediol (MPD), 0.012 M spermine tetrahydrochloride). Following optimization of pH at 6.4 and precipitant concentration at 25%, crystals were grown in the 2 µl of 1:1 protein and buffer solution mixture drops hanging on siliconized glass slides, harvested by soaking the cryo buffer (same as precipitant buffer except that the MPD concentration increased to 50%) and flash-frozen in liquid nitrogen.

Assessment of S-palmitoylation levels of PRDX3 and PRDX5 on ABHD10 knockdown by ABE assay. HEK293T cells plated in 10-cm dishes were transfected when 30–40% confluent with control siRNA (NT) or ABHD10 siRNA. After 44–48 h, cells were lysed and processed as described in the ABE protocol. For quantification, five biological replicates in HEK293T cells were used and S-palmitoylation levels of PRDX3 and PRDX5 were normalized by the following equation using the output signal (S) for corresponding proteins and calnexin from western blots

Relative S−Palmitoylation of PRDX = $[S_{(PRDX-10)} \times S_{(CANX-NT)}]/[S_{(PRDX-NT)} \times S_{(CANX-10)}]$

$S_{(PRDX-10)}$=Chemiluminescence signal of PRDX upon ABHD10 knockdown

$S_{(PRDX-NT)}$=Chemiluminescence signal of PRDX in control cells

$S_{(CANX-10)}$=Chemiluminescence signal of calnexin upon ABHD10 knockdown in control cells

$S_{(CANX-NT)}$=Chemiluminescence signal of calnexin in control cells

Similar experiments in HEK293T cells were performed in three biological replicates to assess S-palmitoylation levels of PRDX3 and PRDX5 on APT1 knockdown. For

assessing S-palmitoylation levels of PRDX3 and PRDX5 in HeLa cells on ABHD10 knockdown, we took 24 mg of total protein as input, and used 211 mg of total protein for biotin enrichment and measured percentages of S-palmitoylation as follows

Relative S−Palmitoylation of protein=[$S_{(Output)}$/211]/[$S_{(Input)}$/24]

$S_{(Output)}$=Chemiluminescence signal of protein in output sample

$S_{(Input)}$=Chemiluminescence signal of protein in input sample

PRDX5 immunoprecipitation ABE assay. HEK293T cells plated in 10-cm culture dishes were transfected with 10 μg of pcDNA3-PRDX5-Flag WT plasmid and PEI (PEI:DNA = 4:1)[42] when 30–40% confluent. After 16 h, the media was removed and transfected with 150 pmol of either ABHD10 or NT siRNA for another 24 h. Cells were then lysed in SDS-free RIPA lysis buffer and rotated end-to-end for 2 h at 4 °C before insoluble material was removed by centrifugation at 14,000 r.p.m. for 15 min at 4 °C. Immunoprecipitation was performed overnight at 4 °C with anti-FLAG antibody-incubated protein G magnetic beads (prepared according to the manufacturer's recommended protocol). Inputs were taken from lysates (10% of the lysate volume) before immunoprecipitation. Beads were washed once with SDS-free RIPA lysis buffer and then incubated with 500 μl SDS-free RIPA lysis buffer containing 50 mM NEM for 2 h at 25 °C with end-to-end rotation. Beads were washed three times with SDS-free RIPA lysis buffer then equally separated into two new tubes. One tube was incubated with SDS-free RIPA lysis buffer containing 0.8 M HA (pH 7.4), and the other was incubated with SDS-free RIPA lysis buffer and rotated end-to-end for 1 h at room temperature. Beads were washed two

times with SDS-free RIPA lysis buffer before incubating with 10 μM EZ-Link HPDP-Biotin for 2 h at 25 °C with end-to-end rotation. Beads were washed twice and eluted with 50 mM glycine solution (pH 2.8). The supernatant was neutralized with 1 M Tris before boiling for 10 min at 95 °C with 6× Laemelli sample buffer. The protein was resolved on 12% SDS–PAGE gels and western blotting was conducted using the protocol described above.

PRDX5 palmitoylation site identification by ABE. HEK293T cells plated in 10-cm culture dishes were transfected when 30–40% confluent with 15 μg of either the pcDNA3-PRDX5-Flag WT plasmid (control) or individual plasmids containing each cysteine to serine point mutant. After 42–48 h, cells were washed with DPBS, lysed and processed as described above for the ABE protocol. Input and output samples for C100S were taken three times more than corresponding samples for WT, C125S and C204S.

PRDX5 palmitoylation site identification by metabolic labeling. HEK293T cells plated in 10-cm culture dishes were transfected when 30–40% confluent with 15 μg of either the pcDNA3-PRDX5-Flag WT or C100S mutant plasmid. After 44 h, cells were metabolically labeled with 50 μM 17-ODYA for 3 h and then processed using the metabolic labeling protocol described above.

Cell viability experiment. For the H_2O_2 experiment, HEK293T or HeLa cells transfected with NT siRNA or ABHD10 siRNA for 24 h were replated into a 96-well plate. After 24 h, the media was replaced with 200 μl pyruvate-free DMEM GlutaMAX (10% FBS) containing either H_2O or 25 or 50 μM H_2O_2. After 36 h incubation at 37 °C, the media was

replaced with 200 µl of 1× MTS reagent (10× PBS stock solution containing 0.6 mM MTS and 0.033 mM phenazine methosulfate, pH 5.2–5.4)[43] in DMEM GlutaMAX and incubated at 37 °C for 1–2 h. The plate was then gently shaken and absorbance was measured at 490 nm using a plate reader. Cells treated with NT or ABHD10 siRNA and no H_2O_2 were set to 100% viability. Each group of cells with various concentrations of H_2O_2 was normalized to respective cells treated with H_2O as follows:

Percentage cell viability(c) = A(c)/A(0) × 100

A(c) = Average absorbance at concentration c

A(0) = Average absorbance at concentration 0

For the H2O2 experiment with PRDX5 knockdown, HEK293T or HeLa cells were transfected with NT siRNA, PRDX5 siRNA, ABHD10 siRNA or cotransfected with ABHD10 siRNA and PRDX5 siRNA (for the non-cotransfected group, NT siRNA was added to make the total amount of siRNA consistent between groups) for 24 h (for the HeLa cells, we replaced the media without siRNA after 12 h to decrease toxicity stemming from the transfection reagent) and then were replated into a 96-well plate. The rest of the protocol was the same as described above.

For the paraquat experiment, HEK293T cells transfected with NT siRNA or ABHD10 siRNA for 24 h were replated into a 96-well plate. After 24 h, the media was replaced with 200 µl pyruvate-free DMEM GlutaMAX (10% FBS) containing either H2O or 50, 100 or 200 µM aqueous paraquat. After 12 h at 37 °C, the media was replaced with 200 µl of pyruvate-free DMEM GlutaMAX (10% FBS). After 24 h, the media was replaced

with 200 µl of 1× MTS reagent (10× PBS stock solution containing 0.6 mM MTS and 0.033 mM phenazine methosulfate, pH 5.2–5.4) in DMEM GlutaMAX and incubated at 37 °C for 1 h. The plate was then gently shaken, and absorbance was measured at 490 nm using a plate reader. Quantification was performed as described above.

3.5 Synthetic procedures

Synthesis of 1. (4-Iodobutyl)triphenylphosphonium[44] (1.2 g, 1.0 equiv., 2.10 mmol) was dissolved in excess triethyl phosphite (1.80 ml, 5.0 equiv., 10.5 mmol) and heated at 155 °C for 4 h. Excess triethyl phosphite was removed at 80 °C under vacuum to yield 1 as a colorless oil (0.79 g), which was used without further purification.

Synthesis of mitoFP (3). Compound 1 (0.79 g, 1.0 equiv., 1.36 mmol) was dissolved in dichloromethane (DCM) (30 ml) and cooled to 0 °C. Bromotrimethylsilane (1.10 ml, 6.0 equiv., 8.33 mmol) was added and the reaction was stirred first for 30 min at 0 °C and then for 2 h at room temperature. Then, 15 ml water was added to quench the reaction. The aqueous phase was separated and an additional 10 ml of water was used to extract the product from the organic phase. The combined aqueous phase was washed once with 15 ml DCM. The aqueous solution was azeotroped with toluene (3×) to yield 2 as a yellow oil, which was used without further purification. Compound 2 was dissolved in 25 ml dry DCM and cooled to 0 °C, followed by dropwise addition of DAST (2.1 ml, 11.7 equiv., 15.9 mmol). The reaction was first stirred at 0 °C for 15 min, and then at room temperature for another 15 min to generate the difluoro intermediate. Octanol (5 ml in total) was added dropwise at 45 °C until no difluoro intermediate was detected by LC–MS. The reaction

was quenched with water and extracted with DCM. The organic layer was washed with water and then brine. The organic layer was then dried over Na_2SO_4, and then concentrated and purified by column chromatography (Silica; 0–5% MeOH in 1:1 DCM:EtOAc) to yield mitoFP (3) (0.264 g, 36%). R_f: 0.45 (Silica; 10% MeOH in 1:1 DCM:EtOAc). ^{1}H-NMR (500 MHz; $CDCl_3$): δ 7.82–7.68 (m, 15H), 4.11 (q, J = 7 Hz, 2H), 3.54–3.48 (m, 2H), 2.07–1.99 (m, 4H), 1.88–1.82 (m, 2H), 1.66–1.62 (m, 2H), 1.31–1.25 (br, 10H), 0.86 (t, J = 6.8 Hz, 3H). ^{13}C-NMR (126 MHz; $CDCl_3$): δ 135.4, 135.3, 133.7, 133.6, 130.8, 130.7, 118.3, 117.6, 67.6, 67.5, 31.8, 30.4, 30.3, 29.2, 29.1, 25.3, 22.7, 14.2. HRA–MS+: calculated for $C_{30}H_{40}FO_2P_2$ [M+] 513.2482; found 513.2587.

3.6 References

(1) Blanc, M.; David, F. P. A.; van der Goot, F. G. SwissPalm 2: Protein S-Palmitoylation Database. *Methods in molecular biology (Clifton, N.J.)* **2019**, *2009*, 203–214.

(2) Kostiuk, M. A.; Corvi, M. M.; Keller, B. O.; Plummer, G.; Prescher, J. A.; Hangauer, M. J.; Bertozzi, C. R.; Rajaiah, G.; Falck, J. R.; Berthiaume, L. G. Identification of palmitoylated mitochondrial proteins using a bio-orthogonal azido-palmitate analogue. *FASEB journal : official publication of the Federation of American Societies for Experimental Biology* **2008**, *22* (3), 721–732.

(3) Tang, M.; Lu, L.; Huang, Z.; Chen, L. Palmitoylation signaling: a novel mechanism of mitochondria dynamics and diverse pathologies. *Acta biochimica et biophysica Sinica* **2018**, *50* (8), 831–833.

(4) Maynard, T. M.; Meechan, D. W.; Dudevoir, M. L.; Gopalakrishna, D.; Peters, A. Z.; Heindel, C. C.; Sugimoto, T. J.; Wu, Y.; Lieberman, J. A.; Lamantia, A.-S. Mitochondrial localization and function of a subset of 22q11 deletion syndrome candidate genes. *Molecular and cellular neurosciences* **2008**, *39* (3), 439–451.

(5) Shen, L.-F.; Chen, Y.-J.; Liu, K.-M.; Haddad, A. N. S.; Song, I.-W.; Roan, H.-Y.; Chen, L.-Y.; Yen, J. J. Y.; Chen, Y.-J.; Wu, J.-Y.; Chen, Y.-T. Role of S-Palmitoylation by ZDHHC13 in Mitochondrial function and Metabolism in Liver. *Scientific reports* **2017**, *7* (1), 2182.

(6) Kathayat, R. S.; Cao, Y.; Elvira, P. D.; Sandoz, P. A.; Zaballa, M.-E.; Springer, M. Z.; Drake, L. E.; Macleod, K. F.; van der Goot, F. G.; Dickinson, B. C. Active and dynamic mitochondrial S-depalmitoylation revealed by targeted fluorescent probes. *Nature communications* **2018**, *9* (1), 334.

(7) Kathayat, R. S.; Dickinson, B. C. Measuring S-Depalmitoylation Activity In vitro and In Live Cells with Fluorescent Probes. *Methods in molecular biology (Clifton, N.J.)* **2019**, *2009*, 99–109.

(8) Duncan, J. A.; Gilman, A. G. A cytoplasmic acyl-protein thioesterase that removes palmitate from G protein alpha subunits and p21(RAS). *The Journal of biological chemistry* **1998**, *273* (25), 15830–15837.

(9) Long, J. Z.; Cravatt, B. F. The metabolic serine hydrolases and their functions in mammalian physiology and disease. *Chemical reviews* **2011**, *111* (10), 6022–6063.

(10) Knoops, B.; Goemaere, J.; van der Eecken, V.; Declercq, J.-P. Peroxiredoxin 5: structure, mechanism, and function of the mammalian atypical 2-Cys peroxiredoxin. *Antioxidants & redox signaling* **2011**, *15* (3), 817–829.

(11) Fröhlich, M.; Dejanovic, B.; Kashkar, H.; Schwarz, G.; Nussberger, S. S-palmitoylation represents a novel mechanism regulating the mitochondrial targeting of BAX and initiation of apoptosis. *Cell death & disease* **2014**, *5*, e1057.

(12) Zorov, D. B.; Juhaszova, M.; Sollott, S. J. Mitochondrial reactive oxygen species (ROS) and ROS-induced ROS release. *Physiological reviews* **2014**, *94* (3), 909–950.

(13) Thinon, E.; Fernandez, J. P.; Molina, H.; Hang, H. C. Selective Enrichment and Direct Analysis of Protein S-Palmitoylation Sites. *Journal of proteome research* **2018**, *17* (5), 1907–1922.

(14) Dekker, F. J.; Rocks, O.; Vartak, N.; Menninger, S.; Hedberg, C.; Balamurugan, R.; Wetzel, S.; Renner, S.; Gerauer, M.; Schölermann, B.; Rusch, M.; Kramer, J. W.; Rauh, D.; Coates, G. W.; Brunsveld, L.; Bastiaens, P. I. H.; Waldmann, H. Small-molecule inhibition of APT1 affects Ras localization and signaling. *Nature chemical biology* **2010**, *6* (6), 449–456.

(15) Dickinson, B. C.; Chang, C. J. A targetable fluorescent probe for imaging hydrogen peroxide in the mitochondria of living cells. *Journal of the American Chemical Society* **2008**, *130* (30), 9638–9639.

(16) Rhee, S. G.; Kil, I. S. Multiple Functions and Regulation of Mammalian Peroxiredoxins. *Annual review of biochemistry* **2017**, *86*, 749–775.

(17) Wan, J.; Roth, A. F.; Bailey, A. O.; Davis, N. G. Palmitoylated proteins: purification and identification. *Nature protocols* **2007**, *2* (7), 1573–1584.

(18) Martin, B. R.; Cravatt, B. F. Large-scale profiling of protein palmitoylation in mammalian cells. *Nature methods* **2009**, *6* (2), 135–138.

(19) Martin, B. R.; Wang, C.; Adibekian, A.; Tully, S. E.; Cravatt, B. F. Global profiling of dynamic protein palmitoylation. *Nature methods* **2011**, *9* (1), 84–89.

(20) Kathayat, R. S.; Elvira, P. D.; Dickinson, B. C. A fluorescent probe for cysteine depalmitoylation reveals dynamic APT signaling. *Nature chemical biology* **2017**, *13* (2), 150–152.

(21) Zielonka, J.; Joseph, J.; Sikora, A.; Hardy, M.; Ouari, O.; Vasquez-Vivar, J.; Cheng, G.; Lopez, M.; Kalyanaraman, B. Mitochondria-Targeted Triphenylphosphonium-Based

Compounds: Syntheses, Mechanisms of Action, and Therapeutic and Diagnostic Applications. *Chemical reviews* **2017**, *117* (15), 10043–10120.

(22) Qiu, T.; Kathayat, R. S.; Cao, Y.; Beck, M. W.; Dickinson, B. C. A Fluorescent Probe with Improved Water Solubility Permits the Analysis of Protein S-Depalmitoylation Activity in Live Cells. *Biochemistry* **2018**, *57* (2), 221–225.

(23) Adibekian, A.; Martin, B. R.; Chang, J. W.; Hsu, K.-L.; Tsuboi, K.; Bachovchin, D. A.; Speers, A. E.; Brown, S. J.; Spicer, T.; Fernandez-Vega, V.; Ferguson, J.; Hodder, P. S.; Rosen, H.; Cravatt, B. F. Confirming target engagement for reversible inhibitors *in vivo* by kinetically tuned activity-based probes. *Journal of the American Chemical Society* **2012**, *134* (25), 10345–10348.

(24) Won, S. J.; Davda, D.; Labby, K. J.; Hwang, S. Y.; Pricer, R.; Majmudar, J. D.; Armacost, K. A.; Rodriguez, L. A.; Rodriguez, C. L.; Chong, F. S.; Torossian, K. A.; Palakurthi, J.; Hur, E. S.; Meagher, J. L.; Brooks, C. L.; Stuckey, J. A.; Martin, B. R. Molecular Mechanism for Isoform-Selective Inhibition of Acyl Protein Thioesterases 1 and 2 (APT1 and APT2). *ACS chemical biology* **2016**, *11* (12), 3374–3382.

(25) Yokoi, N.; Fukata, Y.; Sekiya, A.; Murakami, T.; Kobayashi, K.; Fukata, M. Identification of PSD-95 Depalmitoylating Enzymes. *The Journal of neuroscience : the official journal of the Society for Neuroscience* **2016**, *36* (24), 6431–6444.

(26) Rhee, H.-W.; Zou, P.; Udeshi, N. D.; Martell, J. D.; Mootha, V. K.; Carr, S. A.; Ting, A. Y. Proteomic mapping of mitochondria in living cells via spatially restricted enzymatic tagging. *Science (New York, N.Y.)* **2013**, *339* (6125), 1328–1331.

(27) Iwamura, A.; Fukami, T.; Higuchi, R.; Nakajima, M.; Yokoi, T. Human α/β hydrolase domain containing 10 (ABHD10) is responsible enzyme for deglucuronidation of mycophenolic acid acyl-glucuronide in liver. *The Journal of biological chemistry* **2012**, *287* (12), 9240–9249.

(28) Ito, Y.; Fukami, T.; Yokoi, T.; Nakajima, M. An orphan esterase ABHD10 modulates probenecid acyl glucuronidation in human liver. *Drug metabolism and disposition: the biological fate of chemicals* **2014**, *42* (12), 2109–2116.

(29) Dickinson, B. C.; Huynh, C.; Chang, C. J. A palette of fluorescent probes with varying emission colors for imaging hydrogen peroxide signaling in living cells. *Journal of the American Chemical Society* **2010**, *132* (16), 5906–5915.

(30) Devedjiev, Y.; Dauter, Z.; Kuznetsov, S. R.; Jones, T. L.; Derewenda, Z. S. Crystal Structure of the Human Acyl Protein Thioesterase I from a Single X-Ray Data Set to 1.5 Å. *Structure* **2000**, *8* (11), 1137–1146.

(31) Castello, P. R.; Drechsel, D. A.; Patel, M. Mitochondria are a major source of paraquat-induced reactive oxygen species production in the brain. *The Journal of biological chemistry* **2007**, *282* (19), 14186–14193.

(32) McDonald, C.; Muhlbauer, J.; Perlmutter, G.; Taparra, K.; Phelan, S. A. Peroxiredoxin proteins protect MCF-7 breast cancer cells from doxorubicin-induced toxicity. *International journal of oncology* **2014**, *45* (1), 219–226.

(33) Sugimoto, H.; Hayashi, H.; Yamashita, S. Purification, cDNA cloning, and regulation of lysophospholipase from rat liver. *The Journal of biological chemistry* **1996**, *271* (13), 7705–7711.

(34) Sadeghi, R. S.; Kulej, K.; Kathayat, R. S.; Garcia, B. A.; Dickinson, B. C.; Brady, D. C.; Witze, E. S. Wnt5a signaling induced phosphorylation increases APT1 activity and promotes melanoma metastatic behavior. *eLife* **2018**, *7.*

(35) Amara, N.; Foe, I. T.; Onguka, O.; Garland, M.; Bogyo, M. Synthetic Fluorogenic Peptides Reveal Dynamic Substrate Specificity of Depalmitoylases. *Cell chemical biology* **2019**, *26* (1), 35-47.e7.

(36) Zuhl, A. M.; Mohr, J. T.; Bachovchin, D. A.; Niessen, S.; Hsu, K.-L.; Berlin, J. M.; Dochnahl, M.; López-Alberca, M. P.; Fu, G. C.; Cravatt, B. F. Competitive activity-based protein profiling identifies aza-β-lactams as a versatile chemotype for serine hydrolase inhibition. *Journal of the American Chemical Society* **2012**, *134* (11), 5068–5071.

(37) Parvez, S.; Long, M. J. C.; Poganik, J. R.; Aye, Y. Redox Signaling by Reactive Electrophiles and Oxidants. *Chemical reviews* **2018**, *118* (18), 8798–8888.

(38) Corvi, M. M.; Soltys, C. L.; Berthiaume, L. G. Regulation of mitochondrial carbamoyl-phosphate synthetase 1 activity by active site fatty acylation. *The Journal of biological chemistry* **2001**, *276* (49), 45704–45712.

(39) Garland, M.; Schulze, C. J.; Foe, I. T.; van der Linden, W. A.; Child, M. A.; Bogyo, M. Development of an activity-based probe for acyl-protein thioesterases. *PloS one* **2018**, *13* (1), e0190255.

(40) Ogasawara, D.; Ichu, T.-A.; Vartabedian, V. F.; Benthuysen, J.; Jing, H.; Reed, A.; Ulanovskaya, O. A.; Hulce, J. J.; Roberts, A.; Brown, S.; Rosen, H.; Teijaro, J. R.; Cravatt, B. F. Selective blockade of the lyso-PS lipase ABHD12 stimulates immune responses *in vivo*. *Nature chemical biology* **2018**, *14* (12), 1099–1108.

(41) Liu, Y.; Patricelli, M. P.; Cravatt, B. F. Activity-based protein profiling: the serine hydrolases. *Proceedings of the National Academy of Sciences of the United States of America* **1999**, *96* (26), 14694–14699.

(42) Hsu, C. Y. M.; Uludağ, H. A simple and rapid nonviral approach to efficiently transfect primary tissue-derived cells using polyethylenimine. *Nature protocols* **2012**, *7* (5), 935–945.

(43) Buttke, T. M.; McCubrey, J. A.; Owen, T. C. Use of an aqueous soluble tetrazolium/formazan assay to measure viability and proliferation of lymphokine-dependent cell lines. *Journal of Immunological Methods* **1993**, *157* (1-2), 233–240.

(44) Lin, T.-K.; Hughes, G.; Muratovska, A.; Blaikie, F. H.; Brookes, P. S.; Darley-Usmar, V.; Smith, R. A. J.; Murphy, M. P. Specific modification of mitochondrial protein thiols in response to oxidative stress: a proteomics approach. *The Journal of biological chemistry* **2002**, *277* (19), 17048–17056.

Appendix to Chapter 3: NMR Spectra and LC-MS

Compound 3, mitoFP

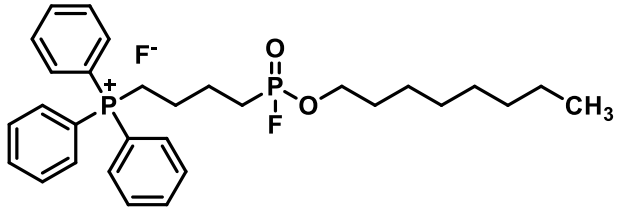

^{1}H-NMR (500 MHz; $CDCl_3$)

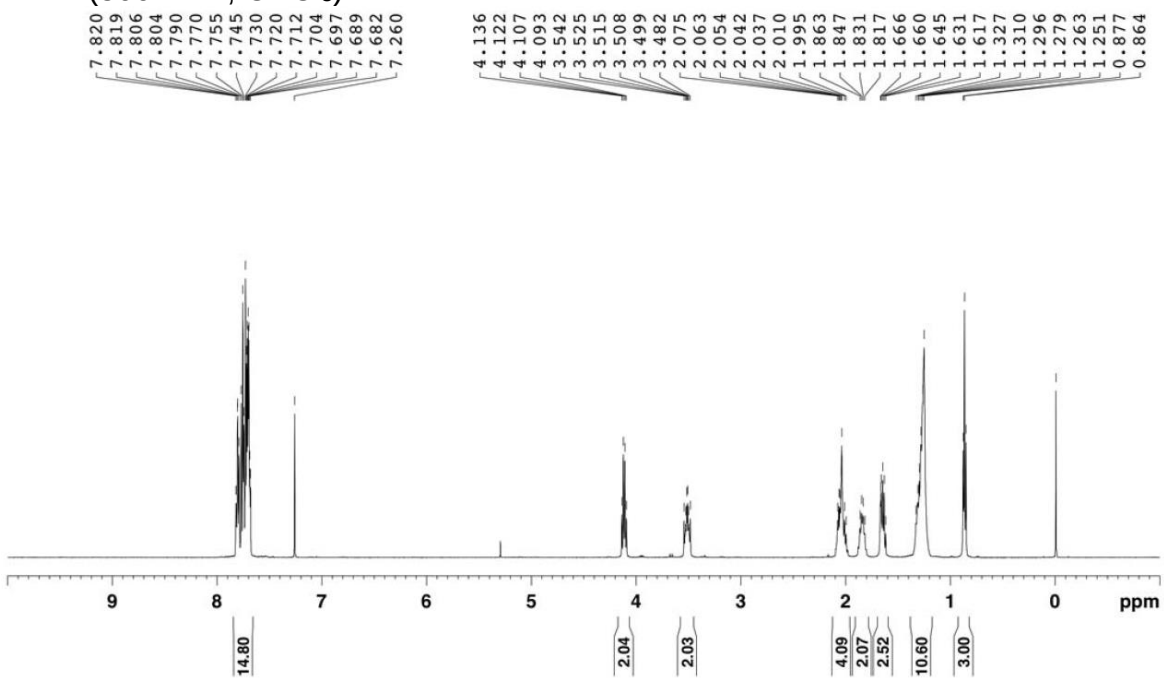

^{13}C-NMR (126 MHz; $CDCl_3$)

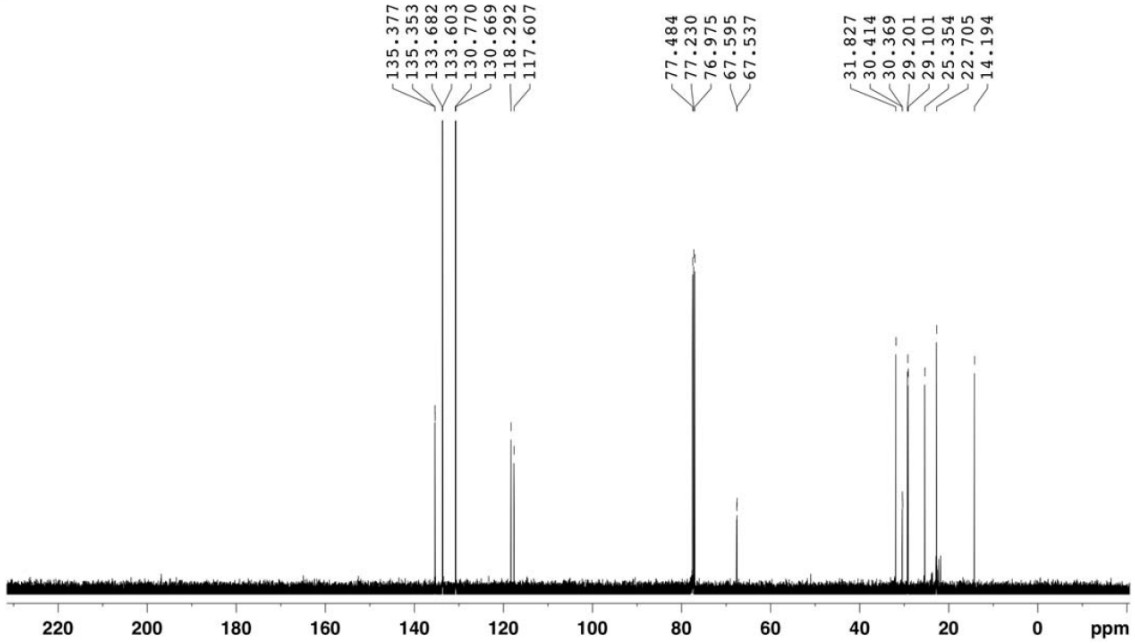

LC-MS Analysis

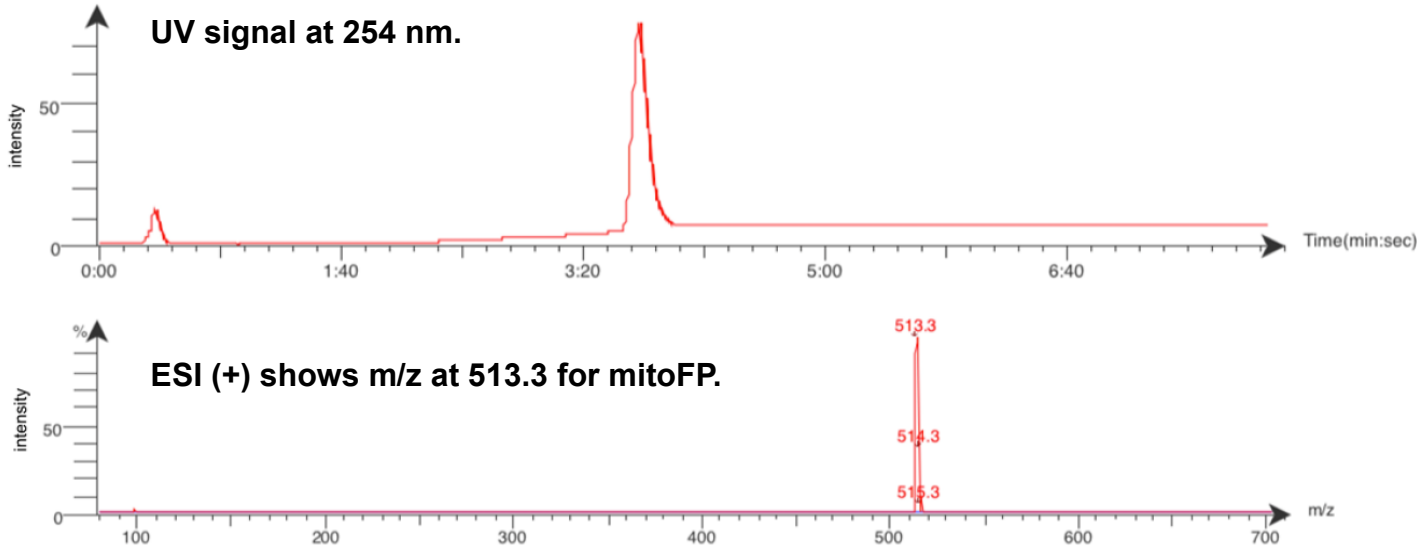

CHAPTER 4

A HIGH-THROUGHPUT FLUORESCENT TURN-ON ASSAY FOR INHIBITORS OF DHHC FAMILY PROTEINS

4.1 Introduction

As stated in 1.5.1, DHHCs and APTs regulate the cycle of proteome-wide acylation/deacylation and subsequent cell signaling, impacting cellular homeostasis and function. Moreover, in recent years, both DHHCs and APTs have emerged as targets for the mitigation of human pathologies. For example, the S-palmitoylation and S-depalmitoylation of N-Ras by zDHHC9[1] and ABHD17[2,3], respectively, drive its activation and signal propagation and therefore could be targeted in N-Ras-dependent cancers. Perturbing the S-palmitoylation cycle of STAT3 by inhibiting either zDHHC7 or APT2 activity can preclude TH17 cell differentiation and reduce symptoms of inflammatory bowel disease[4]. Additionally, zDHHC20 activity has been implicated in cellular transformation and lung tumorigenesis via regulation of epidermal growth factor receptor (EGFR) signaling, while zDHHC20 is upregulated in colorectal cancer[5,6]. Thus, disruption of S-acylation represents an emerging strategy for the treatment of disease.

While potent pan-active and isoform-specific S-deacylase (APT) inhibitors exist, parallel tools – much less ones with clinical potential – for the DHHC-PATs remain scant. As stated in 1.5.4, 2-Bromopalmitate (2BP) is the most commonly used DHHC inhibitor, but low potency, high cytotoxicity, and poor selectivity significantly curtail its applications[7]. Our lab recently developed an acrylamide-based zDHHC inhibitor[8], CMA, which has decreased cytotoxicity and an altered reactivity profile as compared to 2BP. However, like

2BP, CMA is a lipid-based molecule with limited selectivity that targets a broad spectrum of zDHHC family proteins, making it unsuitable for probing the biology of individual zDHHCs.

A central challenge in the identification and development of DHHC inhibitors is a lack of robust high-throughput screening (HTS) assays. Table X lists the main DHHC assays that have been developed. Most recently, the acylation-coupled lipophilic induction of polarization (Acyl-cLIP) assay has been successfully adapted for zDHHC3, 7, and 20[8–10]. In this assay, a fluorophore-labeled peptide is palmitoylated by a zDHHC enzyme and inserted into detergent micelles, resulting in a change in fluorescence polarization (FP). However, the dynamic range of this assay is limited, and It requires large quantities of DHHC protein that is difficult to purify.

Here, we report the development of palmitoyl transferase probes (PTPs), a panel of palmitoyl-CoA mimetic pro-fluorescent probes that report on DHHC activity *in vitro*. Using the PTPs, we develop a DHHC screening assay with a direct, sensitive, and simple readout of enzyme activity. After validating the assay with three human zDHHCs (2, 3, and 20) and confirming its sensitivity to known DHHC family inhibitors 2BP and CMA, we conduct a pilot screen of a library of 1,687 acrylamide-containing molecules against zDHHC20, establishing the suitability of the assay for HTS.

4.2 Results

DHHC catalysis of protein S-acylation is thought to occur via a two-step mechanism[11]. First, the active site cysteine of the signature DHHC (Asp-His-His-Cys) motif is auto-acylated by an acyl-CoA donor, resulting in an acyl:DHHC thioester

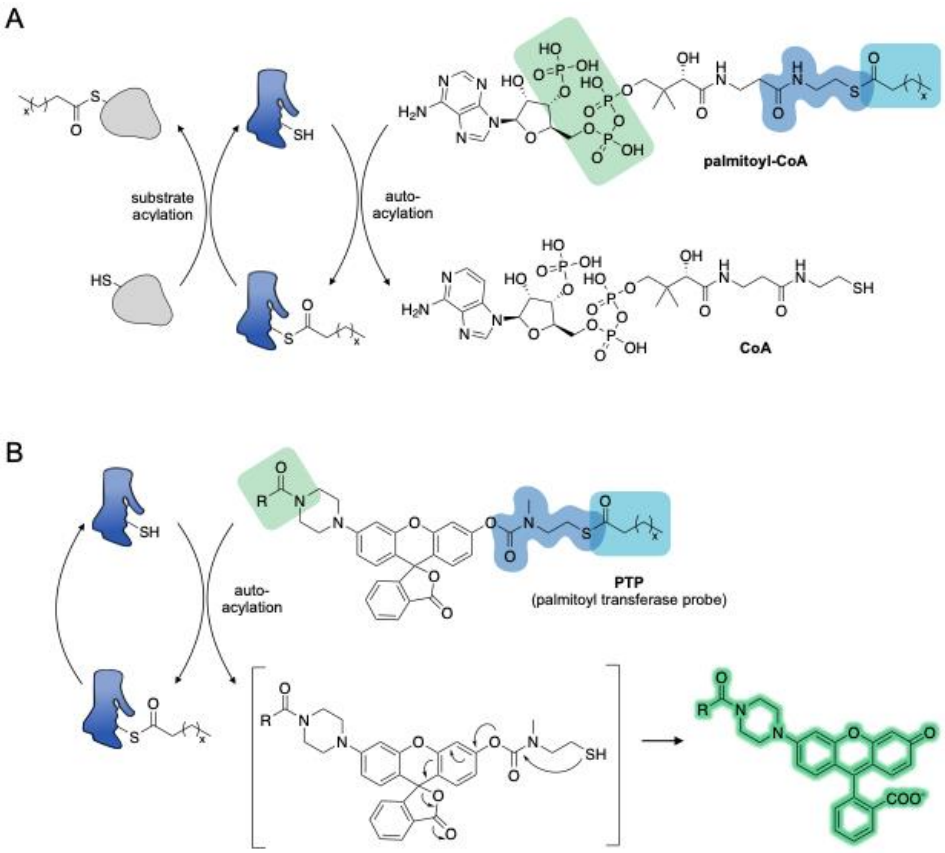

Figure 4.1 Design of palmitoyl transferase probes (PTPs): CoA substrate-based turn-on probes for DHHC activity. (A) The hypothesized two-step mechanism of DHHC acylation. The enzyme first forms an auto-acylated intermediate via nucleophilic attack of the active site cysteine on the acyl-CoA thioester. The DHHC enzyme then transfers the acyl chain to a bound substrate. (B) Design and mechanism of PTPs. An S-acylated cysteamine (blue box) is tethered to a pro-fluorescent molecule by a carbamate linker. A DHHC enzyme recognizes the pro-fluorescent molecule as an acyl donor and cleaves the thioester bond of the probe. The free thiol group then cyclizes and cleaves the carbamate linkage to release a fluorescent product (deep green). The isoform specificity and physical properties of the molecule can be tuned by modulating the acyl modification (turquoise box) and functional groups on the piperidine group (light green box).

intermediate. Then, the acyl moiety is transferred from the DHHC cysteine to a protein substrate via a transacylation reaction (**Figure 4.1A**). In designing a probe to provide a direct readout of DHHC activity, we sought to exploit the DHHC recognition of the acyl (frequently palmitoyl) CoA donor. We hypothesized that a pre-palmitoyl CoA mimetic fluorescent probe could be recognized by DHHC family proteins, with enzyme processing triggering fluorophore release (**Figure 4.1B**). Our lab has previously reported S-

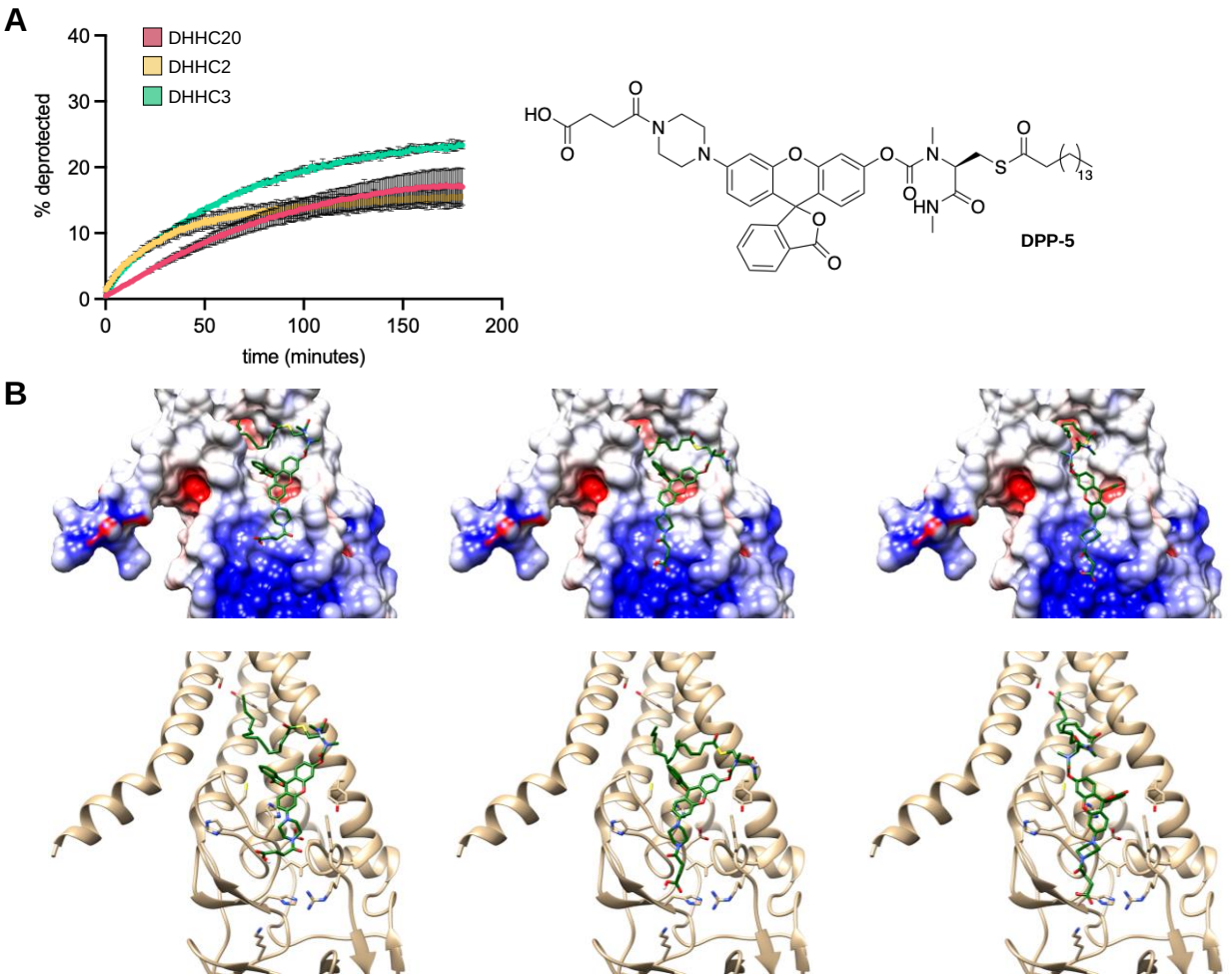

Figure 4.2 *In vitro* and *in silico* validation of the DPP-5/DHHC interaction. (A) DPP-5 can be uncaged by DHHC family interactions. Purified zDHHC2, 3, and 20 were incubated with DPP-5 (4 μM), and the resulting fluorescence signal was normalized to the signal generated by the hydroxylamine (HA)-deprotected probe to give the percent deprotection. Data are presented as the mean ± standard deviation (n = 3). (B) Docking studies of DPP-5 (green) with zDHHC20 (PDB: 6BML). Surface colored by electrostatic potential (top) and cartoon (bottom) views of the representative low energy conformations. Electrostatic surface potential was generated using an Adaptive Poisson-Boltzmann Solver (APBS) server with default settings. Positively (blue) and negatively (red) charged surfaces are displayed at the contour levels of +5 and–5 kBT/e, respectively, where kB is the Boltzmann constant, T is temperature, and e is the charge on an electron. Selected hydrogen bond interactions are shown as dashed yellow lines. The side chain of key residues is highlighted.

depalmitoylation probes (DPPs), whose deacylation results in thiol-initiated cleavage of a carbamate linker and release of the fluorescent product[12]. Intriguingly, we observed that the structure of DPP-5[13] shares some similarities with palmitoyl CoA, namely a palmitoyl

chain, a cysteamine, and a polar terminal functional group – leading us to posit that this probe could be recognized by DHHC family proteins and serve as a starting scaffold for a fluorescence-based DHHC probe. To substantiate this hypothesis, we performed docking in Autodock Vina with a previously reported crystal structure of zDHHC20[14,15]. Analysis of the lowest-energy conformations revealed that the lipid chain of DPP-5 could be docked into the hydrophobic groove, while its carboxylate could engage with the highly positive adenosine diphosphate (ADP) binding pocket (**Figure 4.2B**).

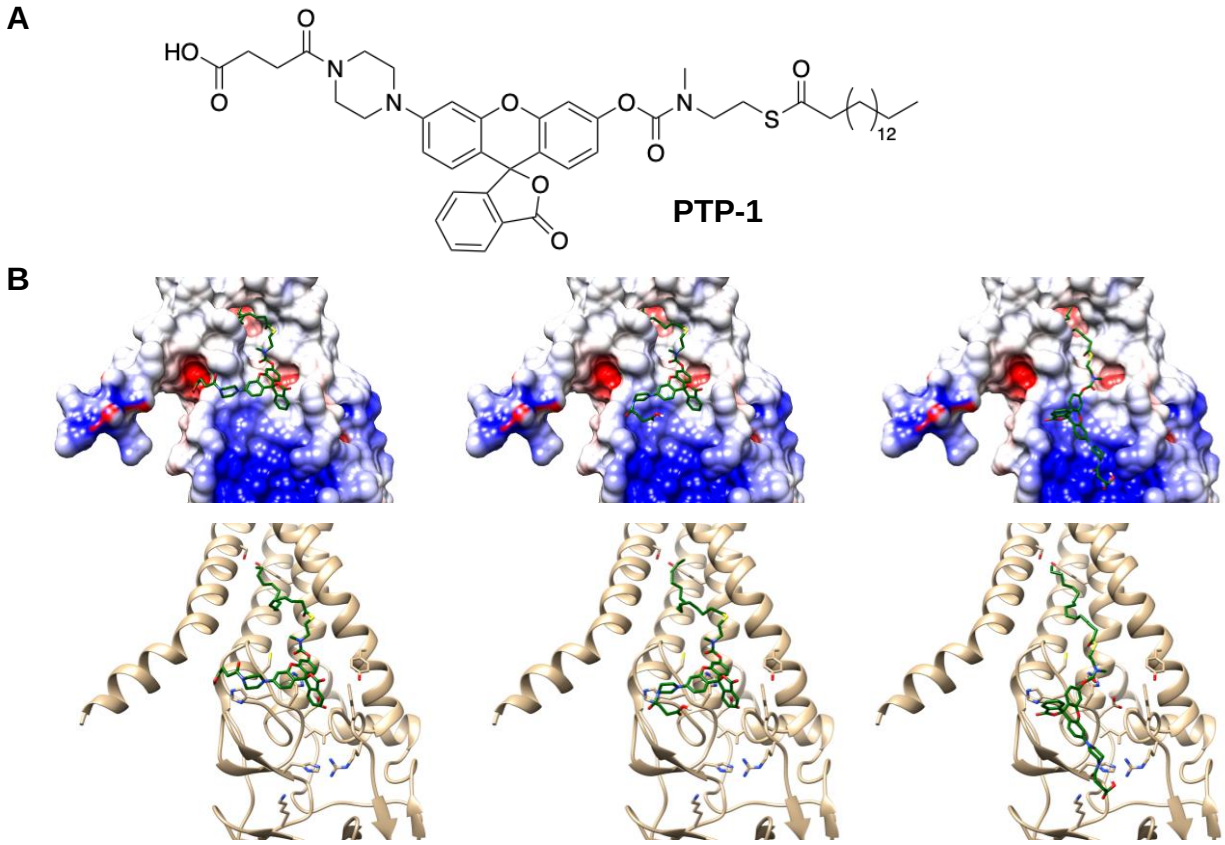

Figure 4.3 Docking studies of PTP-1 with zDHHC20. (A) Structure of PTP-1. (B) Docking studies of PTP-1 (green) with zDHHC20 (PDB: 6BML). Surface colored by electrostatic potential (top) and cartoon (bottom) views of the representative low energy conformations. Electrostatic surface potential was generated using an Adaptive Poisson-Boltzmann Solver (APBS) server with default settings. Positively (blue) and negatively (red) charged surfaces are displayed at the contour levels of +5 and–5 kBT/e, respectively, where kB is the Boltzmann constant, T is temperature, and e is the charge on an electron. Selected hydrogen bond interactions are shown as dashed yellow lines. The side chain of key residues is highlighted.

To validate these in silico observations, we then tested the ability of DHHC family proteins to uncage DPP-5 *in vitro*. Excitingly, incubation of purified human zDHHCs 2, 3, and 20 with DPP-5 resulted in a significant increase in fluorescent signal, confirming that the thioester bond of DPP-5 could be cleaved by DHHC family proteins (**Figure 4.2A**). Therefore, we next aimed to optimize this fluorogenic scaffold for interactions with DHHC family proteins and generate a family of palmitoyl transferase probes (PTPs). As an APT

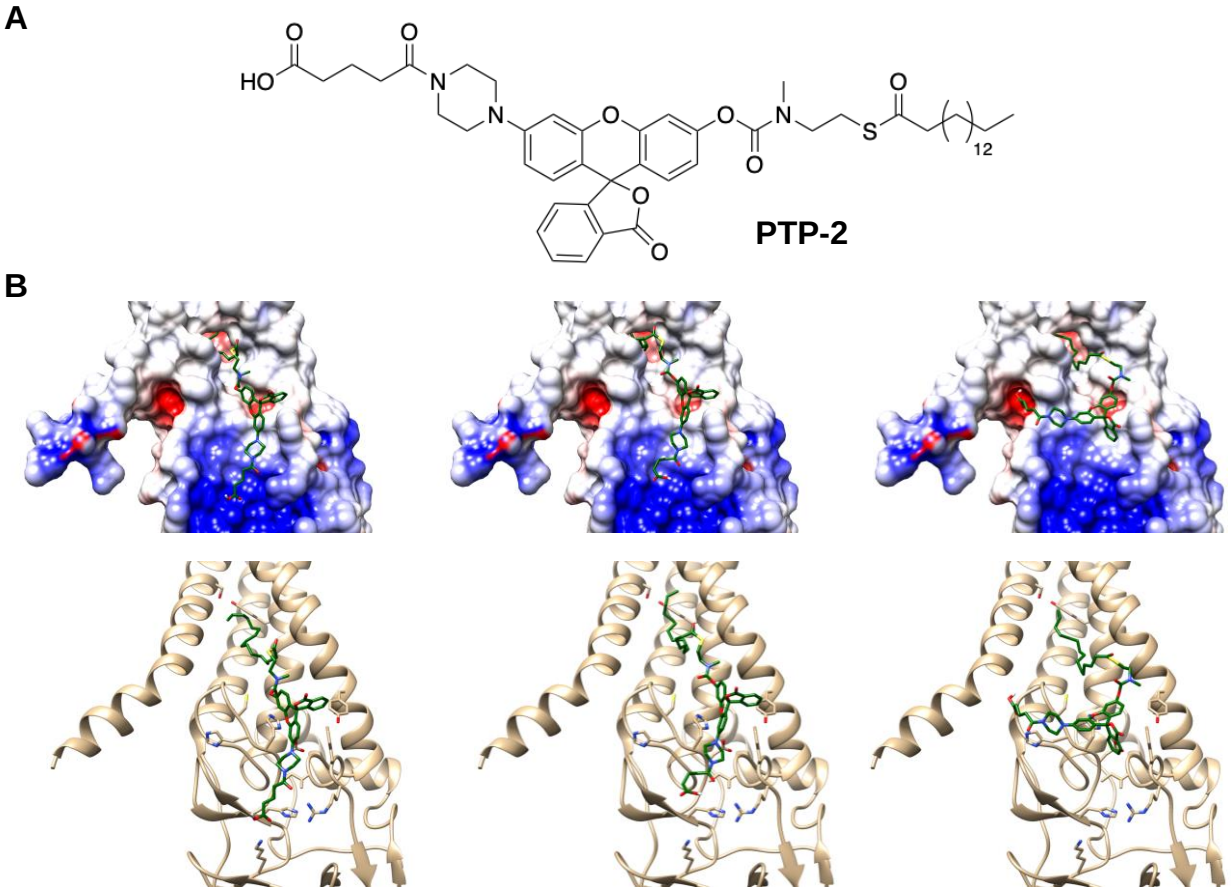

Figure 4.4 Docking studies of PTP-2 with zDHHC20. (A) Structure of PTP-2. (B) Docking studies of PTP-2 (green) with zDHHC20 (PDB: 6BML). Surface colored by electrostatic potential (top) and cartoon (bottom) views of the representative low energy conformations. Electrostatic surface potential was generated using an Adaptive Poisson-Boltzmann Solver (APBS) server with default settings. Positively (blue) and negatively (red) charged surfaces are displayed at the contour levels of +5 and–5 kBT/e, respectively, where kB is the Boltzmann constant, T is temperature, and e is the charge on an electron. Selected hydrogen bond interactions are shown as dashed yellow lines. The side chain of key residues is highlighted.

substrate, DPP-5 contains a palmitoylated cysteine, which is absent in the palmitoyl CoA substrate of DHHCs (**Figure 4.1B, 4.2A**). We thus reasoned that removal of the methyl amide from DPP-5 would both minimize steric clashes and result in a better acyl-CoA mimic (PTP-1) (**Figure 4.3A**). Docking against zDHHC20 revealed a tightly bound ligand-receptor complex, but also that the probe did not engage a highly conserved key residue of the basic patch, Lys135[14,16] (**Figure 4.3B**). In silico screening to maximize this ADP-

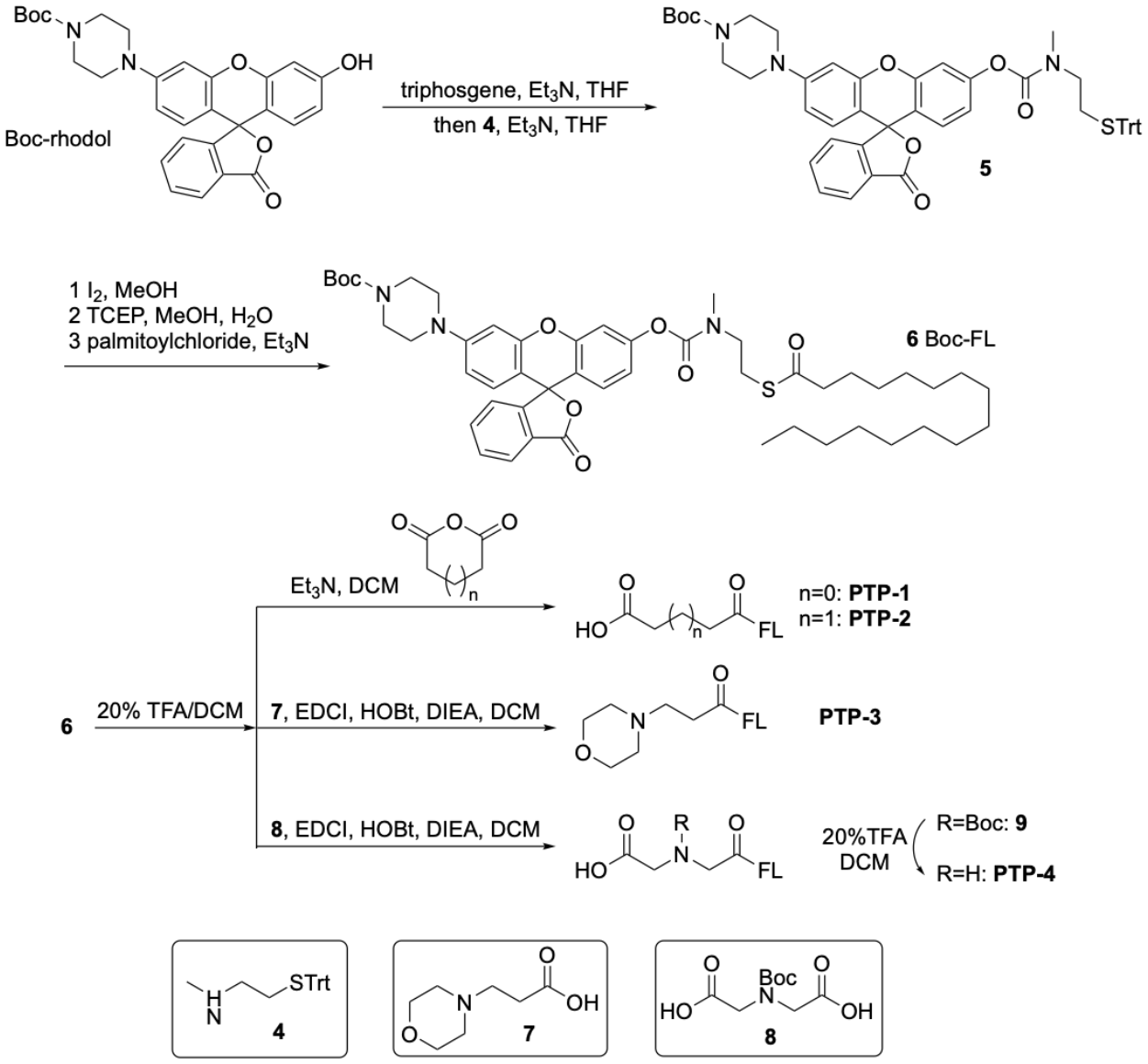

Scheme 4.1 Synthetic scheme for PTPs.

binding pocket interaction demonstrated that replacement of succinic acid with glutaric acid (PTP-2) resulted in further optimized interactions (**Figure 4.4A,B**). Given that different DHHC isoforms might have individuated interactions in the CoA binding region, we also synthesized two additional probes, one with a terminal morpholino group (PTP-3) and one with an internal amino group (PTP-4) (**Figure 4.5A**). Notably, each of these

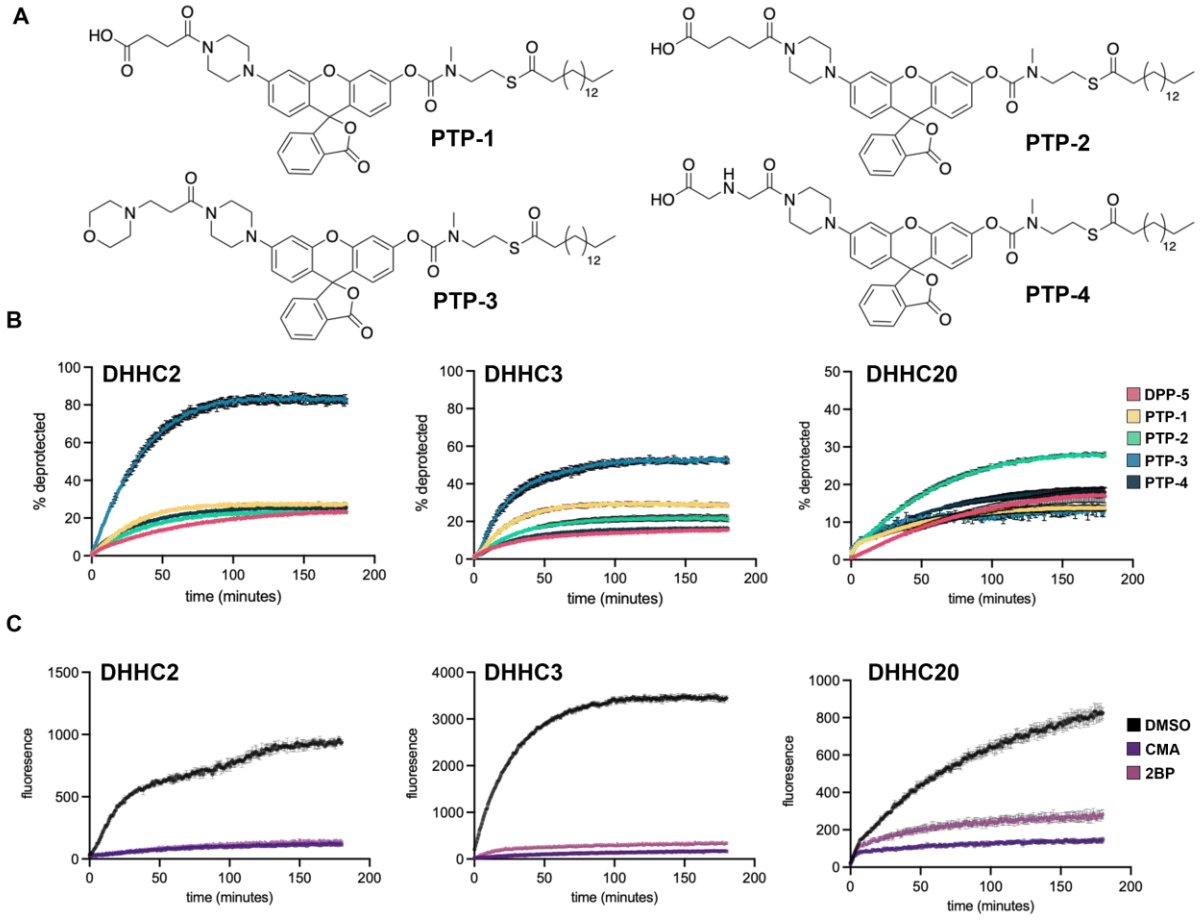

Figure 4.5 PTP family probes report DHHC family protein activity. (A) Structures of the palmitoyl transferase probes (PTPs) synthesized and tested in this work. All probes feature a palmitoylated cysteamine, with variably modified piperidine groups. (B) Uncaging of PTPs by DHHC family proteins. Each PTP (4 μM) was incubated with purified human zDHHCs 2, 3, or 20 for 3 hours. Fluorescent output was monitored over time, normalized to the signal generated by the hydroxylamine (HA)-deprotected probe to give the percent deprotection. Data are presented as the mean ± standard deviation (n = 3). (C) Detection of inhibition by PTPs. Preincubation of each zDHHC (2, 3, and 20) with known DHHC family inhibitors 2BP and CMA (20 μM) abrogated the PTP fluorescent output. Data are presented as the mean ± standard deviation (n = 6).

probes share a native substrate mimetic, a masked fluorophore, and a polar group to facilitate binding. Synthesis of all PTP probes proceeded smoothly via a modular synthetic route (**Scheme 4.1**). In brief, common precursor 5 was synthesized by triphosgene-mediated carbamate formation between trityl protected cysteamine 4 and Boc-rhodol. Following trityl deprotection and lipidation to give PTP precursor 6, a series of functional groups were installed via acylation to yield PTP1-4.

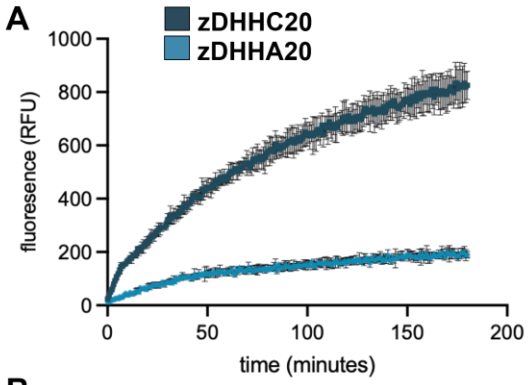

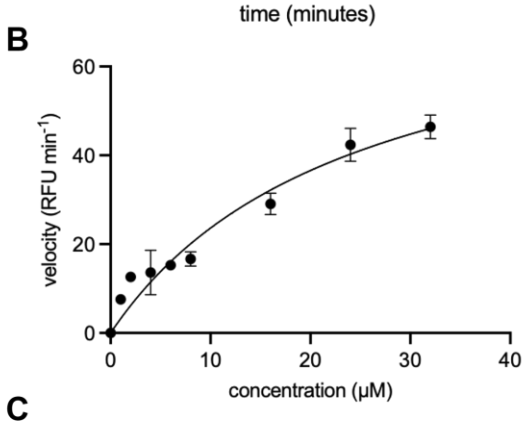

C

	PTP-2	palmitoyl-CoA
K_m	24.3 μM	0.58 μM
k_{cat}	0.16 s^{-1}	0.275 s^{-1}
k_{cat}/K_m	6.58 x 10^3 M^{-1} s^{-1}	4.74 x 10^5 M^{-1} s^{-1}

Figure 4.6 Validation and characterization of PTP-2. (A) PTP-2 (4 μM) was incubated with either WT zDHHC20 or its inactive mutant (DHHA) and the fluorescent output (PTP-2 uncaging) was monitored over time. Data are presented as the mean ± standard deviation (n=3). (B) zDHHC20 was incubated with PTP-2 at a 1, 2, 4, 6, 8, 16, 24, and 32 μM, and the initial velocity (RFU/min) was plotted against the stated concentrations to give the Km and kcat. (C) Tabulation of kinetic parameters for PTP-2 and palmitoyl CoA with zDHHC20) Quantification of (B) (error bars are ± s.e.m, n = 5). Student's *t*-test; $^{**}P < 0.001$. 100 μm scale bar shown.

With this small panel of probes in hand, we first screened them against zDHHC20 to identify the best substrate, i.e., the most uncaged molecule, for this protein. While all probes gave significant fluorescent signal, PTP-2 emerged as the probe most deprotected by zDHHC20, paralleling the docking experiments (**Figure 4.2B, 4.3B, 4.4B, 4.5B**). Moreover, incubation with the DHHA mutant of zDHHC20, a variant lacking a

key catalytic cysteine, resulted in an 80% decrease in fluorescent signal (**Figure 4.6A**). We next measured the enzyme kinetics to elucidate the affinity of the zDHHC20/PTP-2 interaction. We determined the Km and kcat to be 24.3 μM and 0.160 s^{-1}, respectively, while the calculated kcat/Km value was 6.58 x 10^3 $M^{-1}s^{-1}$ (**Figure 4.6B,C**). These kinetic parameters are comparable to those of the natural substrate palmitoyl-CoA, suggesting that PTP-2 could indeed behave as an acyl-CoA mimic. Finally, to establish the adaptability of this assay for other DHHC family proteins, we also screened the probes against zDHHC2 and 3. Interestingly, we observed here that PTP-3, the morpholino compound, was the best substrate for these two zDHHCs (**Figure 4.5B**). Together, these data confirm the ability of the PTP fluorogenic probe family to report on the activity of DHHC family proteins *in vitro*.

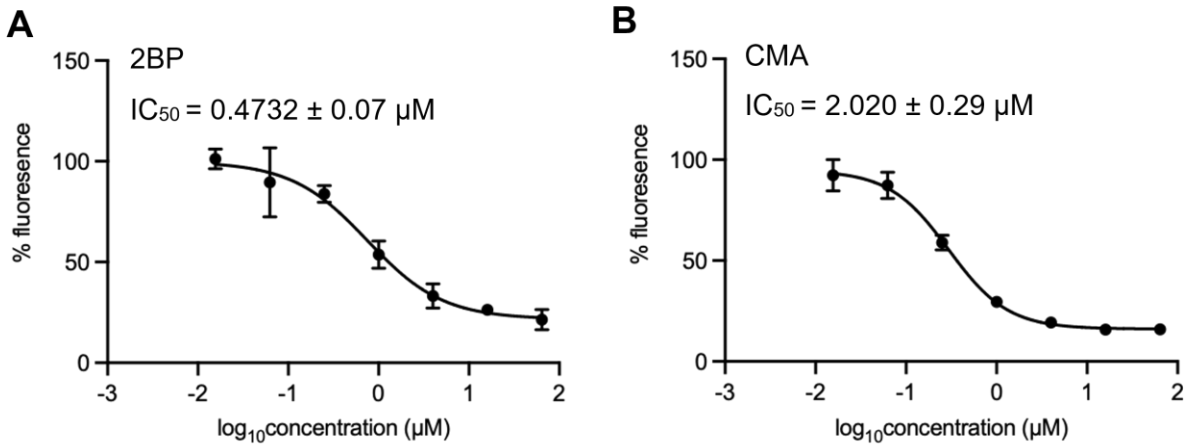

Figure 4.7 Validation of the fluorescence assay using known inhibitors. Dose-response curves of 2BP (A) and CMA (B) inhibition of zDHHC20 with a pre-incubation time of 30 min, measured by the fluorescent assay with PTP-2. The IC50 values were calculated from a four-parameter dose-response curve, and the data represented mean ± standard deviation (n = 3).

We next sought to establish the suitability of this assay for a high-throughput screen. The Z'-factor is a statistical characteristic used to evaluate the quality of an assay, with a Z'-factor > 0.5 indicating congruence with an HTS[17]. Here, evaluation of the Z'-factor during the linear reaction rate time (t = 30 min) afforded a value of 0.77 for

zDHHC20. This Z'-factor compares favorably with other published assays, including DHHC-acyl-cLIP (Z' = 0.553), and reflects the large dynamic range (~1,000 RFU) of the assay. A similarly robust Z'-factor was observed for zDHHCs 2 and 3 (t = 30 min, 0.78 and 0.83, respectively). We then confirmed the ability of this assay to detect zDHHC inhibition using known inhibitors. zDHHC2, 3, and 20 were incubated with 20 μM of either 2BP or CMA and the fluorescent readout recorded. Here, we observed that both CMA and 2BP were able to inhibit zDHHC2, 3, and 20 (**Figure 4.5C**). Specifically, CMA and 2BP were found to have IC_{50}'s of 0.463 ± 0.07 μM and 2.020 ± 0.29 μM (**Figure 4.7A,B**), respectively, comparable to those reported by the zDHHC20 acyl-cLIP assay (1.35 ± 0.26 μM and 5.33 ± 0.77 μM). These results establish the utility of the PTP-based fluorescence assay for HTS.

Having validated the compatibility of the assay for HTS, we next conducted a pilot screen. As our previous work has verified the ability of acrylamide-containing molecules to inhibit DHHC family proteins, we screened a library of 1,687 acrylamide-containing compounds in 384-well plate format at a fixed concentration of 25 μM, with CMA as a positive control and 30 minutes of pre-incubation (Figure 3A). With a threshold set for at least 30% inhibition at 25 μM, we found that 29 molecules from this library moderately inhibited zDHHC20. Re-testing 8 random molecules (Figure 3B) at 25 μM, but with an abbreviated pre-incubation time (10 min), confirmed this finding (Figure 3C). This inhibition was also cross-validated using the DHHC-acyl-cLIP assay, wherein the identified molecules showed moderate inhibition at 25 μM against zDHHC20 (Figure S8). Together, these data confirm the suitability of this assay as a high-throughput method to identify DHHC inhibitors.

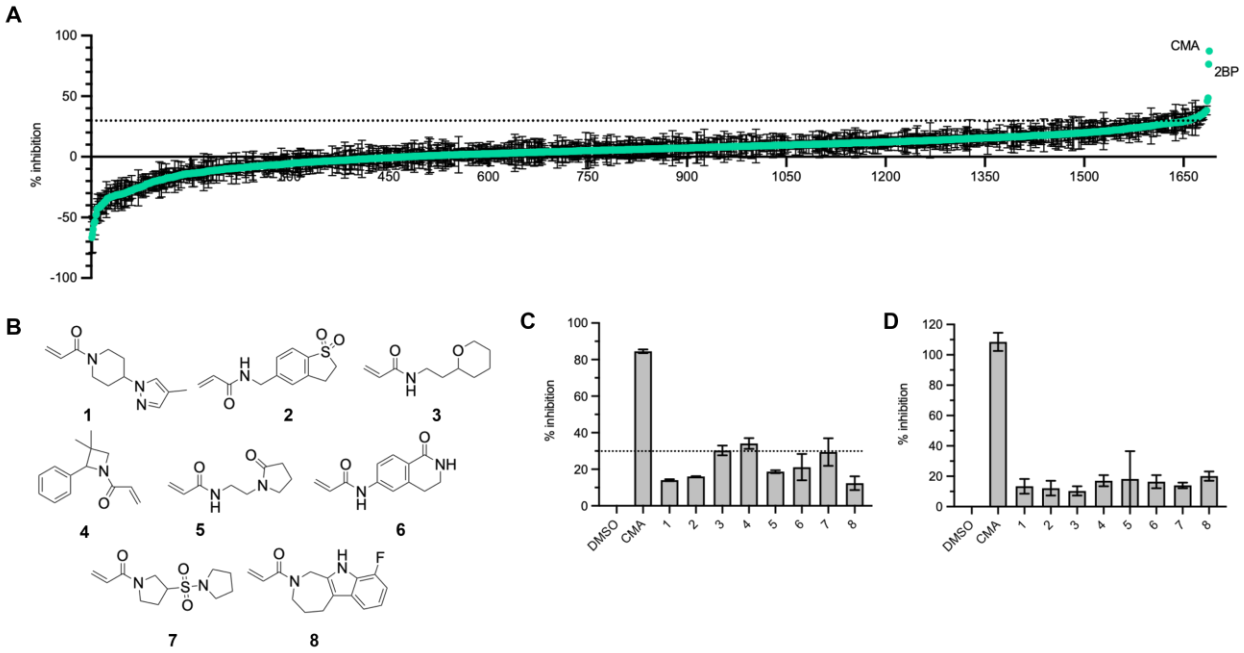

Figure 4.8 High-throughput screen of an acrylamide library against zDHHC20. (A) A 1,687-member acrylamide library was screened against zDHHC20 using PTP-2, with CMA included as a positive control. Data are presented as the mean ± standard deviation (n = 2). Hits were defined as inhibiting enzyme activity by at least 30% at 25 μM (dotted line). (B) Structures of a panel of molecules identified in the screen described in (A). (C) Re-screening of a selection of hit compounds shown in (B) against zDHHC20 using PTP-2 and with a 10 min inhibitor preincubation time. (D) Secondary validation of screening hits using a fluorescence polarization assay. Fluorescence polarization (FP) screening of selected hit compounds against zDHHC20, with activity normalized to DMSO. Data are presented as the mean ± standard deviation (n=3) in (C) and (D).

4.3 Discussion

The increasing awareness of the importance of DHHC activity in both health and disease states underscores the need for chemical inhibitors to probe the biology and therapeutic potential of these targets. However, the development of inhibitors is hindered by the limitations of current biochemical assays for DHHC activity. In this letter, we introduce a fluorescence-based assay for DHHC activity based on CoA substrate mimetics – a rare small molecule-based assay for a PTM writer protein. Using in silico modeling as a guide, we rationally designed a panel of pro-fluorescent PTPs that

capitalize on DHHC recognition of palmitoyl-CoA during the auto-acylation step of its catalytic cycle, uncaging the probe and providing a turn-on fluorescent readout of DHHC activity. The flexible and modular synthesis of the PTPs suggests that the PTP library could be easily expanded to other DHHC family members and even adapted to other transferases, such as N-myristoyltransferase family proteins (NMTs). We demonstrate that this assay is amenable to high throughput screening of zDHHC inhibitors based on the fluorescence readout, reagent cost and quantity, and excellent Z'-factors for three DHHC protein family members (0.77-0.84). As a proof-of-concept, we screened 1,687 acrylamide-based molecules against zDHHC20 in duplicate in a 384-well plate format. From this pilot screen, we identified several moderately potent, non-lipidic compounds, a selection of which were validated using DHHC-acyl-cLIP. While the activity of these compounds was limited, we anticipate that a larger HTS has the potential to identify more drug-like and perhaps isoform-selective DHHC inhibitors.

4.4 Experimental Details

General materials and methods. For biochemical and biological experiments, TCEP (UBPBio), n-Dodecyl-β-D-maltoside (DDM) (Cayman chemical) and 2-bromopalmitate (Sigma) were purchased from the sources given in parentheses. DPP-5, CMA, and RSK6 were synthesized as previously reported[8]. Docking was performed with the AutoDock Vina (v. 1.2.0). Preparation of the receptor and the ligands was done with the MGL Autodock Tools package (ADT). The human zDHHC20 structure (PDB: 6BML) without 2BP was used as the receptor. The allowed conformational space, the "docking box," was centered on the 2BP binding pocket as defined by Rana et al. (PDB: 6BML). For each

ligand, 100000 models were generated, and 20 protein-ligand complexes with lowest energy were selected for analysis. The results were analyzed with Chimera[18].

Plasmid cloning. All newly cloned plasmids were constructed by Gibson assembly from PCR products generated using Q5 Hot Start DNA Polymerase (New England Biolabs). The human DHHC2/3/20 in pCE-puro backbone was a gift from S. Bamji (University of British Columbia). Plasmid pcDNA 6.1 eGFP-GobX was a gift from M. Machner at NIH, and GobX was cloned into pET-30A containing a His6 tag at N-terminal for E. coli expression as described previously[8]. All customized primers were synthesized by Integrated DNA Technologies (IDT). All of the DHHC library plasmids and newly constructed plasmids used in this work were sequence-verified at the University of Chicago Comprehensive Cancer Center DNA Sequencing and Genotyping Facility and are available on request.

Purification of human zDHHC2, 3, and 20

Expression in Hek293T cells: HEK293T cells (~3 x 106 cells per dish) were plated in a 15 cm dish (Corning). After 24 hours, at ~70-80% confluency, cells were transfected with 33 μg of pCE-puro myc-His6-human zDHHC20 isoform 3 using PEI. Two days post transfection, cells were harvested and washed twice with DPBS.

Expression in Sf9 cells: Recombinant baculovirus encoding myc-His6-human zDHHC20 was generated by cloning myc-His6-human zDHHC20 into a pFastBac1 vector and obtained following transfection and two rounds of amplification in Sf9 cells (Novagen), as previously reported[19]. Then, 200 mL of Sf9 insect cells (2.5 x 10^6 cells/mL) were

infected with the baculovirus encoding cloning human zDHHC20. After incubation at 28 °C for 48 h, infected cells were harvested by centrifugation at 3000xg and then washed with DPBS and flash frozen until purification.

Protein Purification: Cells were lysed with the lysis buffer (50 mM Tris, 150 mM NaCl, 1 mM EDTA, 10% glycerol, 1 mM TCEP, pH 7.4 with 20 mM DDM and a protease inhibitor cocktail) and rotated end-over-end at 4 ˚C for 1 hour. After centrifugation at 12,000xg at 4℃ for 40 min, cell debris was discarded, and the cell lysate was diluted twice with DDM-free lysis buffer before incubation with Takara His60 Ni Superflow Resin (500 µL for a 15 cm dish of HEK293T cells and 3 mL for a 200 mL culture of Sf9 cells) via end-over-end rotation at 4℃ for 1 hour. The Ni resin was then washed with equilibrium buffer (10 mM imidazole, 50 mM Tris, 1 M NaCl, 20% glycerol, 10 mM TCEP, pH 7.5) and spun down at 4,000 rpm in 4℃ for 5 min. After three wash cycles, the His-tagged proteins were eluted via incubation (3x) with a column volume of elution buffer (300 mM imidazole, 50 mM Tris, 1 M NaCl, 20% glycerol, 10 mM TCEP, pH 7.5). The purity of the eluted fractions was assessed by SDS-PAGE gel electrophoresis, and the presence of each zDHHC protein was confirmed via anti-myc Western blotting. The fractions with zDHHC proteins were combined and concentrated as needed using the Amicon Ultra-4 Centrifugal Filter Unit, 10 kDa. The concentration of zDHHC 20 was determined initially by Bradford assay (Bio-Rad) and for subsequent batches, by fluorescence polarization (FP) assay. The concentrations of zDHHC2 and 3 were determined by Coomassie Blue. Purified protein was stored at -20℃ (for immediate use) or -80℃ (for long-term storage).

***In vitro* fluorescence polarization (FP) assay.** The FP assay was adopted from a previously method[8] and used to validate selected compound inhibition. Here, a 48 µl protocol with 1 hour inhibitor preincubation was used, and all inhibitors were tested at 25 µM concentration. Measurements were recorded on Synergy Neo2 Hybrid Multi-Mode Reader (BioTek Instruments, Inc.) with Dual FP Green filter cube. Fluorescence polarization (λex = 485/20 nm, λem = 528/20 nm, gain = 35, top reading with height 8.0 mm, and filter switching method) was measured at 1-min time intervals for 1 hour at 37℃. Assay data were exported in Microsoft Excel. The assay was performed in kinetics mode, and the difference taken between average values at the end (t = 114-120 min) and the beginning (t = 0-6 min) was used to determine the enzyme activity.

***In vitro* fluorescence-based palmitoyl transferase probe (PTP) assay.** PTP screening against DHHC2/3/20. To balance sensitivity, replicability, and resources (DHHC enzyme), 20 µL was determined to be the lowest tractable volume for all studies. For a 20 µL protocol, 1.5 µL of purified human zDHHC2/3/20 enzyme (with the concentration across batches normalized to FP = 40 at 1 hour) in protein storage buffer and 8.5 µL of PTP reaction buffer (PBS, with 2 µM TCEP, pH=7.4) were added to a 384-well optical bottom plate (ThermoFisher). PTP reaction buffer with protein storage buffer (total volume 10uL) was used as a blank. Then, 10 µL of 8 µM of PTPs 1-4 in PTP reaction buffer was added to initiate the reaction, resulting in a final concentration of 4 µM PTP. Fluorescence measurements (λ_{ex} = 485/20 nm, λ_{em} = 528/20 nm, gain=80, top reading with height 8.0 mm) were recorded on Synergy Neo2 Hybrid Multi-Mode Reader (BioTek Instruments,

Inc.) in kinetics mode at 10-min time intervals for 2 hours at 37℃. Assay data were exported to Microsoft Excel and analyzed using Prism 9 (GraphPad).

Known inhibitor validation. For a 20 µL protocol, 1.5 µL of purified human zDHHC2, 3, or 20 in protein storage buffer and 6.5 µL of PTP reaction buffer (PBS, with 2 µM TCEP, pH=7.4) were added to a 384-well optical bottom plate (ThermoFisher). Then, 2 µL of each 5x inhibitor stock (CMA or 2BP) in PTP reaction buffer was added, resulting in a 10 uL total volume mixture with 20 µM inhibitor. The resulting reactions were incubated in 37℃ for 1 hour. Before the addition of the PTP solution, 8 µL of 10 µM PTP (PTP-2 or PTP-3) in PTP reaction buffer was mixed with 2 µL of 5x inhibitor stock in PTP reaction buffer. This solution was added to the 384-well plate to initiate the reaction, resulting in a final PTP concentration of 4 µM while also maintaining the inhibitor concentration. To determine IC50 values, the final concentrations of each inhibitor (2BP and CMA) were 0, 0.0156, 0.0625, 0.25, 1, 4, 16, and 64 µM. Fluorescence measurements (λ_{ex} = 485/20 nm, λ_{em} = 528/20 nm, gain=80, top reading with height 8.0 mm) were recorded on Synergy Neo2 Hybrid Multi-Mode Reader (BioTek Instruments, Inc.) in kinetics model with 45-sec intervals (inhibitor validation) and 2-min time intervals (IC_{50}) for 2 hours at 37℃. Assay data were exported to Microsoft Excel and analyzed using a four-parameter dose-response curve in Prism 9 (GraphPad).

PTP kinetic parameter measurement. 1.5 µL of purified human zDHHC20 enzyme in protein storage buffer and 8.5 µL of PTP reaction buffer (PBS, with 2 µM TCEP, pH=7.4) were added to a 384-well optical bottom plate (ThermoFisher). 10 µL of PTP-2 at a range

of concentrations in PTP reaction buffer was added to initiate the reaction, resulting in 1, 2, 4, 6, 8, 16, 24, and 32 μM PTP-2 in the final reaction. Fluorescence measurements (λ_{ex} = 485/20 nm, λ_{em} = 528/20 nm, gain=80, top reading with height 8.0 mm) were recorded on Synergy Neo2 Hybrid Multi-Mode Reader (BioTek Instruments, Inc.) in kinetics model with 45-second intervals for 2 hours at 37℃. Assay data were exported in Microsoft Excel, and the initial velocity was calculated from linear regression analysis of the first 8 data points.

High-throughput screening. The chemical library (1056890-Y25) was purchased from ENAMINE, and all compounds were screened at 25 μM concentration. The step-by-step protocol can be found in Appendix 1 in this chapter.

4.5 Synthetic procedures

General materials. For chemical synthesis, reagents and solvents were purchased from commercial sources and used without further purification. Silica gel P60 (SiliCycle, 40–63 μM, 230–400 mesh) was used for column chromatography. Analytical thin-layer chromatography was performed using SiliCycle 60 F254 silica gel (pre-coated sheets, 0.25 mm thick) with detection at 214 nm. Low-resolution-mass spectral analysis and liquid chromatography analysis were carried out on an Advion Expression-L mass spectrometer (Ithaca, NY) with electron spray ionization (ESI) in the positive mode coupled to an Agilent 1220 Infinity LC System with an Agilent Poroshell 120 column (Santa Clara, CA). Automated flash column chromatography purification was carried out on a Biotage system Isolera One using SNAP Biotage columns. NMR spectra were recorded on the BRUKER

Ascend 400 at the Department of Chemistry NMR Facility, University of Chicago, for 1H-400 MHz and 13C-101 MHz measurements. Chemical shifts are given in parts per million (δ) referenced to TMS (δ = 0.00 ppm ^{1}H-, ^{13}C-NMR). Coupling constants are given in Hertz. High resolution mass spectra measurements were performed on an Agilent 6224 TOF. Using a combination of atmospheric pressure chemical ionization and electrospray ionization at the Department of Chemistry Mass Spectrometry Facility, University of Chicago.

Boc-Rhodol[13] was synthesized according to the literature.

Synthesis of 3. Compound **1** (1.05 g, 1.0 eq, 1.38 mmol) was dissolved 25 mL DCM/DMF (1:1) solution. Trityl chloride (1.65 g, 1.1 eq, 1.38 mmol) and triethylamine (1.05 g, 1.0 eq, 1.38 mmol) was added, and the solution was stirred at room temperature for 2 hours. Then the mixture was concentrated in vacuo and the crude product was dissolved in 100 mL DCM and washed with saturated $NaHCO_3$ solution and Brine. The organic phase was dried, filtered and concentrated in vacuo. The product **2** was used for the next step without further purification. NaH (1.05 g, 1.0 eq, 1.38 mmol) was suspended in 25 mL dry THF at 0 ℃ under nitrogen. Compound 2 in 10 mL dry was added dropwise. The reaction mixture was stirred for 15 min, followed by the addition of MeI (1.05 g, 1.0 eq, 1.38 mmol). The ice bath was removed after 30 min and the reaction mixture was stirred at room temperature overnight. THF was removed by rotary evaporation, and the crude product was diluted with ethyl acetate and washed with water and brine. The organic phase was dried with Na_2SO_4, filtered, and concentrated. The resultant crude product was purified

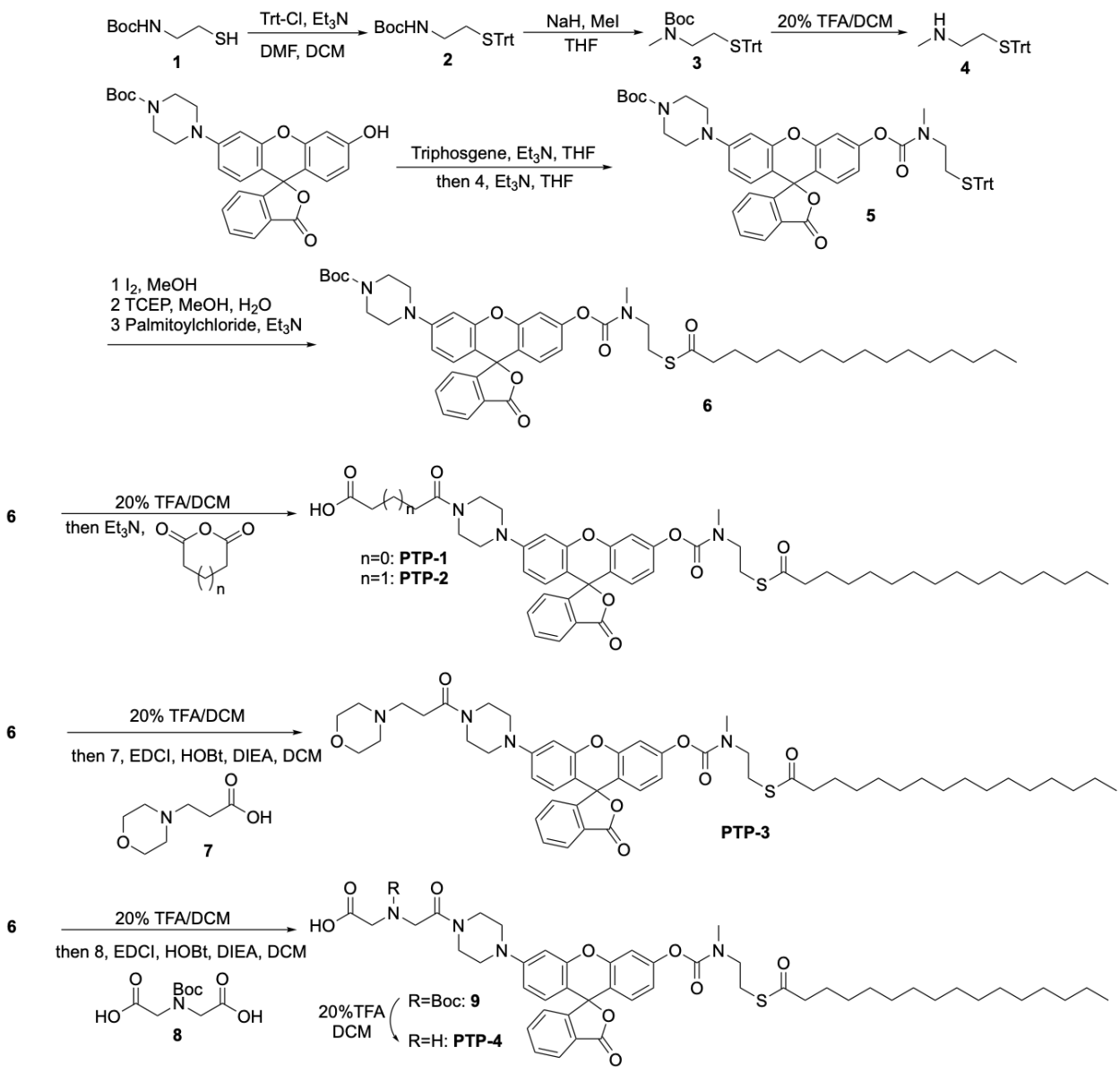

Scheme 4.2 Full synthetic scheme for PTPs.

by column chromatography (Silica; 0-100% DCM:hexane) to yield compound **3** (1.77 g, 67% over two steps) as a colorless oil. R_f: 0.61 (Silica; DCM). ^{1}H NMR (400 MHz, $CDCl_3$): δ 7.49 – 7.39 (m, 6H), 7.30 (dd, J = 8.6, 6.8 Hz, 6H), 7.25 – 7.19 (m, 3H), 3.06 (t, J = 7.5 Hz, 2H), 2.71 – 2.53 (m, 3H), 2.37 (d, J = 8.3 Hz, 2H), 1.43 (s, 9H). ^{13}C NMR (101 MHz,

$CDCl_3$): δ 155.39, 144.83, 129.65, 127.94, 126.72, 79.51, 66.74, 48.06, 34.71, 34.53, 30.23, 28.46. HRA-MS (+): Calculated for $C_{27}H_{31}NO_2S$ [M+] 433.2075; found 433.2094.

Synthesis of 4. A solution of compound **3** (1.77 g, 1.0 eq, 4.09 mmol) in 20% TFA in DCM (20 mL) was stirred for 1 hour at room temperature. Once Boc deprotection was complete, the reaction was diluted with DCM (3x 20 mL) and concentrated via rotary evaporation. The resultant crude product was purified by column chromatography (Silica; 0-10% MeOH:DCM) to yield compound **4** (1.30 g, 95%) as a white solid. R_f: 0.45 (Silica; 10% MeOH in DCM). ^{1}H NMR (400 MHz, $CDCl_3$): δ 9.16 (s, 2H), 7.47 – 7.35 (m, 6H), 7.31 – 7.23 (m, 6H), 7.23 – 7.17 (m, 3H), 2.58 (dd, J = 8.9, 6.3 Hz, 2H), 2.32 (t, J = 7.7 Hz, 2H), 2.24 (s, 3H). ^{13}C NMR (101 MHz, $CDCl_3$): δ 144.09, 129.50, 128.20, 127.07, 67.49, 47.76, 32.42, 27.08. HRA-MS (+): Calculated for $C_{22}H_{23}NS$ [M+] 333.1551; found 333.1559.

Synthesis of 5. To a solution of triphosgene (440 mg, 1 eq, 1.48 mmol) in dry THF (20 mL) at 0°C, a solution of Boc-Rhodol (740 mg, 1 eq, 1.48 mmol) with triethylamine (1.85 mL; 0.80 M in THF; 1 eq) in dry THF (10 mL) was added dropwise over 20 min. The ice bath was then replaced by a 40 °C water bath, and nitrogen was flushed through to evaporate the THF. Dry THF (20 mL) was freshly added to the reaction mixture, followed by slow addition of compound **4** (460.0 mg, 0.93 eq, 1.38 mmol) in 8 mL of THF. This was followed by the dropwise addition of triethylamine (1.76 mL; 0.80 M in THF, 0.95 eq) until the reaction was complete by LC-MS. The reaction mixture was evaporated, and the crude product was purified by column chromatography (Silica; 0-75% EtOAc:hexane) to yield compound **5** (802 mg, 65%) as light red oil. R_f: 0.61 (Silica; 50% EtOAc:hexane). ^{1}H

NMR (400 MHz, $CDCl_3$): δ 8.02 (dd, J = 7.3, 3.9 Hz, 1H), 7.70 – 7.56 (m, 2H), 7.47 – 7.38 (m, 6H), 7.34 – 7.24 (m, 6H), 7.21 (tdd, J = 7.4, 4.8, 1.5 Hz, 3H), 7.19 – 7.12 (m, 1H), 7.07 – 6.96 (m, 1H), 6.80 – 6.56 (m, 5H), 3.65 – 3.52 (m, 4H), 3.22 (q, J = 4.6 Hz, 5H), 3.12 (t, J = 7.4 Hz, 1H), 2.80 (d, J = 14.1 Hz, 3H), 2.51 (q, J = 7.0 Hz, 2H), 1.49 (s, 9H). ^{13}C NMR (101 MHz, $CDCl_3$): δ 169.48, 154.68, 153.69, 153.15, 152.81, 152.66, 152.61, 152.31, 151.95, 144.71, 144.62, 135.00, 129.73, 129.67, 129.60, 128.78, 128.38, 128.02, 127.99, 126.86, 126.79, 126.66, 125.01, 124.09, 117.47, 117.38, 116.19, 112.32, 110.34, 110.23, 109.38, 102.40, 82.88, 80.11, 67.07, 67.02, 48.90, 48.54, 48.23, 35.27, 35.20, 30.20, 29.63, 28.45.

Synthesis of 6. Compound **5** (300.0 mg, 1.0 eq, 0.35 mmol) was dissolved in 15 mL MeOH, then I_2-MeOH solution was slowly added (for 1 eq I_2, add 88.8 mg I_2 to 1 mL MeOH) until the reaction was complete by LC-MS. The reaction mixture was then quenched with a solution of 0.2 M sodium citrate and 0.2 M sodium ascorbate at pH ~3-4 until the yellow color disappeared. The quenched reaction mixture was diluted with DCM (50 mL) and washed with brine (30 mL). The aqueous layer was washed again with DCM (25 mL). The combined organic layers were dried over Na_2SO_4 and solvent was removed by rotary evaporation. The resultant crude product containing the disulfide was resuspended in 9:1 MeOH: H_2O (10 mL), and TCEP•HCl (300 mg, 3 eq, 1.05 eq) was added. The reaction mixture was stirred at room temperature for 30 min until the reaction was complete by LC-MS. The reaction mixture was diluted with 50 mL DCM and washed with brine (30 mL). The aqueous layer was washed again with DCM (25 mL). The

combined organic layers were dried over Na_2SO_4 and solvent was removed by rotary evaporation.

The resultant crude material was dissolved in 10 mL DCM, then palmitoyl chloride (320 µL, 3 eq, 1.05 mmol) was added dropwise, followed by slow addition of triethylamine until the reaction was complete by LC-MS. The reaction mixture was then diluted with 20 mL DCM and quenched with 30 mL 5% HCl. The aqueous layer was washed again with DCM (20 mL). The combined organic layers were dried over Na_2SO_4 and solvent was removed by rotary evaporation. The resultant crude product was purified by column chromatography (Silica; 0-50% EtOAc:hexane) to yield compound **6** (167 mg, 56%) as near white solid. R_f: 0.78 (Silica; 50% EtOAc:hHexane). ^{1}H NMR (400 MHz, $CDCl_3$): δ 8.05 – 7.99 (m, 1H), 7.69 – 7.56 (m, 2H), 7.15 (d, J = 7.4 Hz, 1H), 7.10 (dd, J = 5.8, 2.2 Hz, 1H), 6.86 – 6.73 (m, 2H), 6.71 – 6.63 (m, 2H), 6.60 (dd, J = 8.9, 2.4 Hz, 1H), 3.57 (t, J = 5.2 Hz, 5H), 3.49 (t, J = 7.1 Hz, 1H), 3.21 (t, J = 5.3 Hz, 4H), 3.16 – 3.10 (m, 4H), 3.05 (s, 1H), 2.56 (td, J = 7.6, 5.8 Hz, 2H), 1.64 (p, J = 7.2 Hz, 2H), 1.48 (s, 9H), 1.37 – 1.13 (m, 24H), 0.87 (t, J = 6.8 Hz, 3H). ^{13}C NMR (101 MHz, $CDCl_3$): δ 199.28, 198.93, 169.44, 154.66, 154.03, 153.76, 153.15, 152.82, 152.64, 152.29, 151.99, 134.97, 129.71, 128.88, 128.77, 128.36, 126.66, 125.01, 124.07, 117.38, 116.25, 112.30, 110.26, 110.21, 109.34, 102.38, 82.83, 80.08, 77.24, 49.16, 48.77, 48.21, 44.24, 35.51, 35.47, 31.93, 29.70, 29.67, 29.64, 29.59, 29.41, 29.36, 29.24, 28.95, 28.43, 26.92, 26.33, 25.62, 25.60, 22.70, 14.13.

Synthesis of PTP-1. A solution of compound **6** (50 mg, 1.0 eq, 58 µmol) in 20% TFA in DCM (5 mL) was stirred for 30 min at room temperature. Once Boc deprotection was

complete, the reaction was diluted with DCM (3x 5 mL) and solvent was removed by rotary evaporation. The resulting crude was suspended in DCM (5 mL) and succinic anhydride (36 mg, 420 µmol, 7.2 eq) was added, followed by slow addition of triethylamine until the reaction was completed. The reaction mix was acidified with 10 mL 1M HCl and diluted with DCM (20 mL) then washed with brine (20 mL). The aqueous layer was washed again with DCM (20 mL) and the combined organic layers were dried over Na_2SO_4 and evaporated by rotary evaporation. Purification by column chromatography (Silica; 0-10% MeOH in DCM) afforded **PTP-1** as a pink solid (40.7 mg, 81%). R_f: 0.32 (Silica; 5% MeOH:DCM). ^{1}H NMR (400 MHz, $CDCl_3$): δ 8.01 (d, J = 7.4 Hz, 1H), 7.69 – 7.56 (m, 2H), 7.15 (d, J = 7.4 Hz, 1H), 7.10 (dd, J = 6.5, 2.3 Hz, 1H), 6.82 (td, J = 8.5, 2.3 Hz, 1H), 6.76 (d, J = 8.6 Hz, 1H), 6.71 – 6.63 (m, 2H), 6.59 (dd, J = 8.9, 2.4 Hz, 1H), 3.77 (t, J = 5.2 Hz, 2H), 3.69 (s, 1H), 3.64 (t, J = 5.2 Hz, 2H), 3.57 (t, J = 7.1 Hz, 1H), 3.48 (t, J = 7.1 Hz, 1H), 3.25 (dt, J = 15.4, 5.3 Hz, 4H), 3.17 – 3.02 (m, 5H), 2.70 (tt, J = 10.5, 5.1 Hz, 4H), 2.56 (td, J = 7.5, 5.6 Hz, 2H), 1.65 (h, J = 7.0 Hz, 2H), 1.24 (s, 24H), 0.87 (t, J = 6.7 Hz, 3H). ^{13}C NMR (101 MHz, $CDCl_3$): δ 199.34, 198.99, 176.87, 176.77, 172.68, 170.30, 169.46, 154.04, 153.78, 153.08, 152.66, 152.38, 152.28, 151.93, 135.04, 129.78, 128.89, 128.86, 127.79, 126.61, 125.05, 124.05, 117.47, 117.43, 116.21, 116.18, 113.95, 112.31, 110.29, 110.24, 109.71, 102.50, 82.77, 77.37, 77.05, 76.73, 51.94, 49.18, 48.80, 48.27, 48.09, 45.00, 44.24, 44.21, 41.52, 35.52, 35.51, 31.93, 29.70, 29.69, 29.67, 29.66, 29.63, 29.58, 29.41, 29.36, 29.24, 28.95, 28.83, 28.71, 27.89, 27.08, 26.91, 26.31, 25.62, 25.60, 22.70, 14.13.

Synthesis of PTP-2. A solution of compound **6** (45.5 mg, 1.0 eq, 53 μmol) in 20% TFA in DCM (5 mL) was stirred for 30 min at room temperature. Once Boc deprotection was complete, the reaction was diluted with DCM (3x 5 mL) and solvent was removed by rotary evaporation. The resulting crude was suspended in DCM (5 mL) and glutaric anhydride (46 mg, 403 μmol, 7.6 eq) was added followed, by slow addition of triethylamine until the reaction was completed. The reaction mix was acidified with 10 mL 1M HCl and diluted with DCM (20 mL) then washed with brine (20 mL). The aqueous layer was washed again with DCM (20 mL) and the combined organic layers were dried over Na_2SO_4 and evaporated by rotary evaporation. Purification by column chromatography (Silica; 0-10% MeOH in DCM) afforded **PTP-2** as a light red oil (24.5 mg, 53%). R_f: 0.35 (Silica; 5% MeOH:DCM). ^{1}H NMR (400 MHz, $CDCl_3$): δ 8.08 – 7.97 (m, 1H), 7.71 – 7.57 (m, 2H), 7.20 – 7.07 (m, 2H), 6.91 – 6.71 (m, 2H), 6.71 – 6.67 (m, 1H), 6.65 (s, 0H), 6.60 (dd, J = 8.9, 2.4 Hz, 1H), 4.19 – 3.94 (m, 1H), 3.77 (q, J = 4.5 Hz, 1H), 3.69 – 3.53 (m, 2H), 3.53 – 3.45 (m, 1H), 3.35 (s, 1H), 3.24 (dt, J = 11.4, 5.3 Hz, 4H), 3.20 – 3.08 (m, 3H), 3.05 (s, 1H), 2.56 (td, J = 7.5, 5.4 Hz, 2H), 2.46 (q, J = 7.5 Hz, 4H), 1.99 (p, J = 7.4 Hz, 2H), 1.63 (dd, J = 13.2, 5.6 Hz, 2H), 1.24 (t, J = 2.8 Hz, 24H), 0.87 (t, J = 6.7 Hz, 3H), 0.84 (s, 1H). ^{13}C NMR (101 MHz, $CDCl_3$): δ 198.98, 171.03, 169.46, 153.09, 152.65, 152.44, 152.29, 151.94, 135.03, 129.77, 128.86, 127.80, 126.62, 125.05, 124.05, 117.46, 116.22, 113.95, 112.31, 109.70, 102.50, 82.77, 77.23, 55.99, 48.80, 48.46, 48.17, 45.12, 44.23, 41.28, 35.52, 32.01, 31.93, 29.70, 29.67, 29.64, 29.59, 29.41, 29.36, 29.24, 28.95, 26.90, 26.31, 25.60, 22.70, 20.13, 14.13.

Synthesis of PTP-3. A solution of compound **6** (57.7 mg, 1.0 eq, 67 μmol) in 20% TFA in DCM (5 mL) was stirred for 30 min at room temperature. Once Boc deprotection was complete, the reaction was diluted with DCM (3x 5 mL) and solvent was removed by rotary evaporation. A solution of 7 (51 mg, 4.8 eq, 0.32 mmol), EDCI (61 mg, 4.8 eq, 0.32 mmol), HOBt (43 mg, 4.8 eq, 0.32 mmol) and triethylamine (18.0 μL, 2.0 eq, 0.13 mmol) in 10 mL dry DCM was stirred at room temperature for 10 min. Then the deprotected 6 in 5 mL of DCM was transferred to the reaction and stirred at room temperature until the reaction was complete by LC-MS. The reaction was then diluted with 30 mL of DCM and washed with Sat. $NaHCO_3$. The aqueous layer was washed again with 20 mL DCM, and the combined organic layers were dried with Na_2SO_4, filtered, and concentrated. The resultant crude product was purified by column chromatography (Silica; 0-8% MeOH:DCM) to yield PTP-3 (35.7 mg, 59%) as colorless oil. R_f: 0.44 (Silica; 5% MeOH:DCM). ^1H NMR (400 MHz, $CDCl_3$): δ 8.05 – 7.98 (m, 1H), 7.67 – 7.58 (m, 2H), 7.15 (d, J = 7.4 Hz, 1H), 7.12 – 7.07 (m, 1H), 6.85 – 6.79 (m, 1H), 6.76 (dd, J = 8.7, 1.3 Hz, 1H), 6.71 – 6.64 (m, 2H), 6.60 (dd, J = 8.9, 2.4 Hz, 1H), 3.76 (d, J = 6.0 Hz, 2H), 3.74 – 3.68 (m, 4H), 3.63 (d, J = 5.5 Hz, 2H), 3.57 (t, J = 7.1 Hz, 1H), 3.49 (t, J = 7.1 Hz, 1H), 3.24 (dt, J = 11.8, 5.3 Hz, 4H), 3.17 – 3.08 (m, 3H), 3.05 (s, 1H), 2.75 (dd, J = 8.5, 6.5 Hz, 2H), 2.57 (ddd, J = 10.7, 7.8, 5.7 Hz, 4H), 2.50 (t, J = 4.7 Hz, 4H), 1.70 – 1.59 (m, 3H), 1.24 (t, J = 2.5 Hz, 24H), 0.87 (t, J = 6.8 Hz, 3H). ^{13}C NMR (101 MHz, $CDCl_3$): δ 199.28, 198.93, 170.10, 169.41, 156.28, 154.01, 153.74, 153.09, 152.67, 152.45, 152.30, 151.94, 143.66, 135.01, 129.76, 128.89, 128.86, 127.79, 126.63, 125.04, 124.05, 117.46, 117.41, 116.21, 113.94, 112.29, 110.27, 110.22, 109.75, 102.49, 82.72, 77.24, 68.78, 68.68, 66.90, 54.46, 53.77, 49.18, 48.79, 48.53, 48.20, 45.16, 44.24, 44.21, 41.74, 41.18, 35.52,

35.49, 31.93, 31.03, 30.72, 29.70, 29.69, 29.66, 29.63, 29.58, 29.41, 29.36, 29.24, 28.95, 26.91, 26.32, 25.62, 25.60, 22.70, 14.13.

Synthesis of PTP-4. A solution of compound **6** (59.5 mg, 1.0 eq, 69 μmol) in 20% TFA in DCM (5 mL) was stirred for 30 min at room temperature. Once Boc deprotection was complete, the reaction was diluted with DCM (3x 5 mL) and solvent was removed by rotary evaporation. A solution of 8 (97 mg, 6.0 eq, 0.41 mmol), EDCI (61 mg, 4.6 eq, 0.32 mmol), HOBt (43 mg, 4.6 eq, 0.32 mmol) and triethylamine (19.0 μL, 2.0 eq, 0.13 mmol) in 10 mL dry DCM was stirred at room temperature for 10 min. Then the deprotected 6 in 5 mL of DCM was transferred to the reaction and stirred at room temperature until the reaction was complete by LC-MS. The reaction was then diluted with 30 mL of DCM and washed with 5% HCl. The aqueous layer was washed again with 20 mL DCM, and the combined organic layers were dried with Na_2SO_4, filtered, and concentrated. The resultant crude product was purified by column chromatography (Silica; 0-8% MeOH:DCM) to yield **9** (42.3 mg, 63%) as red oil. R_f: 0.41 (Silica; 5% MeOH:DCM). ^{1}H NMR (400 MHz, $CDCl_3$): δ 8.04 – 7.98 (m, 1H), 7.70 – 7.57 (m, 2H), 7.18 – 7.07 (m, 2H), 6.87 – 6.71 (m, 2H), 6.71 – 6.63 (m, 2H), 6.57 (dd, J = 8.9, 2.5 Hz, 1H), 4.25 (s, 2H), 4.19 – 4.03 (m, 1H), 3.91 (s, 2H), 3.80 (dq, J = 6.2, 3.3 Hz, 2H), 3.63 – 3.52 (m, 3H), 3.47 (q, J = 7.7 Hz, 1H), 3.37 – 3.20 (m, 5H), 3.17 – 3.07 (m, 3H), 3.05 (s, 1H), 2.56 (td, J = 7.5, 5.5 Hz, 2H), 1.71 – 1.59 (m, 2H), 1.45 (s, 9H), 1.25 (q, J = 4.1 Hz, 24H), 0.87 (t, J = 6.7 Hz, 3H). ^{13}C NMR (101 MHz, $CDCl_3$): δ 199.27, 198.93, 170.89, 169.91, 169.39, 156.28, 154.77, 154.23, 153.99, 153.72, 152.97, 152.73, 152.30, 152.27, 152.09, 151.87, 135.10, 129.85, 128.91, 127.79, 126.58, 125.07, 124.04, 117.57, 117.53, 116.16, 113.94, 112.38,

110.32, 110.28, 110.01, 102.66, 82.72, 82.69, 81.98, 77.25, 68.66, 55.99, 53.81, 50.84, 49.20, 48.81, 47.96, 47.88, 44.46, 44.24, 44.21, 42.37, 41.73, 35.52, 31.92, 31.03, 29.69, 29.67, 29.65, 29.63, 29.58, 29.41, 29.36, 29.23, 28.94, 28.16, 28.04, 26.90, 26.30, 25.61, 25.59, 22.69, 14.13.

A solution of compound **9** (9.7 mg) in 20% TFA in DCM (5 mL) was stirred for 30 min at room temperature. Once Boc deprotection was complete, the reaction was diluted with DCM (3x 5 mL) and solvent was removed by rotary evaporation. The residue was dissolved in 970 µL DMSO to make 10 mM **PTP-4** stock solution.

4.6 References

(1) Swarthout, J. T.; Lobo, S.; Farh, L.; Croke, M. R.; Greentree, W. K.; Deschenes, R. J.; Linder, M. E. DHHC9 and GCP16 constitute a human protein fatty acyltransferase with specificity for H- and N-Ras. *The Journal of biological chemistry* **2005**, *280* (35), 31141–31148.

(2) Remsberg, J. R.; Suciu, R. M.; Zambetti, N. A.; Hanigan, T. W.; Firestone, A. J.; Inguva, A.; Long, A.; Ngo, N.; Lum, K. M.; Henry, C. L.; Richardson, S. K.; Predovic, M.; Huang, B.; Dix, M. M.; Howell, A. R.; Niphakis, M. J.; Shannon, K.; Cravatt, B. F. ABHD17 regulation of plasma membrane palmitoylation and N-Ras-dependent cancer growth. *Nature chemical biology* **2021**, *17* (8), 856–864.

(3) Lin, D. T. S.; Conibear, E. ABHD17 proteins are novel protein depalmitoylases that regulate N-Ras palmitate turnover and subcellular localization. *eLife* **2015**, *4*, e11306.

(4) Zhang, M.; Zhou, L.; Xu, Y.; Yang, M.; Xu, Y.; Komaniecki, G. P.; Kosciuk, T.; Chen, X.; Lu, X.; Zou, X.; Linder, M. E.; Lin, H. A STAT3 palmitoylation cycle promotes TH17 differentiation and colitis. *Nature* **2020**, *586* (7829), 434–439.

(5) Kharbanda, A.; Walter, D. M.; Gudiel, A. A.; Schek, N.; Feldser, D. M.; Witze, E. S. Blocking EGFR palmitoylation suppresses PI3K signaling and mutant KRAS lung tumorigenesis. *Science signaling* **2020**, *13* (621).

(6) Runkle, K. B.; Kharbanda, A.; Stypulkowski, E.; Cao, X.-J.; Wang, W.; Garcia, B. A.; Witze, E. S. Inhibition of DHHC20-Mediated EGFR Palmitoylation Creates a Dependence on EGFR Signaling. *Molecular cell* **2016**, *62* (3), 385–396.

(7) Davda, D.; El Azzouny, M. A.; Tom, C. T. M. B.; Hernandez, J. L.; Majmudar, J. D.; Kennedy, R. T.; Martin, B. R. Profiling targets of the irreversible palmitoylation inhibitor 2-bromopalmitate. *ACS chemical biology* **2013**, *8* (9), 1912–1917.

(8) Azizi, S.-A.; Lan, T.; Delalande, C.; Kathayat, R. S.; Banales Mejia, F.; Qin, A.; Brookes, N.; Sandoval, P. J.; Dickinson, B. C. Development of an Acrylamide-Based Inhibitor of Protein S-Acylation. *ACS chemical biology* **2021**, *16* (8), 1546–1556.

(9) Hong, J. Y.; Malgapo, M. I. P.; Liu, Y.; Yang, M.; Zhu, C.; Zhang, X.; Tolbert, P.; Linder, M. E.; Lin, H. High-Throughput Enzyme Assay for Screening Inhibitors of the ZDHHC3/7/20 Acyltransferases. *ACS chemical biology* **2021**, *16* (8), 1318–1324.

(10) Lanyon-Hogg, T.; Ritzefeld, M.; Sefer, L.; Bickel, J. K.; Rudolf, A. F.; Panyain, N.; Bineva-Todd, G.; Ocasio, C. A.; O'Reilly, N.; Siebold, C.; Magee, A. I.; Tate, E. W. Acylation-coupled lipophilic induction of polarisation (Acyl-cLIP): a universal assay for lipid transferase and hydrolase enzymes. *Chemical science* **2019**, *10* (39), 8995–9000.

(11) Stix, R.; Lee, C.-J.; Faraldo-Gómez, J. D.; Banerjee, A. Structure and Mechanism of DHHC Protein Acyltransferases. *Journal of molecular biology* **2020**, *432* (18), 4983–4998.

(12) Azizi, S.-A.; Kathayat, R. S.; Dickinson, B. C. Activity-Based Sensing of S-Depalmitoylases: Chemical Technologies and Biological Discovery. *Accounts of chemical research* **2019**, *52* (11), 3029–3038.

(13) Qiu, T.; Kathayat, R. S.; Cao, Y.; Beck, M. W.; Dickinson, B. C. A Fluorescent Probe with Improved Water Solubility Permits the Analysis of Protein S-Depalmitoylation Activity in Live Cells. *Biochemistry* **2018**, *57* (2), 221–225.

(14) Rana, M. S.; Kumar, P.; Lee, C.-J.; Verardi, R.; Rajashankar, K. R.; Banerjee, A. Fatty acyl recognition and transfer by an integral membrane S-acyltransferase. *Science (New York, N.Y.)* **2018**, *359* (6372).

(15) Trott, O.; Olson, A. J. AutoDock Vina: improving the speed and accuracy of docking with a new scoring function, efficient optimization, and multithreading. *Journal of computational chemistry* **2010**, *31* (2), 455–461.

(16) Lee, C.-J.; Stix, R.; Rana, M. S.; Shikwana, F.; Murphy, R. E.; Ghirlando, R.; Faraldo-Gómez, J. D.; Banerjee, A. Bivalent recognition of fatty acyl-CoA by a human integral membrane palmitoyltransferase. *Proceedings of the National Academy of Sciences of the United States of America* **2022**, *119* (7).

(17) Zhang; Chung; Oldenburg. A Simple Statistical Parameter for Use in Evaluation and Validation of High Throughput Screening Assays. *Journal of biomolecular screening* **1999**, *4* (2), 67–73.

(18) Pettersen, E. F.; Goddard, T. D.; Huang, C. C.; Couch, G. S.; Greenblatt, D. M.; Meng, E. C.; Ferrin, T. E. UCSF Chimera--a visualization system for exploratory research and analysis. *Journal of computational chemistry* **2004**, *25* (13), 1605–1612.

(19) Malgapo, M. I. P.; Linder, M. E. Purification of Recombinant DHHC Proteins Using an Insect Cell Expression System. *Methods in molecular biology (Clifton, N.J.)* **2019**, *2009*, 179–189.

Appendix 1 to Chapter 4: Protocol for PTP-based HTS screen

Notes:

1. The concentration of purified protein can differ among batches; we normalized the concentration to FP=40 (60 min.) for zDHHC20.
2. We suggest including a known inhibitor, such as 2BP or CMA, as a positive control.
3. The recommended 384-well plate layouts for both automated and manual HTS screens are shown at the end of each protocol.

Reagent Preparation

- PTP reaction buffer (1x PBS, 2 μM TCEP, pH=7.4)
- PTP stock solution: 5 mM in DMSO
- 5 mM stocks of library compounds and positive control

Manually HTS screening

1. Determine plate layout (see Plates 1&2)
2. Prepare Master Mix I (MMI): PTP reaction buffer and purified zDHHC enzyme: N samples, two replicates each
    1) Measure enzyme (1.5 μL/reaction): 1.5*(2*(N+8)) μL
    2) Measure buffer (6.5 uL/reaction): 6.5*(2*(N+8)) μL
    3) Add the calculated amount of enzyme (a) into the calculated amount of buffer; (b) mix well, and store on ice.
3. Dilute inhibitors into reaction buffer (note: we found a 96 well plate is superior for solution preparation).
    1) Determine the 96 well plate layout (see Plate 3)

2) Add 117 µL of PTP reaction buffer to each well of 96-well plate A.
3) Add 3 µL 5 mM stock solution of inhibitor/control into the appropriate well to give 25 µM solutions, mixing well; for the negative control, DMSO is added instead.

4. Add 8 µL MMI into the experimental wells of the 384-well plate. For the PTP-only blank well, add 8 µL PTP reaction buffer instead.
5. Using a 10 µL multichannel pipette, transfer 2 µL inhibitor solution from 96 well plate A to the 384-well plate, mixing once. Place the 384-well plate at 37 ˚C for 30 min. of preincubation.
6. Prepare Master Mix II (MMII): PTP and inhibitor solution
    1) Dilute 6 µL of 5 mM PTP stock solution into 3 mL PTP reaction buffer to give a 10 µM PTP solution. Add 2 µL DMSO into 1 mL PTP reaction buffer to give a DMSO control solution.
    2) Add 30 µL of the 10 µM PTP solution to each well in 96 well plate B, using 30 µL DMSO control solution for the well with the enzyme-only blank.
    3) Add 7.5 µL of inhibitor solution or DMSO to corresponding wells to make MMIII MMII contains 8 µM PTP and 25 µM inhibitor.
7. Using 10 µL multichannel pipette, transfer 10 µL of MMII from 96 well plate B to the 384-well plate and mix once. Place plate into plater reader (Synergy Neo2 Hybrid Multi-Mode Reader, BioTek Instruments) immediately.
8. Record fluorescence measurements (λex = 485/20 nm, λem = 528/20 nm, gain=80, from the top with height 8.0 mm) in kinetics model with 10-min time intervals for 2 hours at 37 ˚C and export data to Microsoft Excel.

Plate 1: 384-well plate, screening layout – manual

- A1/A24/P1/P24: positive control
- C1/C24/N1/N24: DMSO
- E1/E24/L1/L24: no enzyme
- G1/G24/J1/J24: no PTP
- A2-A23/C2-C23/E2-E23/G2-G23/I2-I23/K2-K23/M2-M23/O2-O23: Test region
- Compounds screened (considering positive control, DMSO, and blank wells):

  2 Replicates: 86 compounds/plate

  3 Replicates: 58 compounds/plate

Note that we observed manual multichannel pipetting was more reliable than electronic

Plate 2: 384-well plate, screening layout – automatic

- A1/A24/P1/P24: positive control
- A2/A23/P2/P23: DMSO
- A3/A22/P3/P22: no enzyme
- A4/A21/P4/P21: no PTP
- B1-O24: Test region
- Compounds screened (considering positive control, DMSO, and blank wells):

  2 Replicates: 166 compounds/plate

  3 Replicates: 110 compounds/plate

Plate 3: 96-well plate A, dilution of library compounds

In a 96 well plate, A1-H11 contain inhibitors to be tested. The well labels correspond to the inhibitor's final position in the 384-well plate.

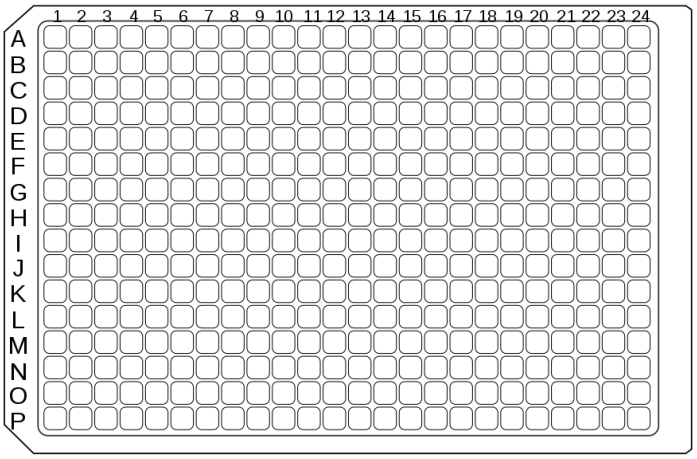

Plates 1&2

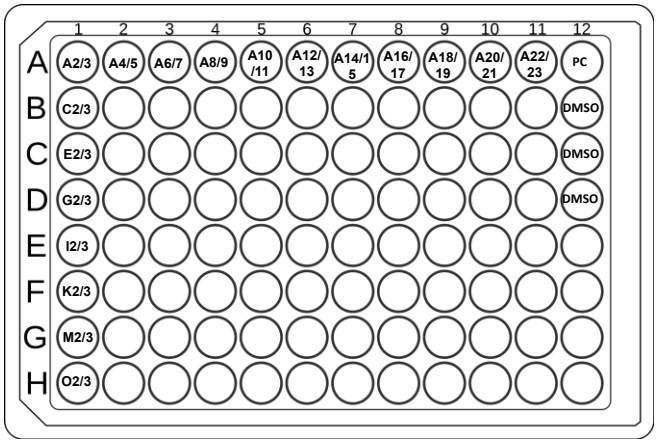

Plate 3

Appendix 2 to Chapter 4: NMR Spectra

Compound 3

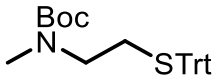

^{1}H-NMR (400 MHz; $CDCl_3$)

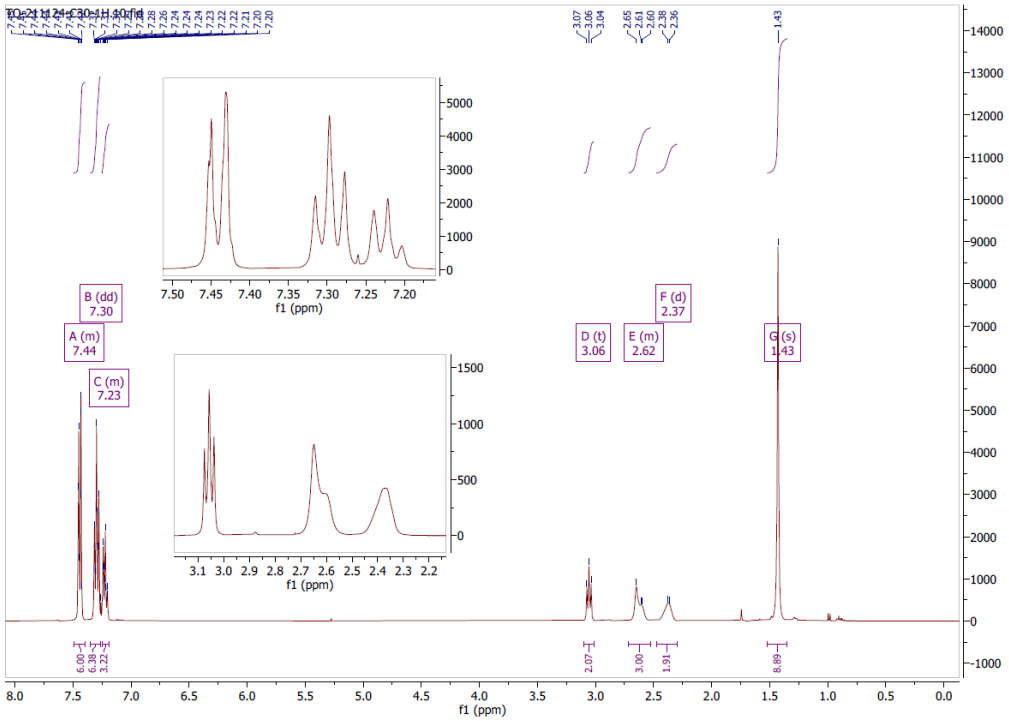

^{13}C-NMR (101 MHz; $CDCl_3$)

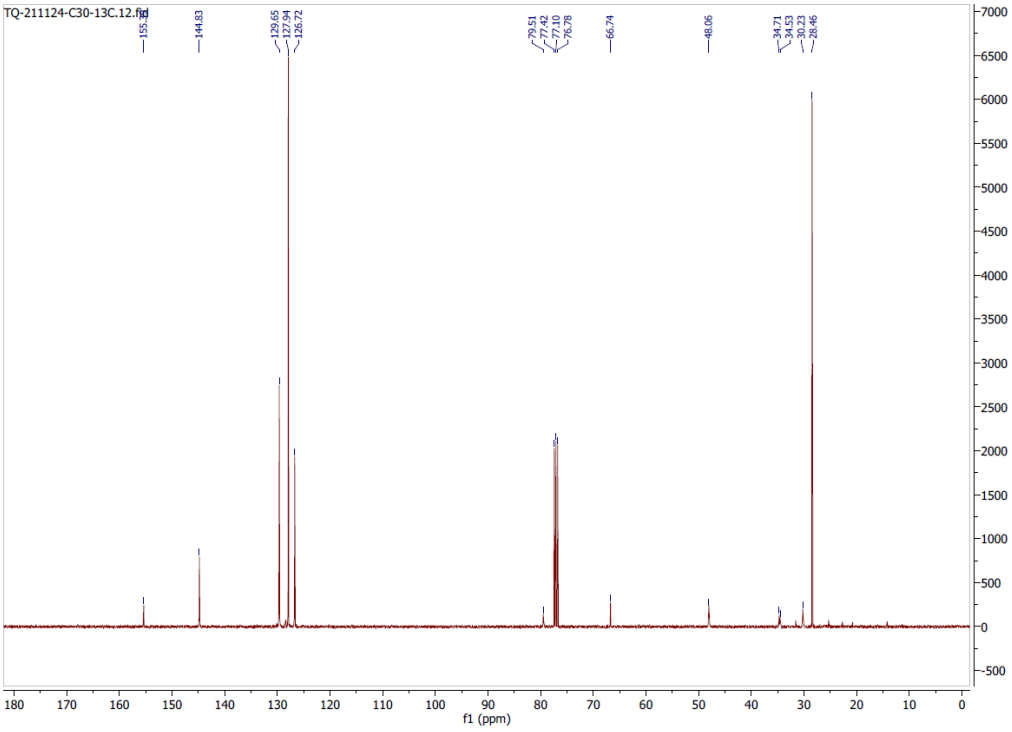

Compound 4

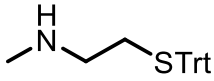

^{1}H-NMR (400 MHz; $CDCl_3$)

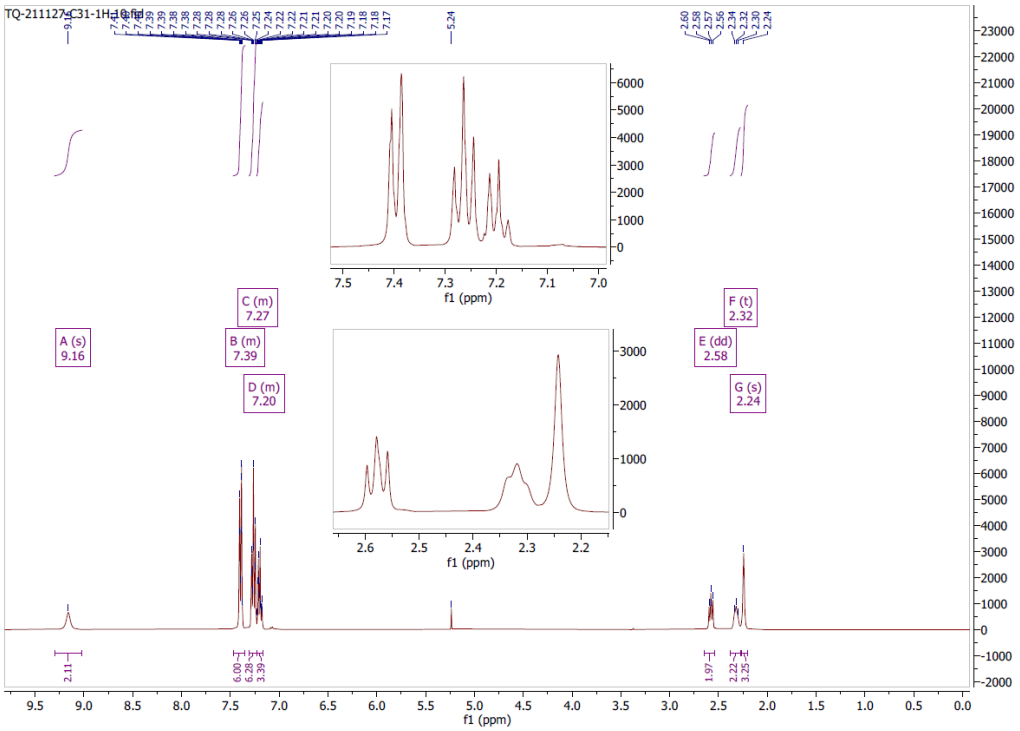

^{13}C-NMR (101 MHz; $CDCl_3$)

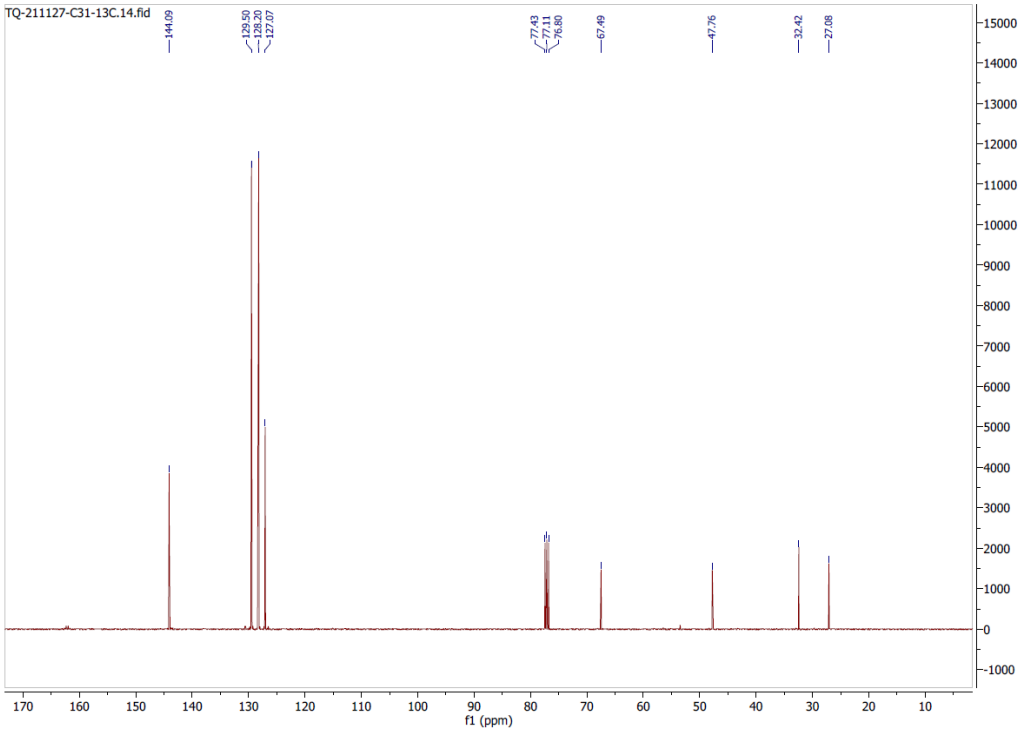

Compound 5

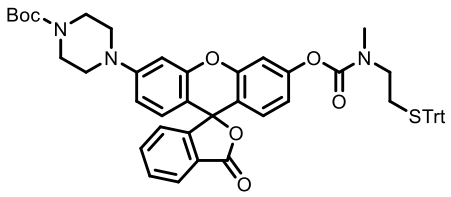

^{1}H-NMR (400 MHz; $CDCl_3$)

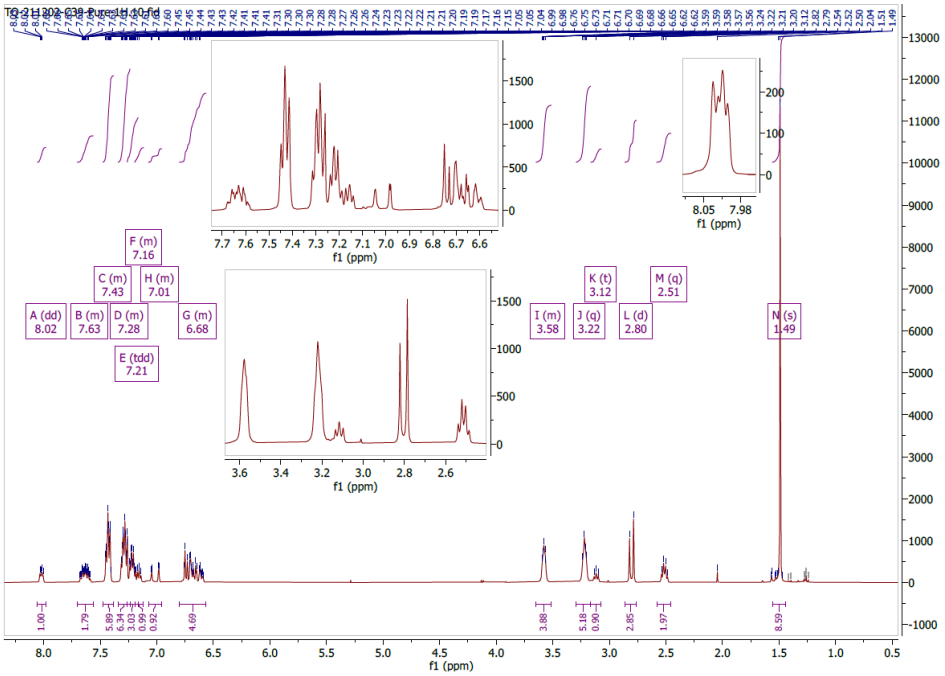

^{13}C-NMR (101 MHz; $CDCl_3$)

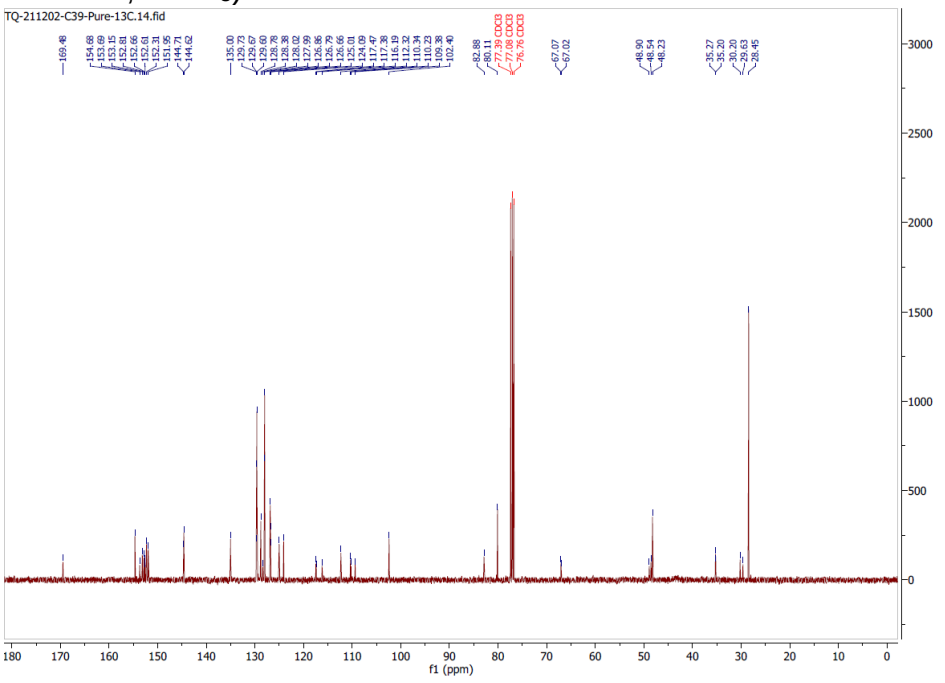

Compound 6

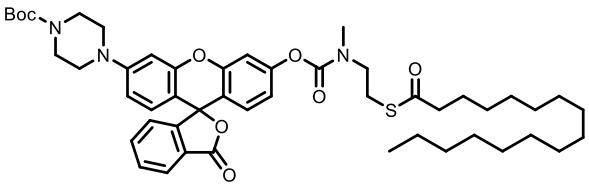

^{1}H-NMR (400 MHz; $CDCl_3$)

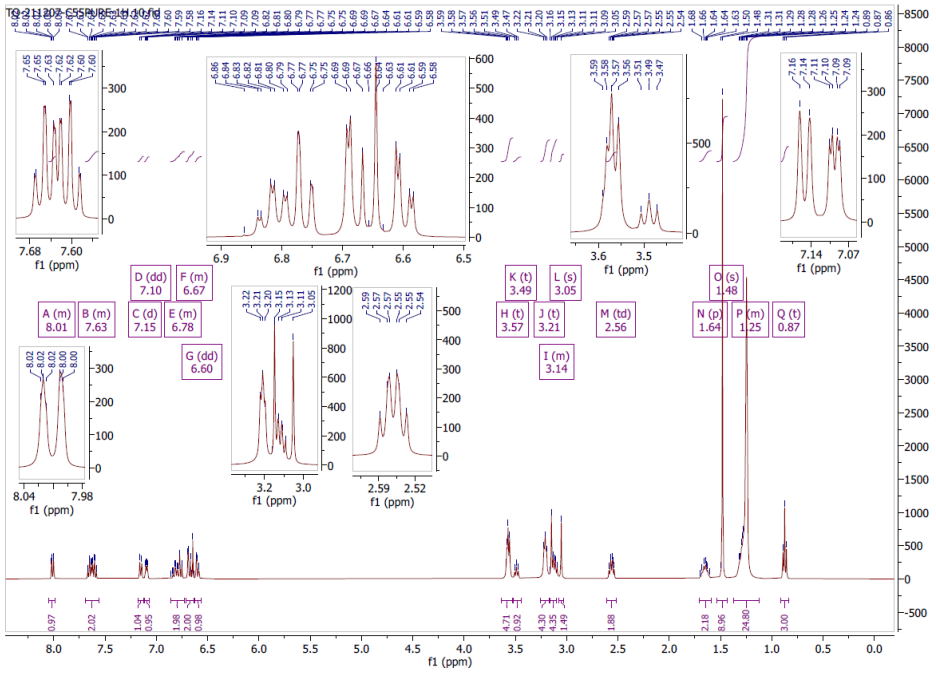

^{13}C-NMR (101 MHz; $CDCl_3$)

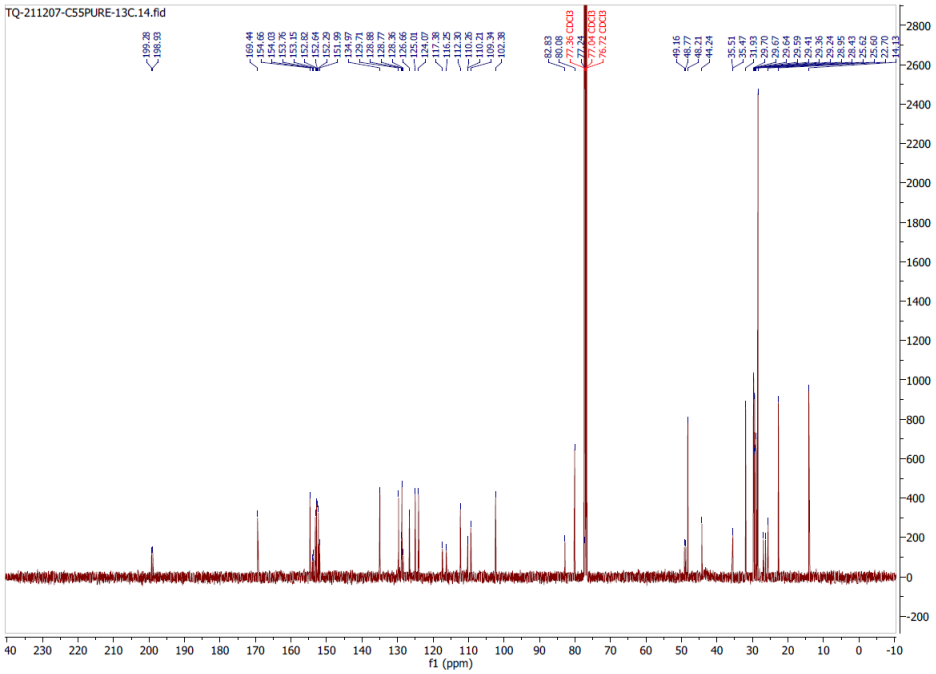

PTP-1

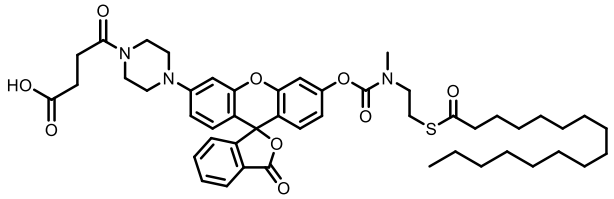

^{1}H-NMR (400 MHz; $CDCl_3$)

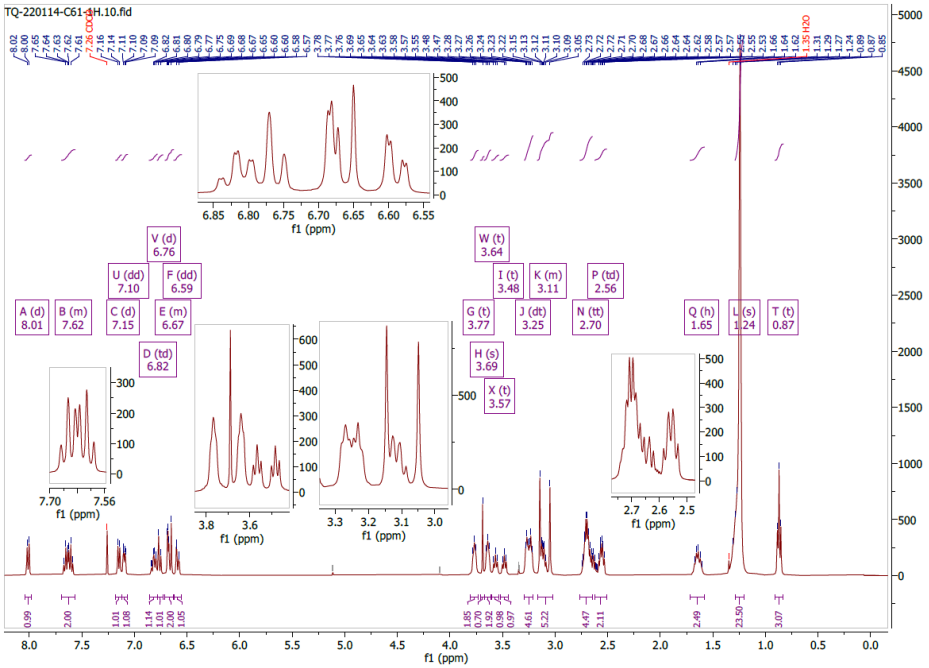

^{13}C-NMR (101 MHz; $CDCl_3$)

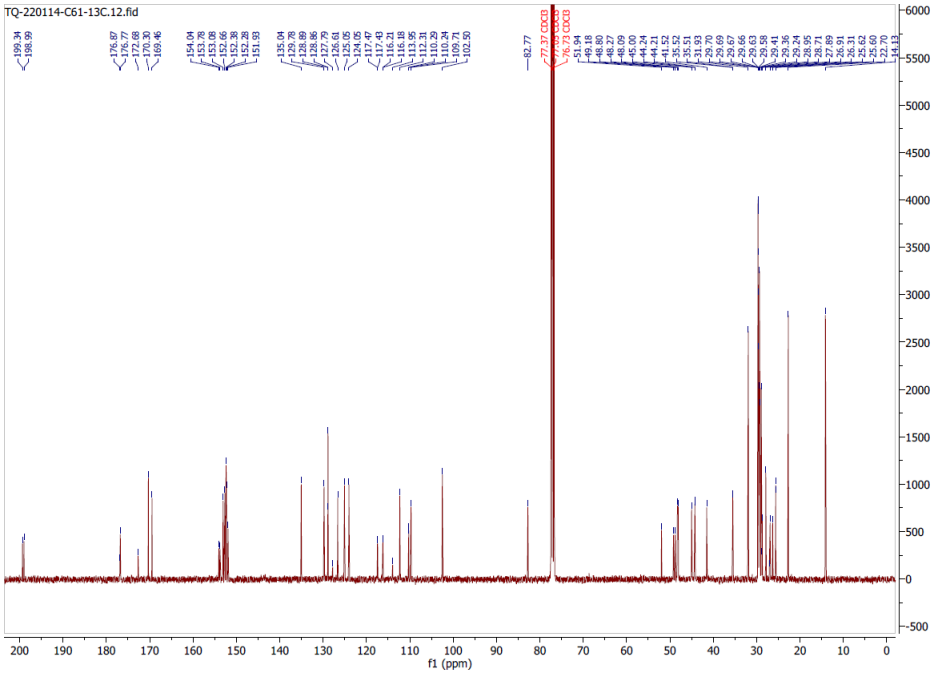

PTP-2

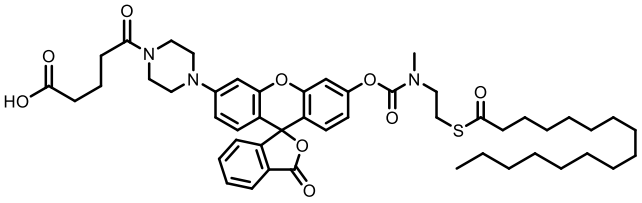

^{1}H-NMR (400 MHz; $CDCl_3$)

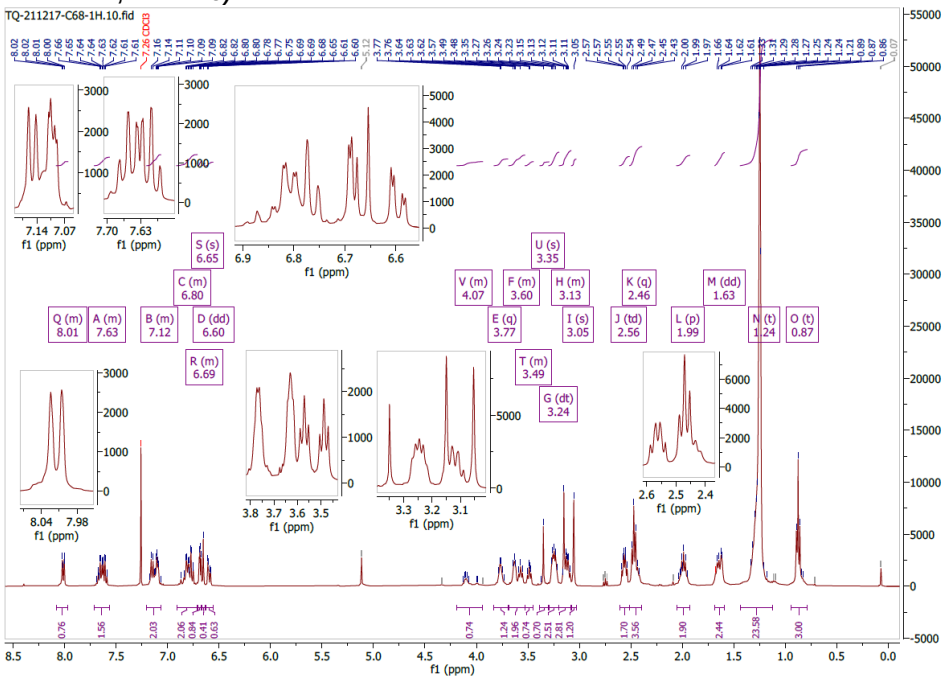

^{13}C-NMR (101 MHz; $CDCl_3$)

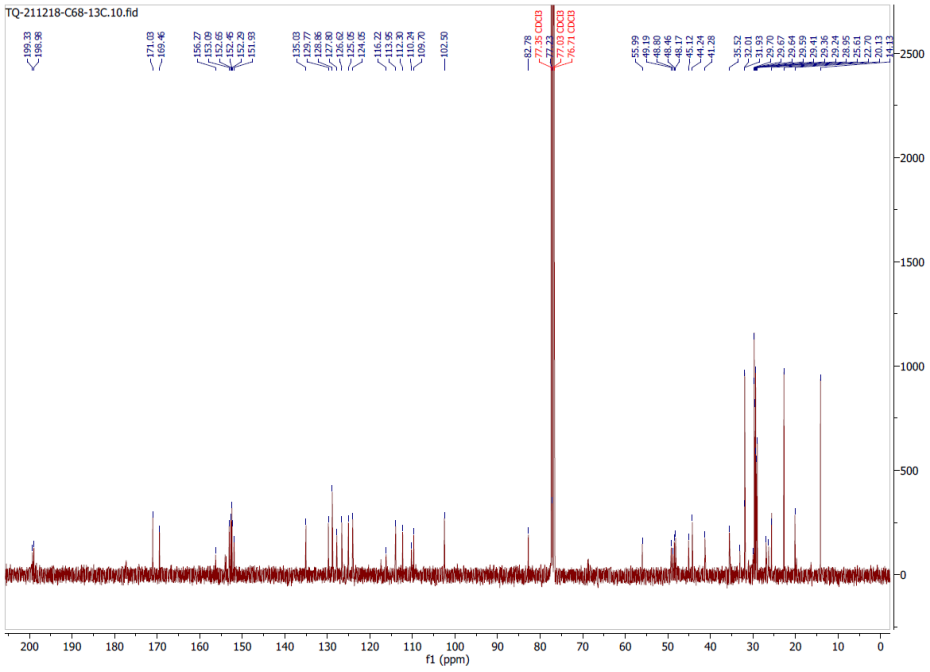

PTP-3

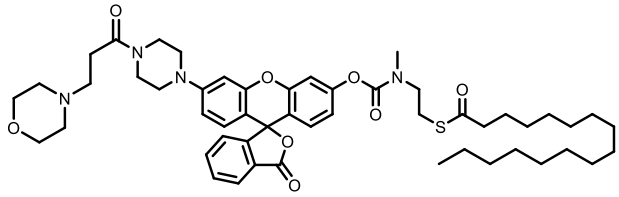

^{1}H-NMR (400 MHz; $CDCl_3$)

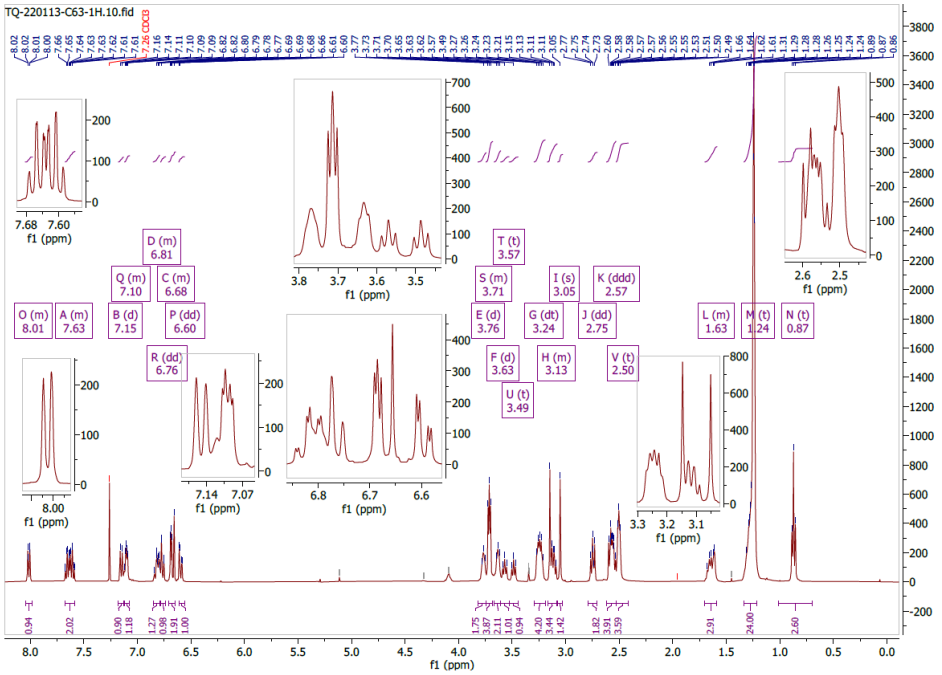

^{13}C-NMR (101 MHz; $CDCl_3$)

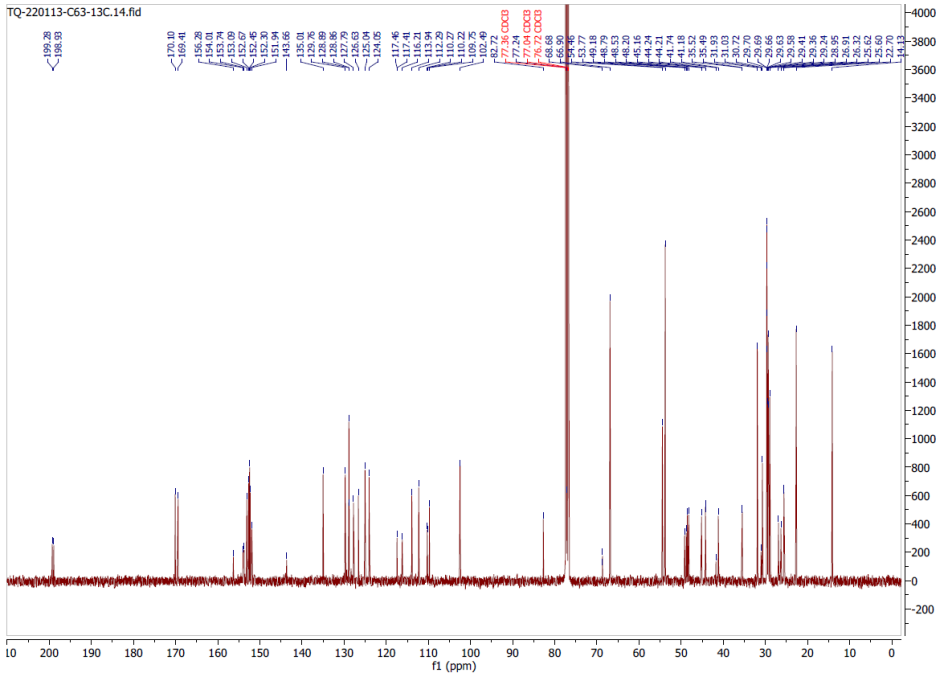

Compound 9

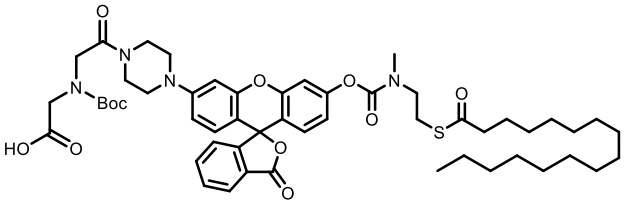

^{1}H-NMR (400 MHz; $CDCl_3$)

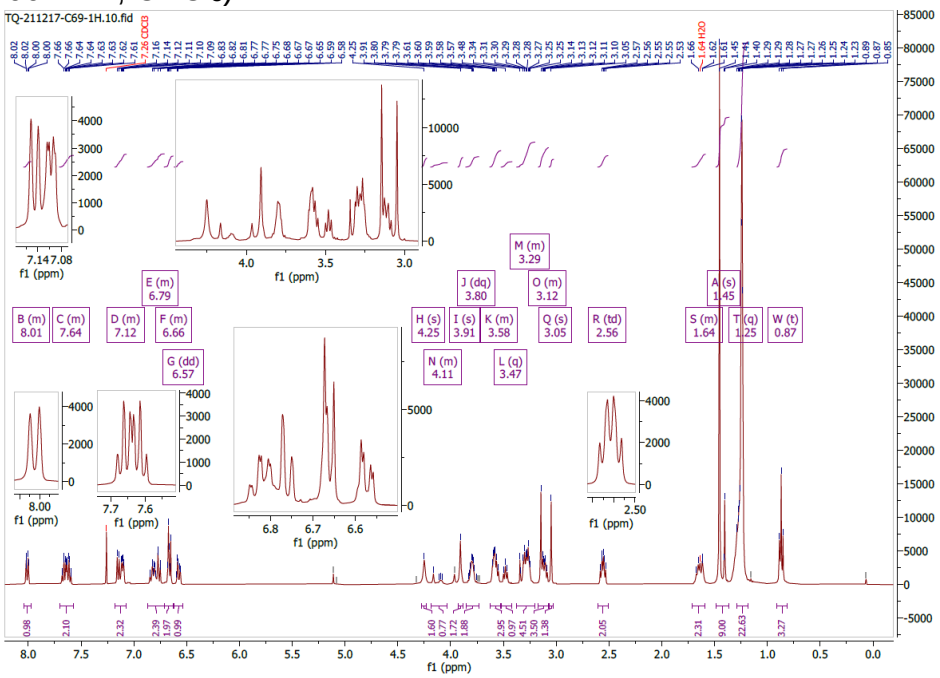

^{13}C-NMR (101 MHz; $CDCl_3$)

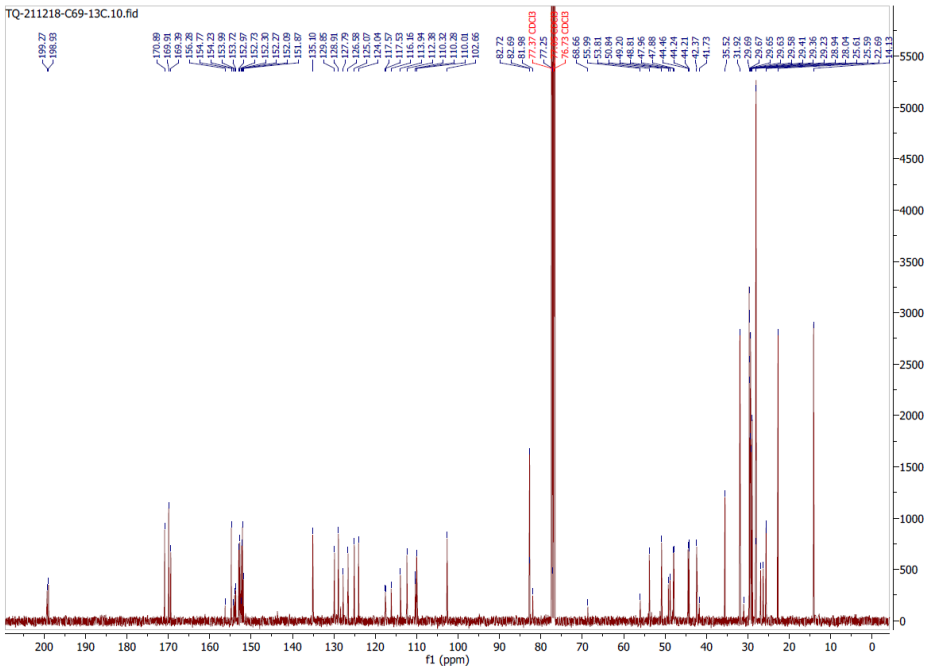

CHAPTER 5

THIOESTER-BASED ACYLATION REAGENT WITH AN ESTER CAGE

5.1 Introduction

Cellular functions are tightly regulated by proteins, nucleic acids and their interactions, including protein–protein interactions (PPIs), protein–RNA interactions and protein–DNA interactions[1,2]. Molecular interaction networks play an important role in most biological processes, while their dysfunction has been linked to a wide range of human diseases, such as cancers, immune system disorders, and neurological disorders. As a result, methods for determining the subcellular organization and localization of these biopolymers have increased in scope and demand[3].

Proximity labeling was developed to provide a novel complementary approach to traditional methods, such as affinity purification[4] and yeast two-hybrid assay[5], for mapping molecular interactions in living cells[6]. Proximity labeling is conceptually based upon the idea of delivering a “catalyst”, most often an enzyme, to a protein or region of interest in a cell to catalyze the conversion of an inert small-molecule substrate to short-lived reactive intermediates, such as radical or activated ester, that can diffuse out from the catalyst active site to covalently tag endogenous biomolecules within a narrow radius[7]. The substrate molecule typically contains functional handles, such as azides or biotins, to enable subsequent enrichment of labeled biomolecules using streptavidin beads and their identification by mass spectrometry (for proteins) or nucleic acid sequencing (for RNA). The labeling radius is determined by both the half-life (usually 1–10 nm in living cells)[8,9] of the reactive intermediates and the concentration of quenchers in the

environment, such as water, glutathione and amines. From chemical perspective, the reactive intermediates include activated esters, radicals, and carbenes[10].

Activated ester usually refers to the Biotin-AMP, which is generated by biotin ligase. The first iteration of this method, BioID, employs a 33.5 kDa variant of the Escherichia coli biotin ligase BirA contains the single mutation R118G[7,11]. Following this initial report, several biotin ligase variants with improved catalytic efficiency have been reported, including BioID2[12], BASU[13], AirID[14], TurboID[15], miniTurbo[15]. The mild nature of this methodology (simple exposure to biotin) has facilitated extensive use in vivo[15–17]. The activated ester species are modestly reactive ($t_{1/2}$ ~ 5min) with ~10 nm practical labeling radius measured by a stable protein complex as a molecular ruler[9].

Phenoxy radicals[18], phenyl aminyl radicals[19] and phenyl nitrenes[20] are generated from peroxidase enzyme by oxidation of phenols, aniline and phenyl azide, respectively. Such radicals are short lived (<1 msec), have a small labeling radius (<10 nm) and can covalently react with electron-rich amino acids such as Tyr, Trp, His and Cys[18]. The first example of using peroxidase for proximity labelling was reported in 2008[20]. The method, termed EMARS (enzyme-mediated activation of radical sources), employed HRP conjugated antibodies to direct labelling to specific cell surface proteins. However, HRP is inactive when expressed in the mammalian cytosol[8,21], which limits the broad application. APEX is a soybean peroxidase that has been engineered to be more catalytically active, smaller, and can be expressed in all cellular compartments, significantly broadening the potential for interrogating cell biology. Since the introduction of the method in 2012, it has been employed extensively to probe intracellular protein–protein interaction networks[6].

Singlet carbenes are usually generated from the photosensitization of diazirines through their exposure to 350nm light[22]. In terms of reactivity, the singlet carbene displays polar reactivity, readily inserting into C–H and X–H bonds, found in all amino acids, in a concerted manner[23]. The primary challenge with all diazirine-based methods is their rapid reactivity with water, which results in hydrated products. While it is necessary to restrict diffusion and maintain a tight labelling radius, it also leads to very low labelling efficiencies which makes the analysis of low abundance proteins extremely challenging. Recently, Macmillan group describes a proximity labeling platform that exploits photocatalytic carbene generation to selectively identify protein-protein interactions on cell membranes, termed MicroMap (μMap)[24,25]. μMap employs an antibody-conjugated iridium photocatalyst which is excited by visible light (450 nm) to convert nearby diazidines into reactive carbenes via Dexter energy transfer, thereby labeling proximal proteins quickly. This energy transfer step only occurs within 1 nm, which when combined with the short solution half-life (t1/2~2 ns) exhibited by carbenes, enforces a tight labelling radius (approx. 4–5 nm).

Building off of the abundance of protein proximity labeling technologies currently available, work has recently begun in the area of RNA proximity labeling. APEX2 labeling has been developed into APEX-seq[26] by taking advantage of the guanine base's propensity to participate in ROS-based reactions. This method has found broad utility in assessing RNA distribution across membrane-bound organelles, membrane-less organelles such as stress granules, and most recently in interrogating RNAs involved in RPIs[27,28]. Neverthless, the requirement of toxic H2O2 in achieving the reaction precludes its utility in vivo, and likely induces cellular stress, making perturbative studies difficult to

deconvolute. To this end, the light-inducible CAP-seq[29] and Halo-seq[30] methods bypass the need for toxic H2O2 by utilizing blue and green light activated enzyme (miniSOG) and ligand (Halo), respectively, to achieve ROS-mediated labeling on the G base.

Recently, our group developed a genetically-encodable protein-fragment complementation technology based on a split esterase[31]. We found that BS2 esterase can bio-orthogonally unmask methylcyclopropyl ester-containing molecules in multiple cell lines, and this work was informed primarily by the notion that a number of molecules can be masked with esters, such that activity is dependent upon an unmasking event. Seeking to continue to leverage this principle, we wondered whether we could mask and unmask a thioester-based acylation reagent with our selective ester-esterase pair, and whether the system could function in a proximity-dependent manner.

In this chapter, I presented the development of thioester-based acylation reagent with an ester cage, and the preliminary data of its application on biomolecule labeling.

5.2 Results

As stated in the 1.1, S-aryl thioester is a highly reactive in the nucleophilic substitution reaction, especially with electron withdrawing group on the aromatic ring. It needs to be masked before deploying in the cells. Given that our masking group is an ester (**Figure 5.1B**), we considered to exploit keto-enol tautomerism (**Figure 5.1C**). Masking the highly disfavored enol form of S-aryl thioester should lead to rapid conversion to the keto form upon an unmasking event, deliver the highly reactive thioester which can then in principle undergo nucleophilic attack by surrounding biomolecules (**Figure 5.1D**). In addition, by using the reference of design principle of SHAPE reagent[32], we reasoned

that a click handle could facilitate downstream enrichment process (**Figure 5.1A**). Take all into consideration, we designed and synthesized the O106 in three steps (**Scheme 5.1**). The key to the successfully synthesis is the discovery of an iridium catalyzed stereo- and regioselective carboxylic addition reaction to thioynol ether to make α-alkoxy thioenol esters.

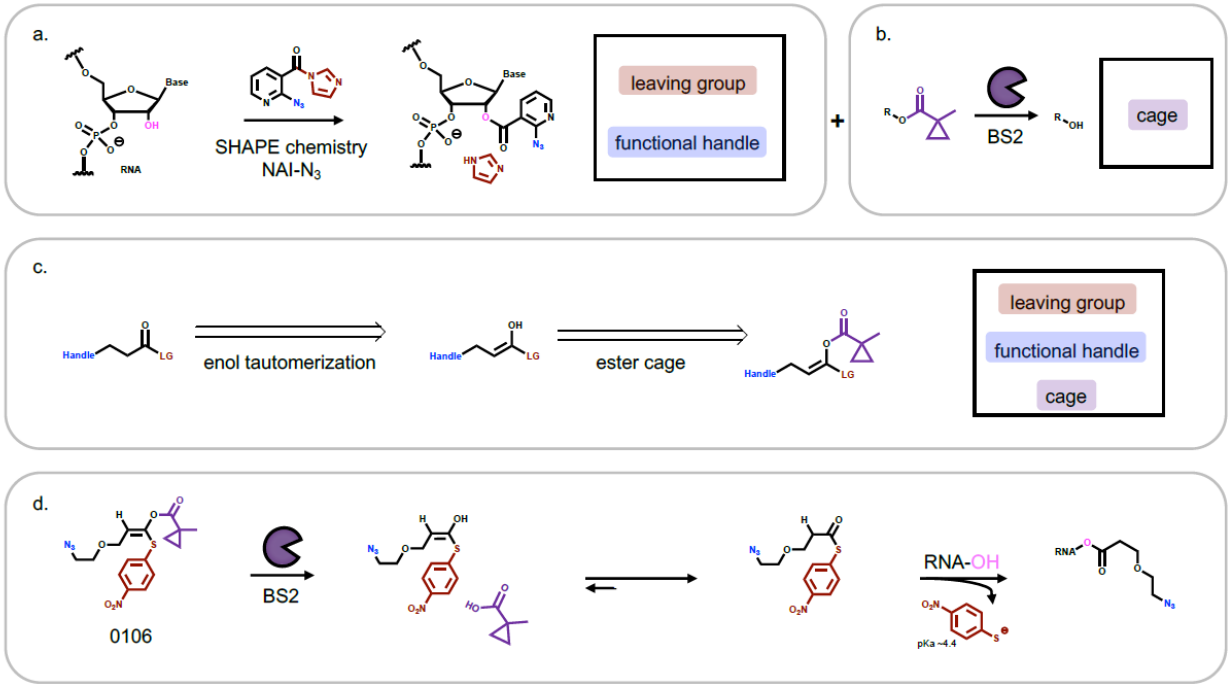

Figure 5.1 Ester caged thioester-based acylation reagent 106: inspiration and design. (a) Functionalizable RNA 2'-OH acylation reagents contain two components: a good leaving group (brown) and a handle (blue). (b) BS2 esterase chemistry and its potential as a caging group (purple). (c) Masking the enol tautomer of a ketone-containing molecule with the BS2 esterase-selective cage. (d) O106 lead probe labeling of RNA.

There is no report of the structure of α-alkoxy thioenol esters, nor the known transformation to make this kind of compounds. The closest reaction that has been ever reported is a silver-catalyzed trans addition of carboxylic acids to ynol ethers to deliver (Z)-α-alkoxy enol esters[33]. The attempts of using various silver-based catalyst on thioynol ether substrates yield more than 90% of 1,2-product with less than 5% idea 1,1-product.

The completely switched reactivity could be contributed to the different polarity on the triple bond owing to the electronegativity difference between sulfur and oxygen[34,35].

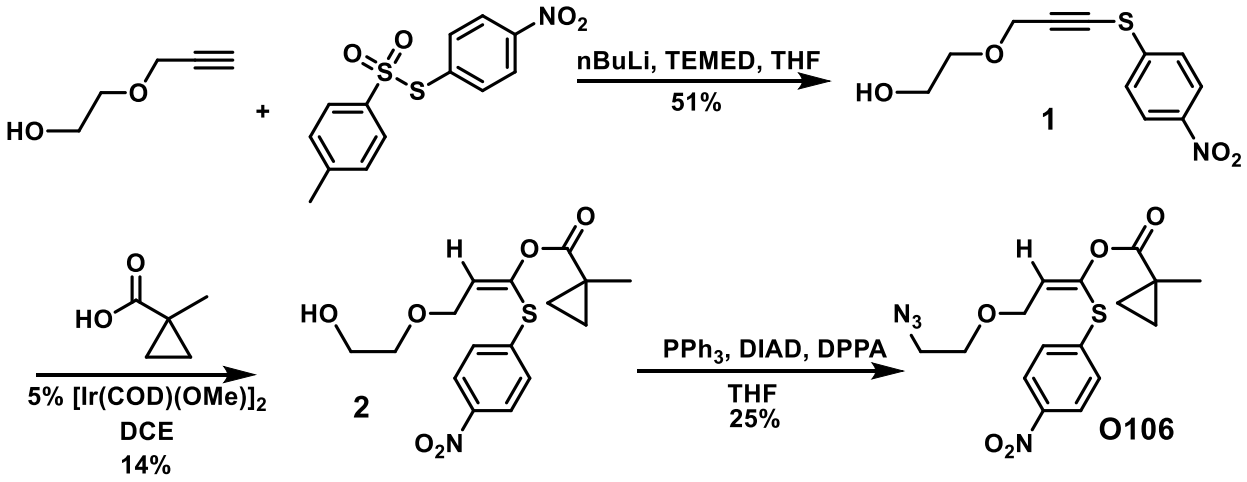

Scheme 5.1 Synthetic scheme for O106.

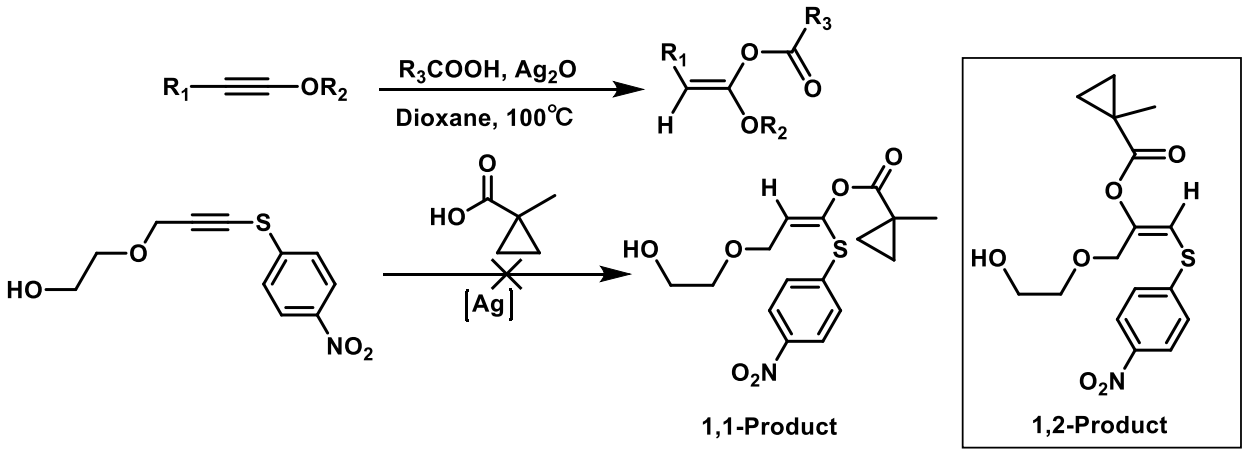

Scheme 5.2 Silver-catalyzed regio- and stereoselective addition of carboxylic acids to ynol ethers and its failed application on thioynol ether.

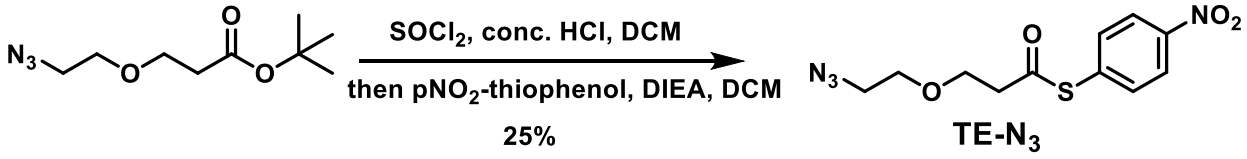

Scheme 5.3 Synthesis scheme for 4-nitrothioester model compound Thioester-N_3

Table 5.1 Optimization of the catalyst

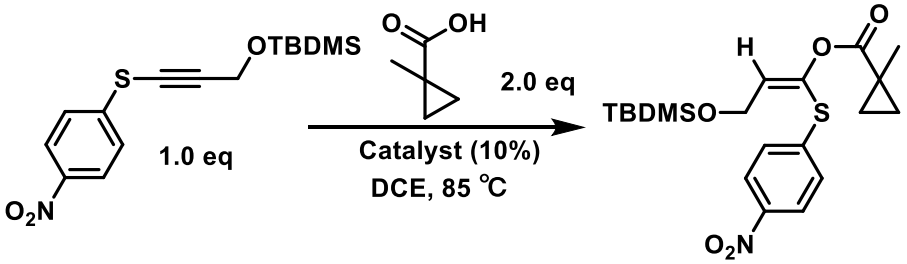

Entry	Catalyst	NMR Yield
1	$Sm(OTf)_3$, $Cu(CH_3CN)_4PF_6$, CuI, CuCl, $Pd(OAc)_2$, $ZnCl_2$, $NiBr_2$, $CoBr_2$, $Pd(dppf)Cl_2$, $ZrCl_4$, $Fe(acac)_3$, $RuCl_3$	N.R.
2	Ag_2O	1,2 - product
3	$[Ir(COD)(MePPh_2)_2]PF_6$	N.R.
4	$[Ir(Cp^*)Cl_2]_2$	N.R.
5	$[Ir(COD)OMe]_2$	28%
6	$[Ir(COD)Cl]_2$	10%
7	$Ir(acac)_3$	21%
8	$[Ir(coe)OMe]_2$	9%

Therefore, a wide range of catalysts are screened in the model reaction and only iridium catalyst gives the right 1,1-product. Iridium catalyst screening reveals that $[Ir(COD)OMe]_2$ gives the best yield (**Table 5.1**). Ligand screening suggested that bidentate ligands completely abolish the reactivity. For the phosphine ligand, electron rich ligands decrease the yield while electron poor ligands slightly increase the yield (**Table 5.2**). Finally, solvent screening suggested the co-solvent of 1,2-dichloroethane (DCE) and acetonitrile works best, probably due to the combination of good catalyst solubility (DCE) and weak coordination property (acetonitrile) (**Table 5.3**).

When apply the optimized reaction condition to the compound 1, the compound 2 is acquired with 14% yield, probably due to the coordination interference by terminal hydroxyl group. The final conversion of the hydroxyl group to azide is challenging, and mitsunobu azidation is the only method that delivers O106 effectively.

Table 5.2 Optimization of the ligand

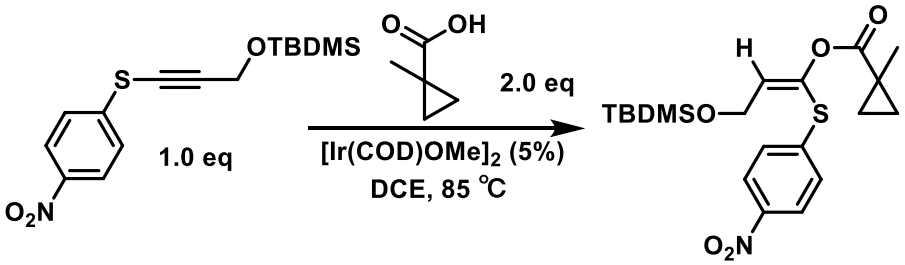

Entry	Ligand	Yield (%)
1	None	28
2	PPh_3	5
3	$AsPh_3$	12
4	CyJohnPhos	12
5	XPhos	12
6	$P(F_5Ph)_3$	35
7	Dibppy (COOMe)	4
8	Dibppy (tBu)	0
9	COD (20%)	31

Based on previous work, we have found that BS2 accepts and unmasks methylcyclopropyl ester-containing molecules robustly regardless of differences in overall structural scaffold. With O106 in hand, we confirmed this activity, finding BS2 was capable of uncaging O106 completely in 3 minutes. We next tried to identify what biomolecule

Table 5.3 Optimization of the solvent

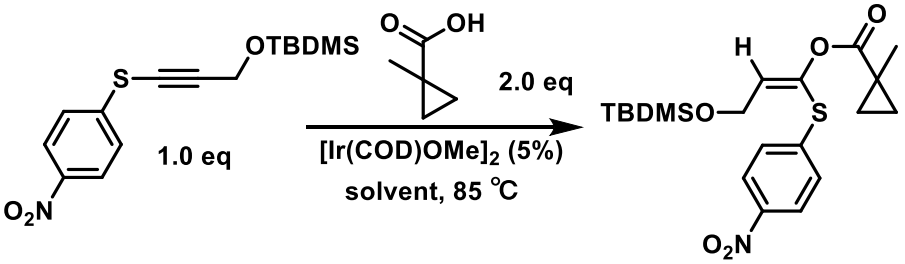

Entry	Solvent	NMR Yield (%)
1	DCE	31
2	Dimethoxyethane	14
3	HPMA	0
4	Toluene	39
5	Octane	37
6	Acetonitrile	45
7	Dimethylformamide	0
8	Dimethylacetamide	0
9	Dioxane	12
10	DCE/Acetonitrile=1:1	42
11	Toluene/Acetonitrile=1:1	30

could be labeled with 4-nitrothioester. The in vitro protein labeling experiment with thioester model compound TE-N_3 suggested that the 4-nitrothioester has poor reactivity with protein under physiological pH, consistent with the observation from the native chemical ligation that thioester selectively react with N-terminal cysteine. We then performed a dot blot experiment to assay RNA labeling. The thioester model compound TE-N_3 and known SHAPE reagent NAI-N_3 were incubated with RNA, followed by click reaction to conjugate a fluorophore. We observed a significant fluorescent signal from thioester treated RNA, though the intensity was much less than SHAPE reagent (**Figure**

5.2A). We next performed *in vitro* dot blot experiment using purified to determine whether the unmasked thioester electrophile would undergo a reaction with *in vitro* transcribed RNA. We found that only in the presence of O106 and BS2 did we see robust clicked DBCO-488 signal, which was promptly abolished with the addition of RNAse A (**Figure 5.2B**). dsDNA and ssDNA corresponding to the RNA was not labeled, nor did we observe

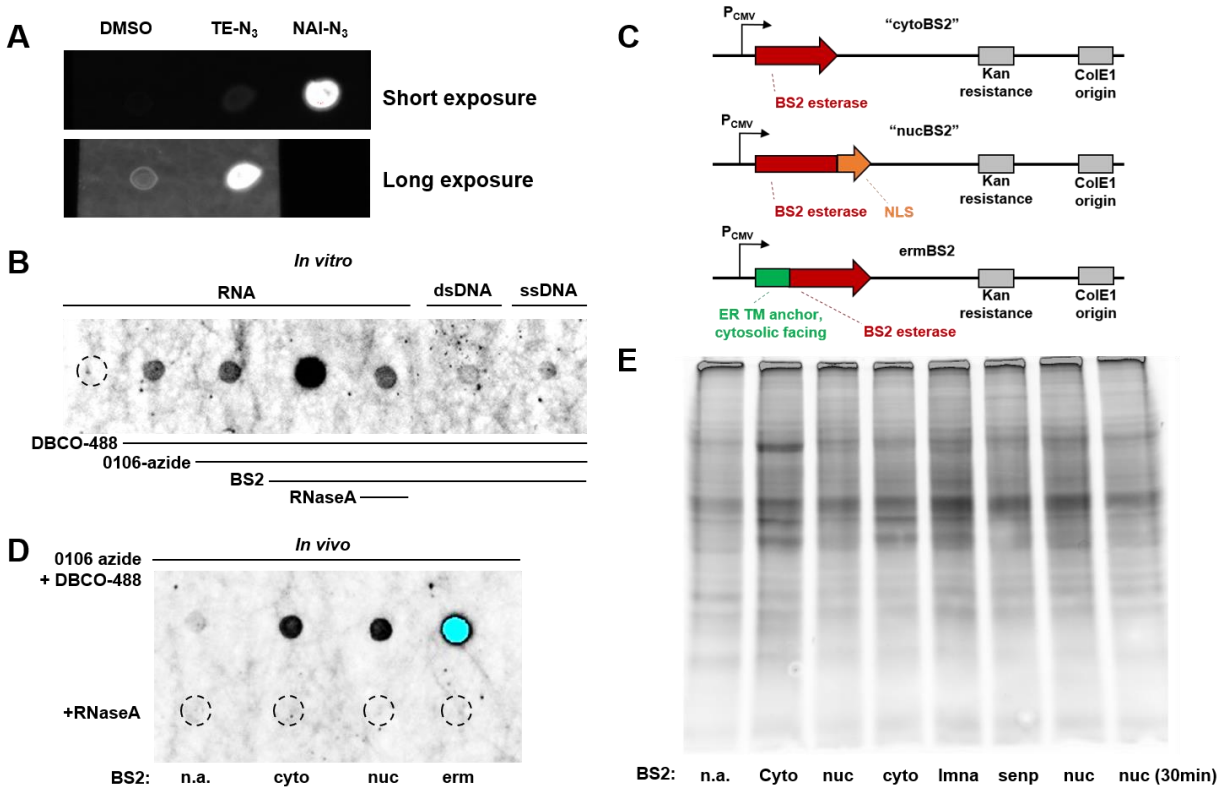

Figure 5.2 BS2/O106 mediated labeling in vitro and in cells. (A) 2 µg RNA is subjected to the reaction DMSO or 10 mM of TE-N_3 or NAI-N_3 and subsequently click with DBCO-488, then blotted. (B) *In vitro* transcribed RNA, dsDNA, and ssDNA (500 ng) is subjected to BS2/O106 (50 µM) or DMSO reaction and subsequent DBCO-488 click reaction followed by RNase A or DMSO treatment and blotted. (C) Example of plasmid maps used in this study (D) RNA extracted from BS2-containing HEK293T cells is treated as in (B) and blotted. (E) Total protein lysates from 6-well dishes of HEK293T cells run on an SDS-PAGE that have been transfected with variably localized BS2s, as indicated by number below. 50 µM O106 was added to the cells for 15 min prior to lysis. DBCO-488 clicked on as described previously and labeled protein shown below. No significant labeling is observed relative to no BS2-containing cells.

any DNAse 1 susceptibility, which we predicted based on the fact that DNA does not contain that 2'-OH group.

Encouraged by these results but recognizing that in vitro labeling experiments bypass any of the nucleophilic noise that would be present in an in-cell environment such as protein side chains or metabolites, we challenged our labeling system further by performing dot blots with RNA purified from cell lysates. Recombinant BS2s localized to three compartments of interest of various degrees of "openness" and "closeness" (cytosol, ER membrane, and nucleus, accomplished via appended localization sequences) were transfected in HEK293T cells (**Figure 5.2C**) and 50 μM O106 was introduced for 15 minutes. We then lysed the cells, purified out the RNA, and subjected it to a click reaction with DBCO-488. Again, excitingly, only the in the presence of both O106 and BS2 did we observe robust labeling, which was susceptible to RNAse A degradation (**Figure 5.2D**). It was especially interesting to note that regardless of where BS2 was localized, strong labeling signal was observed, suggesting a tightly enclosed environment is not required for successful labeling. Unsurprisingly, while no background labeling was observed in an in vitro setting, we did observe some background labeling in the in-cell context, which is presumably mediated by hydrolysis or weak activity by endogenous esterases. In addition, *in cellulo* protein labeling failed again, suggested that 4-nitrothioester were not suitable for protein labeling (**Figure 5.2E**).

Once we determined that BS2-mediated O106 RNA labeling could occur in cells, we wanted to see if the labeling signal was occurring predominantly near where BS2 itself was localized. To do this, we leveraged our azide handle once again, this time through copper-mediated click chemistry of AF488 in cells. We localized BS2 to four

compartments: cytosol, ER membrane, nucleus, and nuclear pore (through a SENP2 pore protein fusion), with each containing an RFP tag. The live cells were labeled with 50 μM O106 for 15 minutes, followed by fixation and permeabilization. The permeabilized cells were subjected to AF488 clicking and subsequently imaged (**Figure 5.3A**). Remarkably, there was very good co-localization between the BS2 signal and the labeling signal, even in the sub-organellar case, suggesting that proximity labeling was a viable option for deploying this technology (**Figure 5.3B**).

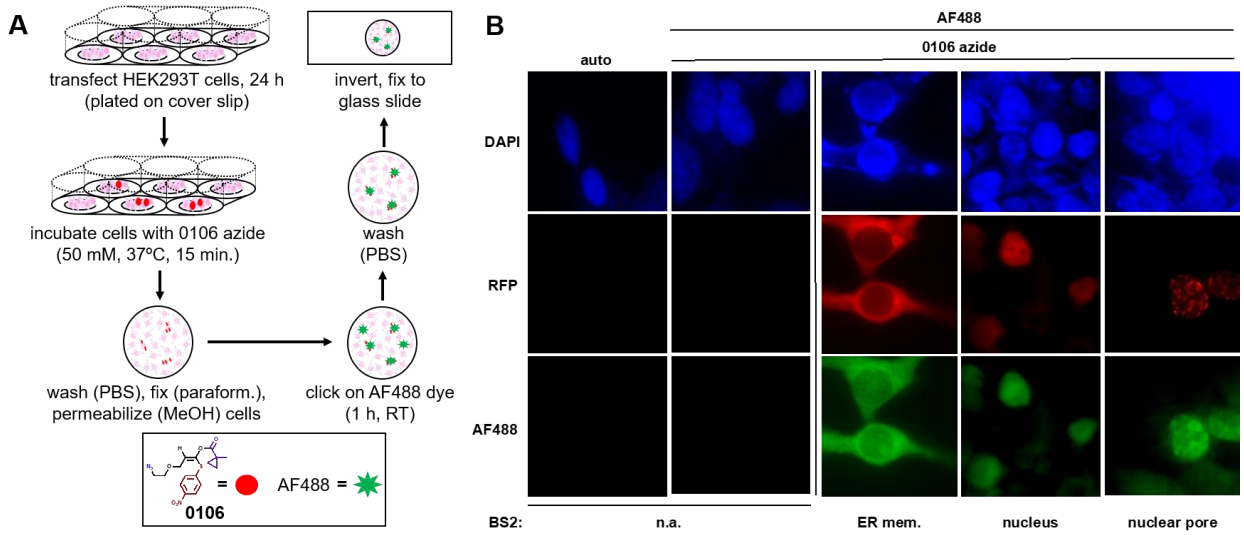

Figure 5.3 Fluorescence imaging of BS2 localization and acylation activity. (A) Scheme of imaging protocol. (B) Live HEK293T cells containing various RFP-tagged BS2s are subjected to O106 labeling (50 μM) for 15 minutes and subsequently washed, fixed, and permeabilized. The azide labeled biomolecules are subjected to click reaction with AF488 dye and labeling events are imaged.

Of additional interest to us was whether labeling was localized to the cell in which O106 uncaging occurred only, as we would predict, or whether it could permeate nearby cells. To test this, we set up a co-culture experiment consisting of mixed populations of HEK293T cells, RFP-positive cells, BS2-positive cells, and RFP-positive/BS2-positive co-cultured cells and performed labeling. Gratifyingly, labeling events were constrained to the cells in which BS2 was present only (**Figure 5.4**).

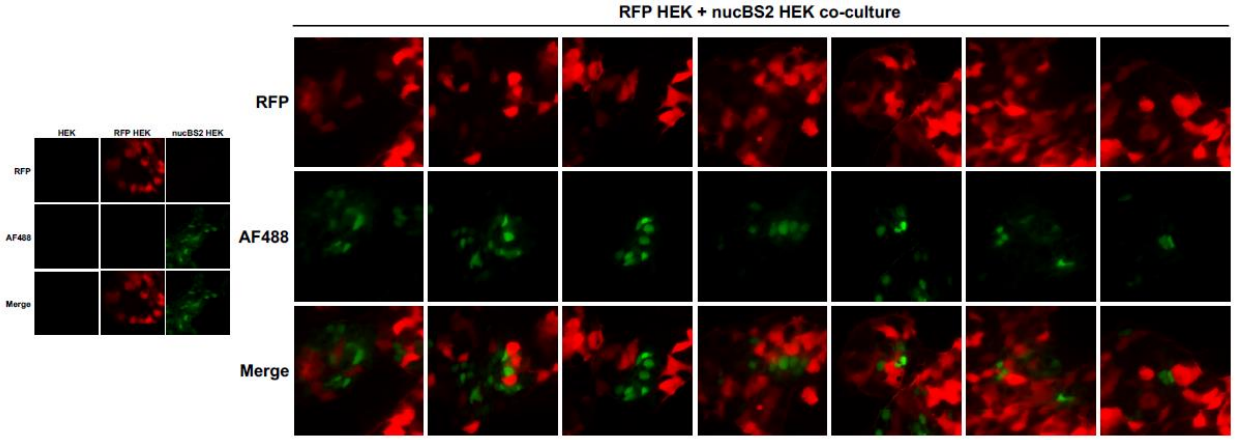

Figure 5.4 BS2/O106 labeling is limited to single cells. HEK293T cells transfected with nucBS2 were co-cultured with RFP-positive HEK293T cells and labeling was performed as above. No substantial labeling overlap between the two populations was observed. 7 biological replicates shown.

5.3 Discussion

In summary, I have demonstrated that 4-Nitrothioester can react with RNA in physiological environment. And a newly developed iridium catalyzed carboxylic addition reaction installs a bio-orthogonal ester to the enol form of thioester. Further, we established that the ester-masked enol thioester acylation reagent O106 can be unmasked efficiently in the presence of BS2 esterase both *in vitro* and *in cellulo* and newly formed 4-nitrothioester can label RNA. Cell imaging experiments demonstrated the colocalization of BS2 and labeled biomolecules, suggested that we may develop a thioester-based RNA proximity labeling with O106 and BS2 pair.

To test the hypothesis, we did the preliminary RNA-seq of organelle targeted BS2 followed the protocol of APEX-seq with minor modification. After O106 labeling, we isolated RNA and conjugated the labeled biomolecule with biotin via click reaction to separate out labeled RNA populations from those that were unlabeled, enabling location-

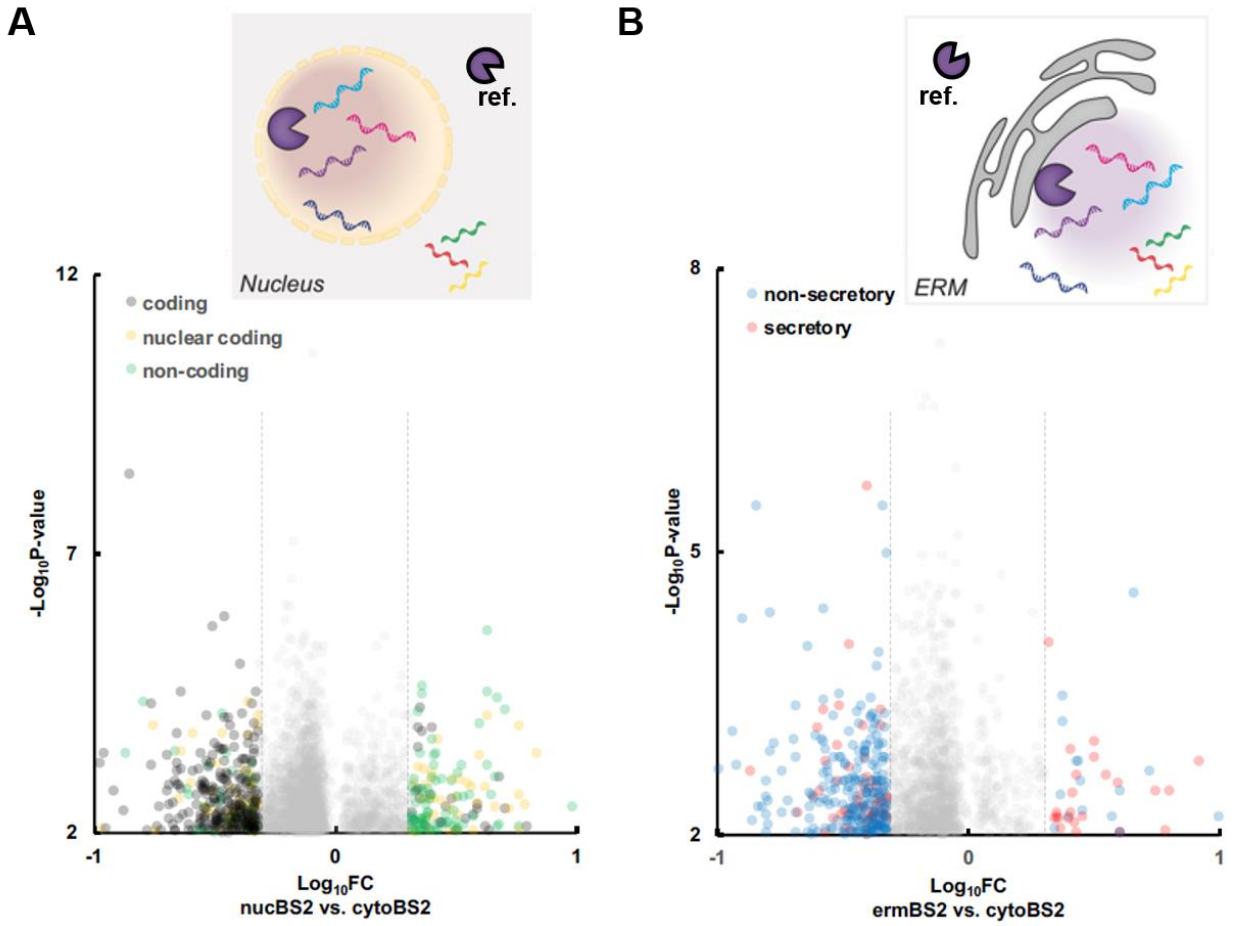

Figure 5.5 RNA-seq quantification of organelle transcripts with organellar targeted BS2. (A) Volcano plot showing nucleus targeted BS2 catalyzed enrichment of nuclear coding mRNA (yellow) and non-coding mRNAs (green) over coding mRNA (gray). (B) Volcano plot showing ER membrane targeted-BS2 catalyzed enrichment of secretory mRNAs (pink) over non-secretory mRNAs (blue). A transcript is considered enriched or de-enriched if it has a fold-change (FC) of $\geqslant$2 and is considered statistically significant if it has a p-value of $\leqslant$0.01.

specific RNA studies. As proof-of-concept, we chose to look first at the ER membrane and the nucleus, as these test cases have been well characterized by current methods[26]. In determining whether a given transcript was enriched specifically in a given organelle, we compared transcript abundances from erm- or nucBS2 with all requisite reaction components vs. general cytosolic BS2 with all requisite reaction components. In this way we could assess true differences across compartments, rather than simply comparing

transcripts enriched in the presence vs. absence of some critical reaction component. We additionally considered any transcript with a P-value of ≤ 0.01 as significant, while any transcript with a fold-change of ≥ 2 was considered enriched or de-enriched (**Figure 5.5A,B**). Gratifyingly, in the ermBS2 vs. cytoBS2 case we observed general enrichment of secretory transcripts and general de-enrichment of non-secretory transcripts, as has been seen by other methods. In addition, in the case of nucBS2 vs. cytoBS2, we observed the general enrichment of non-coding transcripts and the general de-enrichment of coding transcripts. Interestingly, in tune with other current methods, we also observed enrichment of nuclear-associated protein-coding transcripts as well.

Furthermore, we also did a more stringent test of our technology by fusing BS2 to an RBP whose interactions with RNA binding partners has been well-characterized: YTHDF1. YTHDF1 is an m6A reader protein that binds to m6A sites and promotes translation[36,37]. Its binding partners have been well studied through crosslinking- and antibody-based IP methods, PAR-CLIP[38] and RIP-seq[39] respectively. We therefore appended BS2 to YTHDF1 and assessed transcript enrichment vs. general cytosolic BS2. Excitingly, we saw great overlap between the three datasets, with 46% of the transcripts enriched by YTHDF1-BS2 only, vs. 54% enriched by multiple methods (31% enriched by both YTHDF1-BS2 and PAR-CLIP, 4% enriched by both YTHDF1-BS2 and RIP-seq, and 19% enriched by all three methods) (**Figure 5.6A**). Additionally, when assessing enriched transcripts based on m6A presence, we found that an astounding 93% of enriched transcripts were known to contain at least one m6A site[40,41] (**Figure 5.6B**).

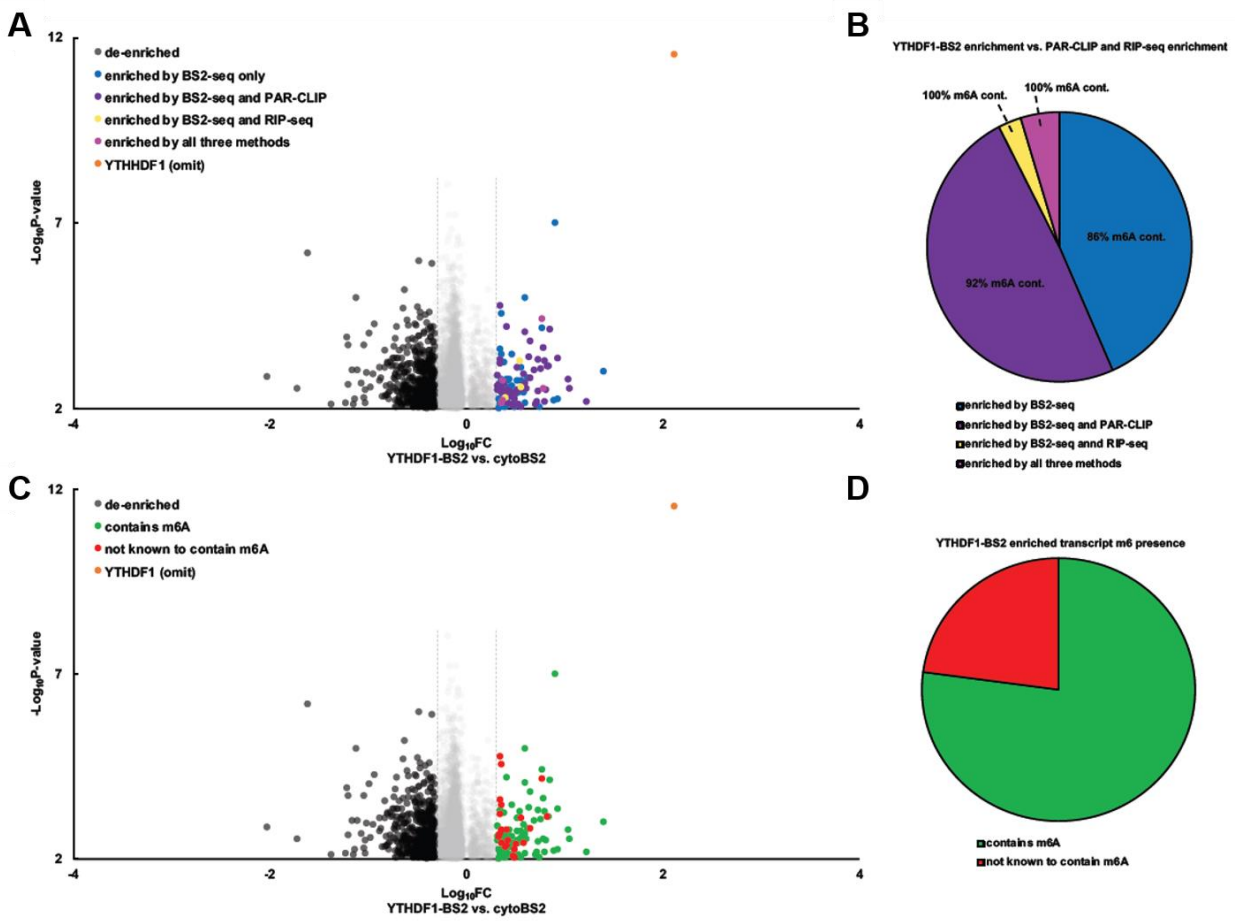

Figure 5.6 RNA-seq quantification of RNA binding protein (RBP) transcripts with YTDHF1 targeted BS2. (A) Volcano plot showing transcripts enriched by YTHDF1-BS2 color-coded for enrichment with other methods (PAR-CLIP, RIP-seq). (B) Venn diagram showing the comparison of transcripts enriched by different combinations of the three methods. (C) Volcano plot showing transcripts enriched by YTHDF1-BS2 color-coded for known presence of m6A. (D) Venn diagram showing the percentages of enriched transcripts that are known/not known to contain m6A. A transcript is considered enriched or de-enriched if it has a fold-change (FC) of $\geqslant$2 and is considered statistically significant if it has a p-value of $\leqslant$0.01.

Despite the preliminary positive results from RNA-seq analysis, more validation experiments, like RT-qPCR and Fluorescence in situ hybridization (FISH), are needed to fully validate the RNA-seq results. These experiments are currently underway. Altogether, these results established that BS2-O106 could potentially be used as a viable new complement tool to current suite of proximity labeling strategies. We view this work as an

important contributor to the RNA proximity labeling toolbox and hope that it is of broad use for those interested in understanding these types of complex interactions.

5.4 Experimental Details

Cloning. All plasmids were constructed by Gibson Assembly with PCR products generated using Q5 or Phusion DNA polymerases (NEB). The plasmids were sequenced by the University of Chicago Comprehensive Cancer Center DNA Sequencing and Genotyping facility. Full vector sequences are also available upon request. APEX2 vectors used in this work were obtained through Addgene.

***In vitro* transcription.** A gene block containing an upstream T7 promoter (95 bp) was obtained from IDT and served as the reaction template. The template was PCR amplified to yield about 50 µg DNA. The following components were mixed together for the IVT in the following final concentrations: 10x transcription buffer (NEB, M0251S), 100 µL (final conc. 1x); 1 M $MgCl_2$, 25 µL (final conc. 25 mM); 1 M DTT, 10 µL (final conc. 10 mM); SUPERase-in 30U/µL (Thermo, AM2694), 1 µL (final conc. 30U/mL); 25 mM NTP mix (100 mM NTPs, 50 µL ea.), 200 µL (final conc. 4 mM/NTP); DNA template, 50 µg (final conc. 50 µg/mL); T7 RNA polymerase (NEB, M0251S), 6.25 µL (final conc. 40 µg/mL); RNAse/DNAse-free H_2O, to bring total reaction volume to 1 mL. All reaction components were mixed thoroughly by pipetting up and down several times, and incubated overnight at 37°C. 5 µL of Dnase was then added and incubated for an additional 30 min. at 37°C. The sample was then concentrated down to 150 µL and cleaned up using the RCC-5 RNA Clean & Concentrator Kit (Zymo, R1013). Loading dye was added and the sample was

boiled for 5 min. at 90°C. The sample was then loaded onto an 8M urea gel (pre-run for 30 min. at 120V) for gel purification by splitting the sample evenly across 10 wells. After the run, the proper RNA band was excised from the gel using UV shadowing, and the RNA was extracted out of the urea gel using the ZR small-RNA PAGE Recovery Kit (Zymo, R1070).

Recombinant protein expression and purification. The pET-BS2 plasmid (Table 4.1) was transformed into chemically-competent E. coli BL21 cells. 1 L cultures were grown at 37°C in LB broth (40 μg/mL Kan) to mid log-phase (OD600 of 0.65). The cultures were then induced with 0.2 mM IPTG and incubated at 30°C overnight. Cells were harvested by 4°C centrifugation (4000xg for 15 min), the supernatants discarded, and the pellets were resuspended in lysis buffer (50 mM Tris (pH 7.5), 1 M NaCl, 10 mM TCEP, 20% glycerol) and protease inhibitor tablet (Thermo, A32963). The mixtures were then sonicated (total on time: 10 min; 10s on/20s off; amplitude 30%) and spun down at 12,000 rpm for 40 min. BS2 was purified from the supernatants by nickel affinity chromatography and dialyzed into 50 mM sodium phosphate buffer (pH 7.5). Prior to storage at -80°C, 15% glycerol was added. Final BS2 concentrations were measured using a standard BCA assay.

***In vitro* dot blot.** IVT RNA obtained as described above, as well as corresponding dsDNA and ssDNA (IDT), was subjected to reaction with BS2 (purified, as described above) and O106 as follows: 500 ng nucleic acid in 1x PBS was reacted with 50 μM O106 or DMSO control in the presence or absence of 200 nM BS2 for 15 min. at 37°C in a thermomixer

at 950 rpm. 100 μM DBCO-488 (Click Chemistry Tools, 1278-1) or DMSO control was added to the samples and they were incubated at 37°C in a thermomixer at 950 rpm for 30 min. Samples were RCC-5 or DCC-5 cleaned up. Samples were subjected to RNAse A (Thermo, EN0531), DNAse I (Thermo, EN0525), or DMSO control at 37°C in a thermomixer at 950 rpm for 30 min. Samples were RCC-5 or DCC-5 cleaned up, blotted, and imaged on a BioRad ChemiDoc imager.

Mammalian cell culture and plasmid transfection. HEK293T (ATCC) cells were cultured in DMEM (L-glutamine, high glucose, sodium pyruvate, phenol red; Corning) supplemented with 10% (vol/vol) fetal bovine serum (FBS, Gemini Benchmark) and 1% (vol/vol) penicillin/streptomycin (Gibco/Life Technologies). Cells were maintained in a water-saturated, 5% CO_2-containing, 37°C incubator. Cells were used for experiments never exceeding passage number 25. Fresh HEK293T cells were obtained from ATCC and frozen down at an early passage number (5) in individual aliquots. There was no testing for mycoplasma infection as a result. Transient transfections were performed using Lipofectamine 3000 (Invitrogen; Thermo, L3000015) following the manufacturer's protocol.

***In vivo* dot blot.** HEK293T cells were transfected with cytoBS2 (KJ128), nucBS2 (47-17), ermBS2 (43-52), or a no BS2-containing dummy plasmid in biological duplicate. 24 h post-transfection, 50 μM O106 was added to all wells and incubated for 15 min at 37°C. The cells were then washed 2x with 1x PBS, lysed, and the RNA was extracted and purified from the lysates using the Rneasy Plus Mini Kit (Qiagen, 74136). 100 μM DBCO-

488 was added to the samples and they were incubated at 37°C in a thermomixer at 950 rpm for 30 min. Samples were RCC-5 cleaned up, and subjected to RNAse A or DMSO control at 37°C in a thermomixer at 950 rpm for 30 min. Samples were RCC-5 cleaned up, blotted, and imaged on a BioRad ChemiDoc imager.

Fluorescence microscopy. Cell treatment and CuAAC reaction. HEK293T cells were plated, on glass coverslips pre-treated with 0.1 mg/mL Poly-D-Lysine (for 2 h at RT) and contained within a 24-well dish, and transfected with cytoBS2-RFP (52-60), ermBS2-RFP (52-12), nucBS2-RFP (52-70), SENP2-BS2-RFP (nuclear poreBS2, 52-62), or no BS2-containing dummy plasmid in biological duplicate. 24 h post-transfection, 50 μM O106 or DMSO control was added for 15 min. at 37°C. The cells were then washed 2x with 1x PBS, fixed with 4% paraformaldehyde solution for 30 min. at RT, washed 2x with 1x PBS, permeabilized with ice cold MeOH for 5 min. at RT, and washed 2x with 1x PBS. The samples were then bathed in a CuAAC reaction solution composed in 1x PBS with the following final concentrations, adapted from a previously published method: 2 mM BTTAA (Click Chemistry Tools, 1236-100), 1 mM $CuSO_4$, 10 μM 488-PEG4-alkyne (Sigma, 761621), and 10 mM sodium ascorbate (prepared fresh). The BTTAA, CuSO4, and 488-PEG4-alkyne were pre-mixed in 1x PBS for 5 min., and the sodium ascorbate was added immediately prior to cell bathing. The cells were incubated in this bath for 1 h at RT, followed by 3x washes with 1x PBS for 5 min. each, the second of which contained DAPI. The last 1x PBS wash was removed, and the cell-containing coverslips were then lifted from the 24-well plate, inverted, and transferred to fixative pre-dotted on a glass slide. The slides were dried for 5 h away from light prior to imaging. The cells on slides prepared

as above were imaged on an inverted epifluorescence microscope (Leica Dmi8) equipped with a camera (Hamamatsu Orca-Flash 4.0) with a 63x oil objective and light source (Sutter Lambda XL, 300W Xenon). The filters ET490/x, Quad-S, ET 525/x for 488-PEG4-alkyne, Etx/x, Quad-S, Etx/x for RFP, ET402/x, Quad-S ET455/x, and brightfield were used accordingly, and navigated utilizing the Leica LAS X software. Image analysis was performed in ImageJ.

RT-qPCR experiment of ERM targets with BS2 panel. Azide labeling and copper-free click reaction to install biotin on labeled RNAs. HEK293T cells plated in a 6-well dish were transfected with cytoBS2 (KJ128), ermBS2 (43-52), or a no BS2-containing dummy plasmid in biological triplicate. 24 h post-transfection, 50 μM O106 was added to all wells and incubated for 15 min at 37°C. The cells were then washed 2x with 1x PBS, lysed, and the RNA was extracted and purified from the lysates using the Rneasy Plus Mini Kit (Qiagen, 74136). The azide-labeled samples were eluted in 84 μL RNAase/DNAse-free H_2O, to which 10 μL 10x PBS, 1 μL SUPERase-in, and 5 μL 25 mM DBCO-PEG4-Biotin (Sigma, 760749) were added for a total reaction volume of 100 μL/sample. The samples were incubated at 37°C, 950 rpm on a thermomixer for 2 h, followed by an RCC-25 (Zymo, R1017) cleanup. The biotin-labeled samples were eluted with 125 μL RNAse/DNAse-free H_2O and, if not proceeding immediately, stored at -20°C overnight or -80°C long-term until ready to proceed with bead enrichment.

Enrichment of biotin-labeled RNAs. Enrichment of labeled RNAs was performed using the previously-reported APEX-seq enrichment method, with some modification.173

Briefly, 10 µL Pierce Streptavidin Magnetic Beads (Thermo, 88816) were utilized per 25 µg RNA sample. Beads were washed three times on/off the magnet with 500 µL binding & wash buffer (5 mM Tris-HCl, pH 7.5, 0.5 mM EDTA, 1 M NaCl, 0.1% Tween-20) per sample, followed by two 500 µL washes with solution A (100 mM NaOH, 50 mM NaCl) per sample, one 500 µL wash with solution B (100 mM NaCl), and a final resuspension of the beads in 125 µL solution B containing 1 µL SUPERase-in per sample. The resuspended beads were mixed thoroughly with the eluted, biotin-labeled RNA from above and incubated at 4°C for 2 h on a rotator. After this incubation, samples were washed three times with binding & wash buffer as described above, and enriched RNAs were digested off the beads by proteinase K as follows: washed beads were resuspended in 54 µL RNAse/DNAse-free H_2O and 35 µL 3x digestion buffer (330 µL 10x PBS, pH 7.5, 330 µL 20% N-laurylsarcosine sodium solution (Sigma, L7414), 66 µL 0.5 M EDTA, 16.5 µL 1 M DTT, and 357.5 µL RNAse/DNAse-free H_2O) was added to each sample. 1µL SUPERase-in and 10 µL of 20 mg/mL proteinase K (Sigma, P2308) was also added, bringing the total volume for the digestion to 100 µL. The samples were then incubated at 950 rpm on a thermomixer at 42°C for 1 h, followed by 55°C for 1 h. The beads were then placed on the magnet, and the supernatant was extracted and cleaned up using the RCC-5 kit for downstream applications (samples eluted in 6.5 µL water). Concentrations of RNA/sample were recorded. If not proceeding immediately, the samples were stored at -20°C overnight or -80°C long-term until ready to proceed.

Reverse-transcription. The PrimeScript RT Reagent Kit was used to generate cDNA (Takara, RR037B). The RT reaction was assembled as follows: to each 6.5 µL enriched

RNA sample, 2 µL 5x PrimeScript buffer, 0.5 µL random 6-mer primers, 0.5 µL oligo-dT primers, and 0.5 µL PrimeScript RT enzyme were added for a total of 10 µL/reaction. The samples were thoroughly mixed and placed on a thermocycler with the following protocol: 15 min. at 37°C followed by a 5 sec. 85°C RT inactivation step and a cooling to 4°C. If not proceeding immediately, cDNA samples were stored at 4°C overnight or -20°C long-term.

NovaSeq library preparation. HEK293T cells plated in a 6-well dish were transfected with an array of BS2s or a no BS2-dummy plasmid in biological quadruplicate. The samples were treated as described in the above RT-qPCR experiment protocol, except the samples were not RT-ed or qPCR-ed. Instead, the total enriched RNA samples eluted in 6.5 µL H_2O were diluted to a total volume of 50 µL and transformed into NovaSeq libraries using the KAPA mRNA HyperPrep Kit (Roche, KK8581, KK8441), containing an mRNA capture step prior to library generation. Typically, we yield 50-150 ng RNA from our enrichments, which is on the low end of KAPA's recommended input, but we get high quality libraries using this kit. The manufacturer's protocol is followed exactly, with the following exception: typically, 18-22 PCR cycles are required to achieve sufficient amplification, contrary to the 13-16 cycles recommended by the manufacturer, due to the relatively low total RNA input. The number of amplification cycles required for each library was pre-determined using qPCR prior to amplification of the entire libraries.

Analysis of BS2-seq enrichment libraries. Kallisto was used to quantify transcript level abundances of the BS2-seq libraries. A fasta file corresponding to GRCh38 and hg38 was downloaded from the Ensembl website and a kallisto index was generated using the index

command with default arguments. Fold-change calculations were performed for ermBS2 tpms+1 vs. cytoBS2 tpms+1 to assess transcripts enriched by BS2 at the ER membrane vs. those enriched by general cytosolic BS2. Transcripts with a FC ≥ 2 ($Log_{10}FC \geq 0.30$) and a P-value ≤ 0.01 ($-Log_{10}P\text{-value} \geq 2$) were considered significantly enriched. Transcripts were highlighted as secretory or non-secretory using previously published datasets and GO ontology. Similar analysis was performed for nucBS2 tpms+1 vs. cytoBS2 tpms+1 to assess transcripts enriched by BS2 in the nucleus vs. those enriched by general cytosolic BS2. Transcripts were highlighted as coding or non-coding according to the GRCh38 transcriptome annotations, and transcripts were specified as nuclear coding using GO ontology. Similar analysis was performed to assess subnuclear BS2 targets, this time with BS2-SENP2 (nuclear pore BS2) or LMNA-BS2 tpms+1 vs. nucBS2 tpms+1 to assess transcripts enriched by BS2 in subnuclear space vs. those enriched by general nucBS2. Transcript types were identified according to the GRCh38 transcriptome annotations, and comparisons of hits were made against nucAPEX-seq and APEX-SENP2/LMNA-seq hits and nuclear MERFISH hits.175 Similar analysis was performed when assessing DNA/RNA binding protein-fused BS2 targets, with the BS2-YTHDF1 tpms+1 vs. cytoBS2 tpms+1 comparison made to assess transcripts enriched by BS2-YTHDF1 vs. general cytosolic BS2. Hits were compared to published PAR-CLIP and RIP-seq datasets as well as an m6A transcript database.

5.5 Synthetic procedures

Azide-PEG-tBu ester[42] were synthesized according to the literature.

Synthesis of TE-N_3. To a 20 mL vial with the stir bar, 0.394 g azide-PEG-tBu ester is added into 2.6 mL $SOCl_2$, followed by addition of 150 µL of con. HCl. Seal the reaction with a rubber cap and punctuate with 21G needle then react for 1d under room temperature. Remove the $SOCl_2$ by rotavapor and 4-nitrothiophenol (455 mg) and DIEA (500µL) is added and react 1 d under room temperature. The reaction is quenched 4M HCl and extract by EtOAc (20 mL x 3) and washed by Brine. The combined organic layers were dried with Na_2SO_4, filtered, and concentrated. The resultant crude product was purified by column chromatography (Silica; 0-25% EtOAc:Hexane) to yield **TE-N_3** (120 mg) as yellow solid. Rf: 0.30 (Silica; 25% EtOAc/Hexane). ^{1}H NMR (400 MHz, $CDCl_3$): δ 8.22 – 8.14 (m, 2H), 7.59 – 7.51 (m, 2H), 3.78 (t, *J* = 6.0 Hz, 2H), 3.59 (dd, *J* = 5.5, 4.4 Hz, 2H), 3.34 – 3.26 (m, 2H), 2.92 (t, *J* = 6.0 Hz, 2H). ^{13}C NMR (101 MHz, $CDCl_3$) δ 193.29, 148.18, 135.97, 134.75, 123.97, 70.17, 66.32, 50.60, 44.27. HRA-MS(+): Calculated for $C_{11}H_{12}NO_4S$ [M+] 253.0409; found 253.0402.

Synthesis of 1. To a stirred solution of tert-Butyldimethyl(2-propynyloxy)silane (2.0 mL, 1.0 eq., 9.9 mmol) and Tetramethylethylenediamine (1.5 mL, 1.0 eq., 9.9 mmol) in dry THF (100 mL) at 0 ℃ under an N2 atmosphere was added dropwise of 2.5 M solution of nBuLi in hexane (4.2 mL, 1.0 eq., 9.9 mmol). After 5 min, thiosulfonates (*Chin. J. Chem. 2012, 30, 1611—1616*) (3.1 g, 1.0 eq., 9.9 mmol) was added in one portion. The mixture was stirred and warmed to room temperature for 15 min. The reaction completion was checked by LC-MS and reaction mixture was quenched with a saturated solution of NH_4Cl (150 mL). The solution was extracted by EtOAc (100 mL x 3) and washed by Brine. The combined organic layers were dried with Na_2SO_4, filtered, and concentrated. The

resultant crude product was purified by column chromatography (Silica; 0-20% EtOAc:Hexane) to yield **1** (2.12 g, 56%) as yellow solid. R_f: 0.63 (Silica; 10% EtOAc/Hexane). ^{1}H NMR (400 MHz, $CDCl_3$) δ 8.21 – 8.13 (m, 2H), 7.58 – 7.50 (m, 2H), 4.58 (s, 2H), 0.92 (s, 9H), 0.15 (s, 6H). ^{13}C NMR (101 MHz, $CDCl_3$) δ 146.27, 142.64, 125.69, 124.20, 100.95, 77.39, 77.07, 76.76, 68.82, 52.57, 25.80, 18.32, -5.09. HRA-MS(+): Calculated for $C_{15}H_{21}NO_3SSi$ [M+] 296.0579; found 296.0582.

Synthesis of 2. In a 25 mL vial equipped with a stir bar, compound **1** (0.76 g) and 1-Methylcyclopropanecarboxylic acid (0.36 g) are dissolved in DCE/CAN (1:1) (10 mL), then Ir catalyst (100 mg) is added. Seal the tube and allow the reaction to perform 16h at 85℃. Cool down the reaction and filter through the celite, use DCM to wash the reaction flask. The organic solution is washed with Sat. $NaHCO_3$ and Brine. The combined organic layers were dried with Na_2SO_4, filtered, and concentrated. The resultant crude product was purified by column chromatography (Silica; 0-15% DCM:EtOAc) to yield **2** (0.144 g, 14%) as yellow oil. R_f: 0.12 (Silica; 10% DCM:EtOAc).

Synthesis of O106. In a 25 mL vial equipped with a stir bar in ice bath, compound **2** (0.133 g), and PPh_3 (0.148 g) are dissolved in 4 mL THF. Then Diisopropyl azodicarboxylate (135 µL) and Diphenylphosphoryl azide (165µL) are added slowly at 0℃. After 30 min, remove the ice bath and let the reaction continue overnight at room temperature. Concentrate the reaction and the resultant crude product was purified by column chromatography (Silica; 0-75% EtOAc/Hexane) to yield **O106** (35 mg, 25%) as light-yellow oil. R_f: 0.63 (Silica; 25% EtOAc/Hexane).

5.6 References

(1) Keskin, O.; Tuncbag, N.; Gursoy, A. Predicting Protein-Protein Interactions from the Molecular to the Proteome Level. *Chemical reviews* **2016**, *116* (8), 4884–4909. DOI: 10.1021/acs.chemrev.5b00683. Published Online: Apr. 13, 2016.

(2) Hentze, M. W.; Castello, A.; Schwarzl, T.; Preiss, T. A brave new world of RNA-binding proteins. *Nature reviews. Molecular cell biology* **2018**, *19* (5), 327–341. DOI: 10.1038/nrm.2017.130. Published Online: Jan. 17, 2018.

(3) Moses, L.; Pachter, L. Museum of spatial transcriptomics. *Nature methods* **2022.** DOI: 10.1038/s41592-022-01409-2. Published Online: Mar. 10, 2022.

(4) Dunham, W. H.; Mullin, M.; Gingras, A.-C. Affinity-purification coupled to mass spectrometry: basic principles and strategies. *Proteomics* **2012**, *12* (10), 1576–1590. DOI: 10.1002/pmic.201100523.

(5) Uetz, P.; Giot, L.; Cagney, G.; Mansfield, T. A.; Judson, R. S.; Knight, J. R.; Lockshon, D.; Narayan, V.; Srinivasan, M.; Pochart, P.; Qureshi-Emili, A.; Li, Y.; Godwin, B.; Conover, D.; Kalbfleisch, T.; Vijayadamodar, G.; Yang, M.; Johnston, M.; Fields, S.; Rothberg, J. M. A comprehensive analysis of protein-protein interactions in Saccharomyces cerevisiae. *Nature* **2000**, *403* (6770), 623–627. DOI: 10.1038/35001009.

(6) Qin, W.; Cho, K. F.; Cavanagh, P. E.; Ting, A. Y. Deciphering molecular interactions by proximity labeling. *Nature methods* **2021**, *18* (2), 133–143. DOI: 10.1038/s41592-020-01010-5. Published Online: Jan. 11, 2021.

(7) Kwon, K.; Beckett, D. Function of a conserved sequence motif in biotin holoenzyme synthetases. *Protein science : a publication of the Protein Society* **2000**, *9* (8), 1530–1539. DOI: 10.1110/ps.9.8.1530.

(8) Martell, J. D.; Deerinck, T. J.; Sancak, Y.; Poulos, T. L.; Mootha, V. K.; Sosinsky, G. E.; Ellisman, M. H.; Ting, A. Y. Engineered ascorbate peroxidase as a genetically encoded reporter for electron microscopy. *Nature biotechnology* **2012**, *30* (11), 1143–1148. DOI: 10.1038/nbt.2375. Published Online: Oct. 21, 2012.

(9) Kim, D. in; Birendra, K. C.; Zhu, W.; Motamedchaboki, K.; Doye, V.; Roux, K. J. Probing nuclear pore complex architecture with proximity-dependent biotinylation. *Proceedings of the National Academy of Sciences of the United States of America* **2014**, *111* (24), E2453-61. DOI: 10.1073/pnas.1406459111. Published Online: Jun. 3, 2014.

(10) Seath, C. P.; Trowbridge, A. D.; Muir, T. W.; MacMillan, D. W. C. Reactive intermediates for interactome mapping. *Chemical Society reviews* **2021**, *50* (5), 2911–2926. DOI: 10.1039/d0cs01366h. Published Online: Jan. 18, 2021.

(11) Roux, K. J.; Kim, D. in; Raida, M.; Burke, B. A promiscuous biotin ligase fusion protein identifies proximal and interacting proteins in mammalian cells. *The Journal of cell biology* **2012**, *196* (6), 801–810. DOI: 10.1083/jcb.201112098. Published Online: Mar. 12, 2012.

(12) Kim, D. in; Jensen, S. C.; Noble, K. A.; Kc, B.; Roux, K. H.; Motamedchaboki, K.; Roux, K. J. An improved smaller biotin ligase for BioID proximity labeling. *Molecular biology of the cell* **2016**, *27* (8), 1188–1196. DOI: 10.1091/mbc.e15-12-0844. Published Online: Feb. 24, 2016.

(13) Ramanathan, M.; Majzoub, K.; Rao, D. S.; Neela, P. H.; Zarnegar, B. J.; Mondal, S.; Roth, J. G.; Gai, H.; Kovalski, J. R.; Siprashvili, Z.; Palmer, T. D.; Carette, J. E.; Khavari, P. A. RNA-protein interaction detection in living cells. *Nature methods* **2018**, *15* (3), 207–212. DOI: 10.1038/nmeth.4601. Published Online: Feb. 5, 2018.

(14) Kido, K.; Yamanaka, S.; Nakano, S.; Motani, K.; Shinohara, S.; Nozawa, A.; Kosako, H.; Ito, S.; Sawasaki, T. AirID, a novel proximity biotinylation enzyme, for analysis of protein-protein interactions. *eLife* **2020**, *9.* DOI: 10.7554/eLife.54983. Published Online: May. 11, 2020.

(15) Branon, T. C.; Bosch, J. A.; Sanchez, A. D.; Udeshi, N. D.; Svinkina, T.; Carr, S. A.; Feldman, J. L.; Perrimon, N.; Ting, A. Y. Efficient proximity labeling in living cells and organisms with TurboID. *Nature biotechnology* **2018**, *36* (9), 880–887. DOI: 10.1038/nbt.4201. Published Online: Aug. 20, 2018.

(16) Varnaitė, R.; MacNeill, S. A. Meet the neighbors: Mapping local protein interactomes by proximity-dependent labeling with BioID. *Proteomics* **2016**, *16* (19), 2503–2518. DOI: 10.1002/pmic.201600123. Published Online: Jul. 27, 2016.

(17) Uezu, A.; Kanak, D. J.; Bradshaw, T. W. A.; Soderblom, E. J.; Catavero, C. M.; Burette, A. C.; Weinberg, R. J.; Soderling, S. H. Identification of an elaborate complex mediating postsynaptic inhibition. *Science (New York, N.Y.)* **2016**, *353* (6304), 1123–1129. DOI: 10.1126/science.aag0821.

(18) Rhee, H.-W.; Zou, P.; Udeshi, N. D.; Martell, J. D.; Mootha, V. K.; Carr, S. A.; Ting, A. Y. Proteomic mapping of mitochondria in living cells via spatially restricted enzymatic tagging. *Science (New York, N.Y.)* **2013**, *339* (6125), 1328–1331. DOI: 10.1126/science.1230593. Published Online: Jan. 31, 2013.

(19) Zhou, Y.; Wang, G.; Wang, P.; Li, Z.; Yue, T.; Wang, J.; Zou, P. Expanding APEX2 Substrates for Proximity-Dependent Labeling of Nucleic Acids and Proteins in Living Cells. *Angewandte Chemie (International ed. in English)* **2019**, *58* (34), 11763–11767. DOI: 10.1002/anie.201905949. Published Online: Jul. 26, 2019.

(20) Kotani, N.; Gu, J.; Isaji, T.; Udaka, K.; Taniguchi, N.; Honke, K. Biochemical visualization of cell surface molecular clustering in living cells. *Proceedings of the National Academy of Sciences of the United States of America* **2008**, *105* (21), 7405–7409. DOI: 10.1073/pnas.0710346105. Published Online: May. 21, 2008.

(21) Li, X.-W.; Rees, J. S.; Xue, P.; Zhang, H.; Hamaia, S. W.; Sanderson, B.; Funk, P. E.; Farndale, R. W.; Lilley, K. S.; Perrett, S.; Jackson, A. P. New insights into the DT40 B cell receptor cluster using a proteomic proximity labeling assay. *The Journal of biological chemistry* **2014**, *289* (21), 14434–14447. DOI: 10.1074/jbc.M113.529578. Published Online: Apr. 4, 2014.

(22) Wang, J.; Burdzinski, G.; Kubicki, J.; Platz, M. S.; Moss, R. A.; Fu, X.; Piotrowiak, P.; Myahkostupov, M. Ultrafast spectroscopic study of the photochemistry and

photophysics of arylhalodiazirines: direct observation of carbene and zwitterion formation. *Journal of the American Chemical Society* **2006**, *128* (51), 16446–16447. DOI: 10.1021/ja067205d.

(23) West, A. V.; Muncipinto, G.; Wu, H.-Y.; Huang, A. C.; Labenski, M. T.; Jones, L. H.; Woo, C. M. Labeling Preferences of Diazirines with Protein Biomolecules. *Journal of the American Chemical Society* **2021**, *143* (17), 6691–6700. DOI: 10.1021/jacs.1c02509. Published Online: Apr. 20, 2021.

(24) Geri, J. B.; Oakley, J. V.; Reyes-Robles, T.; Wang, T.; McCarver, S. J.; White, C. H.; Rodriguez-Rivera, F. P.; Parker, D. L.; Hett, E. C.; Fadeyi, O. O.; Oslund, R. C.; MacMillan, D. W. C. Microenvironment mapping via Dexter energy transfer on immune cells. *Science (New York, N.Y.)* **2020**, *367* (6482), 1091–1097. DOI: 10.1126/science.aay4106.

(25) Buksh, B. F.; Knutson, S. D.; Oakley, J. V.; Bissonnette, N. B.; Oblinsky, D. G.; Schwoerer, M. P.; Seath, C. P.; Geri, J. B.; Rodriguez-Rivera, F. P.; Parker, D. L.; Scholes, G. D.; Ploss, A.; MacMillan, D. W. C. µMap-Red: Proximity Labeling by Red Light Photocatalysis. *Journal of the American Chemical Society* **2022**, *144* (14), 6154–6162. DOI: 10.1021/jacs.2c01384. Published Online: Apr. 1, 2022.

(26) Fazal, F. M.; Han, S.; Parker, K. R.; Kaewsapsak, P.; Xu, J.; Boettiger, A. N.; Chang, H. Y.; Ting, A. Y. Atlas of Subcellular RNA Localization Revealed by APEX-Seq. *Cell* **2019**, *178* (2), 473-490.e26. DOI: 10.1016/j.cell.2019.05.027. Published Online: Jun. 20, 2019.

(27) Yap, K.; Chung, T. H.; Makeyev, E. V. Hybridization-proximity labeling reveals spatially ordered interactions of nuclear RNA compartments. *Molecular cell* **2022**, *82* (2), 463-478.e11. DOI: 10.1016/j.molcel.2021.10.009. Published Online: Nov. 5, 2021.

(28) Li, R.; Zou, Z.; Wang, W.; Zou, P. Metabolic incorporation of electron-rich ribonucleosides enhances APEX-seq for profiling spatially restricted nascent transcriptome. *Cell chemical biology* **2022.** DOI: 10.1016/j.chembiol.2022.02.005. Published Online: Feb. 28, 2022.

(29) Wang, P.; Tang, W.; Li, Z.; Zou, Z.; Zhou, Y.; Li, R.; Xiong, T.; Wang, J.; Zou, P. Mapping spatial transcriptome with light-activated proximity-dependent RNA labeling. *Nature chemical biology* **2019**, *15* (11), 1110–1119. DOI: 10.1038/s41589-019-0368-5. Published Online: Oct. 7, 2019.

(30) Engel, K. L.; Lo, H.-Y. G.; Goering, R.; Li, Y.; Spitale, R. C.; Taliaferro, J. M. Analysis of subcellular transcriptomes by RNA proximity labeling with Halo-seq. *Nucleic acids research* **2022**, *50* (4), e24. DOI: 10.1093/nar/gkab1185.

(31) Jones, K. A.; Kentala, K.; Beck, M. W.; An, W.; Lippert, A. R.; Lewis, J. C.; Dickinson, B. C. Development of a Split Esterase for Protein-Protein Interaction-Dependent Small-Molecule Activation. *ACS central science* **2019**, *5* (11), 1768–1776. DOI: 10.1021/acscentsci.9b00567. Published Online: Sep. 24, 2019.

(32) Flynn, R. A.; Zhang, Q. C.; Spitale, R. C.; Lee, B.; Mumbach, M. R.; Chang, H. Y. Transcriptome-wide interrogation of RNA secondary structure in living cells with

icSHAPE. *Nature protocols* **2016**, *11* (2), 273–290. DOI: 10.1038/nprot.2016.011. Published Online: Jan. 14, 2016.

(33) Yin, J.; Bai, Y.; Mao, M.; Zhu, G. Silver-catalyzed regio- and stereoselective addition of carboxylic acids to ynol ethers. *The Journal of organic chemistry* **2014**, *79* (19), 9179–9185. DOI: 10.1021/jo501615a. Published Online: Sep. 15, 2014.

(34) Stang, P. J. Ynol esters and alkynyl(phenyl)iodonium chemistry. *Russ Chem Bull* **1993**, *42* (1), 12–23. DOI: 10.1007/BF00699967.

(35) Gray, V. J.; Wilden, J. D. The chemistry of ynol and thioynol ethers. *Organic & biomolecular chemistry* **2016**, *14* (41), 9695–9711. DOI: 10.1039/C6OB01776B.

(36) Zaccara, S.; Ries, R. J.; Jaffrey, S. R. Reading, writing and erasing mRNA methylation. *Nature reviews. Molecular cell biology* **2019**, *20* (10), 608–624. DOI: 10.1038/s41580-019-0168-5. Published Online: Sep. 13, 2019.

(37) Shi, H.; Wei, J.; He, C. Where, When, and How: Context-Dependent Functions of RNA Methylation Writers, Readers, and Erasers. *Molecular cell* **2019**, *74* (4), 640–650. DOI: 10.1016/j.molcel.2019.04.025.

(38) Dassi, E. *Post-transcriptional gene regulation*, 2nd edition; Methods in molecular biology, Vol. 1358; Humana Press, 2016.

(39) McIntyre, A. B. R.; Gokhale, N. S.; Cerchietti, L.; Jaffrey, S. R.; Horner, S. M.; Mason, C. E. Limits in the detection of m6A changes using MeRIP/m6A-seq. *Scientific reports* **2020**, *10* (1), 6590. DOI: 10.1038/s41598-020-63355-3. Published Online: Apr. 20, 2020.

(40) Dierks, D.; Garcia-Campos, M. A.; Uzonyi, A.; Safra, M.; Edelheit, S.; Rossi, A.; Sideri, T.; Varier, R. A.; Brandis, A.; Stelzer, Y.; van Werven, F.; Scherz-Shouval, R.; Schwartz, S. Multiplexed profiling facilitates robust m6A quantification at site, gene and sample resolution. *Nature methods* **2021**, *18* (9), 1060–1067. DOI: 10.1038/s41592-021-01242-z. Published Online: Sep. 3, 2021.

(41) Tang, Y.; Chen, K.; Song, B.; Ma, J.; Wu, X.; Xu, Q.; Wei, Z.; Su, J.; Liu, G.; Rong, R.; Lu, Z.; Magalhães, J. P. de; Rigden, D. J.; Meng, J. m6A-Atlas: a comprehensive knowledgebase for unraveling the N6-methyladenosine (m6A) epitranscriptome. *Nucleic acids research* **2021**, *49* (D1), D134-D143. DOI: 10.1093/nar/gkaa692.

(42) Doroszuk, J.; Musiejuk, M.; Ponikiewski, Ł.; Witt, D. Convenient and Efficient Diastereoselective Preparation of Functionalized Z -Alkenyl Sulfides. *Eur. J. Org. Chem.* **2018**, *2018* (45), 6333–6337. DOI: 10.1002/ejoc.201801181.

Chapter 6

SUMMARY AND PERSPECTIVES

6.1 Thesis summary

The thermodynamic stability of thioesters places them at the center of a reactivity scale for nucleophile addition among acyl compounds, somewhere above unreactive amides and poorly reactive oxoesters, but below overactivated carboxylic acid anhydrides and acyl chlorides. Therefore, thioesters are effectively many orders of magnitude more reactive than oxoesters as thiol or nitrogen nucleophiles as well as alkoxide[1–3], while being relatively resistant to hydrolysis at neutral pH[1,2,4,5], especially for *S*-alkyl thioesters. The intrinsic high stability of *S*-alkyl thioesters makes them an important biological species involved in various biological processes[6]. And *S*-aryl thioester reactivity can be tuned by changing the substitution group on the aromatic ring, making it an attractive acylation reagent in chemical biology application[7].

The first part of my thesis focused on the exploration of the biological roles of *S*-alkyl thioester, and in particular, protein *S*-palmitoylation. *S*-palmitoylation is an abundant and dynamic post-translational modification that facilitates protein trafficking and function[8,9]. The addition of this modification is catalyzed by ‘writer’ (DHHC-PATs), which attaches a 16-carbon fatty acyl group to specific cysteines. The reverse reaction is catalyzed by ‘eraser’ (APTs), which hydrolyze the thioester bond to participate in palmitate turnover. Chapters 2, 3 and 4 describe my efforts in the development of chemical approaches to study both writer and eraser enzymes of protein S-palmitoylation.

Chapter 2 presented the development of new generation DPPs with improved *S*-depalmitoylase specificity. The first-generation DPPs are capable of monitoring dynamic APT activity in live cells. However, use of a natural C16 lipid limits the water solubility of the probe, requiring that the natural lipid be substituted by a C8 surrogate lipid. In DPP-5, the inclusion of succinylated piperazine improved solubility and enabled modification of the masking cysteine with the highly hydrophobic, natural C16 lipid substrate. The higher solubility and enhanced enzyme specificity of DPP-5 make it an excellent tool for visualizing global *S*-depalmitoylase activity both *in vitro* and in live cells[10]. During the discovery of ABHD10, DPP-5 also played a crucial role in validating the *S*-depalmitoylase activity of ABHD10[11]. We anticipate that DPP-5 can be a useful new tool to assay *S*-depalmitoylase activity. DPP-5 has been shared with many other groups since it was disclosed, and it helped one group discover and validate a new class of *S*-palmitoylation eraser[12].

Chapter 3 described the development of mitoFP, a mitochondria-targeted APT inhibitor, and the journey to discover a new mitochondrial APT, ABHD10[11]. Previously, our lab has developed chemical tools to selectively visualize APT activity in the mitochondria with mitoDPPs and identified APT1 as the first regulator of mitochondrial *S*-depalmitoylation. To further understand the functional consequences of *S*-depalmitoylase activity in this organelle, I designed and synthesized the spatially constrained mitochondrial pan-APT inhibitor, mitoFP. Live cell imaging of mitochondrial H_2O_2 in combination with mitochondrial APT perturbation leads us to uncover that mitochondrial APT inhibition diminishes mitochondrial antioxidant buffering capacity. However, this effect was not mediated by APT1, the only known mitochondrial APT[13], but rather by another mitochondrial resident protein, ABHD10, for which no endogenous function was yet known.

Biochemical assays, including the DPP-5 assay, demonstrated that ABHD10 is a new member of the *S*-palmitoylation eraser family. We then identified a key cellular antioxidant protein, peroxiredoxin 5 (PRDX5), as the first target of ABHD10 *S*-depalmitoylase activity. Furthermore, we show that *S*-palmitoylation exclusively occurs at the active site cysteine residue in PRDX5, providing a mechanism connecting ABHD10-mediated S-depalmitoylation of PRDX5 and its antioxidant capacity. More broadly, expanding the APT family by the addition of ABHD10 will help assign more substrates and functions to mitochondrial *S*-depalmitoylation. Additionally, the new mitochondrial-targeted APT inhibitor will help the *S*-palmitoylation research community to further explore the function and regulation of this process in mitochondria.

Chapter 4 presented the development of a turn-on fluorescence-based high-throughput screening method for DHHC-PATs. By combining the docking and rational design, I repurposed the APT probes to measure DHHC-PATs activity in vitro. The modified PTPs serve as mimetics of DHHC-PATs cofactor Palm-CoA, and it can be recognized by DHHC-PATs. As a proof of concept, we performed an initial high-throughput screen with over 1,600 acrylamide compounds and identified a few that moderately inhibit DHHC20. Although we have only screened three DHHC isoforms, we anticipate that the modular and flexible synthesis of the PTPs may allow expansion of the library to other members of the DHHC family, and perhaps even adapted for other transferases, such as N-myristoyltransferase family proteins (NMTs).

Chapter 5 presented the efforts toward the development of an RNA proximity labeling method that utilizes an ester-caged *S*-aryl thioester that reacts with the 2'-OH position of RNA nucleosides in the presence of BS2 esterase. First, we showed that 4-

nitrothioester can acylate RNA and designed an ester cage to mask the high reactivity of 4-nitrothioester. Then an iridium-catalyzed regio- and stereoselective addition reaction was discovered to install the ester on the enol form of the thioester. We showed that the ester-caged thioester can be processed by BS2 esterase and it can label RNA in cells that express the BS2 enzyme. Preliminary RNA-Seq data suggested that the BS2 esterase-ester caged thioester pair can be used for RNA proximity labeling.

6.2 Future perspectives on APTs

The chemical tools presented in this thesis, such as DPP5 and mitoFP, enable us to gain a more discriminating view of APTs and can be used to gain insight into the subcellular organization and geographic distribution of *S*-depalmitoylase activity. However, we still do not fully understand how *S*-depalmitoylation is regulated, nor its biological consequences, particularly at the level of individual APTs. Next-generation DPPs should feature targeting capabilities for individual APTs and different organelles. For example, histone H3 is found to be *S*-palmitoylated[14], but no APTs have been found present in the nucleus. A nuclear-targeted DPP would be very useful to examine APT activity in this organelle.

Substrate annotation also remains extremely challenging, owing to the highly dynamic process of protein *S*-palmitoylation and compensation between APTs. Take ABHD10 for example, where we identified PRDX5 as the first substrate and showed it played a crucial role in mitochondrial redox homeostasis. However, global substrate profiling remains a challenge: our attempt to profile ABHD10 substrates by combining the ABE assay and proteomics resulted in no clear substrates due to the compensation between APTs. Fortunately, a selective inhibitor of ABHD10 is already available, which will facilitate the study of APT function in live cells with temporal control[15]. In addition, a

fluorescent-quenched substrate library has been developed to map the substrate specificity APTs *in vitro*. These peptide substrates contain a palmitoylated cysteine that releases the quencher molecule upon thioester hydrolysis, thus generating a fluorescence signal. Furthermore, the authors demonstrated that a Scribble-derived peptide sequence was preferentially hydrolyzed by APT2 and not APT1, correlating with a published cellular study that showed APT2 was the enzyme that depalmitoylated Scribble[16]. This library could be potentially used to map the peptide specificity of ABHD10.

By comparing enzyme kinetics with APT1, we noticed that ABHD10 has a lower turnover rate but it binds more tightly to the substrate. This measurement agrees with the observation of the presence of a unique cap domain in the structure of ABHD10, which might contribute to substrate recognition. Solving the lipid-bound ABHD10 structure and co-crystal structure of ABHD10-PRDX5 would provide insight into how lipid substrates are accommodated in the enzyme active site and engage in the catalytic reaction and ABHD10 substrate recognition, respectively. In addition, unnatural amino acid photo-crosslinking followed by mass spectrometry could be applied to identify ABHD10 interacting proteins. Genetically engineering ABHD10 in proximity to the active sites or potential binding sites with a diazirine unnatural amino acid[17,18] may capture its substrate. Using the ABHD10 crystal structure as a guide, such incorporation sites could be within the cap domain. However, a high-throughput *in vitro* screening may be necessary to identify optimal incorporation position(s).

MitoFP provides a useful tool to study the biological function of mitochondrial protein S-palmitoylation. In addition to the regulation of redox homeostasis, as demonstrated in this thesis, mitochondrial APTs may regulate lipid homeostasis since mitochondria contain

a variety of unique lipid classes. Indeed, preliminary metabolomics experiments suggest that ABHD10 regulates cellular lipid composition to a certain degree. More metabolomics experiments with purified mitochondria and mitoFP treatment may result in a more dramatic effect. Furthermore, using mitoFP in combination with chemo-proteomic approaches[19], we have now been able to evaluate the effects of perturbing the mitochondrial *S*-palmitoylome, identify targeted proteins, and assess the biological roles of mitochondrial APTs. The design principle of mitoFP described in this thesis work could also be applied to develop other organelle-targeted APT/DHHC inhibitors.

6.3 Future perspectives on DHHC-PATs

Mounting evidence has suggested that DHHC-PATs are involved in both physiological and pathological processes. Isozyme-selective inhibitors or pan-active inhibitors can be used to block a specific protein or a group of related proteins, thereby enhancing the understanding of S-acylation-mediated events by DHHC. It is anticipated that these methods will permit studies of the acute effects of *S*-acylation disruption without reliance on longer-term zDHHC depletion (e.g., using RNAi or CRISPR technology). In addition, the application of chemical inhibitors to DHHC proteins allows the direct evaluation of their potential as drug targets in cells and could provide a platform for future drug development.

Despite the turn-on fluorescence-based assay described in this thesis being proven to be suitable for high-throughput screening, our preliminary screening of 1600 compounds failed to yield good hit compounds. A large library of compounds is needed to increase the chance to find lead compounds. For example, a study recently describes a FRET-based high throughput assay for the discovery of compounds that interfere with the auto-acylation

of zDHHC2. A screen of >350,000 compounds identified two related tetrazole-containing compounds that inhibited both zDHHC2 auto-acylation and substrate *S*-acylation in cell-free systems[20].

The majority of the DHHC assays developed to date have been *in vitro* tests, but improved cell-based assays are also needed in this field. DHHC activity in cells can be monitored by tracking both the auto-acylation and substrate protein *S*-acylation, but the dynamic regulation of multiple DHHCs and APTs must be considered. For example, a recently developed novel yeast-based high-throughput method utilizes a reporter gene that responds to the acylation status of a palmitoylation substrate fused to a transcription factor[21]. However, the method relies on a highly specific DHHC-substrate pair that is uncommon in mammalian cells.

In summary, a new era of pursuing highly potent and selective DHHC-PATs inhibitors is emerging, and the development of truly selective inhibitors of the zDHHC family would be a remarkable breakthrough for the field.

6.4 Future perspectives on thioester-based acylation reagent

The inspiration for applying 4-nitrothioester for RNA labeling comes from the RNA SHAPE chemistry that acylation reagent can react with 2'-OH on the RNA. The fact that 4-nitrothioester reacts with RNA but not DNA provides strong evidence that the labeling event is installing 2'-O-acylation, but the further characterization of reaction products is required to fully understand the mechanism. In combination with the biorthogonal ester-esterase pair, our preliminary suggested 4-nitrothioester may serve as a reactive intermediate in the RNA proximity labeling. Thus, if 4-nitrothioester is proven to function as a SHAPE reagent, preparing RNA-seq libraries with RTs that go through stop sites and install mutations, or by

processing samples differently and looking at RT stops, would provide information not only about where a given transcript is located or which protein it interacts with, but also information about the shape of that RNA in the given context.

The use of ester to mask the enol form of the acyl compound is key to linking esterase activity with the generation of the thioester intermediate. To use α-alkoxy thioenol esters as a thioester precursor in live cells for labeling purposes, both stability and thioester reactivity need to be considered. 4-nitrothioester has thus far proven to strike the best balance. Some leaving groups were too reactive and hydrolyzed immediately, while others were completely unreactive after ester unmasking and had half-lives on the order of tens of days. Efforts are currently underway to continue to tune the leaving group (and thus the reactivity) of our masked acylating probe. In principle, therefore, one goal could be to develop a suite of variably reactive probes to react with different biomolecules with various labeling radii.

Despite our BS2 esterase / methylcyclopropyl ester selective unmasking-based genetically encoded technologies having been proven to be useful[22], their widespread use will be considerably hindered by a critical failure: the methylcyclopropyl mask proved insufficiently bio-orthogonal in many cell lines, such as HepG2 cells. A better bio-orthogonal ester/esterase pair would facilitate the application *in vivo*. Our preliminary experiments have already established that a bulkier ester is stable in HepG2 cells and a large screen is currently underway to find a BS2 variant that can process the bulky ester effectively.

6.5 References

(1) CONNORS, K. A.; BENDER, M. L. The Kinetics of Alkaline Hydrolysis and n-Butylaminolysis of Ethyl p-Nitrobenzoate and Ethyl p-Nitrothiolbenzoate. *J. Org. Chem.* **1961**, *26* (7), 2498–2504.

(2) Hupe, D. J.; Jencks, W. P. Nonlinear structure-reactivity correlations. Acyl transfer between sulfur and oxygen nucleophiles. *J. Am. Chem. Soc.* **1977**, *99* (2), 451–464.

(3) Um Ik-Hwan; Kim Ga-Ryung; Kwon Dong-Sook. The Effects of Solvation and Polarizability on the Reaction of S-p-Nitrophenyl Thiobenzoate with Various Anionic Nucleophiles. *Bulletin of the Korean Chemical Society* **1994**, *15* (7), 585–589.

(4) Jencks, W. P.; CORDES, S.; CARRIUOLO, J. The free energy of thiol ester hydrolysis. *The Journal of biological chemistry* **1960**, *235*, 3608–3614.

(5) Yang, W.; Drueckhammer, D. G. Understanding the relative acyl-transfer reactivity of oxoesters and thioesters: computational analysis of transition state delocalization effects. *J. Am. Chem. Soc.* **2001**, *123* (44), 11004–11009.

(6) Song, J.; Wang, J.; Jozwiak, A. A.; Hu, W.; Swiderski, P. M.; Chen, Y. Stability of thioester intermediates in ubiquitin-like modifications. *Protein science: a publication of the Protein Society* **2009**, *18* (12), 2492–2499.

(7) Agouridas, V.; El Mahdi, O.; Diemer, V.; Cargoët, M.; Monbaliu, J.-C. M.; Melnyk, O. Native Chemical Ligation and Extended Methods: Mechanisms, Catalysis, Scope, and Limitations. *Chemical reviews* **2019**, *119* (12), 7328–7443.

(8) Lanyon-Hogg, T.; Faronato, M.; Serwa, R. A.; Tate, E. W. Dynamic Protein Acylation: New Substrates, Mechanisms, and Drug Targets. *Trends in biochemical sciences* **2017**, *42* (7), 566–581.

(9) Blanc, M.; David, F. P. A.; van der Goot, F. G. SwissPalm 2: Protein S-Palmitoylation Database. *Methods in molecular biology (Clifton, N.J.)* **2019**, *2009*, 203–214.

(10) Qiu, T.; Kathayat, R. S.; Cao, Y.; Beck, M. W.; Dickinson, B. C. A Fluorescent Probe with Improved Water Solubility Permits the Analysis of Protein S-Depalmitoylation Activity in Live Cells. *Biochemistry* **2018**, *57* (2), 221–225.

(11) Cao, Y.; Qiu, T.; Kathayat, R. S.; Azizi, S.-A.; Thorne, A. K.; Ahn, D.; Fukata, Y.; Fukata, M.; Rice, P. A.; Dickinson, B. C. ABHD10 is an S-depalmitoylase affecting redox homeostasis through peroxiredoxin-5. *Nature chemical biology* **2019**, *15* (12), 1232–1240.

(12) Luebben, A. V.; Bender, D.; Becker, S.; Crowther, L. M.; Erven, I.; Hofmann, K.; Söding, J.; Klemp, H.; Bellotti, C.; Stäuble, A.; Qiu, T.; Kathayat, R. S.; Dickinson, B. C.; Gärtner, J.; Sheldrick, G. M.; Krätzner, R.; Steinfeld, R. Cln5 represents a new type of cysteine-based S -depalmitoylase linked to neurodegeneration. *Sci. Adv.* **2022**, *8* (15).

(13) Kathayat, R. S.; Cao, Y.; Elvira, P. D.; Sandoz, P. A.; Zaballa, M.-E.; Springer, M. Z.; Drake, L. E.; Macleod, K. F.; van der Goot, F. G.; Dickinson, B. C. Active and dynamic

mitochondrial S-depalmitoylation revealed by targeted fluorescent probes. *Nature communications* **2018**, *9* (1), 334.

(14) Wilson, J. P.; Raghavan, A. S.; Yang, Y.-Y.; Charron, G.; Hang, H. C. Proteomic analysis of fatty-acylated proteins in mammalian cells with chemical reporters reveals S-acylation of histone H3 variants. *Molecular & cellular proteomics: MCP* **2011**, *10* (3), M110.001198.

(15) Zuhl, A. M.; Mohr, J. T.; Bachovchin, D. A.; Niessen, S.; Hsu, K.-L.; Berlin, J. M.; Dochnahl, M.; López-Alberca, M. P.; Fu, G. C.; Cravatt, B. F. Competitive activity-based protein profiling identifies aza-β-lactams as a versatile chemotype for serine hydrolase inhibition. *J. Am. Chem. Soc.* **2012**, *134* (11), 5068–5071.

(16) Hernandez, J. L.; Davda, D.; Cheung See Kit, M.; Majmudar, J. D.; Won, S. J.; Gang, M.; Pasupuleti, S. C.; Choi, A. I.; Bartkowiak, C. M.; Martin, B. R. APT2 Inhibition Restores Scribble Localization and S-Palmitoylation in Snail-Transformed Cells. *Cell chemical biology* **2017**, *24* (1), 87–97.

(17) Chou, C.; Uprety, R.; Davis, L.; Chin, J. W.; Deiters, A. Genetically encoding an aliphatic diazirine for protein photocrosslinking. *Chem. Sci.* **2011**, *2* (3), 480–483.

(18) Hoffmann, J.-E.; Dziuba, D.; Stein, F.; Schultz, C. A Bifunctional Noncanonical Amino Acid: Synthesis, Expression, and Residue-Specific Proteome-wide Incorporation. *Biochemistry* **2018**, *57* (31), 4747–4752.

(19) Wan, J.; Roth, A. F.; Bailey, A. O.; Davis, N. G. Palmitoylated proteins: purification and identification. *Nature protocols* **2007**, *2* (7), 1573–1584.

(20) Salaun, C.; Takizawa, H.; Galindo, A.; Munro, K. R.; McLellan, J.; Sugimoto, I.; Okino, T.; Tomkinson, N. C.; Chamberlain, L. H. *Development of a novel high-throughput screen for the identification of new inhibitors of protein S-acylation*, 2022. DOI: 10.1101/2022.03.17.484726.

(21) Coronel Arrechea, C.; Giolito, M. L.; García, I. A.; Soria, G.; Valdez Taubas, J. A novel yeast-based high-throughput method for the identification of protein palmitoylation inhibitors. *Open biology* **2021**, *11* (8), 200415.

(22) Jones, K. A.; Kentala, K.; Beck, M. W.; An, W.; Lippert, A. R.; Lewis, J. C.; Dickinson, B. C. Development of a Split Esterase for Protein-Protein Interaction-Dependent Small-Molecule Activation. *ACS central science* **2019**, *5* (11), 1768–1776.